



HAL
open science

Syntheses, Crystal Structures and Characterizations of Mono- and Polynuclear Ni- and Co-based Molecular Magnets

Yiting Wang

► **To cite this version:**

Yiting Wang. Syntheses, Crystal Structures and Characterizations of Mono- and Polynuclear Ni- and Co-based Molecular Magnets. Inorganic chemistry. Université Paris Saclay (COMUE), 2019. English. NNT : 2019SACLS225 . tel-03331627

HAL Id: tel-03331627

<https://theses.hal.science/tel-03331627>

Submitted on 2 Sep 2021

HAL is a multi-disciplinary open access archive for the deposit and dissemination of scientific research documents, whether they are published or not. The documents may come from teaching and research institutions in France or abroad, or from public or private research centers.

L'archive ouverte pluridisciplinaire **HAL**, est destinée au dépôt et à la diffusion de documents scientifiques de niveau recherche, publiés ou non, émanant des établissements d'enseignement et de recherche français ou étrangers, des laboratoires publics ou privés.

Syntheses, Crystal Structures and Characterizations of Mono- and Polynuclear Ni- and Co-based Molecular Magnets

Thèse de doctorat de l'Université Paris-Saclay
préparée à l'Université Paris-Sud

École doctorale n°571 Sciences chimiques : molécules, matériaux,
instrumentation et biosystèmes (2MIB)
Spécialité de doctorat : Chimie

Thèse présentée et soutenue à Orsay, le 26 juillet 2019, par

Mme Yiting WANG

Composition du Jury :

M. Pierre Mialane Professeur, MIM, Université Versailles Saint-Quentin-en-Yvelines	Président
M. Guillem Aromí Professeur, GMMF, Universitat de Barcelona	Rapporteur
M. Smaïl Triki Professeur, CEMCA, Université de Bretagne Occidentale	Rapporteur
M. Laurent Lisnard Chargé de recherche, ERMES, Sorbonne Université	Examineur
M. Talal Mallah Professeur, ICMMO, Université Paris-Sud	Directeur de thèse

Université Paris-Saclay

Espace Technologique / Immeuble Discovery

Route de l'Orme aux Merisiers RD 128 / 91190 Saint-Aubin, France



Acknowledgment

It is indeed my great fortune and honor to have the opportunity to pursue my Ph.D. degree in the Laboratoire Chimie Inorganique (LCI), Institut de Chimie Moléculaire et des Matériaux d'Orsay (ICMMO). I am very grateful to everyone that has made this possible and rewarding.

Foremost I would like to express my deep gratitude to my supervisor: Prof. Talal Mallah, for accepting me as a Ph.D. student and making everything possible. His insightful vision, guidance, support and understanding help me to grow up as a Ph.D. student. I also deeply appreciate his careful revision of my thesis.

I also thank the China Scholarship Council, funded my Ph.D. study abroad for four years. I express my deep gratitude to all the jury members for their coming.

Heartfelt thanks go to Zakaria Halime, who paid much attention to conduct the electrochemical measurements with my samples and analyze the results. François Lambert also deserves my gratitude for the efforts he devoted to help me with my chemical experiments and some organic ligands he prepared for me. Without their aid and support, my research would not go that smooth.

I would like to thank Eric Rivière and Régis Guillot, our distinguished magnetic engineer and excellent crystallographer. Their nice work makes up an indispensable part of this dissertation.

My sincere thanks go to Benjamin Cahier, Nicolas Suaud and Nathalie Guihéry for their pretty work on theoretical parts in the dissertation, which make it more complete and more convincing.

Acknowledgement

I'd like to express my sincere thanks to all the technical services and the administrations in ICMMO. I am also grateful to all the group members in LCI (present and past), who make the working days in LCI full of laughter and no more boring, especially Feng, Fatima, Axel, Tam, Amanda, Adama, Linh, Luqiong, Jo, Khaled, Antoine.

A special thanks goes to Eason Chan for his spiritual support, without whom it could be hard to get over the tough moments. His laughter can always heal me when I feel bad and encourage me to have a positive and optimistic attitude to face difficulties.

I'd like to thank my dear friends, both in China and abroad, for their encouragement and comfort whenever I needed. I appreciate the friendship and all the wonderful memories they brought to me. Finally, heartfelt thanks go to my family members for their deeply love and understanding, which is always my most powerful backup. It's impossible for me to finish my study abroad without their continuous support.

Abstract

The objective of elaborating “magnets by design” can be achieved by tailoring the molecular structures of coordination complexes. The designed molecules are expected to exhibit the characteristics required for specific applications, virtually resulting from their rich structural diversity. Mononuclear Ni-based complexes with large magnetic anisotropy and polynuclear Ni- and Co-based molecules are designed in this dissertation. The syntheses, magnetic studies, and electrochemical properties of the complexes containing non-innocent bridge ligand are investigated.

The Ni(II) mononuclear complexes with trigonal bipyramid geometry are prepared by tuning the axial ligands and the counter anions. The effect of the nature of the axial ligands and the structural change induces by the counter anions on magnetic anisotropy is studied experimentally and analyzed with the help of theoretical calculations.

Large organic molecules are used to design trinuclear complexes with large magnetic anisotropy and weak exchange coupling. Several polynuclear Ni- and Co-based complexes with TTC^{3-} acting as an innocent bridging ligand and HHTP as a typical non-innocent ligand, are crystalized with various structures (TTC = Trithiocyanurate; HHTP = Hexahydroxytriphenylene). For the complexes containing the non-innocent ligand (HHTP), radical anions are produced by electrochemistry. The combination of spectroelectrochemical and Electron Paramagnetic Spectroscopy coupled to electrochemistry studies allow investigating the delocalization of the electrons on the generated organic radicals and the exchange coupling among the metal ions.

Résumé

L'objectif consistant à élaborer des «aimants par conception» peut être atteint en adaptant les structures moléculaires des complexes de coordination. Les molécules conçues devraient présenter les caractéristiques requises pour des applications spécifiques, qui résultent de leur riche diversité structurale. Des complexes mononucléaires à base de Ni avec une grande anisotropie magnétique et des molécules polynucléaires à base de Ni et de Co sont préparés et étudiés dans cette thèse. Les synthèses, les études magnétiques et les propriétés électrochimiques des complexes contenant un ligand pontant non innocent sont étudiées. Les complexes mononucléaires Ni(II) à géométrie bipyramide trigonale sont préparés avec des ligands axiaux et les contre-anions différents. L'effet de la nature des ligands axiaux et du changement structural induit par les contre-anions sur l'anisotropie magnétique est étudié expérimentalement et analysé à l'aide de calculs théoriques. Des molécules organiques sont utilisées pour concevoir des complexes trinucéaires à grande anisotropie magnétique et à couplage d'échange faible. Plusieurs complexes polynucléaires à base de Ni et de Co où le TTC^{3-} agit comme un ligand pontant innocent et le HHTP^{3-} comme un ligand non innocent typique sont cristallisés avec diverses structures (TTC = Trithiocyanurate; HHTP = Hexahydroxytriphénylène). Pour les complexes contenant le ligand non innocent (HHTP), les anions radicalaires sont produits par électrochimie. La combinaison de la spectro-électrochimie et de la spectroscopie à résonance paramagnétique électronique couplée à des études d'électrochimie permet d'étudier la délocalisation des électrons sur les radicaux organiques générés et le couplage d'échange entre les ions métalliques.

Table of Contents

<i>Acknowledgment</i>	<i>I</i>
<i>Abstract</i>	<i>III</i>
<i>Résumé</i>	<i>IV</i>
<i>Table of Contents</i>	<i>V</i>
<i>Chapter I Introduction</i>	<i>1</i>
1.1 General introduction	1
1.1.1 Background	1
1.1.2 Motivation and objectives	2
1.2 Molecular magnetism	3
1.2.1 A brief introduction of the history of magnetism	3
1.2.2 Molecular magnets	4
1.2.3 Some important principles in molecular magnetism	4
1.2.3.1 Zeeman effect and Zero-field splitting (ZFS).....	5
1.2.3.2 Exchange coupling	7
1.2.3.3 Total Spin Hamiltonian	8
1.2.3.4 Jahn-Teller effect	8
1.2.4 Magnetic characterizations and data analysis	9
1.2.5 The first Molecular magnet.....	12
1.3 Mononuclear molecules with anisotropy	13
1.3.1 Design of anisotropic mononuclear complexes	14
1.3.2 Some mononuclear complexes based on Ni(II) and Co(II)	17
1.3.2.1 Some Ni(II) molecular magnet	17
1.3.2.2 Some Co(II) molecular magnets.....	18
1.4 Polynuclear magnetic complexes built from anisotropic mononuclear species.....	21
1.4.1 The choice of bridging ligand	22
1.4.1.1 Innocent ligands	23
1.4.1.2 Non-innocent ligands.....	23
1.4.2 Polynuclear complexes with bridging ligands	27
1.4.2.1 Polynuclear complexes based on Ni	27
1.4.2.2 Polynuclear complexes based on Co	30
1.4.2.3 Polynuclear complexes based on other transition metal ions	33
1.5 This thesis.....	37

Table of contents

1.6 References.....	38
<i>Chapter II Engineering the Ising-type anisotropy in Ni(II) complexes based on Tris(2-(dimethylamino)ethyl)amine (Me₆tren)</i>	<i>45</i>
2.1 Introduction.....	45
2.2 Experimental section.....	48
2.2.1 Syntheses	48
2.2.2 Physical Measurements	53
2.3 Results and discussion.....	55
2.3.1 Molecular Structures Description	55
2.3.1.1 Molecular structure of Complex 2-1.....	55
2.3.1.2 Molecular structures of Complexes 2-2, 2-3 and 2-4	58
2.3.1.3 Molecular structure of Complexes 2-5, 2-6 and 2-7	60
2.3.2 Magnetism	63
2.3.2.1 Magnetic properties of Complex 2-1.....	63
2.3.2.2 Magnetic properties of Complexes 2-2, 2-3, 2-4	67
2.3.2.3 Magnetic properties of Complexes 2-5 and 2-6.	72
2.3.2.4 Magnetic properties of Complex 2-7.....	74
2.4 Theoretical Calculations	77
2.5 Conclusions.....	83
2.6 References.....	84
<i>Chapter III Ni(II) and Co(II) molecular magnets based on Trithiocyanurate (TTC)</i>	<i>87</i>
3.1 Introduction.....	87
3.2 Experimental section.....	89
3.2.1 Syntheses	89
3.2.2 Physical Measurements	92
3.3 Results and discussion.....	93
3.3.1 Molecular Structures Description	93
3.3.1.1 Molecular structure of Complexes 3-1 and 3-2	93
3.3.1.2 Molecular structure of Complexes 3-3 and 3-4	97
3.3.1.3 Molecular structure of Complex 3-5.....	102
3.3.2 Magnetism	102
3.3.2.1 Magnetic properties of Complex 3-1 and 3-2.....	103
3.3.2.2 Magnetic properties of Complex 3-3 and 3-4.....	106
3.3.2.3 Magnetic properties of Complex 3-5.....	108
3.4 Theoretical Calculations	110
3.4.1 Theoretical studies for Complexes 3-1 and 3-2	110
3.4.2 Theoretical studies for Complex 3-3	117

Table of contents

3.4.3 Theoretical studies for Complex 3-5	119
3.5 Conclusions.....	123
3.6 References.....	124
<i>Chapter IV Ni(II) and Co(II) molecular magnets based on Hexahydroxytriphenylene (HHTP)</i>	<i>127</i>
4.1 Introduction.....	127
4.2 Experimental section.....	130
4.2.1 Syntheses	130
4.2.2 Physical Measurements	133
4.3 Results and discussion.....	134
4.3.1 Molecular Structures Description	134
4.3.1.1 Molecular structure of Complex 4-1.....	134
4.3.1.2 Molecular structure of Complex 4-2.....	137
4.3.1.3 Molecular structure of Complex 4-3.....	139
4.3.2 Magnetism	142
4.3.2.1 Magnetic properties of Complex 4-1.....	142
4.3.2.2 Magnetic properties of Complex 4-2.....	144
4.3.2.3 Magnetic properties of Complex 4-3.....	146
4.3.3 Electronic Spectra and Electrochemical properties	148
4.3.3.1 Electronic spectrum and electrochemistry of Complex 4-1	149
4.3.3.2 Electronic spectrum and electrochemistry of Complex 4-2	150
4.3.3.3 Electronic spectrum and electrochemistry of Complex 4-3	153
4.4 Theoretical Calculations	155
4.5 Conclusions.....	156
4.6 References.....	157
<i>Chapter V Conclusion and future work</i>	<i>161</i>
5.1 Conclusion	161
5.2 Future work	163
<i>Appendix I The Crystallographic data</i>	<i>165</i>
1.1 The complexes based on ligand Me ₆ tren.....	165
1.2 The complexes based on ligand TTC	168
1.3 The complexes based on ligand HHTP	171
<i>Résumé</i>	<i>173</i>

Chapter I

Introduction

1.1 General introduction

1.1.1 Background

Since the theory of coordination complexes was first reported by Werner in 1893,¹ it has been developed for more than one century and has become one of the most active and innovative research frontiers in inorganic chemistry. It crosses other branches of chemistry, like physical chemistry, organic chemistry and analytical chemistry. Furthermore, it extends to materials, physics, biology and other disciplines, forming some new emerging research topics.^{2,3} The study of Prussian blue analogues⁴⁻⁶ and metal phosphonates,^{7,8} the prototypes of coordination polymers, laid a solid foundation for the later research on coordination chemistry.

With the development of technology in the area of electronics, information, energy and medicine, such complexes with special physical,⁹ chemical^{10,11} and biologic functions^{12,13} are booming in the international community.

Coordination complexes,¹⁴ which are constructed by coordination bonds and weak interaction forces between molecules, have potential applications in many areas, such as ion exchange,¹⁵ adsorption and selective catalysis,¹⁶ optoelectronics¹⁷ and magnetic materials.¹⁸ By changing the metal ions, ligands or the ratio of metal ions to ligands, the coordination modes will be various, which plays a significant role in molecular properties. The flexibility and tunability of coordination complex make it possible to create new molecules and new units for building one, two- and three- dimensional frameworks.¹⁹

Therefore, the design and synthesis of these complexes attract considerable attention from all over the world.

As an essential part of multifunctional materials, magnetic materials have shown significant economic and social benefits in the modern high-tech field. Traditional magnetic materials are limited in some high technologies and cutting-edge technologies due to their high density and huge magnetic loss. While molecular magnets have small volume, are relatively light, possess high transparency, good solubility in comparison with traditional magnetic materials. And through changing metal ions and organic ligands, structure diversification and composite process can be achieved much more easily. The magnetic properties are greatly influenced by the structure and composite of the complexes, thus, development of magnetic materials with desirable and controllable magnetic properties becomes extremely important.

1.1.2 Motivation and objectives

As magnetism is a crucial part in many aspects of our daily life and particularly in electric technology, it is important to create new molecule-based materials and gain a better understanding of their magnetic properties. As more investigation and research efforts has been made in this field, new magnetic materials with promising and desirable properties are desperately needed. The main advantage of molecular magnets is their tailorability, resulting from the rich structural diversity, to exhibit the required properties for targeted applications, realizing "Magnets by design".

In this context, three main objectives to be achieved in this dissertation: the design of mononuclear complexes with large magnetic anisotropy, the design of polynuclear complexes built from anisotropic mononuclear species and the design of polynuclear complexes with non-innocent ligand that can be electrically addressed.

1.2 Molecular magnetism

1.2.1 A brief introduction of the history of magnetism

The history of magnetic materials dates back to ancient Greece and China. The first definite statement of magnetism owes to a Greek philosopher Thales of Miletus in the 6th century BC.²⁰ He proposed that the attraction of iron was the natural feature of lodestone rather than the action by some god. In ancient China, there is evidence of a use of magnetic compass as divination devices as early as 2nd century BC and later used for navigation and orientation in the 11th century.

The man who regarded the science of magnetism in earnest was William Gilbert, who was considered as the “father of magnetism”. He wrote the book named “De Magnete” that was first published in 1600, giving a clear understanding why the earth itself is a giant magnet.²¹ A “little earth”, *terrella* in Latin, was constructed to show the field of the earth. A key experiment was conducted by Oersted, in 1820, that opened new perspectives in the understanding of magnetism by showing that an electric current influenced the magnetism, and subsequently Maxwell provided the mathematical frame to describe electromagnetism. While Pierre Curie who investigated the temperature dependence of the magnetization, discovered the law named after him. He introduced three types of magnetic bodies: diamagnets, paramagnets and ferromagnets in his thesis, translating as “Magnetic properties of matter at variable temperatures”.

Moving to the first decades of the 20th century, the discovery of electron by Joseph John Thomson and the ensuing refinement of the theory through quantum mechanics opened a new era of scientific discovery. Heisenberg, as one of the founding fathers of modern quantum mechanics, discovered the tools for describing the magnetic properties, starting a revolution that we are still observing. The quantum mechanics provided a base for the modern understanding of magnetism nowadays, based on the theory of the motion and interactions of electrons in atoms.²² During this period, many new concepts were introduced, among which the most important are spin and exchange, that had a

fundamental impact on magnetism. Meanwhile, there has been a shift in the size and number of objects under investigation. Investigations were focused on two main aspects, one was to measure in average a grain of matter which contained a huge number of molecules; and another that require more efforts concerned isolated objects and then single molecules.^{23,24}

1.2.2 Molecular magnets

With the development of structural, magnetic characterization methods and quantum mechanical approach, molecular magnets soon developed as a vital area of interdisciplinary science, which produced novel types of magnetic materials.

Molecular magnetism deals with the magnetic properties of an assembly of molecules, which contain one or more magnetic centers and also with the properties of individual molecules. It provides the potential to build novel spintronic devices,²⁵ high-density storage devices,²⁶ magnetic refrigerant^{27,28} as well as quantum bites (qubits).²⁹ Molecular magnetism is the natural continuation of the old field of research named “Magnetochemistry”,³⁰ based on the use of magnetic measurements to obtain structural information. And later Olivier Kahn, who founded our laboratory when his research work was carried out, is considered as the father of molecular magnetism. He made a key contribution in understanding the exchange coupling in coordination complexes, promoting the Goodenough-Kanamori rules both in theoretical and experimental ways.³¹⁻

34

1.2.3 Some important principles in molecular magnetism

Any discussion about magnetism must start with electrons. The magnetism of an atom originates from the motion of electrons, which results in two types of magnetic moment for free atoms in zero field. One is called spin magnetic moment, resulting from the movement of electron around its own axis; the other one is called orbital magnetic moment that is associated with the circulation of electron around nucleus. Generally, the

spin magnetic moment is roughly a thousand times larger than orbital magnetic moment in transition metallic complexes, playing a key role in magnetism.

Before talking about molecular magnets materials, it is essential to introduce some basic definitions and principles in molecular magnetism.

When a paramagnet is placed in a magnetic field H , the magnetic moments tend to align with this field, lowering the energy of the system. The magnetization is defined as: $M = -\delta E/\delta H$, and the magnetic susceptibility, $\chi = \delta M/\delta H$, shows how fast the paramagnet is magnetized in an external field. The magnetization is linear to susceptibility when magnetic field is much weaker than thermal energy and the following equation holds: $M = \chi H$.

The spin Hamiltonian approach is generally used to interpret the magnetic data. The spin Hamiltonian replaces all the orbital coordinates with spin coordinates according to the idea that orbital moment is normally quenched by ligand field. This is the case in many systems because, in most cases, real molecules possess enough distortion to lead to orbitally non-degenerate state and justifies the use of a spin Hamiltonian to interpret the magnetic data.

1.2.3.1 Zeeman effect and Zero-field splitting (ZFS)

Paramagnetism originates from unpaired electrons. The orientation of the electronic spin S is quantized with the projection of the spin on the axis of quantization, described by the quantum number M_S , taking the values from $-S$ to $+S$ in integer step. Therefore, the state S is $2S+1$ -fold degenerate. In an external magnetic field, the degeneracy of energy states is called "Zeeman effect", and the energy of these states can be described as:

$$E = g \beta H M_S$$

Here, g is the Landé factor, β the Bohr magneton, H the applied magnetic field and M_S is the projection of the spin S .

In the situation where the applied magnetic field is much weaker than thermal energy $M = \chi H$ and the molar susceptibility is given by:

$$\chi = M/H = \frac{N\beta^2}{3kT} g^2 S(S + 1)$$

where N is the Avogadro number, k the Boltzmann constant, T the temperature. Therefore, χ is inversely proportional to T . This is the Curie's Law: $\chi = C/T$. And the Curie constant C is a material-dependent property.

The lift of the degeneracy of the spin sub-levels M_S can also be observed in the absence of a magnetic field, this is called Zero-Field Splitting (ZFS). It mainly occurs in transition complexes due to the presence of more than one unpaired electron. ZFS originates from the simultaneous effects of a distortion from high symmetry (cubic for example) and Spin-Orbit Coupling (SOC). In the presence of a magnetic field, ZFS leads to magnetic anisotropy. For molecules with strict axial symmetry, axial magnetic anisotropy is present leading either to an easy axis (Ising type) or to an easy plane (XY type) of magnetization: the magnetic moment can, thus, either be blocked along one axis or freely rotate within a plane. If the symmetry is lower than axial, an additional anisotropy appears within the plane.³⁵ The ZFS parameters are mainly defined via D and E parameters, where D describes the axial component and E the transversal component (in the unit of cm^{-1}). In the magnetic-frame axes, the axes of the anisotropy tensor are the magnetization axes. If $E = 0$, the main axis of the anisotropy tensor is often collinear with the principle symmetry axis of the complex. From the shape of the ZFS spin Hamiltonian, an easy axis of magnetization corresponds to a negative D value ($D < 0$) while an easy plane corresponds to positive D value ($D > 0$):

$$E(M_S) = D \left[M_S^2 - \frac{1}{3} S(S + 1) \right]$$

Consequently, when $D < 0$ the largest M_S sub-levels have lower energy, while for positive D value the smallest M_S sub-levels have lower energy.³⁶

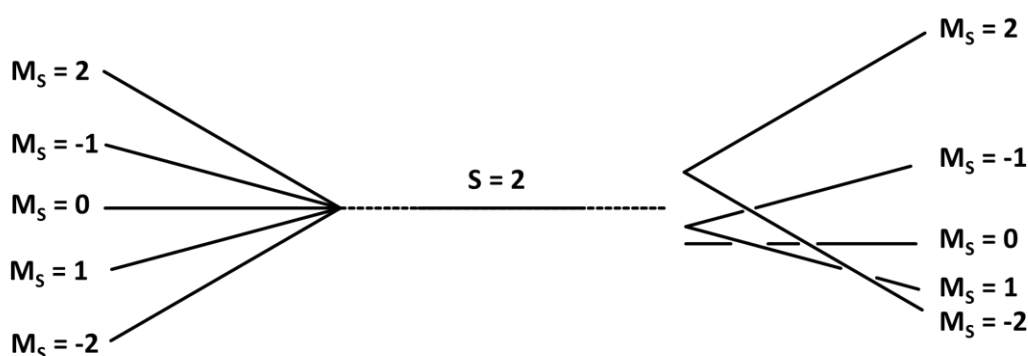


Figure I.1 The behavior of an $S = 2$ state (center), and in an applied magnetic field, the Zeeman splitting and the effect of ZFS with a positive D value are illustrated on left and right, respectively.

Figure I.1 displays the case of an $S = 2$ system (represents d^4 transition metals) that ground state is orbitally non-degenerate (in the middle). In the presence of an applied magnetic field, the energy levels with different quantum numbers ($M_S = 0, \pm 1, \pm 2$) are separated, referring to Zeeman effect (left). In the absence of applied magnetic field, the degeneracy is partially resolved due to ZFS before introducing the influence of external magnetic field (right). In this case, before the external magnetic field affecting the energy levels, the energy is lowest when $M_S = 0$ ($D > 0$).

1.2.3.2 Exchange coupling

When more than one magnetic center is present in the molecule, there is a magnetic interaction via the bridging ligands, which affects the magnetic properties of the molecules, named exchange coupling interaction. For example, two magnetic center of spin S_A and S_B in a binuclear system, respectively, we define a total spin number for the pair which will take all values from $|S_A + S_B|$ to $|S_A - S_B|$ in steps of 1. When two spin 1 ions interact with each other, the total spin value will be $S = 2, 1, 0$. Exchange coupling can be expressed by an isotropic exchange parameter J . Considering the Hamiltonian below, a positive value for J is obtained when the two spins are parallel in the ground states, described as ferromagnetic coupling interaction. In contrast, an antiparallel alignment of spins in the ground state correspond to a negative J value, responding to antiferromagnetic coupling.

$$H = -2J \cdot \hat{S}_A \cdot \hat{S}_B$$

1.2.3.3 Total Spin Hamiltonian

The total spin Hamiltonian is the sum of the ZFS, the exchange and Zeeman Hamiltonians.

To deal with ZFS, the spin Hamiltonian without first-order angular momentum is:

$$\hat{H} = \beta \cdot \mathbf{g} \cdot \hat{S} \cdot \vec{H} + \hat{S} \cdot \hat{D} \cdot \hat{S} + (-2J_{AB} \cdot \hat{S}_A \cdot \hat{S}_B)$$

$$\hat{H}_{ZFS} = \hat{S} \cdot \hat{D} \cdot \hat{S}$$

where \hat{D} is a symmetric and traceless tensor, \hat{S} the spin operator and \mathbf{g} the g-tensor.

It can be rewritten in the form below:

$$\hat{H} = \beta \cdot \mathbf{g} \cdot \hat{S} \cdot \vec{H} + D \left[\hat{S}_z^2 - \frac{S(S+1)}{3} \right] + E(\hat{S}_x^2 - \hat{S}_y^2) + (-2J_{AB} \cdot \hat{S}_A \cdot \hat{S}_B)$$

Here, \hat{S}_x , \hat{S}_y and \hat{S}_z are the components of the spin operators, S the spin state; \vec{H} the magnetic field. J_{AB} is the exchange coupling parameter, and \hat{S}_A and \hat{S}_B the corresponding spin operators. D is the axial ZFS parameter, and E the ZFS rhombic parameter. D and E are related to the diagonal D_{ii} components of the ZFS tensor.³¹

$$D = 3D_{zz}/2$$

$$E = |D_{xx} - D_{yy}|/2$$

1.2.3.4 Jahn-Teller effect

The Jahn-Teller effect, also named Jahn-Teller distortion, is an internal disposition of complex for the geometrical distortion of molecules to lower the overall energy of the species and thus remove the degeneracy, originating from the electronic configuration.

In an octahedral complex of transition metals, the Jahn-Teller distortion occurs when the ground state is orbitally degenerate. For example, when the e_g orbitals are occupied with an odd number of electrons: d^9 , d^7 in low spin or d^4 in high spin. In the case of d^9 system,^{30,37} the t_{2g} orbitals are fully occupied (6 electrons) and e_g orbitals are filled with the remaining 3 electrons: two electrons occupy the d_{z^2} orbital and one electron in the $d_{x^2-y^2}$ orbital or

the opposite situation. For the former state, the Jahn-Teller effect would push the axial ligands away to minimize the overall energy, leading to an elongated octahedron, while for the latter situation, a compressed octahedron would be generated.

The Jahn-Teller effect is also present in other symmetries than octahedral. In an ideal high spin trigonal bipyramidal Ni(II) complex (d^8), three electrons occupy the degenerated d_{xy} and $d_{x^2-y^2}$ orbitals (Figure I.2, left).³⁸ The Jahn-Teller effect lowers the energy of the molecule by removing the degeneracy of the orbitals (Figure I.2, right), leading to a non-degenerate ground state.

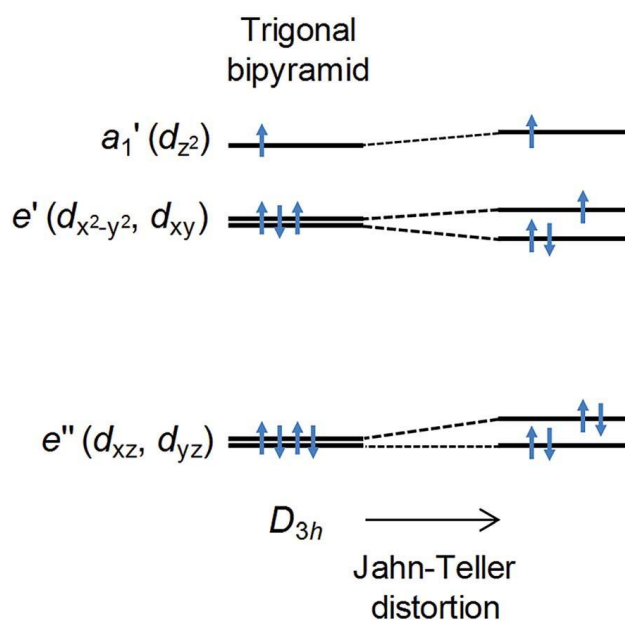


Figure I.2 The ideal trigonal bipyramidal d-orbital splitting (left) and the orbital splitting mode after removing the degeneracy by Jahn-Teller effect (right) for a high-spin Ni(II) complex. Reproduced from reference [38].³⁸

1.2.4 Magnetic characterizations and data analysis

To discover the magnetic properties of molecular magnets, several measurements should be carried out. First, molecular structure should be collected through Single Crystal X-Ray Diffraction. Subsequently, the measurements for magnetic susceptibility and magnetization data are performed using a Superconducting QUantum Interference Device (SQUID). Through fitting the magnetic susceptibility and magnetization data, the spin state,

magnetic anisotropy (both magnitude and sign) can, in principle, be determined, as well as exchange interaction coupling between adjacent metal ions for polynuclear complexes.

SQUID is a very sensitive device for measuring even extremely weak magnetic field. The SQUID we use for direct-current (dc) measurement in our laboratory is SQUID XL7, which can measure the magnetic moments from 2 K to 400 K, within an applied magnetic field up to 7 Tesla.

Significant information on the magnetic properties of the complexes can be provided by the plots of magnetization (M) vs. field (H) and the susceptibility (χ) vs. temperature (T). In general, energy variation affects the magnetization of a sample in an external applied magnetic field, and their relationship can be described in the following way:

$$M = -\frac{\partial E}{\partial H}$$

The molar magnetization M is calculated by summing the magnetic moments which weighted by Boltzmann law:³¹

$$M = \frac{N_A \sum_n (\partial E_n / \partial H) e^{-E_n / k_B T}}{\sum_n e^{-E_n / k_B T}}$$

Here M is the magnetization, N_A Avogadro's number, H the dc magnetic field, k_B the Boltzmann constant and T temperature. More simplified equations were proposed based on some assumptions and approximations,³¹ for example the van Vleck formula:

$$M = \frac{N_A H \sum_n \left(\frac{E_n^{(1)}}{k_B T} - E_n^{(2)} \right) e^{-E_n^{(0)} / k_B T}}{\sum_n e^{-E_n^{(0)} / k_B T}}$$

$$\chi = \frac{N_A \sum_n \left(\frac{E_n^{(1)}}{k_B T} - E_n^{(2)} \right) e^{-E_n^{(0)} / k_B T}}{\sum_n e^{-E_n^{(0)} / k_B T}}$$

And the Brillouin function is written as follows:

$$M = N_A g \mu_B S [B_S(x)]$$

$$\text{Here: } B_S(x) = \frac{2S+1}{2S} \coth \frac{2S+1}{2S} x - \frac{1}{2S} \coth \left(\frac{x}{2S} \right)$$

$$x = \frac{g \mu_B S H}{k_B T}$$

$E_n^{(0)}$ is the energy of level n in zero dc magnetic field, $E_n^{(1)}$ and $E_n^{(2)}$ are first- and second-order Zeeman coefficients, respectively.

If $H \gg k_B T$, the Brillouin function approximately equals to 1, the system reaches a maximum; saturated magnetization:

$$M = N_A g \mu_B S$$

This situation corresponds to the alignment of all spins in the direction of the applied magnetic field.

When $H \ll k_B T$, the equation below is the simplified Van Vleck equation when the external applied magnetic field is low and the temperature is high.³⁹ It can explain the dc susceptibility data for polynuclear complexes at high temperature.

$$M = N_A g \mu_B S \frac{x(S+1)}{3} = N_A g \mu_B S \frac{g \mu_B H (S+1)}{3 k_B T} = \frac{N_A g^2 \mu_B^2 S(S+1)}{3 k_B T} H$$

it reflects the state which can satisfy the Curie Law:³⁰

$$\chi = \frac{C}{T} = \frac{N_A g^2 \mu_B^2 S(S+1)}{3 k_B T}$$

Generally, M_S is expressed as a Bohr Magneton per mole, noted as $N\beta$. The spin S of ground state can be obtained when the value reaches its saturation, thus the measurement at low temperature is necessary, to minimize thermal agitation. As an indication, it should be noted that a value of the applied magnetic field of 7 Tesla corresponds to an energy close to 7 cm^{-1} (10 K) for a $1/2$ spin. It is therefore necessary to perform the measurements of

magnetization at temperatures below this value in order to saturate the magnetization, otherwise the thermal agitation would randomly orient the magnetic moments.

1.2.5 The first Molecular magnet

Before introducing the molecular magnets based on Ni(II) and Co(II), an extremely significant complex is necessary to mention: $\text{Mn}^{\text{III}}_8\text{Mn}^{\text{IV}}_4\text{O}_{12}(\text{O}_2\text{C}_2\text{H}_3)_{16}(\text{H}_2\text{O})_4$ ($\text{Mn}_{12}(\text{OAc})$), the first molecular magnet.

This molecule was first synthesized by Lis *et al.* in 1980,⁴⁰ and the dodecanuclear molecular structure is shown in Figure I.3. The mixed valences of Mn is displayed in this “Core-Shell” structure: four Mn(IV) made up the cubane core and eight Mn(III) surrounded as a shell.

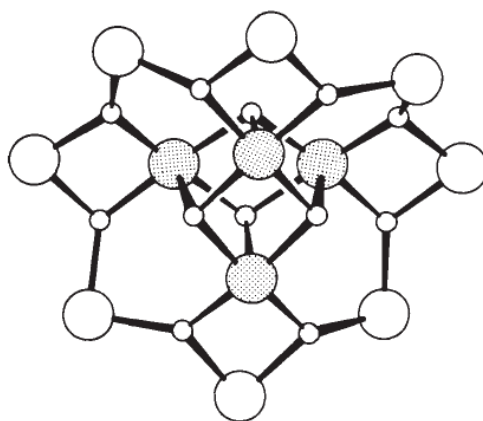


Figure I.3 Schematic view of $\text{Mn}_{12}(\text{OAc})$ cluster. The eight large white circles represent the Mn(III) ions ($S = 2$), and the shaded circles are Mn(IV) ions ($S = 3/2$). Reproduced from reference [41].⁴¹

Caneschi and his colleagues provided the main evidence of a ground state $S = 10$ using magnetization measurements in 1991,⁴² and the simultaneous use of high field EPR and alternating-current (ac) susceptibility confirmed the result of magnetization. Later in 1993, Sessoli *et al.* discovered that the magnetization of this Mn_{12} cluster was highly anisotropic. The magnetization hysteresis loop illustrated the difference from an ordered bulk magnetic material (see Figure I.4), in which the magnetization hysteresis resulting from the movement of domain walls.⁴¹ Hill *et al.* used a multifrequency, high sensitive electron paramagnetic resonance (EPR) technique to make an extremely detailed investigation of

the energy level diagram of this $\text{Mn}_{12}(\text{OAc})$ single crystals in 1998,⁴³ confirming that the D value was negative (easy axis of magnetization).

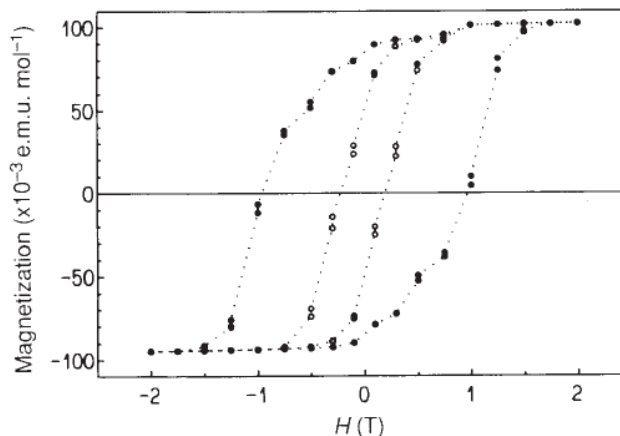


Figure I.4 Magnetization hysteresis loops of $\text{Mn}_{12}(\text{OAc})$, collecting along the crystal c axis. Measurement temperatures were 2.2 K (●) and 2.8 K (○). Reproduced from reference [41].⁴¹

The study on $\text{Mn}_{12}(\text{OAc})$ opened up a new field of exploration, marking a breakthrough in the field of magnetism. More and more molecular magnets were synthesized with transition metals, first with polynuclear complexes and later with mononuclear ones. We will focus, here, on Ni and Co containing molecules in this dissertation. I will present some results from the literature and try, when adequate, to do comments.

1.3 Mononuclear molecules with anisotropy

Since the molecular magnets have emerged as promising materials in many fields mentioned above, more and more efforts are paid in exploring new approaches for designing new complexes with large magnetic anisotropy. Magnetic anisotropy causes a preferred direction of a spin, so it is aligned with the easy direction in the presence of a very weak magnetic field. Thus, molecules which possess a strong magnetic anisotropy may have large remnant magnetization and behave as an individual magnet without external magnetic field. Till recently, the prediction and control of magnetic anisotropy in transition metal ions have remained elusive, even though the crystal field theory can give some instructions to the main parameters, such as the electronic configuration and the symmetry. ZFS is the most common source of magnetic anisotropy in first-row transition

metal complexes. It stems from the simultaneous effects of low symmetry (than cubic) and SOC.

1.3.1 Design of anisotropic mononuclear complexes

In the simple case of axial anisotropy responsible of ZFS, magnetic anisotropy may be the Ising type (easy axis of magnetization) or XY type (easy plane of magnetization). This depends on many parameters such as the number of single electrons, the symmetry of the complex (C_{4v} , D_{4h} , C_{3v} , D_{3d} , etc...), the electronic structure of the ligands that may impose a weak or a strong electronic interaction along the z axis, etc.... Rajaraman and his coworkers studied a series of Ni(II) mononuclear complexes⁴⁴ and confirmed that the magnetic anisotropy was determined by the coordination environment: the donor ligand, coordination numbers, coordination geometry etc.... To realize the design of molecules with predictable magnetic properties, it is essential to study the relationship between magnetic anisotropy and coordination environment.

As the magnetic anisotropy is closely related to the molecular structure features: the coordination numbers, the corresponding symmetries and the electronic configuration. The calculations on the fundamental understanding of the relationship between magnetic anisotropy and molecular structure are still a prevalent field.^{35,44-48} Oshio *et al.* correlated the magnetic anisotropy with electronic configuration and symmetry of complexes, in the case of O_h and D_{4h} systems.⁴⁹

Actually, there are seldom molecular complexes with absolute high symmetry, which demands simply constructed ligands and the lack of Jahn-Teller distortion. The complexes which are described as specific shapes, such as octahedron, trigonal bipyramid, are based on the relative positions of metal ions and donor atoms in the principle of similarity. In most cases, the complexes have more asymmetry than what is considered for calculations, resulting from the interaction among the molecules in the lattice by, for example, hydrogen bonds or electrostatic that impact the electronic configuration of the ligands linked to the metal ions. These tiny effects are important because magnetic anisotropy energies are relatively weak, in the orders of few cm^{-1} in many cases. It is, however, possible to use

calculations in order to have a general trend on the effect of the electronic configuration of the metal ion and its symmetry on the magnitude and nature of the ZFS that is directly related to magnetic anisotropy.

Gomez-Coca *et al.* did some calculations on the molecular orbitals of mononuclear complexes $\text{Fe}^{\text{II}}(\text{NH}_3)_x$ models, attempting to predict the orbital energies through using the extended-Hückel method.⁴⁵ The influences of electronic configuration and coordination geometry on magnetic anisotropy are summarized in the Figure I.5. What needs to be noticed is that the D values can have the opposite signs due to the distortion originated from Jahn-Teller effect. In this report, d^6 electronic configuration with σ -donor ligands is considered as the one that most likely to induce a large and negative D value. The work reported by Mossin provides a similar conclusion.⁵⁰ While for π -donor ligands, leads to large and negative D -value for the d^2 and d^7 electronic configuration.

	d^1 / d^6	d^2 / d^7	d^3 / d^8	d^4 / d^9
linear-2	■	■	■	■
divacant tetrahedron-2	■	■	■	■
tetravacant octahedron or bent-2	■	■	■	■
trigonal planar-3	■	■	■	■ ■
vacant tetrahedron-3	■	■	■	■ ■
fac-trivacant octahedron-3	■ ■	■ ■	■ ■	■ ■
mer-trivacant octahedron-3	■	■	■	■
square-4	■	■	■ ■	■
tetrahedron-4	■ ■	■ ■	■ ■	■ ■
seesaw-4	■	■	■	■
trigonal pyramid-4	■	■	■	■
pentagon-5	■	■	■	■ ■
vacant octahedron-5	■	■	■	■
trigonal bipyramid-5	■	■	■	■
square pyramid-5	■	■	■	■
hexagon-6	■	■	■	■ ■
pentagonal pyramid-6	■	■	■	■ ■
octahedron-6	■ ■	■ ■	■ ■	■ ■
trigonal prism-6	■	■	■	■ ■
heptagon-7	■	■	■	■ ■
hexagonal pyramid-7	■	■	■	■ ■
pentagonal bipyramid-7	■	■	■ ■	■
capped octahedron-7	■	■	■ ■	■ ■
capped trigonal prism-7	■	■	■ ■	■ ■
octagon-8	■	■	■	■ ■
heptagonal pyramid-8	■	■	■	■ ■
hexagonal bipyramid-8	■	■	■ ■ ■	■ ■ ■
cube-8	■	■	■ ■ ■	■ ■ ■
square antiprism-8	■	■	■	■ ■
dodecahedron-8	■	■	■	■ ■
biaugmented trigonal prism-8	■	■	■ ■	■ ■

Figure I.5 Estimation of the D Values for High-Spin Mononuclear Transition-Metal Complexes with Different Electronic Configurations and Coordination Modes Using Ammonia Ligands. Green and blue squares indicate large and small negative values, while red and orange represent large and small positive values, respectively. Cases with more than one color indicate that the non-distorted structure has a zero D value, and different options are possible depending on the symmetry of the Jahn–Teller distortion. Reproduced from reference [45].⁴⁵

Considering the electronic configuration of the metal ions and their coordination geometries, the results of the paper of Ruiz *et al.* are displayed in Figure I.5. They can be used to rationally design mononuclear complexes with predictable magnetic anisotropy, providing the possibility to link the electronic density on the metal ions to its symmetry.

1.3.2 Some mononuclear complexes based on Ni(II) and Co(II)

1.3.2.1 Some Ni(II) molecular magnet

[Ni(pydc)(pydm)]·H₂O

A mononuclear complex [Ni(pydc)(pydm)]·H₂O (Figure I.6), showing two slow relaxation processes, was reported by Miklovič and his coworkers in 2015.^{51,52} (here, pydc = pyridine-2,6-dicarboxylate, pydm = 2,6 bis(hydroxymethyl)pyridine), which is the first example of a field-induced single molecular magnet in the class of hexacoordinated Ni(II) complexes. In this crystal structure, significant intermolecular interactions (hydrogen bonds and π - π stacking) were identified.^{51,52}

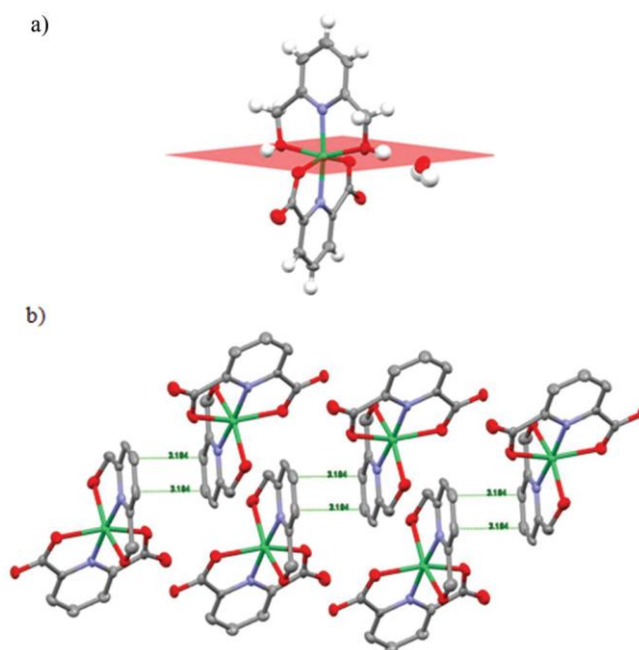


Figure I.6 (a) molecular structure; (b) π - π interactions of molecular units (C-C = 3.194 Å). Reproduced from reference [51].⁵¹

In the study of its magnetic properties, they found that it behaves magnetically as typical $S = 1$ spin system with ZFS. By fitting the dc magnetic data in Figure I.7, a relatively large and negative D value (-13.7 cm^{-1}) can be obtained, resulting from its highly axially compressed pseudo-octahedral chromophore [NiO₄N₂] with significant rhombic contribution. From its dynamic magnetic data obtained by applying an oscillating magnetic

field, two relaxation processes were evident: one was attributed to the single molecule and the other to the presence of π - π interactions.

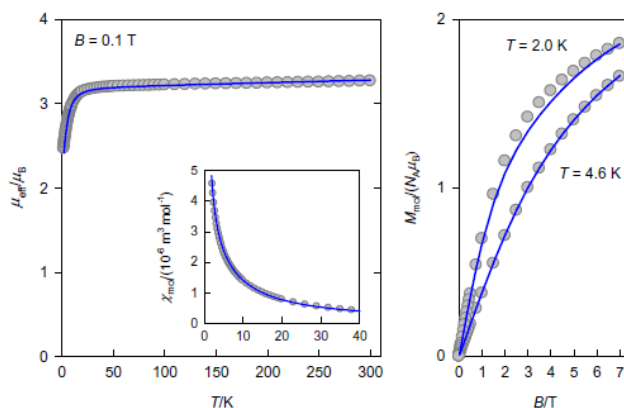


Figure I.7 Magnetic functions of this complex: left – temperature dependence of the effective magnetic moment (inset – molar magnetic susceptibility); right – field dependence of the magnetization per formula units. Lines – fitted. Reproduced from reference [52].⁵²

1.3.2.2 Some Co(II) molecular magnets

[Co(Me₆tren)Cl](ClO₄) (**1**) and [Co(Me₆tren)Br](Br) (**2**)

Two Co(II) mononuclear complexes: [Co(Me₆tren)Cl](ClO₄) (**1**) and [Co(Me₆tren)Br](Br) (**2**), both of which are pentacoordinate trigonal complexes were reported.⁵³ Figure I.8 shows the molecular structure of **1** that has a perfect C_{3v} symmetry and the ClO₄⁻ ion is omitted for clarity. Complex **2** is isostructural with complex **1**, containing a perfect C_{3v} symmetry.

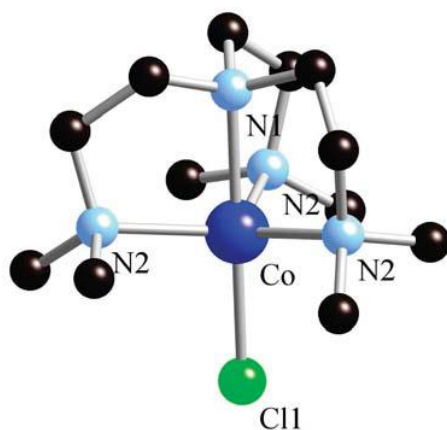


Figure I.8 View of molecular structure of $[\text{Co}(\text{Me}_6\text{tren})\text{Cl}]^+$ cation. Reproduced from reference [53].⁵³

Negative D values were obtained from fitting the experimental magnetization data (see Figure I.9), corresponding to the *ab initio* calculation results, expressing Ising-type anisotropy for the two complexes. For these two complexes, the $|D|$ value is larger for complex **1** ($8.12 \pm 0.06 \text{ cm}^{-1}$) than complex **2** ($2.40 \pm 0.05 \text{ cm}^{-1}$), arising from the weaker σ -donating from the N atoms in the equatorial plane of the ligand and the stronger π -donating from the Br^- in the axial position. The origin of the negative D value is due to the fact that the coupling between the ground and the first excited states involves the z component of the spin orbit operator (L_z) leading to non-zero component along the z direction of the spin (S_z) and thus to an alignment of the magnetic moment along the one axis (easy axis of magnetization). This paper gives us instructions in predicting the magnetic anisotropy.

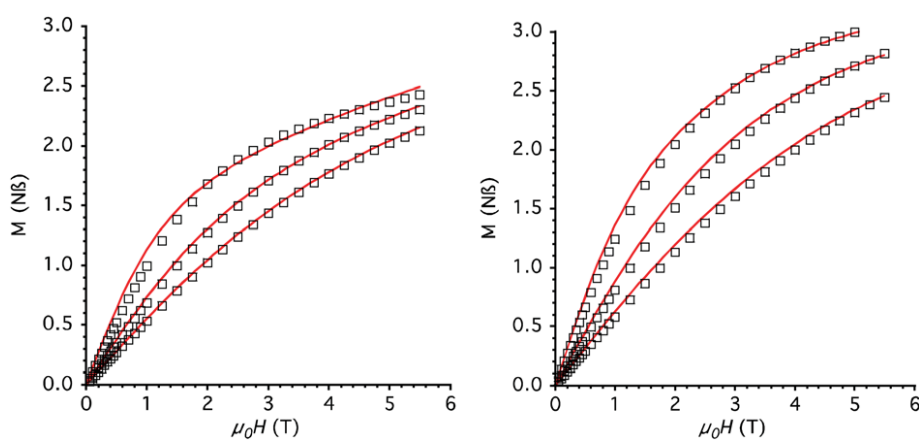


Figure I.9 Experimental (\square) and calculated ($-$) M vs. μ_0H plots collected at 2, 4, and 6 K for **1** (left) and **2** (right). Reproduced from reference [53].⁵³

[Co(N₃)LH₃]Cl₄ and [Co(N₃)CoL]Cl₃

A mononuclear Co(II) molecular magnet and its antiferromagnetically coupled binuclear derivative, possessing a quasi-identical local C_{3v} symmetry, were prepared in our group in 2017.⁵⁴ In the binuclear complex, an azido ligand was used as a bridge to connect the two Co(II) ions due to its large distance (Figure I.10).

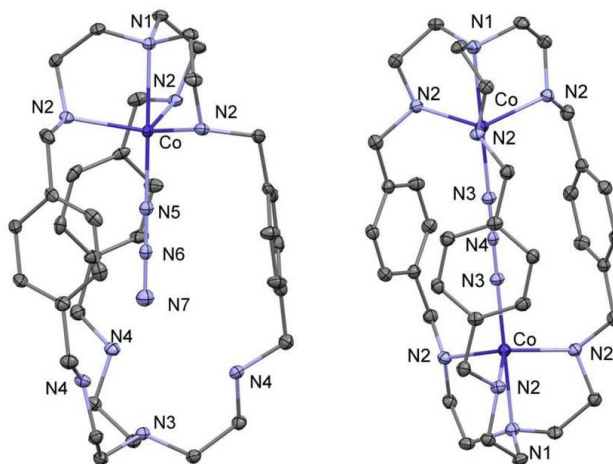


Figure I.10 ORTEP drawing of the mononuclear and binuclear complexes [Co(N₃)LH₃]⁴⁺ (left) and [Co(N₃)CoL]³⁺ (right) of **1** and **2**, respectively. hydrogen atoms are omitted for clarity. Reproduced from reference [54].⁵⁴

The mononuclear complex behaves as a single molecule magnet because of its easy axis of magnetization. The magnetic data can be fitted with a negative D value as expected for its trigonal symmetry. The magnetic properties of the binuclear complex are mainly governed by the antiferromagnetic coupling between the Co(II) ions despite the negative local negative D values of the mononuclear species. Through fitting the susceptibility and magnetization results (Figure I.11 and Figure I.12), the parameters were obtained as follows: $D_1 = -7.1 \text{ cm}^{-1}$ for **1** and for **2**, $D_2 = -5.35 \text{ cm}^{-1}$, $J = -6.6 \text{ cm}^{-1}$.

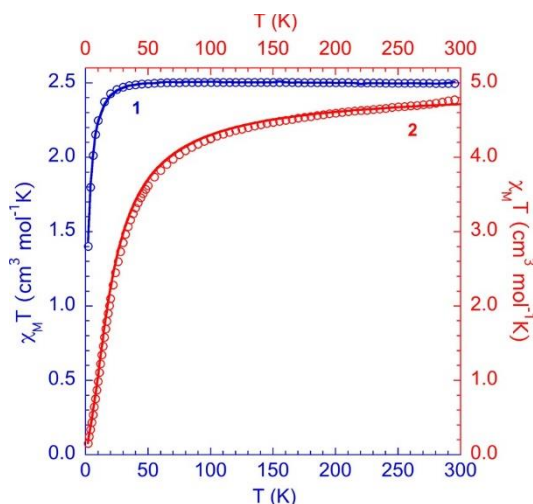


Figure I.11 $\chi_M T = f(T)$ for **1** and **2**: (○) experimental data and (—) calculated data. Reproduced from reference [54].⁵⁴

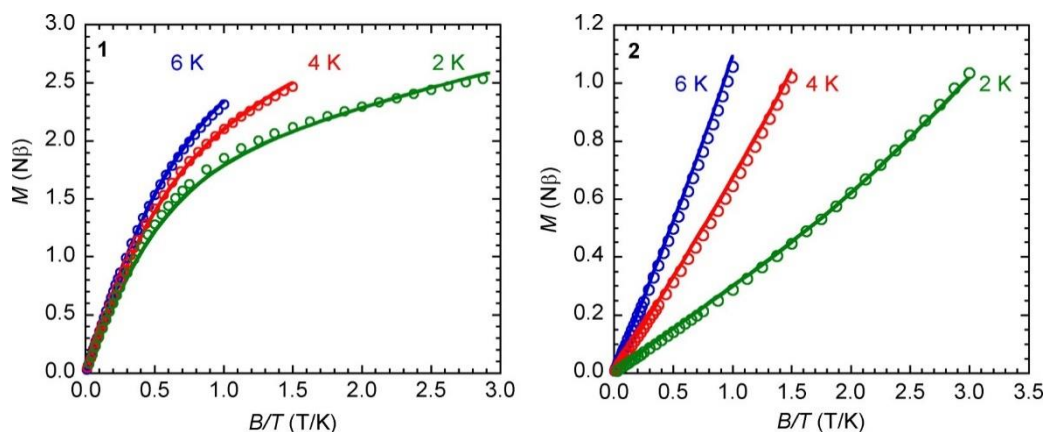


Figure I.12 $M = f(B/T)$ for **1** and **2**: (○) experimental data and (—) calculated data. Reproduced from reference [54].⁵⁴

1.4 Polynuclear magnetic complexes built from anisotropic mononuclear species

A molecular complex possessing ZFS will have two low-lying levels as the ground state that are degenerate for half integer spins ($M_S = \pm 3/2$ or $\pm 1/2$ for $S = 3/2$). The application of a small magnetic field lifts the degeneracy of the M_S ground levels and leads to a two-level system, which can be considered as a qubit. For integer value of the spin ($S = 1$ for example), ZFS must be such that the $M_S = \pm 1$ is the ground level. Usually, a rhombic term is also

present so that the degeneracy of the $M_S = \pm 1$ levels are lifted and lead to a two level system in zero applied magnetic field. Such systems are also interesting in qubits. If one needs to go further and build a quantum gate, it is necessary to have two qubits very weakly interacted together. This can be achieved by designing bi- and trinuclear molecular complexes with large single ion ZFS and weak antiferromagnetic exchange coupling interaction. It is also possible to use non-innocent ligands that can be addressed electrically or by light to couple the mononuclear species. In the following, we present some systems from the literatures that may be candidates for weakly interacting qubits systems.

1.4.1 The choice of bridging ligand

In coordination and organometallic chemistry, the nature of bridge ligands has a great influence on the properties of the polynuclear complexes.

Ligands were first described as “innocent” or “suspect” (“non-innocent”) by Jørgensen: Ligands are innocent when they allow oxidation states of the central atoms to be defined.⁵⁵ An innocent ligand was defined as a ligand in a metal complex where the oxidation state is unequivocal. They do not actively participate in reactions where they preserve their electronic structure. Non-innocent ligands are the ones that display redox active behavior, leading to a variability of oxidation states. Typically, the redox reactions within the complexes with non-innocent ligands occur either in metal ions or ligands.

It is necessary to state that:

- i) The term “non-innocent” not simply applied to redox-active ligands alone, but also refers to the complexes where the metal ions can change oxidation state.
- ii) A redox-active ligand can be both innocent and non-innocent.^{56,57}

As the nature of bridging ligands greatly influences the behavior of complexes in polynuclear complexes, we will discuss the complexes with both non-innocent ligands and innocent ligands.

1.4.1.1 Innocent ligands

The electronic and steric structure of ligands are key factors to the characteristics of molecular complexes based on transition metals. In most instances, ligands play a role of spectator in reactions.⁵⁸⁻⁶⁰ Since the number of innocent ligands is very large and so we will only comment on them when we describe some polynuclear complexes with innocent ligands. Furthermore, there is very few reports in the literature on complexes with very weak antiferromagnetic exchange coupling interaction and large local ZFS.

1.4.1.2 Non-innocent ligands

In contrast to innocent ligands, the non-innocent ligands are ligands cooperative in reactions. Figure I.13 lists many representative structures which probably behave as non-innocent ligands and their charge transfer process.⁵⁷

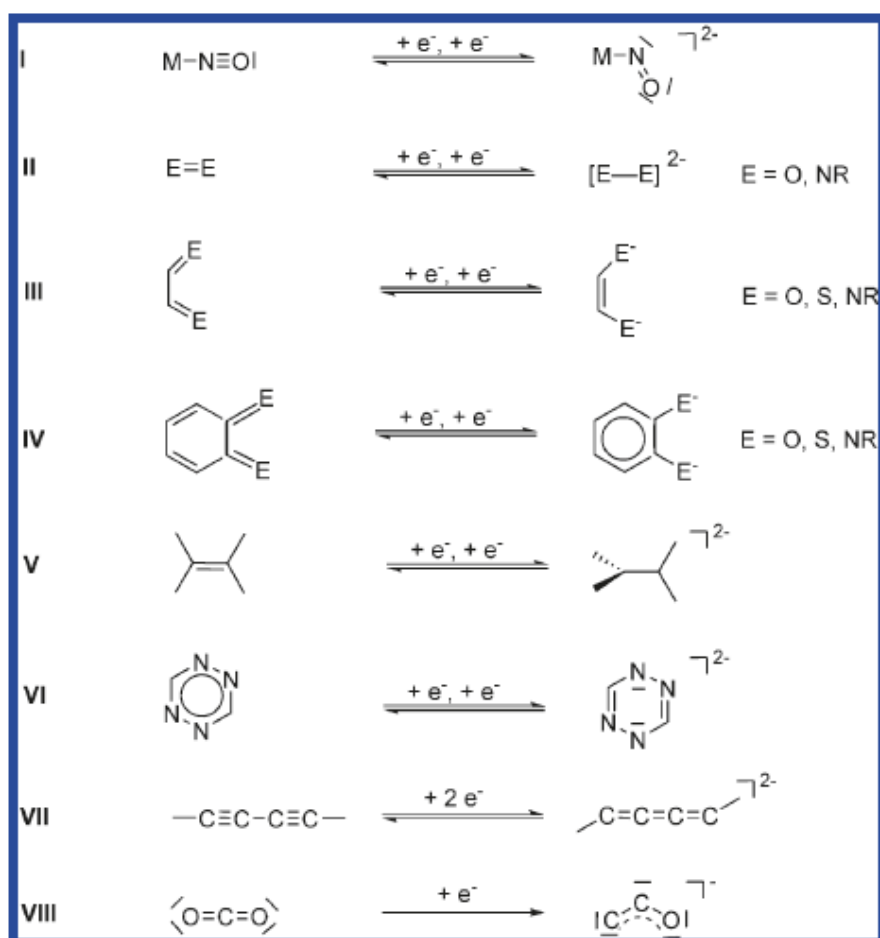


Figure I.13 Representative structural changes associated with electron transfer to selected molecules, including potentially redox-active ligands. Reproduced from reference [57].⁵⁷

In the complexes with non-innocent ligands, bridge ligands not only act as a linker, but also provide a place for electron transfer.

Radical containing

Single electron reduction from neutral ligands or single electron oxidation from dianions will probably result to radical containing ligands, as either intermediate products or final complexes. The coupling between radical and metal ions broaden the scope of research area to the interaction between two different paramagnetic centers.⁶¹ Many research works on radical containing redox-active ligands have been reported.⁶²⁻⁶⁶ For mononuclear transition complexes, nitronyl nitrroxides with an unpaired electron that can delocalized over the coordinating oxygen atoms, are the most common ligands that used for stable

free radicals.⁶⁷ While derivatives of benzoquinone are widely used in producing radical containing complexes.⁶⁸⁻⁷¹

T. David Harris *et al.* introduced chloranilic acid (CA) as a linker to obtain new metal-organic frameworks (MOFs) based on iron. The CA, a bis-bidentate ligand, has readily access to three oxidation states and have the potential to generate an organic radical through redox reactions (Figure I.14).⁶⁵

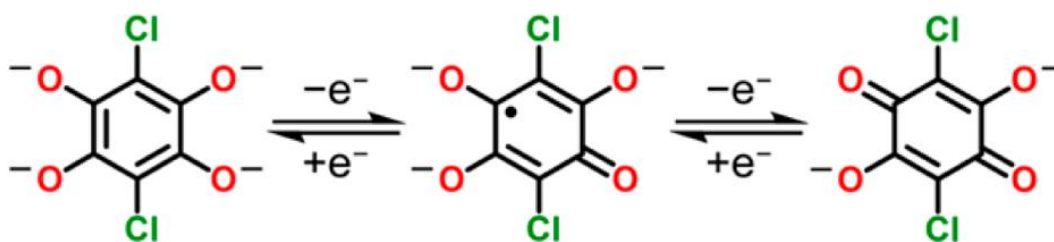


Figure I.14 Redox series of deprotonated benzoquinoid bridge based on CA: Left to right, L^4 , $L^{3\bullet}$ and L^{2-} . Reproduced from reference [65].⁶⁵

The structures of compounds $(Me_2NH_2)_2[Fe_2L_3] \cdot 2H_2O \cdot 6DMF$ (**1**) and $(Cp_2Co)_{1.43}(Me_2NH_2)_{1.57}[Fe_2L_3] \cdot 4.9DMF$ (**2**) that two-dimensional networks are reported in Figure I.15. Compound **1** has a trigonal structure comprised of Fe ion centers bridged with L^n : $[(Fe^{III})_2 (L^{3\bullet})_2 (L^{2-})]^{2-}$. By reduction, the L^{2-} in **1** results in **2**: $[(Fe^{III})_2 (L^{3\bullet})_3]^{3-}$ that has three radicals. Compound $(Me_2NH_2)_2[Zn_2L_3] \cdot 2H_2O \cdot 6DMF$ (**3**) is $[(Zn^{II})_2 (L^{2-})_3]^{2-}$. The bands observed at 1491, 1487, 1617 cm^{-1} for compounds **1-3** in Raman spectra are assigned to C-O stretching mode of the bridging ligand. The one for **3** can be L^{2-} , and the shift to lower frequency represents the ligand-based reduction from **1** to **2**.

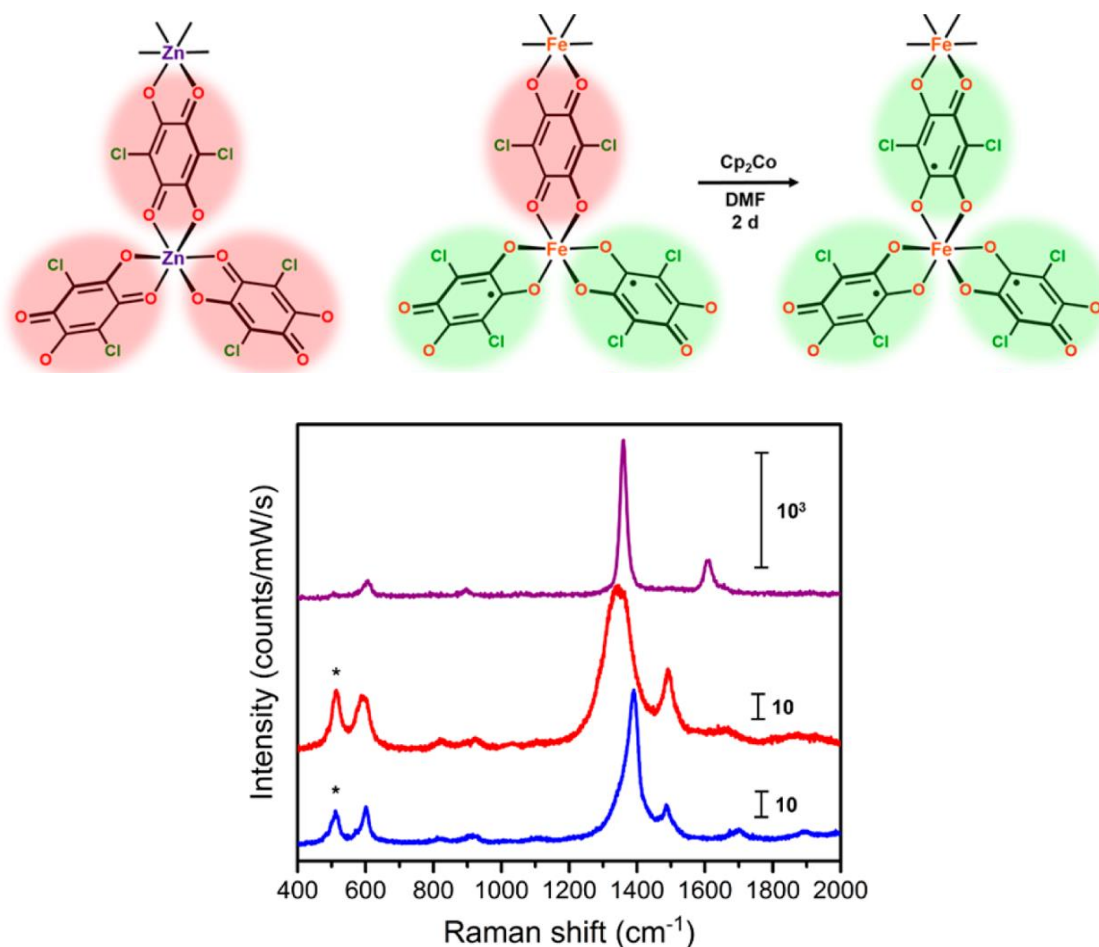


Figure I.15 Top: the repeating unit of complex **3** (left), **1** (middle) and **2** (right); Bottom: Raman spectra collected for complex **3** (purple), **1** (red) and **2** (blue), following excitation at 473 nm (**1** and **2**) and 405 nm (**3**). Reproduced from reference [65].⁶⁵

Valence tautomerism

Besides the radical containing, another significant feature related to non-innocent ligands is valence tautomerism. In general, valence tautomerism (Figure I.16) occurs in the system where the metal ions can easily be oxidized and reduced, such as Cu(I)/Cu(II)^{72,73} and Co(II)/Co(III).⁷⁴⁻⁷⁷

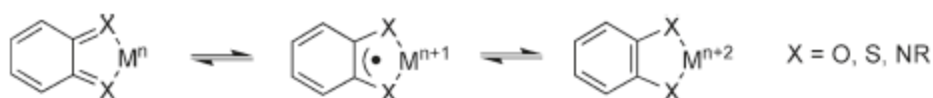


Figure I.16 Valence tautomer equilibria of complexes with quinonoid chelating ligands. Reproduced from reference [57].⁵⁷

A dinuclear cobalt complex $[(\text{CoTPA})_2(\text{DHBQ})](\text{PF}_6)_3$ **1**· $(\text{PF}_6)_3$, TPA is tris(2-pyridylmethyl)amine, and DHBQ is deprotonated 2,5-dihydroxy-1,4-benzoquinone was successfully synthesized by Tao and coworkers.⁷⁰ The crystal structure analysis reveals that the oxidation state of the complex is 3+, and the spin state can be expressed as $\text{Co}^{\text{III-LS}}-\text{DHBQ}^{3-}-\text{Co}^{\text{III-LS}}$. At 5 K, the $\chi_M T$ value is $0.33 \text{ cm}^3 \text{ K mol}^{-1}$, corresponding to $S = 1/2$ state (right of Figure I.17). While at high temperature, the complex is high spin. A thermal crossover is observed due to thermally activated electron transfer, with large hysteresis loop attributed to the $\pi-\pi$ interactions of the TPA ligands (left of Figure I.17).

By irradiating under a 532 nm light at 5 K for 30 min, the complex changes from $\text{Co}^{\text{III-LS}}-\text{DHBQ}^{3-}-\text{Co}^{\text{III-LS}}$ to $\text{Co}^{\text{III-LS}}-\text{DHBQ}^{2-}-\text{Co}^{\text{II-HS}}$, and the light-induced $\text{Co}^{\text{III-LS}}-\text{DHBQ}^{2-}-\text{Co}^{\text{II-HS}}$ can relax back to its original state.

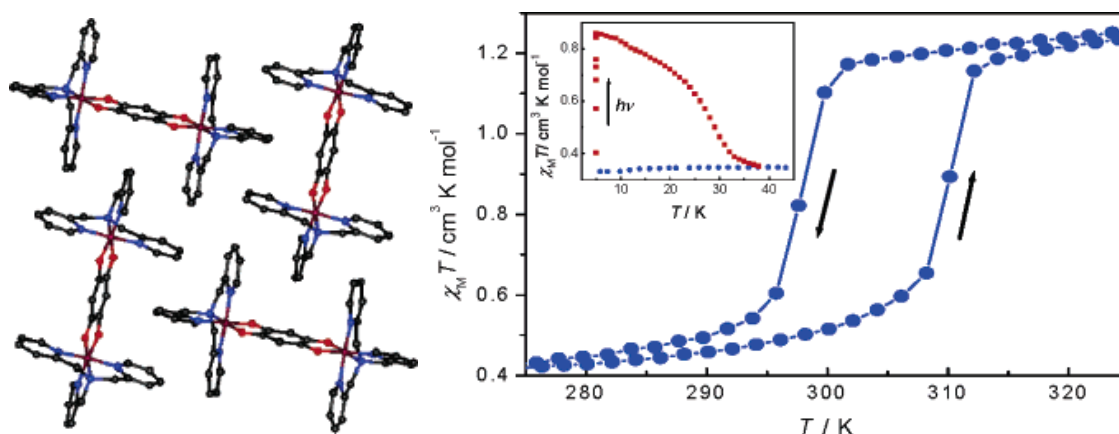


Figure I.17 Left: 2D cationic network; Right: temperature dependence of $\chi_M T - T$ plots and the insert is photoinduced changes after irradiation at 532 nm. Reproduced from reference [70].⁷⁰

1.4.2 Polynuclear complexes with bridging ligands

1.4.2.1 Polynuclear complexes based on Ni

$[\text{Ni}(\mu\text{-Im})\text{NiL}](\text{ClO}_4)_3$

Our group prepared a binuclear Ni(II) complex,⁷⁸ with a cryptand organic chelating ligand and an imidazolate bridge (Figure I.18, left). The imidazolate can undergo $\pi-\pi$ stacking with

two benzene rings of the chelating ligand, contributing to the stabilization of the whole structure. Large magnetic anisotropy of Ising type (easy axis of magnetization) and weak antiferromagnetic coupling were reported as shown by the magnetic susceptibility (Figure I.18, middle) and magnetization results (Figure I.18, right).

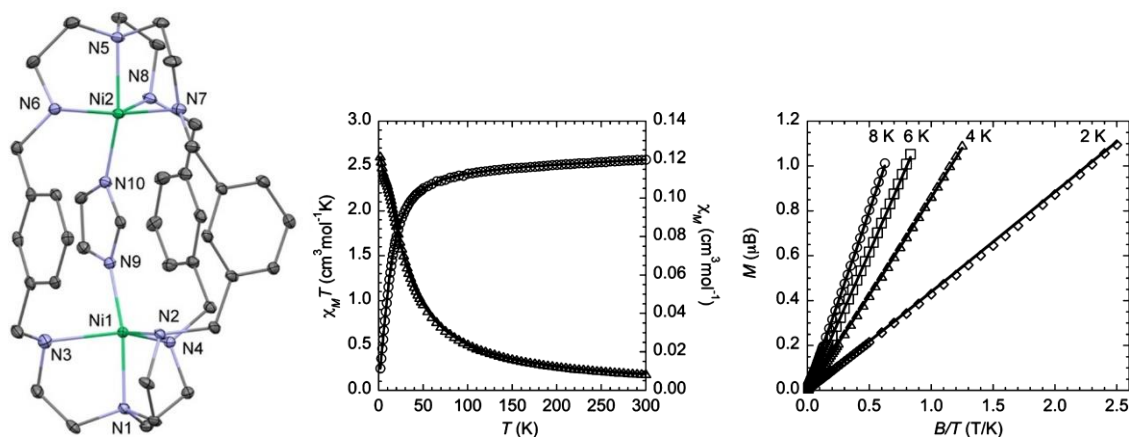


Figure I.18 Left: molecular structure of the binuclear complex; Middle: Thermal dependence of $\chi_M T$ (experimental, \circ) and χ_M (experimental, Δ); Right: magnetization vs. B/T . Reproduced from reference [78].⁷⁸

The large magnetic anisotropy results from the penta-coordination of Ni ions, especially a slight distortion of the coordination geometry of Ni(II) from square pyramid to trigonal bipyramid. Two Ni ions are found to have easy axis of magnetization that are almost collinear even though their geometries are different. The ZFS values for the Ni1(II) species was found larger than 50 cm^{-1} , while the exchange coupling parameter J is around -5 cm^{-1} . This is one of the rare examples where exchange coupling is weaker than the axial ZFS parameters.

$[\text{Ni}_6(\text{amox})_6(\mu_6\text{-O})(\mu_3\text{-OH})_2]\text{Cl}_2 \cdot 6\text{H}_2\text{O}$

An oxime-bridged hexanuclear Ni(II) complex: $[\text{Ni}_6(\text{amox})_6(\mu_6\text{-O})(\mu_3\text{-OH})_2]\text{Cl}_2 \cdot 6\text{H}_2\text{O}$ (amoxH = 4-amino-4-methyl-2-pentanone oxime), was reported, and its structure is showed below (Figure I.19, left).⁷⁹ Each Ni^{2+} ion was surrounded by two N atoms of an amox⁻ ligand and four O atoms of two bridging oxime groups, one $\mu_6\text{-O}^{2-}$ and one $\mu_3\text{-OH}^-$. In this complex, the six Ni^{2+} were arranged to form a Chinese-lantern like cage with a $\mu_6\text{-O}^{2-}$ in the center (Figure I.19, right).

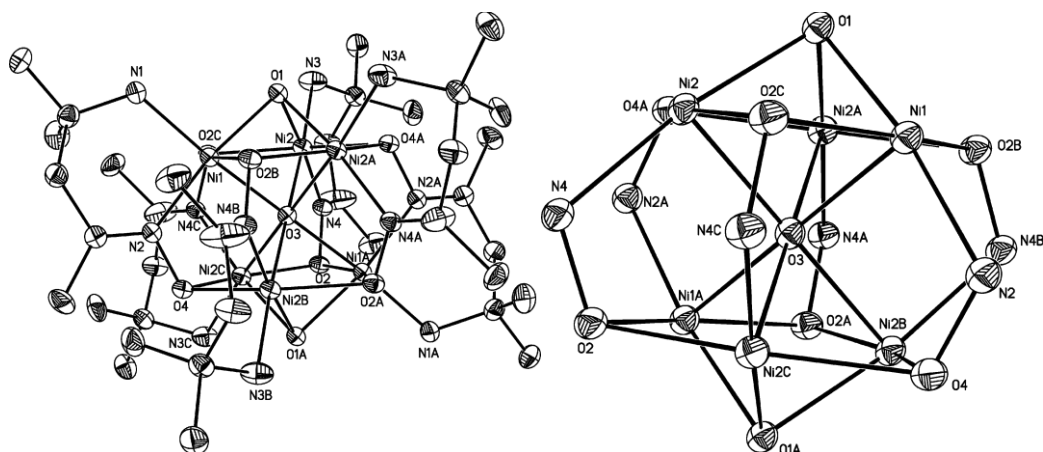


Figure I.19 Left: plot of the polynuclear $[\text{Ni}_6(\text{amox})_6(\mu_6\text{-O})(\mu_3\text{-OH})_2]^{2+}$ cation; right: the Chinese lantern-like Ni_6 cage of this complex. Reproduced from reference [79].⁷⁹

Three possible magnetic pathways are assumed to explain the coupling interactions between the six Ni^{2+} ions (Figure I.20), corresponding to three different J values. J_1 represents the interactions between the Ni^{2+} ions in the trans position: Ni-O-Ni, and J_2 is the Ni-O-Ni coupling interactions within each triangle (upper and lower), and, finally, the J values between the upper or lower triangles through the central oxo bridge and the Ni-N-O-Ni of the oxime, named J_3 . Through fitting their magnetic data, three J values are as follows: $J_1 = -150.4(2) \text{ cm}^{-1}$, $J_2 \approx 0 \text{ cm}^{-1}$, $J_3 = -25.0(1) \text{ cm}^{-1}$, $g = 2.26$, among which J_1 is the dominant coupling parameter. And strong antiferromagnetic couplings are observed.

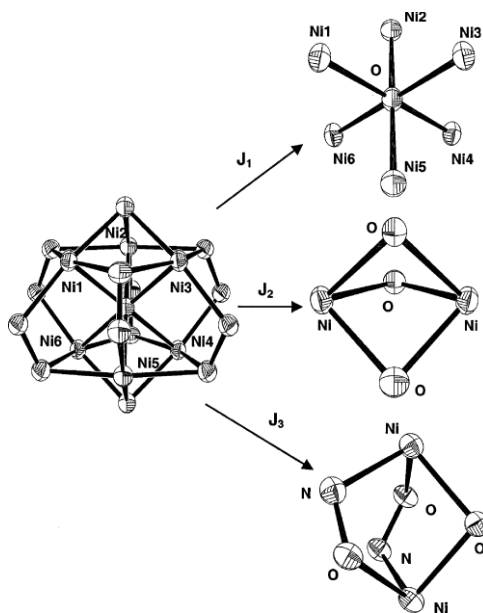


Figure I.20 Three possible magnetic pathway (J_1 , J_2 and J_3) in this complex. Reproduced from reference [79].⁷⁹

1.4.2.2 Polynuclear complexes based on Co

(LCo)₂(μ-bpym) (**1**) and [(LCo)₂(μ-bpym)][BPh₄]⁻ (**2**)

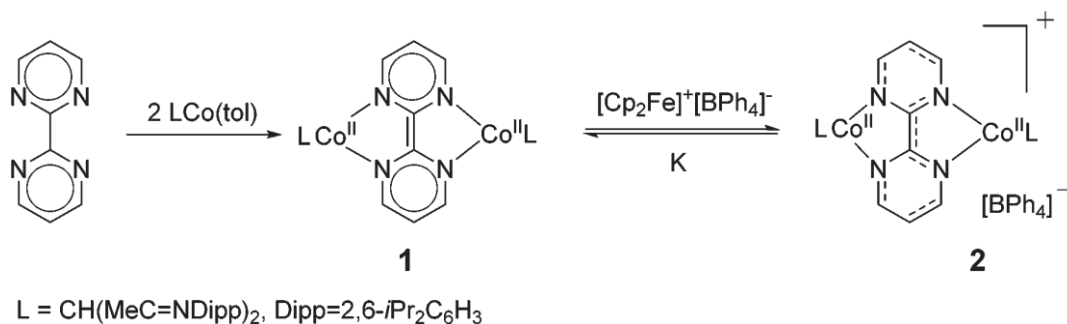


Figure I.21 Synthesis of the binuclear cobalt complexes **1** and **2**. Reproduced from reference [80].⁸⁰

2,2-bipyrimidine (bpym) has the potential to execute reduction reactions by accepting one or two electrons from metal ions and thus forming the bpym^{•-} radical anion or bpym²⁻ dianion. Wang *et al.* firstly obtained a binuclear Co(II) complex **1**: (LCo)₂(μ-bpym), and then complex **2**,⁸⁰ in which the bpym moiety is oxidized to bpym^{•-} anion (Figure I.21).

The χ_{MT} value at room temperature are 3.52 and 4.96 cm³ K mol⁻¹ for **1** and **2**, respectively (Figure I.22). The results are in good agreement with two high spin Co(II) for **1** and two high

spin Co(II) and one radical anion for **2**. Reasonable results are obtained by fitting: $D = -16.6 \text{ cm}^{-1}$ and $J = -17.5 \text{ cm}^{-1}$ (the exchange coupling between Co ions) for complex **1**; $D = -23.0 \text{ cm}^{-1}$, $J_1 = -160.5 \text{ cm}^{-1}$ and $J_2 = -0.147 \text{ cm}^{-1}$ for complex **2** (J_1 is the magnetic coupling between Co ion and radical, J_2 presents the magnetic coupling between two Co ions). Complex **1** has no single molecule magnet behavior while the radical mediate magnetic coupling between high-spin cobalt ions leads to single molecule magnets behavior. Complex **1** can be reproduced by reduction, which make it possible to exhibit a reversible magnetic “on-off” switch.

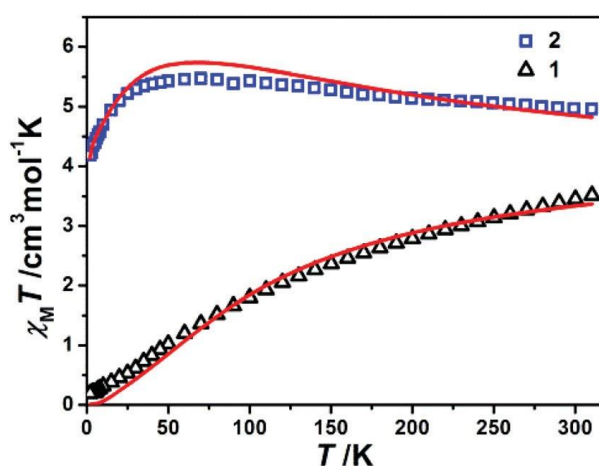


Figure I.22 dc magnetization susceptibility measurements of **1** and **2** from 2–310 K. The red lines represent the best fits as discussed in the text. Reproduced from reference [80].⁸⁰

[Co₃(HHTP)(TPA)₃](BF₄)₄

A trinuclear Co(III) complex was prepared with a tri-bidentate bridging ligand, 2,3,6,7,10,11-hexahydroxytriphenylene (HHTP), and three blocking ligand: Tris-(2-pyridylmethyl)amine (TPA).⁸¹ Molecular structure and its packing structure are displayed in Figure I.23. The valence Co ions in the molecule is +3, leading to the -5 [cat, cat, sq] oxidation state of the HHTP ligand. The threefold symmetry of the cation, linked by π - π interactions, demonstrates that the bridging ligand has its charge delocalized.

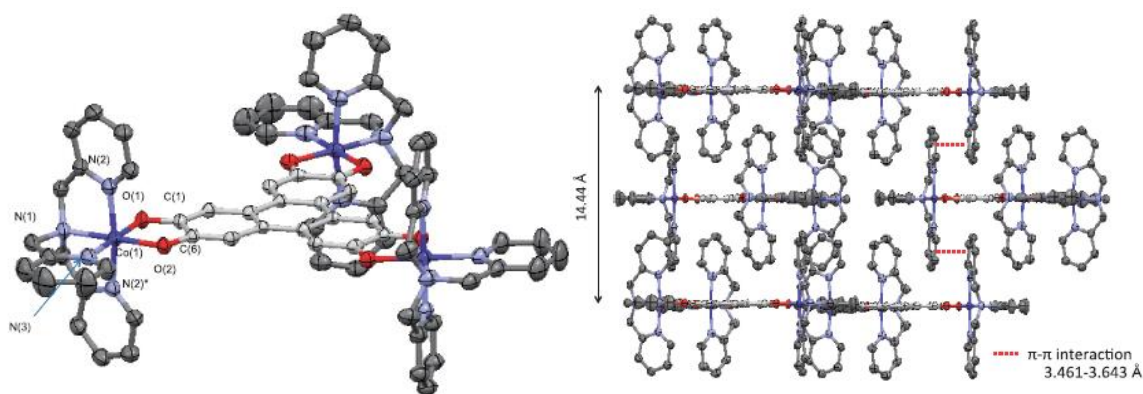


Figure I.23 Left: Perspective view of the complex cation $[\text{Co}_3(\text{HHTP})(\text{TPA})_3]^{4+}$; Right: View of the packing structure. H and BF_4 anions are omitted for clarity. Reproduced from reference [81].⁸¹

The magnetic measurement result (Figure I.24, left) shows that the $\chi_M T$ value at room temperature is around $0.44 \text{ cm}^3 \text{ K mol}^{-1}$, which corresponding to the spin-only state of a $S = 1/2$ paramagnet. The $\chi_M T$ value decreases slightly to $0.33 \text{ cm}^3 \text{ K mol}^{-1}$ when cooling down to 2 K, verifying the charge delocalization over the whole triphenylene ring. Three reversible wave peaks can be observed in the electrochemical measurement (Figure I.24, right). The redox reaction occurs from state [sq, sq, sq] to state [cat, sq, sq], state [cat, cat, sq] and state [cat, cat, cat]. The stepwise oxidation and reduction can be considered as the evidence of their ligand-centered nature.

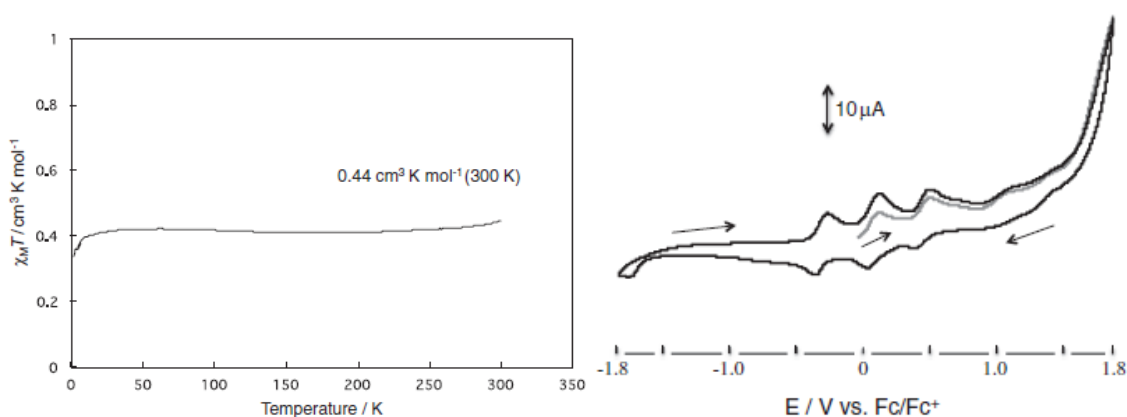


Figure I.24 Left: Plot of $\chi_M T$ versus T for $[\text{Co}_3(\text{HHTP})(\text{TPA})_3](\text{BF}_4)_4$. Right: Cyclic voltammetry of $[\text{Co}_3(\text{HHTP})(\text{TPA})_3](\text{BF}_4)_4$ in CH_3CN . Reproduced from reference [81].⁸¹

1.4.2.3 Polynuclear complexes based on other transition metal ions

(PPh₄)₃[Fe^{III}₃(hftp)(CN)₆]

A non-innocent ligand containing three coordination sites is introduced in preparing a trinuclear Fe(III) complex: (PPh₄)₃[Fe^{III}₃(hftp)(CN)₆] (hftp = N,N',N'',N''',N''''',N''''''-(triphenylene-2,3,6,7,10,11-hexayl)-hexapicolinamide).⁸² The obtained crystals contain 6 or 6.5 MeCN molecules, possessing almost identical structures (Figure I.25, left).

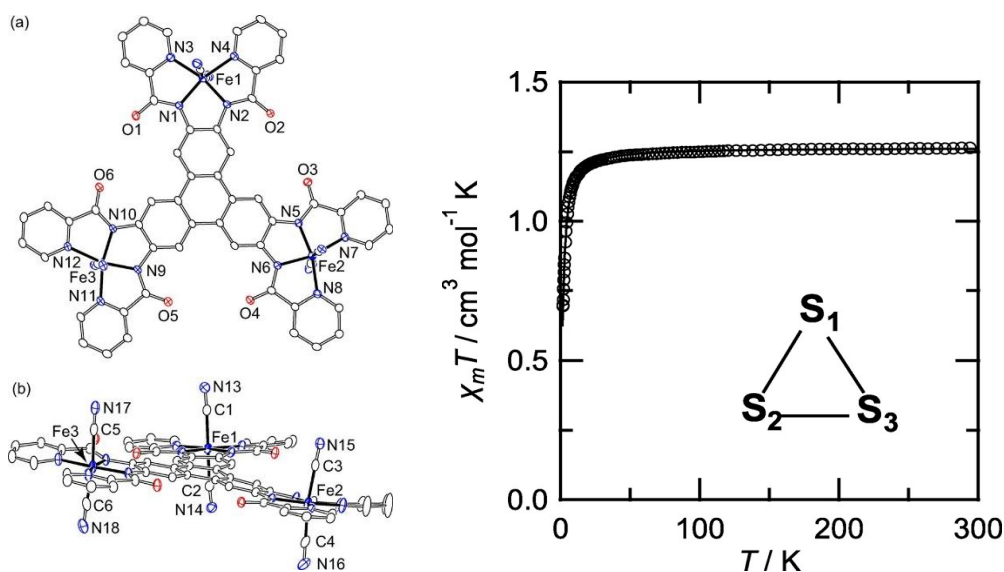


Figure I.25 Left: top view and side view of [Fe^{III}₃(hftp)(CN)₆]³⁺ in a crystal of (PPh₄)₃[Fe₃(hftp)(CN)₆] \cdot 6.5MeCN. Right: $\chi_M T$ vs. T plot for dried crystals. Reproduced from reference [82].⁸²

The $\chi_M T$ versus T plot (Figure I.25, right) is carried out on the dried crystals (PPh₄)₃[Fe^{III}₃(hftp)(CN)₆]. At room temperature, the $\chi_M T$ value found is 1.26 cm³ K mol⁻¹, which is consistent with the simultaneous effects of three isolated low spin Fe(III) species. The fit of the data with a regular triangular model $H = -2J(S_1 \cdot S_2 + S_2 \cdot S_3 + S_3 \cdot S_1)$ can be employed to fit the magnetic data, resulting in $g = 2.12$, and $J = -1.0 \text{ cm}^{-1}$. The very weak antiferromagnetic is proved by calculations.

The non-innocent ligand is able to generate radicals. The Cyclic voltammetry and a differential pulse voltammetry (DPV) results (Figure I.26) reveal one reversible wave peak for three-electron process for 3Fe^{III}/3Fe^{II} and three stepwise reversible wave peaks, which are assigned to the one-electron process of the bridging ligand: hftp⁶⁻/(hftp^{ox1})⁵⁻

$/(hptp^{ox2})^4/(hptp^{ox3})^3$. Radicals are revealed in the intermediate products by diverse measurements, so as the strong coupling between the electrons in the d orbitals of Fe(III) ions and those of the π -radicals in bridge ligand.

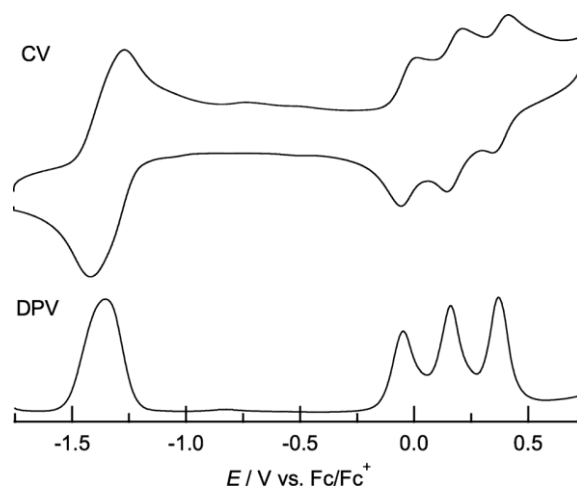


Figure I.26 Cyclic voltammetry and a differential pulse voltammetry (DPV) results for $(PPh_4)_3[Fe_3(hptp)(CN)_6]$ in $(n-Bu_4N)BF_4-PhCN$. Reproduced from reference [82].⁸²

$[(Me_3TPyA)_2Fe_2L]^{n+}$ ($n = 2/3$)

The quinonoid bridging ligand was introduced to synthesize single molecule magnets based on Fe. A dinuclear complex $[(Me_3TPyA)_2Fe_2L]^{2+}$ (**1**) was obtained (top of Figure I.27), and the Fe ions are both +2.⁸³

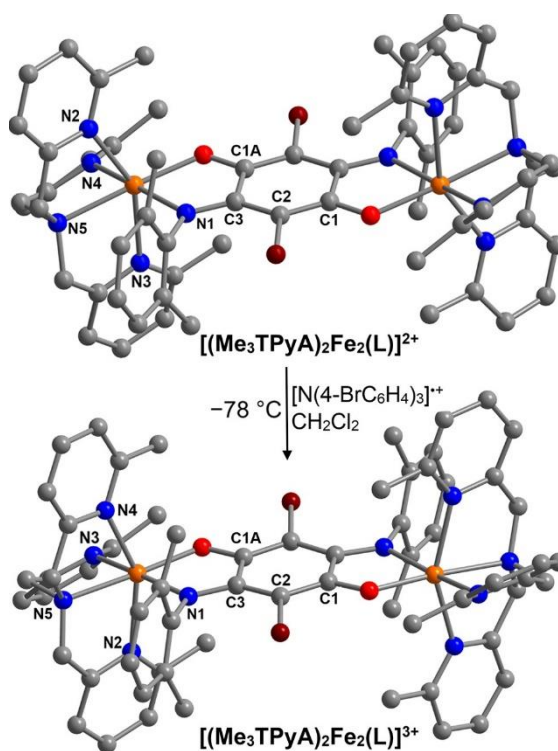


Figure I.27 Oxidation of complex **1** (upper) to **2** (lower). Reproduced from reference [83].⁸³

The $\chi_M T$ value is $6.65\text{ cm}^3\text{ K mol}^{-1}$ at room temperature and reaches its maximum ($8.9\text{ cm}^3\text{ K mol}^{-1}$) at 12 K (blue line in Figure I.28), indicating a weak ferromagnetic coupling ($J = 1.21\text{ cm}^{-1}$) between iron centers through the bridging ligand and giving the ground state $S = 4$, with a $D_{S=4} = -4.9\text{ cm}^{-1}$. The ac magnetic measurements reveal the relaxation barrier is $U_{\text{eff}} = 14\text{ cm}^{-1}$. However, after one-electron oxidation, the slow magnetic relaxation can be switched off by generating a mixed-valence Fe(II)/Fe(III) dinuclear complex: $[(\text{Me}_3\text{TPyA})_2\text{Fe}_2\text{L}]^{3+}$ (**2**) (bottom of Figure I.27). The $\chi_M T$ value equals to $9.97\text{ cm}^3\text{ K mol}^{-1}$ at 300 K, and $12.38\text{ cm}^3\text{ K mol}^{-1}$ at around 40 K, which is consistent with the $S = 9/2$ ground state (the red line in Figure I.28). The magnetic data is fitted with $D_{S=9/2} = +3.4\text{ cm}^{-1}$ and $J = 8.9\text{ cm}^{-1}$. The strong ferromagnetic exchange is attributed to electron hopping through a double-exchange mechanism,⁸⁴ and the double-exchange parameter $B = 69(4)\text{ cm}^{-1}$.

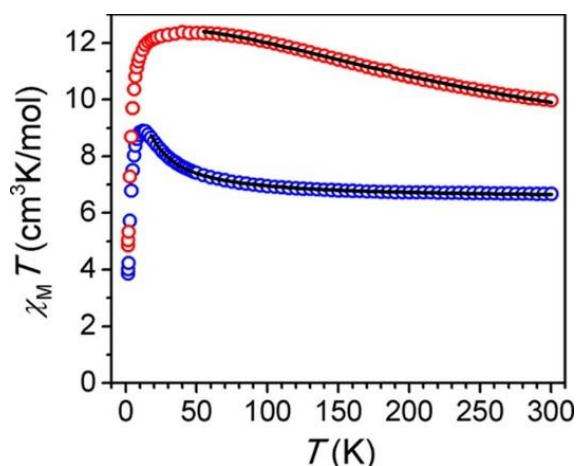


Figure I.28 Variable-temperature dc magnetic susceptibility data for **1** (blue) and **2** (red), collected under an applied field of 1 T. The black lines correspond to fits of the data. Reproduced from reference [83].⁸³

$\text{Mn}_3(\text{Tp}^{\text{Cum,Me}})_3((\text{TBSQ})_3\text{Ph})$ and $\text{Ni}_3(\text{CTH})_3((\text{TBSQ})_3\text{Ph})(\text{PF}_6)_3$

A tris-bidentate ligand 1,3,5-tris(5'-*tert*-butyl-3',4'-dihydroxyphenyl)benzene ((TBCat)₃Ph) was prepared as a bridge for Mn(II) and Ni(II) complexes: the manganese(II)-hydrotris[3-(4'-cumenyl)-5-methylpyrazolyl]borate complex $\text{Mn}_3(\text{Tp}^{\text{Cum,Me}})_3((\text{TBSQ})_3\text{Ph})$ and $\text{Ni}_3(\text{CTH})_3((\text{TBSQ})_3\text{Ph})(\text{PF}_6)_3$ (CAT = *dl*-5,7,7,12,14,14-hexamethyl-1,4,8,11-tetraazacyclotetradecane).⁸⁵

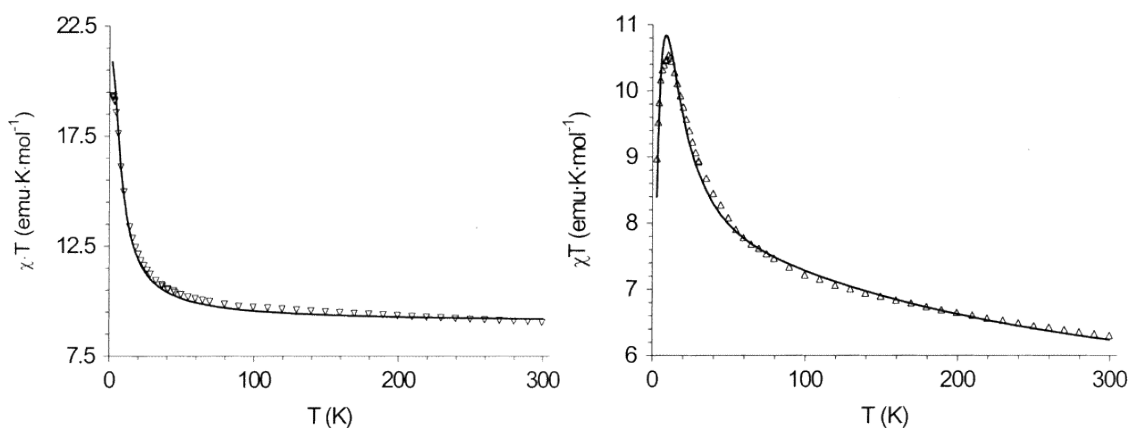


Figure I.29 χT vs. T curve for the Mn(II) complex (left) and Ni(II) complex (right). Reproduced from reference [85].⁸⁵

The magnetic measurements results (Figure I.29) are consistent with the ground states of Mn complex and Ni complex $S = 6$ and $S = 9/2$, respectively, which suggests the

tris(semiquinone) form of the bridging ligand in these complexes (Figure I.30). The magnetic properties provide a clear indication that each paramagnetic center has a strong antiferromagnetic coupling with each semiquinone radical, while the interactions between the metal centers, on one hand and the radicals, on the other hand are ferromagnetic. The ferromagnetic coupling between the three semiquinone units is enhanced by the π -connectivity of the ligand.

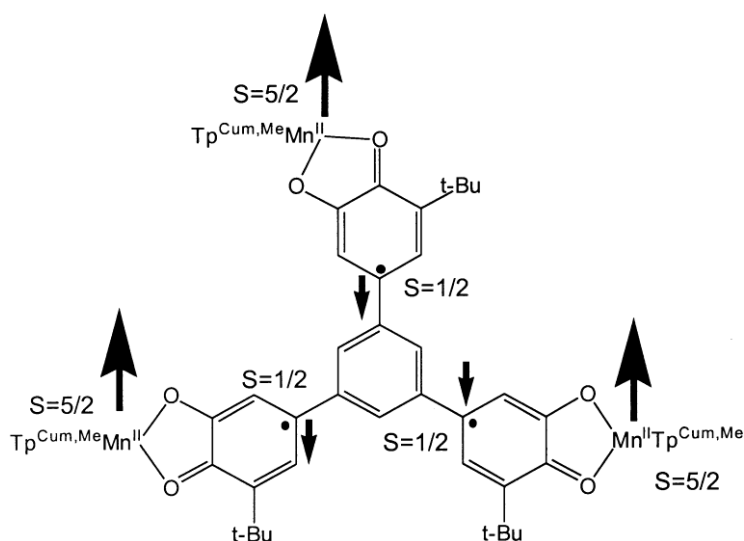


Figure I.30 The ground state of $\text{Mn}_3(\text{Tp}^{\text{Cum,Me}})_3((\text{TBSQ})_3\text{Ph})$. Reproduced from reference [85].⁸⁵

1.5 This thesis

The main topic of this thesis aims at obtaining some active polynuclear magnetic complexes built from anisotropic mononuclear species. It is constituted by two key parts. The first part focus on the syntheses and the study of magnetic properties of Ni(II) mononuclear complexes with trigonal bipyramidal geometry, and the second part is the design of polynuclear Ni(II) and Co(II) complexes with multiple structures with innocent ligand and non-innocent ligand and the study of their characterizations.

The overall architecture of this dissertation is organized as follows:

In Chapter I, starting from the background, motivation and objectives, historical evolution of molecular magnetism is introduced, and then some key items in the field of molecular

magnetism. The syntheses of mononuclear species and polynuclear complexes are followed.

A family of mononuclear Ni(II) complexes based on Me₆tren (Me₆tren = tris(2-(dimethylamino)ethyl)amine) are studied in Chapter II, including their molecular structures, magnetic properties.

Chapter III focus on the polynuclear Ni(II) and Co(II) complexes with TTC³⁻ (TTC = Trithiocyanurate) as the bridging ligand. Their molecular structures and magnetic properties are discussed.

Molecular structures of three polynuclear Ni(II) and Co(II) complexes, bridged by HHTP (HHTP = 2,3,6,7,10,11-Hexahydroxytriphenylene), are studied in Chapter IV. Their magnetic properties, electrochemical properties are also presented.

The overall conclusions and perspectives of this dissertation are presented in Chapter V.

1.6 References

- 1 Werner, A. Beitrag zur konstitution anorganischer verbindungen. *Zeitschrift für anorganische Chemie* **3**, 267-330 (1893).
- 2 Atkins, S. *Inorganic Chemistry*. (2010).
- 3 Tarr, G. L. M. P. J. F. D. A. *Inorganic Chemistry*. (2014).
- 4 Brown, J. Observations and Experiments upon the Foregoing Preparation. By Mr. John Brown, Chymist, FRS. *Philosophical Transactions (1683-1775)* **33**, 17-24 (1724).
- 5 Itaya, K., Uchida, I. & Neff, V. D. Electrochemistry of polynuclear transition metal cyanides: Prussian blue and its analogues. *Accounts of Chemical Research* **19**, 162-168 (1986).
- 6 Ferlay, S., Mallah, T., Ouahes, R., Veillet, P. & Verdaguer, M. A room-temperature organometallic magnet based on Prussian blue. *Nature* **378**, 701 (1995).
- 7 Clearfield, A. (New York: John Wiley & Sons Inc, 1998).
- 8 Clearfield, A. & Stynes, J. The preparation of crystalline zirconium phosphate and some observations on its ion exchange behaviour. *Journal of Inorganic and Nuclear Chemistry* **26**, 117-129 (1964).

- 9 Ilmi, R., Al-Busaidi, I. J., Haque, A. & Khan, M. S. Recent progress in coordination chemistry, photo-physical properties and applications of pyridine-based Cu (I) complexes. *Journal of Coordination Chemistry*, 1-51 (2018).
- 10 Omann, L., Königs, C. D. F., Klare, H. F. & Oestreich, M. Cooperative Catalysis at Metal–Sulfur Bonds. *Accounts of chemical research* **50**, 1258-1269 (2017).
- 11 Yen, Y.-S., Chou, H.-H., Chen, Y.-C., Hsu, C.-Y. & Lin, J. T. Recent developments in molecule-based organic materials for dye-sensitized solar cells. *Journal of Materials Chemistry* **22**, 8734-8747 (2012).
- 12 Qiu, K., Chen, Y., Rees, T. W., Ji, L. & Chao, H. Organelle-targeting metal complexes: From molecular design to bio-applications. *Coordination Chemistry Reviews* (2017).
- 13 Renfrew, A. K., O'Neill, E. S., Hambley, T. W. & New, E. J. Harnessing the properties of cobalt coordination complexes for biological application. *Coordination Chemistry Reviews* (2017).
- 14 Öhrström, L. & Larsson, K. *Molecule-based materials: The structural network approach*. (Elsevier, 2005).
- 15 Oh, M. & Mirkin, C. A. Ion exchange as a way of controlling the chemical compositions of nano - and microparticles made from infinite coordination polymers. *Angewandte Chemie International Edition* **45**, 5492-5494 (2006).
- 16 Seo, J. S. *et al.* A homochiral metal–organic porous material for enantioselective separation and catalysis. *Nature* **404**, 982 (2000).
- 17 Wang, Q. H., Kalantar-Zadeh, K., Kis, A., Coleman, J. N. & Strano, M. S. Electronics and optoelectronics of two-dimensional transition metal dichalcogenides. *Nature nanotechnology* **7**, 699 (2012).
- 18 Bar, A. K., Pichon, C. & Sutter, J.-P. Magnetic anisotropy in two-to eight-coordinated transition–metal complexes: Recent developments in molecular magnetism. *Coordination Chemistry Reviews* **308**, 346-380 (2016).
- 19 Bowman-James, K. Alfred Werner revisited: the coordination chemistry of anions. *Accounts of chemical research* **38**, 671-678 (2005).
- 20 Fowler, M. Historical beginnings of theories of electricity and magnetism. *Physics Department, University of Virginia* (1997).
- 21 Gilbert, W. *De magnete*. (Courier Corporation, 1958).
- 22 Van Vleck, J. H. Quantum mechanics-The key to understanding magnetism. *Reviews of Modern Physics* **50**, 181 (1978).
- 23 Gatteschi, C. B. D. Introduction to Molecular Magnetism. (2015).
- 24 Coey, J. Magnetism in future. *Journal of Magnetism and Magnetic Materials* **226**, 2107-2112 (2001).

- 25 Bogani, L. & Wernsdorfer, W. Molecular spintronics using single-molecule magnets. *Nature Materials* **7**, 179-186 (2008).
- 26 Kahn, O. & Martinez, C. J. Spin-transition polymers: from molecular materials toward memory devices. *Science* **279**, 44-48 (1998).
- 27 Tegus, O., Brück, E., Buschow, K. & De Boer, F. Transition-metal-based magnetic refrigerants for room-temperature applications. *Nature* **415**, 150 (2002).
- 28 Low, D. M. *et al.* Solvothermal synthesis of a tetradecametallic FeIII cluster. *Angewandte Chemie* **42**, 3781-3784, doi:10.1002/anie.200351865 (2003).
- 29 Castelvechi, D. Quantum computers ready to leap out of the lab in 2017. *Nature News* **541**, 9 (2017).
- 30 Carlin, R. L. *Magnetochemistry*. (1986).
- 31 Kahn, O. *Molecular Magnetism*. (1993).
- 32 Goodenough, J. B. Theory of the role of covalence in the perovskite-type manganites [La, M (II)] Mn O₃. *Physical Review* **100**, 564 (1955).
- 33 Goodenough, J. B. An interpretation of the magnetic properties of the perovskite-type mixed crystals La_{1-x}Sr_xCoO_{3-λ}. *Journal of Physics and Chemistry of Solids* **6**, 287-297 (1958).
- 34 Kanamori, J. Superexchange interaction and symmetry properties of electron orbitals. *Journal of Physics and Chemistry of Solids* **10**, 87-98 (1959).
- 35 Cahier, B. *et al.* Magnetic Anisotropy in Pentacoordinate NiII and CoII Complexes: Unraveling Electronic and Geometrical Contributions. *Chemistry—A European Journal* **23**, 3648-3657 (2017).
- 36 McInnes, E. J. L. & Winpenny, R. E. P. Molecular Magnets. 371-395, doi:10.1016/b978-0-08-097774-4.00419-8 (2013).
- 37 Deeth, R. J. & Hitchman, M. A. Factors influencing Jahn-Teller distortions in six-coordinate copper (II) and low-spin nickel (II) complexes. *Inorganic Chemistry* **25**, 1225-1233 (1986).
- 38 Marriott, K. E. R. *et al.* Pushing the limits of magnetic anisotropy in trigonal bipyramidal Ni(ii). *Chemical Science* **6**, 6823-6828, doi:10.1039/C5SC02854J (2015).
- 39 Gispert, J. R. *Coordination chemistry*. Vol. 483 (Wiley-VCH Weinheim, 2008).
- 40 Lis, T. Preparation, structure, and magnetic properties of a dodecanuclear mixed - valence manganese carboxylate. *Acta Crystallographica Section B* **36**, 2042-2046 (1980).
- 41 Sessoli, R., Gatteschi, D., Caneschi, A. & Novak, M. Magnetic bistability in a metal-ion cluster. *Nature* **365**, 141 (1993).

- 42 Caneschi, A. *et al.* Alternating current susceptibility, high field magnetization, and millimeter band EPR evidence for a ground $S=10$ state in $[\text{Mn}_{12}\text{O}_{12}(\text{CH}_3\text{COO})_{16}(\text{H}_2\text{O})_4] \cdot 2\text{CH}_3\text{COOH} \cdot 4\text{H}_2\text{O}$. *Journal of the American Chemical Society* **113**, 5873-5874 (1991).
- 43 Hill, S. *et al.* high-sensitivity electron paramagnetic resonance of Mn 12-acetate. *Physical review letters* **80**, 2453 (1998).
- 44 Singh, S. K., Gupta, T., Badkur, P. & Rajaraman, G. Magnetic anisotropy of mononuclear Ni(II) complexes: on the importance of structural diversity and the structural distortions. *Chemistry* **20**, 10305-10313, doi:10.1002/chem.201402694 (2014).
- 45 Gomez-Coca, S., Cremades, E., Aliaga-Alcalde, N. & Ruiz, E. Mononuclear single-molecule magnets: tailoring the magnetic anisotropy of first-row transition-metal complexes. *J Am Chem Soc* **135**, 7010-7018, doi:10.1021/ja4015138 (2013).
- 46 Gruden-Pavlović, M., Perić, M., Zlatar, M. & García-Fernández, P. Theoretical study of the magnetic anisotropy and magnetic tunnelling in mononuclear Ni(II) complexes with potential molecular magnet behavior. *Chemical Science* **5**, 1453, doi:10.1039/c3sc52984c (2014).
- 47 Llanos, L. & Aravena, D. Effect of Low Spin Excited States for Magnetic Anisotropy of Transition Metal Mononuclear Single Molecule Magnets. *Inorganics* **6**, 24 (2018).
- 48 Verdaguer, M. Rational synthesis of molecular magnetic materials: a tribute to Olivier Kahn. *Polyhedron* **20**, 1115-1128, doi:10.1016/s0277-5387(01)00700-8 (2001).
- 49 Oshio, H. & Nakano, M. High-spin molecules with magnetic anisotropy toward single-molecule magnets. *Chemistry* **11**, 5178-5185, doi:10.1002/chem.200401100 (2005).
- 50 Mossin, S. *et al.* A mononuclear Fe (III) single molecule magnet with a $3/2 \leftrightarrow 5/2$ spin crossover. *Journal of the American Chemical Society* **134**, 13651-13661 (2012).
- 51 Miklović, J., Valigura, D., Boca, R. & Titiš, J. A mononuclear Ni(II) complex: a field induced single-molecule magnet showing two slow relaxation processes. *Dalton transactions* **44**, 12484-12487, doi:10.1039/c5dt01213a (2015).
- 52 Miklović, J. *et al.* Synthesis, crystal structures, spectral and magnetic properties of nickel(II) pyridinecarboxylates with N-heterocyclic ligands. *Inorganica Chimica Acta* **429**, 73-80, doi:10.1016/j.ica.2015.01.046 (2015).
- 53 Ruamps, R. *et al.* Ising-type magnetic anisotropy and single molecule magnet behaviour in mononuclear trigonal bipyramidal Co (II) complexes. *Chemical Science* **5**, 3418-3424 (2014).

- 54 El-Khatib, F. *et al.* Design and Magnetic Properties of a Mononuclear Co(II) Single Molecule Magnet and Its Antiferromagnetically Coupled Binuclear Derivative. *Inorg Chem* **56**, 4602-4609, doi:10.1021/acs.inorgchem.7b00205 (2017).
- 55 Jørgensen, C. K. Differences between the four halide ligands, and discussion remarks on trigonal-bipyramidal complexes, on oxidation states, and on diagonal elements of one-electron energy. *Coordination Chemistry Reviews* **1**, 164-178 (1966).
- 56 Ward, M. D. & McCleverty, J. A. Non-innocent behaviour in mononuclear and polynuclear complexes: consequences for redox and electronic spectroscopic properties. *Journal of the Chemical Society, Dalton Transactions*, 275-288, doi:10.1039/b110131p (2002).
- 57 Kaim, W. Manifestations of noninnocent ligand behavior. *Inorg Chem* **50**, 9752-9765, doi:10.1021/ic2003832 (2011).
- 58 Zhang, Y. & Popov, A. A. Transition-Metal and Rare-Earth-Metal Redox Couples inside Carbon Cages: Fullerenes Acting as Innocent Ligands. *Organometallics* **33**, 4537-4549, doi:10.1021/om5000387 (2014).
- 59 Collins, T. J., Nichols, T. R. & Uffelman, E. S. A square-planar nickel(III) complex of an innocent ligand system. *Journal of the American Chemical Society* **113**, 4708-4709, doi:10.1021/ja00012a064 (1991).
- 60 Jain, M., Sharma, R. & Jain, P. Ligational behavior of thiosemicarbazide and thiosemicarbazone (VI): Some trivalent metal complexes of innocent ligands. *Journal of Inorganic and Nuclear Chemistry* **42**, 1229-1233 (1980).
- 61 Caneschi, A., Gatteschi, D., Sessoli, R. & Rey, P. Toward molecular magnets: the metal-radical approach. *Accounts of chemical Research* **22**, 392-398 (1989).
- 62 Dei, A., Gatteschi, D. & Pardi, L. Sextet ground state in a dinuclear nickel (II) complex containing a tetraoxolene radical as bridging ligand. *Inorganica chimica acta* **189**, 125-128 (1991).
- 63 Dei, A., Gatteschi, D., Pardi, L. & Russo, U. Tetraoxolene radical stabilization by the interaction with transition-metal ions. *Inorganic chemistry* **30**, 2589-2594 (1991).
- 64 Zhang, P. *et al.* Exchange coupling and single molecule magnetism in redox-active tetraoxolene-bridged dilanthanide complexes. *Chem Sci* **9**, 1221-1230, doi:10.1039/c7sc04873d (2018).
- 65 DeGayner, J. A., Jeon, I. R., Sun, L., Dinca, M. & Harris, T. D. 2D Conductive Iron-Quinoid Magnets Ordering up to T_c = 105 K via Heterogenous Redox Chemistry. *J Am Chem Soc* **139**, 4175-4184, doi:10.1021/jacs.7b00705 (2017).

- 66 Jeon Ie, R., Negru, B., Van Duyne, R. P. & Harris, T. D. A 2D Semiquinone Radical-Containing Microporous Magnet with Solvent-Induced Switching from $T_c = 26$ to 80 K. *J Am Chem Soc* **137**, 15699-15702, doi:10.1021/jacs.5b10382 (2015).
- 67 Demir, S., Jeon, I.-R., Long, J. R. & Harris, T. D. Radical ligand-containing single-molecule magnets. *Coordination Chemistry Reviews* **289-290**, 149-176, doi:10.1016/j.ccr.2014.10.012 (2015).
- 68 Carbonera, C., Dei, A., Létard, J. F., Sangregorio, C. & Sorace, L. Thermally and Light - Induced Valence Tautomeric Transition in a Dinuclear Cobalt - Tetraoxolene Complex. *Angewandte Chemie* **116**, 3198-3200 (2004).
- 69 Min, K. S., DiPasquale, A. G., Golen, J. A., Rheingold, A. L. & Miller, J. S. Synthesis, structure, and magnetic properties of valence ambiguous dinuclear antiferromagnetically coupled cobalt and ferromagnetically coupled iron complexes containing the chloranilate (2-) and the significantly stronger coupling chloranilate (\bullet 3-) radical trianion. *Journal of the American Chemical Society* **129**, 2360-2368 (2007).
- 70 Tao, J., Maruyama, H. & Sato, O. Valence Tautomeric Transitions with Thermal Hysteresis around Room Temperature and Photoinduced Effects Observed in a Cobalt-Tetraoxolene Complex. *Journal of the American Chemical Society* **128**, 1790-1791 (2006).
- 71 Ward, M. D. A dinuclear Ruthenium (II) complex with the dianion of 2, 5-dihydroxy-1, 4-benzoquinone as bridging ligand. Redox, spectroscopic, and mixed-valence properties. *Inorganic chemistry* **35**, 1712-1714 (1996).
- 72 Roy, S. *et al.* Stabilizing the elusive ortho-quinone/copper (I) oxidation state combination through π/π interaction in an isolated complex. *Journal of the American Chemical Society* **130**, 15230-15231 (2008).
- 73 Kaim, W. The chemistry and biochemistry of the copper-radical interaction. *Dalton transactions*, 761-768 (2003).
- 74 Yu, F. *et al.* Valence tautomerism and photodynamics observed in a dinuclear cobalt-tetraoxolene compound. *Inorganica Chimica Acta* **426**, 146-149, doi:10.1016/j.ica.2014.11.021 (2015).
- 75 Li, B., Chen, L. Q., Tao, J., Huang, R. B. & Zheng, L. S. Unidirectional charge transfer in di-cobalt valence tautomeric compound finely tuned by ancillary ligand. *Inorg Chem* **52**, 4136-4138, doi:10.1021/ic4000268 (2013).
- 76 Li, B. *et al.* Side-effect of ancillary ligand on electron transfer and photodynamics of a dinuclear valence tautomeric complex. *Chemical communications*, 2269-2271, doi:10.1039/b801171k (2008).
-

- 77 Schweinfurth, D. *et al.* Redox-induced spin-state switching and mixed valency in quinonoid-bridged dicobalt complexes. *Chemistry* **20**, 3475-3486, doi:10.1002/chem.201302858 (2014).
- 78 El-Khatib, F. *et al.* Design of a Binuclear Ni(II) Complex with Large Ising-type Anisotropy and Weak Anti-Ferromagnetic Coupling. *Inorg Chem* **56**, 10655-10663, doi:10.1021/acs.inorgchem.7b01609 (2017).
- 79 Jiang, Y.-B., Kou, H.-Z., Wang, R.-J., Cui, A.-L. & Ribas, J. Synthesis, crystal structure, and magnetic properties of oxime-bridged polynuclear Ni (II) and Cu (II) complexes. *Inorganic chemistry* **44**, 709-715 (2005).
- 80 Wang, Y. *et al.* Magnetic on-off switching in redox non-innocent ligand bridged binuclear cobalt complexes. *Dalton transactions* **47**, 17211-17215, doi:10.1039/c8dt04157a (2018).
- 81 Suenaga, Y. *et al.* Crystal Structure and Characterization of Trinuclear Cobalt(III) Complex with 2,3,6,7,10,11-Hexahydroxytriphenylene. *Chemistry Letters* **43**, 562-564, doi:10.1246/cl.131090 (2014).
- 82 Hoshino, N. & Akutagawa, T. A Trinuclear Iron(III) Complex of a Triple Noninnocent Ligand for Spin-Structured Molecular Conductors. *Chemistry* **24**, 19323-19331, doi:10.1002/chem.201804280 (2018).
- 83 Gaudette, A. I. *et al.* Electron Hopping through Double-Exchange Coupling in a Mixed-Valence Diiminobenzoquinone-Bridged Fe₂ Complex. *J Am Chem Soc* **137**, 12617-12626, doi:10.1021/jacs.5b07251 (2015).
- 84 Blondin, G. & Girerd, J. J. Interplay of electron exchange and electron transfer in metal polynuclear complexes in proteins or chemical models. *Chemical Reviews* **90**, 1359-1376 (1990).
- 85 Caneschi, A. *et al.* High-spin metal complexes containing a ferromagnetically coupled tris (semiquinone) ligand. *Inorganic chemistry* **41**, 1086-1092 (2002).

Chapter II

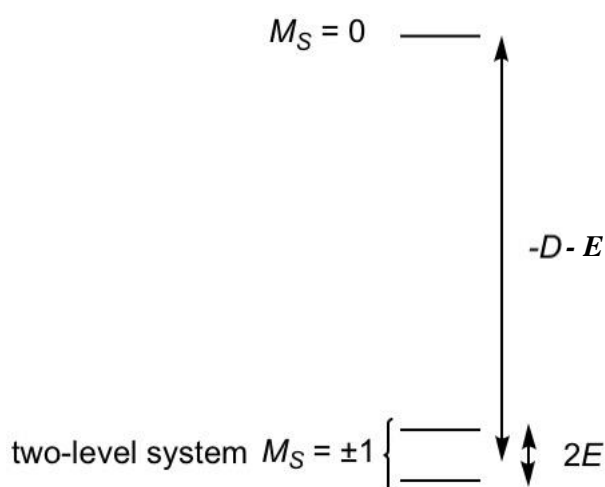
Engineering the Ising-type anisotropy in Ni(II) complexes based on Tris(2-(dimethylamino)ethyl)amine (Me₆tren)

2.1 Introduction

Single molecule magnets (SMMs) are molecules that are able to display a slow relaxation of their magnetization leading to a magnetic hysteresis loop, a significant feature of SMMs. The first SMM is a polynuclear molecule based on transition metal ions Mn^{III} and Mn^{IV}: Mn₁₂(OAc)₁₆. It has a large spin ground state ($S = 10$) and an Ising type magnetic anisotropy due to the fact that the largest M_S values (± 10) are the ground sub-levels (negative axial zero-field splitting parameter D value).¹⁻⁴ Magnetic hysteresis is interesting if one aims to design bistable molecules for classical information storage. That is why much efforts were devoted during the last twenty years to prepare polynuclear complexes with a high spin ground state and Ising type anisotropy. It turned out, however, that it was difficult to produce molecules based on transition metal ions possessing magnetic bistability at high temperature. Efforts were then focused on designing new mononuclear complexes with half integer spin values (mainly $S = 3/2$ Co(II) complexes) with large negative axial ZFS parameter D in order to observe magnetic bistability.⁵⁻¹⁰

Another motivation in this area of research is the design of magnetic molecules that can behave as quantum bits (qbits) for quantum information. The very first molecular magnets investigated (Mn₁₂ and Fe₈) were evaluated as possible qbits and the first proposals to use molecular magnets as qbits were based on the quantum properties of Mn₁₂. However, these polynuclear complexes are too fragile to be manipulated in solution and organized

on surfaces and particularly to be assembled in arrays of interacting molecules. Mononuclear complexes may be excellent candidates for qubits and among them Ni(II) complexes may have the required properties and more importantly their magnetic behavior may be tuned by chemical design. As stated in the previous chapter, a qubit is a two quantum levels system and Ni(II) complexes that have a spin $S = 1$ can be driven to have two quantum levels if ZFS leads to $M_S = \pm 1$ sub-levels as the ground levels and if a weak rhombicity is present as shown in the scheme II. 1.



Scheme II.1. Zero-field splitting of a $S = 1$

Therefore, in order to have a robust two-level system, a mononuclear Ni(II) complex must be designed to present a large axial ZFS parameter (D) and a weak rhombic parameter E . If $|D|$ is large, the characteristics of the two-level system are entirely determined by the magnitude of the rhombic parameter. Recently, several mononuclear molecular magnets based on Ni(II) were reported, where large and negative D value were obtained, presenting the Ising-type magnetic anisotropy.¹¹⁻¹⁵ It is worth noting that for Ni(II) complexes where $S = 1$, a blocking of the magnetization is very difficult to achieve because quantum tunneling remains important. This is due to the difficulty to make the rhombic term of the ZFS strictly equal to zero. Such systems are, thus, good candidates for quantum and not classical information.

As mentioned in chapter I, the magnetic anisotropy is closely related to the symmetry of the molecules. To enlarge the value of the axial ZFS parameter D and thus magnetic anisotropy, molecules with low symmetry must be prepared. Generally, Ni(II) complexes tend to be hexa-coordinated, with octahedral or distorted octahedral geometries, in which the angular momentum is quenched. In order to have appreciable orbital angular momentum, low symmetry that can be obtained by controlling the coordination sphere using suitable organic ligands is thus necessary.

Our group is involved in the study of the relationship between magnetic anisotropy and molecular structures. Several Ni(II) and Co(II) complexes possessing trigonal bipyramidal symmetry were reported with large and negative axial ZFS parameters.^{5,12,16,17} The ligands employed in these systems are the Tris(2-(dimethylamino)ethyl)amine (Me₆tren) and the related sulfur containing ligand 2-(tert-butylthio)-N-(2-(tert-butylthio)ethyl)-N((neopentylthio)methyl)ethan-1-amine (NS₃^{tBu}). The complex [Ni(Me₆tren)Cl](ClO₄) shows a giant and negative magnetic anisotropy (D close to -200 cm^{-1}), due to near first-order spin orbit coupling (SOC) imposed by the quasi C_{3v} symmetry of the complex. The effect of the halides ligand field was demonstrated by substituting Cl by Br in the Ni(II) coordination sphere in [Ni(Me₆tren)Br]Br, that gave $D = -147\text{ cm}^{-1}$. However, as expected no blocking of the magnetization was observed in both complexes because of the quantum tunneling of magnetization (QTM) due to the presence of a very weak rhombic parameter ($E = 1.5\text{ cm}^{-1}$) that mixes the low-lying $M_S = \pm 1$ sublevels.¹² For the related Co(II) containing complexes [Co(Me₆tren)Cl](ClO₄) and [Co(Me₆tren)Br]Br, the D values were much weaker in absolute values (-8.1 cm^{-1} and -2.4 cm^{-1} respectively), but a blocking of the magnetization was observed leading to an opening of the hysteresis loop at low temperature for [Co(Me₆tren)Cl](ClO₄).⁵ The difference in the magnetic behavior between the Ni(II) and the Co(II) complexes is due to the nature of the spin state; the Kramers ion (Co(II), $S = 3/2$) may have a strict C_{3v} symmetry and thus a strict zero rhombic parameter, while this is not the case for the Ni(II) non Kramers ion ($S = 1$) that is subject to a Jahn-Teller effect that slightly reduces the axial C_{3v} symmetry and leads to a non-zero rhombic parameter and thus to QTM that prevents the blocking of the magnetization. Three Co(II)

complexes with different axial ligands were prepared with the NS₃^{tBu} to perform the correlation between geometrical structures and the magnitude of anisotropy: [Co(NS₃^{tBu})Cl](ClO₄), [Co(NS₃^{tBu})Br](ClO₄) and [Co(NS₃^{tBu})NCS](ClO₄). It was found that the complex with a strict zero rhombic ZFS parameter has a slower relaxation of magnetization, even though the magnitude of its axial ZFS parameter is smaller than the other two. The main reason is that the rhombic terms in the other two complexes provide channels for quantum tunneling.¹⁷ This confirms that the blocking of the magnetization is controlled by the rhombic parameter rather than by the axial ZFS parameter.

Based on the existing results, we expanded the research on Ni(II) containing complexes by preparing a series of [Ni(Me₆tren)X]Y (X = Cl, Br, I; Y = X⁻, ClO₄⁻, BPh₄⁻ ...). Changing the axial ligand X and the nature of the counter anion Y leads to complexes with various geometrical structures, allowing us to explore (i) the effect of the axial ligand/counter anion on the overall structure and on the local structure of Ni(II) and (ii) the effect of the local structure on the ZFS parameters. The prepared complexes were characterized by infrared spectroscopy, element analysis, X-ray single crystal diffraction and magnetic measurements. We did not carry out any Electron Paramagnetic Resonance studies to accurately determine the values of the ZFS parameters, we rely only the magnetic data. For one case (X = Y = Cl), we performed theoretical calculations that allows rationalizing the magnetic behavior observed.

2.2 Experimental section

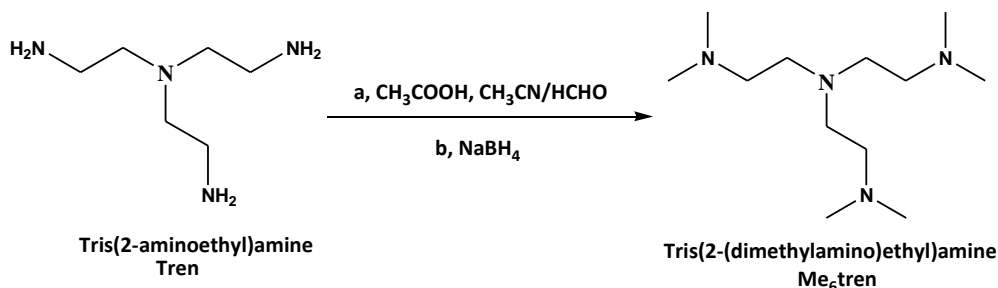
2.2.1 Syntheses

All the reagents used for these syntheses were purchased commercially and were used directly without further purification unless exceptionally stated.

Caution: The Perchlorate salts may have unpredictable behavior and may explode. They must be handled with care under a protected hood and must never be heated.

Tris(2-(dimethylamino)ethyl)amine: Me₆tren

The ligand Me₆tren was synthesized according to a previous report.¹⁸



Scheme II.2 Synthesis of Ligand Me₆tren

Aqueous formaldehyde (49.0 mL, 660 mmol, 37 wt%) was added to a solution of 3.00 mL (19.9 mmol) of tris(2-aminoethyl) amine and 135 mL of acetic acid in acetonitrile (600 mL) and allowed to stir for 1 h. Subsequently, the reaction mixture was cooled to 0 °C and 10.0 g (26.4 mmol) of sodium borohydride was slowly added. After being stirred for 48 h, all solvents were removed, the residue was made strongly basic with 3 M aqueous sodium hydroxide and extracted several times with dichloromethane (DCM). The DCM extracts were combined, dried (MgSO₄), and the solvent removed. The residue was dissolved in pentane, filtered, and the filtrate reduced to dryness to give **Me₆tren** as pale-yellow oil (4.32 g, 94%). ¹H NMR (CDCl₃, 300 MHz, ppm from TMS): δ 2.56 (m, 6H, CH₂N(CH₃)₂), 2.32 (m, 6H, NCH₂CH₂N(CH₃)₂), 2.19 (s, 18H, NCH₃).

[Ni(Me₆tren)Cl]Cl (Complex 2-1)

A 3 mL EtOH solution of Me₆tren (150 μL, 0.6 mmol) was added dropwise to a 5 mL EtOH solution of NiCl₂·6H₂O (119 mg, 0.5 mmol) with stirring. A green solution was obtained immediately. After 3 h stirring, diethyl ether was diffused into the abovementioned solution to obtain X-ray quality crystals **2-1**. Yield: 65%. Space group: from Orthorhombic [40 K (**a**), 100 K (**b**)] to Cubic [200 K (**c**)], *P*₂₁₂₁₂₁ to *P*₂₁₃. Elem. Anal. for [Ni(Me₆tren)Cl]Cl(H₂O)_{0.3} Calc: C, 39.44; H, 8.44; N, 15.33. Found: C, 39.54; H, 8.17; N, 15.25. Mw = 369.40 g/mol. The structure was studied at three different temperatures. At 40 K, the space group is orthorhombic: single-crystal unit cell of **2-1(a)**: Orthorhombic, space

group $P2_12_12_1$, $a = 11.374(4)$ Å, $b = 11.919(5)$ Å, $c = 12.038(4)$ Å, $\alpha = 90^\circ$, $\beta = 90^\circ$, $\gamma = 90^\circ$, $V = 1632.0(10)$ Å³. When the temperature increases to 100 K, the space group remains the same except for some small changes of the cell parameters, leading to the single-crystal unit cell of **2-1(b)**: Orthorhombic, space group $P2_12_12_1$, $a = 11.478(6)$ Å, $b = 11.966(7)$ Å, $c = 12.096(8)$ Å, $\alpha = 90^\circ$, $\beta = 90^\circ$, $\gamma = 90^\circ$, $V = 1661.5(16)$ Å³. At 200 K, a phase transition is observed: -single-crystal unit cell of **2-1(c)**: Cubic, space group $P2_13$, $a = 11.8520(5)$ Å, $b = 11.8520(5)$ Å, $c = 11.8520(5)$ Å, $\alpha = 90^\circ$, $\beta = 90^\circ$, $\gamma = 90^\circ$, $V = 1664.8(2)$ Å³. When the crystals were exposed to air for a few weeks, their aspect was altered with the appearance of “oily” like powder as if they have captured water molecules from the atmosphere (it is worth noting that they keep their pristine aspect if kept in a closed vial). Then, three weeks later crystals suitable for X-ray diffraction are obtained from the “oily” like powder. The structural resolution shows the presence of two water molecules within the crystal lattice: [Ni(Me₆tren)Cl]Cl·(H₂O)₂ **2-1(d)**. Single-crystal unit cell: Orthorhombic, space group $Pbca$, $a = 9.1699(4)$ Å, $b = 15.6319(5)$ Å, $c = 26.5895(10)$ Å, $\alpha = 90^\circ$, $\beta = 90^\circ$, $\gamma = 90^\circ$, $V = 3811.4(3)$ Å³. IR (KBr) ν/cm^{-1} : 3432 (m), 2988 (m), 2927 (s), 2878 (s), 2839 (w), 1640 (w), 1486 (s), 1474 (s), 1458 (s), 1440 (m), 1393 (m), 1352 (m), 1290 (s), 1273 (m), 1239(m), 1168 (m), 1096 (s), 1047 (m), 1032 (s) 1016 (s), 1002 (s), 935 (s), 910 (s), 804 (m), 773 (s), 743 (w), 598 (w), 477 (m), 411 (w), 378 (w), 319 (w).

[Ni(Me₆tren)Cl]BPh₄ (Complex 2-2)

A 3 mL EtOH solution of Me₆tren (150 μL, 0.6 mmol) was added dropwise to a 5 mL EtOH solution of NiCl₂·6H₂O (119 mg, 0.5 mmol) with stirring. After one hour, NaBPh₄ (200 mg, 0.58 mmol) was added slowly, a green solid formed. The solid was filtered and then washed with EtOH for three times and then dried in air. Yield: 295 mg, 92%. Crystals suitable for X-ray single crystal diffraction were obtained by dissolving the solid into acetone and then leaving the solution to evaporate slowly. Elem. Anal. for [Ni(Me₆tren)Cl]BPh₄ Calc: C, 67.16; H, 7.83; N, 8.70. Found: C, 67.11; H, 7.74; N, 8.58. Mw = 643.77 g/mol. Single-crystal unit cell: Monoclinic, space group $P2_1/n$, $a = 12.5673(3)$ Å, $b = 12.3077(3)$ Å, $c = 21.6480(6)$ Å, $\alpha = 90^\circ$, $\beta = 97.7550(10)^\circ$, $\gamma = 90^\circ$, $V = 3317.77(15)$ Å³. IR (KBr) ν/cm^{-1} : 3458 (w), 3055 (m), 3034 (m), 3010 (m), 2982 (m), 2895 (w), 2875 (w), 1947 (w), 1885 (w), 1812 (w), 1760 (w),

1578 (m), 1475 (s), 1426 (m), 1343 (w), 1287 (m), 1270 (m), 1239 (m), 1172 (w) 1135 (w), 1100 (m), 1043 (m), 1016 (m), 935 (m), 905 (m), 844 (w), 803 (m), 774 (s), 752 (s), 736 (s), 708 (s), 612 (s), 468 (w).

[Ni(Me₆tren)Cl]PF₆ (Complex 2-3)

A 3 mL EtOH solution of Me₆tren (150 μL, 0.6 mmol) was added dropwise to a 5 mL EtOH solution of NiCl₂·6H₂O (119 mg, 0.5 mmol) with stirring. After one hour, KPF₆ (100 mg, 0.54 mmol) was added slowly, a green solid formed. It was filtered, washed with EtOH for three times and then dried in air. Yield: 180 mg, 38%. Crystals suitable for X-ray single crystal diffraction were obtained by recrystallization from a hot MeOH solution. Elem. Anal. for [Ni(Me₆tren)Cl]PF₆ Calc: C, 30.70; H, 6.44; N, 11.93. Found: C, 30.72; H, 6.38; N, 11.90. Mw = 469.50 g/mol. Single-crystal unit cell: Trigonal, space group *R*3-2, *a* = 10.2529(5) Å, *b* = 10.2529(5) Å, *c* = 16.0206(9) Å, $\alpha = 90^\circ$, $\beta = 90^\circ$, $\gamma = 120^\circ$, *V* = 1458.49(16) Å³. IR (KBr) v/cm⁻¹: 3440 (w), 2990 (m), 2928 (m), 2906 (m), 2855 (w), 1629 (w), 1485 (s), 1476 (s), 1461 (m), 1437 (m), 1411 (w), 1358 (w), 1299 (m), 1250 (w), 1105 (s), 1052 (s), 1043 (s), 1025 (s), 940 (m), 911 (m), 877 (s), 839 (s), 809 (s), 776 (s), 557 (s), 479 (w), 419 (w), 383 (w), 322 (w).

[Ni(Me₆tren)Cl]CF₃SO₃ (Complex 2-4)

A 3 mL EtOH solution of Me₆tren (150 μL, 0.6 mmol) was added dropwise to a 5 mL EtOH solution of NiCl₂·6H₂O (119 mg, 0.5 mmol) with stirring. After one hour, NaCF₃SO₃ (100 mg, 0.58 mmol) was added slowly, a green solid formed. It was filtered, washed with EtOH for three times and then dried in air. Yield: 155 mg. 33%. Crystals suitable for X-ray single crystal diffraction were obtained by recrystallization from a hot CHCl₃ solution. Elem. Anal. for [Ni(Me₆tren)Cl]CF₃SO₃ Calc: C, 32.97; H, 6.38; N, 11.83. Found: C, 33.41; H, 6.53; N, 11.84. Mw=473.61 g/mol. Single-crystal unit cell: Orthorhombic, space group *Pnma*, *a* = 16.1142(4) Å, *b* = 10.3982(3) Å, *c* = 12.2412(3) Å, $\alpha = 90^\circ$, $\beta = 90^\circ$, $\gamma = 90^\circ$, *V* = 2051.12(9) Å³. IR (KBr) v/cm⁻¹: 3441 (w), 2987 (m), 2905 (m), 2851 (m), 2296 (w), 1623 (w), 1474 (s), 1461 (m), 1435 (w), 1355 (w), 1270 (s), 1226 (s), 1202 (w), 1151 (s), 1101 (s), 1050 (m), 1032 (s), 950 (m), 938 (s) 910 (m), 807 (m), 776 (s), 755 (w), 639 (s), 572 (m), 517 (m), 479 (w), 414 (w), 291 (m).

[Ni(Me₆tren)Br]ClO₄ (Complex 2-5)

A 3 mL EtOH solution of Me₆tren (150 μL, 0.6 mmol) was added dropwise to a 10 mL EtOH hot solution (45 °C) of NiBr₂·3H₂O (136 mg, 0.5 mmol) with stirring. After one hour, NaClO₄ (70 mg, 0.57 mmol) was added slowly, a yellow-green solid formed [*Hazardous: Perchlorate salts are explosive and must be handled with caution, we always take care to use very small amount*]. It was filtered, washed with EtOH for three times and then dried in air. Yield: 167 mg, 36%. Crystals suitable for X-ray single crystal diffraction were obtained by recrystallization in a hot MeOH solution. Elem. Anal. for [Ni(Me₆tren)Br]ClO₄ Calc: C, 30.77; H, 6.46; N, 11.96. Found: C, 30.62; H, 6.32; N, 12.04. Mw = 468.44 g/mol. Single-crystal unit cell: Cubic, space group $P2_13$, $a = 12.4541(7) \text{ \AA}$, $b = 12.4541(7) \text{ \AA}$, $c = 12.4541(7) \text{ \AA}$, $\alpha = 90^\circ$, $\beta = 90^\circ$, $\gamma = 90^\circ$, $V = 1931.7(3) \text{ \AA}^3$. IR (KBr) ν/cm^{-1} : 3436 (w), 2983 (m), 2900 (m), 2850 (m), 2014 (w), 1630 (w), 1486 (s), 1474 (s), 1459 (s), 1434 (m), 1355 (w), 1296 (m), 1245 (w), 1172 (w), 1091 (s), 1051 (m), 1019 (m), 1004 (w), 937 (m), 910 (m), 806 (m), 775 (s), 740 (w), 622 (s), 480 (w), 418 (w), 385 (w).

[Ni(Me₆tren)Br]PF₆ (Complex 2-6)

A 3 mL EtOH solution of Me₆tren (150 μL, 0.6 mmol) was added dropwise to a 10 mL EtOH hot solution (45 °C) of NiBr₂·3H₂O (136 mg, 0.5 mmol) with stirring. After one hour, KPF₆ (100 mg, 0.54 mmol) was added slowly, a green solid formed. It was filtered, washed with EtOH for three times and then dried in air. Yield: 130 mg, 38%. Crystals suitable for X-ray single crystal diffraction were obtained by recrystallization in MeOH. Elem. Anal. for [Ni(Me₆tren)Br]PF₆ Calc: C, 28.04; H, 5.88; N, 10.90. Found: C, 28.10; H, 6.03; N, 10.73. Mw = 513.96 g/mol. Single-crystal unit cell: Trigonal, space group $R3-2$, $a = 10.3670(8) \text{ \AA}$, $b = 10.3670(8) \text{ \AA}$, $c = 15.9714(13) \text{ \AA}$, $\alpha = 90^\circ$, $\beta = 90^\circ$, $\gamma = 120^\circ$, $V = 1486.6(3) \text{ \AA}^3$. IR (KBr) ν/cm^{-1} : 3437 (w), 2989 (m), 2927 (m), 2906 (m), 2855 (w), 1629 (w), 1485 (s), 1475 (s), 1460 (m), 1437 (m), 1357 (w), 1299 (m), 1247 (w), 1174 (w), 1104 (m), 1053 (m), 1043 (m), 1022 (m), 939 (m), 912 (m), 876 (s), 838 (s), 807 (s), 775 (s), 601 (w), 557 (s), 479 (w), 419 (w), 384 (w).

[Ni(Me₆tren)]I (Complex 2-7)

A 5 mL EtOH solution of Me₆tren (202 μ L, 0.8 mmol) was added dropwise to a 10 mL EtOH solution of NiI₂ (210 mg, 0.67 mmol) with stirring. A red solution was obtained immediately. After 3 h stirring, it was filtered and then diethyl ether was diffused into the filtrate to obtain X-ray quality crystals. Yield: 65%. Elem. Anal. for [Ni(Me₆tren)]I Calc: C, 26.55; H, 5.57; N, 10.32. Found: C, 26.48; H, 5.37; N, 10.14. Mw = 542.90 g/mol. Single-crystal unit cell: Cubic, space group $P2_13$, $a = 12.3830(3)$ Å, $b = 12.3830(3)$ Å, $c = 12.3830(3)$ Å, $\alpha = 90^\circ$, $\beta = 90^\circ$, $\gamma = 90^\circ$, $V = 1898.79(14)$ Å³. IR (KBr) ν/cm^{-1} : 3445 (w), 3011 (w), 2969 (m), 2916 (m), 2873 (m), 2802 (w), 1645 (w), 1480 (s), 1471 (s), 1454 (s), 1439 (m), 1352 (m), 1289 (s), 1271 (s), 1237 (m), 1167 (w), 1097 (m), 1059 (w), 1051 (w), 1033 (s), 1013 (s), 998 (s), 933 (s), 908 (s), 801 (s) 770 (s), 740 (w), 601 (w), 581 (w), 475 (m), 410 (w), 375 (w).

2.2.2 Physical Measurements

General Procedures

Elemental analyses for C, H, N were performed on a Thermo Scientific Flash analyzer. IR spectra were recorded on a Bruker TENSOR - 27 FT - IR spectrometer equipped with an attenuated total reflectance (ATR) sample holder in the 4000 - 250 cm^{-1} range. NMR spectra were recorded on a Bruker Aspect 300 NMR spectrometer. X-ray diffraction data were collected by using a Bruker Kappa VENTURE PHOTON 100 diffractometer with graphite-monochromatic Mo $K\alpha$ radiation ($\lambda = 0.71073$ Å). Magnetic data were collected using a Quantum Design MPMS XL7 SQUID magnetometer.

Crystallography

X-ray diffraction data for complexes **2-1(a, b, c, d)**, **2-3**, **2-5** and **2-6** were collected by using a VENTURE PHOTON100 CMOS Bruker diffractometer with Micro-focus IuS source Mo $K\alpha$ radiation. X-ray diffraction data for complexes **2-2**, **2-4** and **2-7** were collected by using a X8 APEXII CCD Bruker diffractometer with graphite-monochromated Mo $K\alpha$ radiation. All crystals were mounted on a CryoLoop (Hampton Research) with Paratone-N (Hampton

Research) as cryoprotectant and then flashfrozen in a nitrogen-gas stream at 100 K. The temperature of the crystal was maintained at the selected value by means of a 700 series Cryostream (for X8) or N-Helix (for VENTURE) cooling device to within an accuracy of ± 1 K. The data were corrected for Lorentz polarization, and absorption effects. The structures were solved by direct methods using SHELXS-97¹⁹ and refined against F^2 by full-matrix least-squares techniques using SHELXL-2018²⁰ with anisotropic displacement parameters for all non-hydrogen atoms. All calculations were performed by using the Crystal Structure crystallographic software package WINGX.²¹

The crystal data collection and refinement parameters are given in Table A 1, Table A 2 and Table A 3 (all the crystallographic data are presented in Appendix).

Magnetic Measurements

The direct-current (dc) magnetic measurements were performed on powdered samples that were milled in eicosane to prevent torqueing of the samples in high applied magnetic fields on a Quantum Design MPMS-XL7 SQUID magnetometer operating with a working temperature range of 1.8 – 300 K and dc-applied fields ranging from -7 to 7 T. Polycrystalline samples were ground using a small mortar and pestle, transferred to a gelatin capsule of known mass, and weighed. A small amount of melted eicosane was added and left to solidify. The entire capsule was then weighed, and a piece of brown tape was applied to hold the capsule together. The capsule was then inserted into a clear plastic drinking straw. Holes were punched into the straw to allow air to escape. Diamagnetic corrections were applied for the sample holder from previous direct measurements, and molar diamagnetic susceptibilities were calculated from Pascal's constants. The use of eicosane to prevent torqueing effects is fine when magnetization data are being measured at low temperature, where the diamagnetism of eicosane is relatively weak. This is not the case for magnetic susceptibility data above 50 K, where the diamagnetism of eicosane must be exactly evaluated in order to have the right behavior for the thermal dependence of χT . This is important in order to have an accurate evaluation of the g -value that is used subsequently to fit the magnetization data at low temperature. Therefore, we have carried

out the magnetic measurements using eicosane as explained above and also using a pellet of the compound to be studied. Only when perchlorate is present, no pellet was used.

The fit of the magnetic data is always made considering the $\chi T = f(T)$ and the magnetization data at different temperatures simultaneously, using the PHI software or a modified version of the MAGPACK software.^{22,23}

2.3 Results and discussion

2.3.1 Molecular Structures Description

For complexes **2-1** to **2-7**, the general structure of the cation is the same: penta-coordinated Ni(II) is linked to four amino nitrogen atoms from ligand Me₆tren and one halogen ion (Cl⁻, Br⁻ or I⁻) acting as an axial ligand, resulting in the trigonal bipyramid coordination geometry. The charge balances are provided by a series of anions: halogen ions (Cl⁻ or I⁻), ClO₄⁻, PF₆⁻, CF₃SO₃⁻, BPh₄⁻. Some selected interatomic distances and angles of these complexes are listed in Table II.1.1, Table II.2 and Table II.3.

2.3.1.1 Molecular structure of Complex 2-1

For the complex **2-1**, a phase transition is observed below 200 K from cubic to orthorhombic (see above for details). At $T = 40$ K, the complex **2-1(a)** crystallizes in the orthorhombic system and the structure was solved and refined in the $P2_12_12_1$ space group. The Ni-N bond distances and the \widehat{NNiN} angles in the equatorial plane are different (Figure II.1, left and Table II.1) leading to a distorted trigonal bipyramid geometry. The Ni atom lies 0.225 Å below the equatorial plane of the three N atoms with the axial angle $\widehat{N2NiCl1}$, $\widehat{N3NiCl1}$, $\widehat{N4NiCl1}$ of 98.355°, 95.922° and 94.271°, respectively. The axial length of Ni-N1 is 2.1088 Å, slightly longer than Ni-N2 (2.0883 Å) and shorter than the other two equatorial distance (2.1634 Å for Ni-N3, and 2.1237 Å for Ni-N4). The Ni-Cl distance is 2.3116 Å, with a $\widehat{N1NiCl1}$ angle of 177.512°. When increasing the temperature to 100 K, the main molecular structure is maintained except for a slight change in cell parameters. All the distances of Ni-N bonds and Ni-Cl1 bond become slightly longer than the corresponding

ones at $T = 40$ K, leading to a longer axial bond distances, while the $\widehat{N1NiCl1}$ angle (177.405°) is slightly smaller. At $T = 200$ K, the structure of the crystal changes to cubic (space group $P2_13$) and the molecular symmetry becomes strictly C_{3v} . In this structure, the distance between Ni and the plane formed by three equatorial N2 atoms is 0.224 \AA , similar to **2-1(a)**. The Ni-N1 bond is 2.1066 \AA , the Ni-Cl1 bond is 2.3100 \AA and the Ni-N2 bonds are 2.1208 \AA , shorter than the corresponding axial distance and the average equatorial bond lengths in **2-1(a)** and **2-1(b)**. The $\widehat{N2NiCl1}$ angle is equal to 96.067° and the $\widehat{N2NiN2}$ angle to 118.897° .

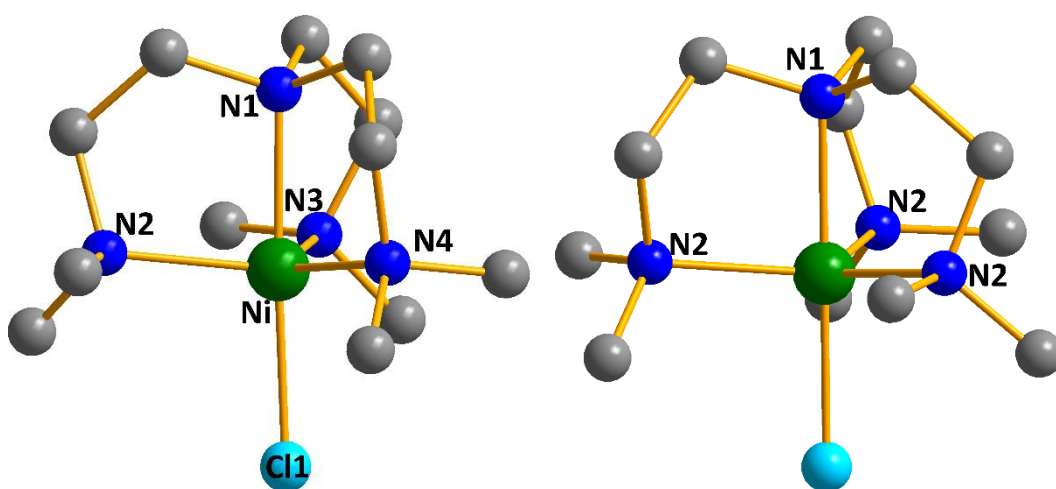


Figure II.1 A view of the cation for complex **2-1** at 40 K (left) and 200 K (right), respectively. C – grey; Cl – sky blue; H and counterions were omitted for clarity.

During our experiment, we tried to do the powder X-ray diffraction on the crystals at variable temperatures to discover when the phase transition happens. However, the microcrystalline powder captured water molecules during the measurements leading to an X-ray powder diffraction pattern with many peaks showing the alteration of the powder. Therefore, the attempt to explore the temperature of phase transition by PXRD failed. Later, we found that the crystals turned from solid to “oily” like after being exposing to air for two hours or more, indicating its strong hygroscopicity. When left in air for about one month, the “oily” like compound recrystallized and yielded a single crystal **2-1(d)** with two water molecules in the structure. The new complex **2-1(d)** crystallizes in the orthorhombic system (the same with **2-1(b)**) and the structure was solved and refined in the $Pbca$ space group at $T = 100$ K. There is no phase transition in this case when the temperature changes.

The comparison with **2-1(b)** (measured at 100 K) shows that the molecular structure of **2-1(d)** is slightly different. The axial bonds are shorter (2.0866 Å for Ni-N1 and 2.2815 Å for Ni-Cl1), accompanied with a smaller axial angle $\widehat{N1NiCl1}$ of 176.591°.

The packing structure of **2-1(d)** is displayed in Figure II.2. From the right of Figure II.2, we can observe that four H-bonds: Cl \cdots H-O are formed in the structure. The Cl-H distances are 2.3458 Å, 2.4344 Å, 2.2777 Å, and 2.3531 Å, respectively, which have a key impact on stabilizing the molecule structure.

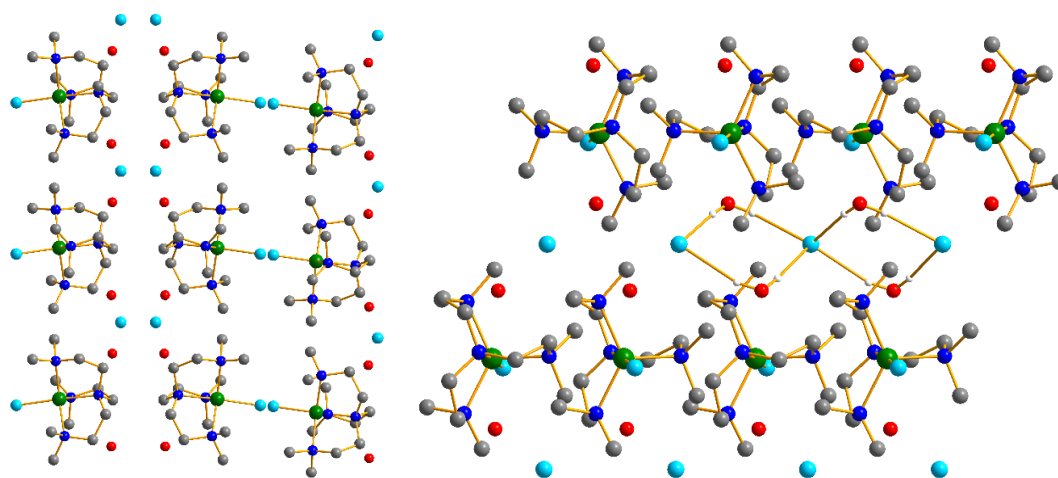


Figure II.2 Left: the packing structure of **2-1(d)**; Right: the H-bonds in **2-1(d)**. C – grey; Cl – sky blue; O – red; N – blue; Ni – green; H – white. Some H atoms were omitted for clarity.

More information about the molecular structures and the details comparison of these four structures are shown in Table II.I.1. And the crystallographic data structure refinements for complex **2-1(a,b,c,d)** are shown in Table A 1.

Table II.I.1 The selected distances and angles of complex **2-1**

Complexes	2-1(a)	2-1(b)	2-1(c)	2-1(d)
Temperature	40 K	100 K	200 K	100 K ($2H_2O$)
d_{Ni-N1} (Å)	2.1088(48)	2.1140(37)	2.1066(13)	2.0866(22)
d_{Ni-N2} (Å)	2.0883(48)	2.0978(37)	2.1208(16)	2.1618(20)
d_{Ni-N3} (Å)	2.1634(49)	2.1693(38)	/	2.1576(20)
d_{Ni-N4} (Å)	2.1237(48)	2.1267(37)	/	2.0802(19)
d_{Ni-Cl1} (Å)	2.3116(15)	2.3198(14)	2.3100(4)	2.2815(80)
$\widehat{N2NiN3}$ (°)	113.883(18)	113.924(14)	/	129.627(78)

$\widehat{N3NiN4}$ (°)	128.531(18)	128.177(14)	/	111.888(72)
$\widehat{N2NiN4}$ (°)	114.225(18)	114.598(14)	/	115.328(72)
$\widehat{N2NiN2}$ (°)	/	/	118.897(61)	/
$\widehat{N1NiN2}$ (°)	83.976(18)	84.406(14)	83.932(56)	82.709(77)
$\widehat{N1NiN3}$ (°)	83.878(18)	83.972(14)	/	84.478(77)
$\widehat{N1NiN4}$ (°)	83.948(18)	83.632(14)	/	85.461(78)
$\widehat{N1NiCl1}$ (°)	177.512(14)	177.405(10)	180.00	176.591(65)
$\widehat{N2NiCl1}$ (°)	98.355(14)	98.020(10)	96.067(44)	94.238(60)
$\widehat{N3NiCl1}$ (°)	95.922(13)	95.837(10)	/	96.376(60)
$\widehat{N4NiCl1}$ (°)	94.271(13)	94.488(10)	/	97.250(63)

2.3.1.2 Molecular structures of Complexes 2-2, 2-3 and 2-4

The cations of the complexes **2-2**, **2-3** and **2-4** possess a similar structure to complex **2-1** (Figure II.3), the main difference being the nature of the counter ions: BPh₄⁻ for **2-2**, PF₆⁻ for **2-3**, and CF₃SO₃⁻ for **2-4**, which causes some geometrical distortion. These complexes crystallize in the monoclinic, trigonal and orthorhombic system, respectively. Their structures were solved and refined in the *P2₁/n*, *R3-2*, and *Pnma* space group. For **2-2**, large differences of the bond lengths can be found in the structure. For the axial direction, Ni-N1 and Ni-Cl bond distances are equal to 2.0963 Å and 2.2909 Å, respectively, with an axial $\widehat{N1NiCl}$ angle of 173.833°. The equatorial distances of Ni-N vary from 2.0795 Å to 2.1665 Å, with the angles $\widehat{NNiN'}$ from 106.647° to 138.829°. Compound **2-3** has a strict *C_{3v}* symmetrical structure. The Ni-N1_{ax}, Ni-N2_{eq} and Ni-Cl1 bond lengths are equal to 2.0888 Å, 2.1326 Å and 2.2909 Å, respectively. The axial ($\widehat{N1NiN2}$) and equatorial ($\widehat{N2NiN2}$) angles are equal to 83.789° and 118.849° respectively. In the structure of **2-4**, the carbon atoms of the Me₆tren ligand are disordered. The distance Ni-Cl (2.3031 Å) is longer than the ones in **2-2** and **2-3**. The Ni-N1 bond length is 2.0915 Å, the Ni-N2 bond is 2.1407 Å and the Ni-N3 bond is 2.1077 Å. $\widehat{N1NiCl}$ is 178.619°, and the equatorial angles are 121.992° ($\widehat{N2NiN3}$) and 113.001° ($\widehat{N3NiN3}$), separately. More details of the three structures can be found in Table II.2. The crystallographic data structure refinements for complex **2-2**, **2-3** and **2-4** are shown in Table A 2.

If we focus on the Ni-N equatorial distances that capture the main features of the coordination sphere geometry around the Ni(II) ions, we can summarize the differences among the three complexes as follows: the coordination sphere of complex **2-2** is very distorted because it has three different Ni-N_{eq} bond distances ranging from 2.08 to 2.17 Å; for complex **2-4**, the coordination sphere in the equatorial plane is less distorted because two Ni-N_{eq} bond distances are the same, while complex **2-3** has a perfect *C_{3v}* symmetry with the same Ni-N_{eq} bond distances. These differences must have an impact on the ZFS parameters.

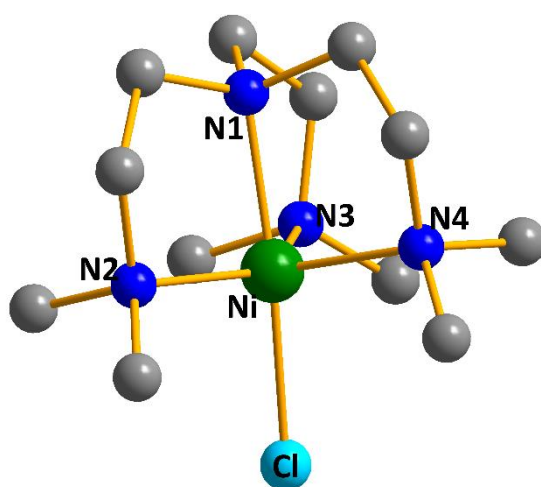


Figure II.3 A view of the cation for complex **2-2**. C – grey; Cl – sky blue; H and counterions were omitted for clarity.

Table II.2 The selected distances and angles of complexes **2-2**, **2-3**, **2-4**.

complexes	2-2	2-3	2-4
$d_{\text{Ni-N1}}$ (Å)	2.0963(7)	2.0888(80)	2.0915(90)
$d_{\text{Ni-N2}}$ (Å)	2.1199(7)	2.1326(40)	2.1407(12)
$d_{\text{Ni-N3}}$ (Å)	2.1665(7)	/	2.1077(80)
$d_{\text{Ni-N4}}$ (Å)	2.0795(7)	/	/
$d_{\text{Ni-Cl}}$ (Å)	2.2909(5)	2.2909(20)	2.3031(4)
$\widehat{\text{N2NiN3}}$ (°)	138.829(28)	/	121.992(21)
$\widehat{\text{N3NiN4}}$ (°)	111.321(28)	/	/
$\widehat{\text{N2NiN4}}$ (°)	106.647(28)	/	/

$\widehat{N2NiN2}$ (°)	/	118.849(78)	/
$\widehat{N3NiN3}$ (°)	/	/	113.001(28)
$\widehat{N1NiN2}$ (°)	84.184(26)	83.798(86)	83.739(40)
$\widehat{N1NiN3}$ (°)	83.070(27)	/	84.490(21)
$\widehat{N1NiN4}$ (°)	86.134(26)	/	/
$\widehat{N1NiCl1}$ (°)	173.833(25)	180.000	178.619(29)
$\widehat{N2NiCl1}$ (°)	95.215(22)	96.202(86)	94.879(33)
$\widehat{N3NiCl1}$ (°)	93.464(20)	/	96.263(21)
$\widehat{N4NiCl1}$ (°)	99.899(25)	/	/

2.3.1.3 Molecular structure of Complexes 2-5, 2-6 and 2-7

The complexes **2-5**, **2-6** and **2-7** crystallize in the cubic, trigonal and cubic systems respectively. Their structures were solved and refined in the $P2_13$, $R3-2$, and $P2_13$ space groups respectively. All of the three complexes have strict C_{3v} symmetry (Figure II.4) and the coordination sphere around the Ni(II) ion is almost the same for the three complexes. The only difference concerns the Ni-X bond distances, it increases when going from **2-5** to **2-7** (Table II.3). The crystallographic data structure refinements for complexes **2-5**, **2-6** and **2-7** are shown in Table A 3.

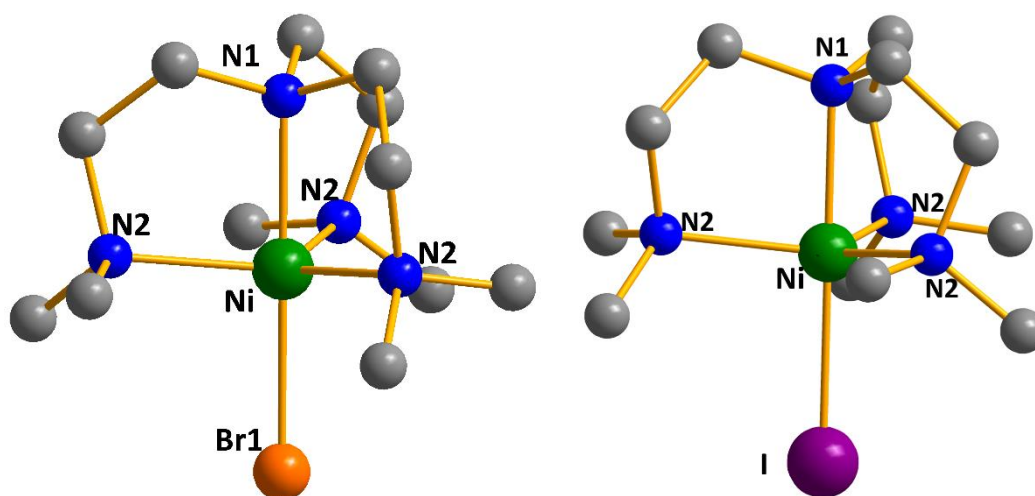


Figure II.4 A view of the cations for complexes **2-5** (left) and **2-7** (right). C – grey; H and counterions were omitted for clarity.

Table II.3 The selected distances and angles of complexes **2-5**, **2-6**, **2-7**.

complexes	2-5	2-6	2-7
d _{Ni-N1} (Å)	2.1008(25)	2.0932(32)	2.1025(25)
d _{Ni-N2} (Å)	2.1265(34)	2.1345(27)	2.1230(25)
d _{Ni-X} (Å)	2.3116(1)	2.4454(60)	2.6420(40)
N ² NiN ² (°)	118.952(12)	118.776(59)	118.952(96)
N ¹ NiN ² (°)	84.086(11)	83.603(68)	84.087(96)
N ¹ NiX (°)	180.000	180.000	180.000
N ² NiX (°)	95.914(85)	96.397(68)	95.913(68)

X = Br for **2-5** and **2-6**; X = I for **2-7**

The comparison of the structures of the different compounds (Table II.1.4) allows making some comments on the influence of the counter anions on the coordination sphere of Ni(II), on one hand, and on the organization of the molecules in the lattice, on the other hand. First, it is important to remind that a Ni(II) in a trigonal bipyramid geometry is not stable because Jahn-Teller effect should lead to distortion of its coordination sphere (mainly in the equatorial plane) to minimize its electronic energy. This is because the electronic ground state is orbitally degenerate and is thus subject to a Jahn-Teller distortion. It is, thus, not expected for these complexes to have a strict C_{3v} symmetry. However, the Jahn-Teller stabilization may be weak and be only observed at very low temperature or be dynamic so that even at low temperature it cannot be detected by crystallographic measurements. This was the case of the first compound of this series ([Ni(Me₆tren)Cl]ClO₄) that was reported by our group.¹² Crystal packing may also be responsible of precluding the distortion if the stabilizing energy is not so large.

However, it is possible to have general conclusion on the role of the anion. From the above data, we observe that ClO₄⁻ and PF₆⁻ generate trigonal structures for the crystal with a strict C_{3v} symmetry for the complexes; aligned with their local three-fold axes along the *c* crystallographic axis of the crystal (see Table II.1.4). This can be attributed to the possibility of these two anions of tetrahedral and octahedral geometry to adapt the trigonal symmetry of the complex. There is one exception for X = Br⁻ and Y = ClO₄⁻, where a cubic

structure is obtained, but still with a local three-fold axis for the complex. The situation is similar but different when the anion is a spherical object such as a halide, the local complex symmetry is C_{3v} but the crystal structure is cubic (for $X = Y = \text{Cl}$, this happens only at 200 K). These results confirm the idea that a potential trigonal anion directs the overall structure to be trigonal while a spherical anion leads to a more “symmetrical” cubic structure except the one exception mentioned above. The fact that the local Ni complex structure for all these complexes remains strictly trigonal (above 100 K for $X = \text{I}$ and Br and above 200 K for $X = \text{Cl}$) supports the idea that when the anion possesses itself a high symmetry, the complex keeps its three-fold axis. This is consistent with the fact that the stabilization energy brought by the Jahn-Teller effect remains weaker than the thermal energy at which the structure is solved.

When the anion is CF_3SO_3^- , the complex has a mirror plane with two equal Ni-N_{eq} bond distances. Despite the trigonal structure of the anion, the three-fold axis of the complex is lost. This may be due to the size of the anion and the nature of the packing in the crystal. We will not analyze more these effects. When BPh_4^- is used, the three Ni-N_{eq} bond distances are different, and the local symmetry is the lowest probably reflecting the low symmetry of the anion.

The most interesting situation occurs when $X = Y = \text{Cl}$. As mentioned above, at $T = 200$ K the complex crystallizes in the cubic system with a C_{3v} symmetry for the complex. A phase transition to the orthorhombic system is observed when cooling down to 100 K accompanied by a local distortion of the coordination sphere of the complex. This distortion could be driven by the Jahn-Teller effect where the vibronic coupling in this case might be larger than for the other compounds. Further cooling down to 40 K induces only very slight changes in the structural parameters. The other interesting feature is the capture of water molecules with a change to the orthorhombic system in the $Pbca$ space group with the Ni-Cl bonds, corresponding to the pseudo three fold axis where the easy anisotropy magnetic axis is, almost (ClNiNiCl torsion angle of 17°) all aligned along the c crystallographic axis (Figure II.2, left). The three Ni-N_{eq} bond distances are different as for the complex with BPh_4^- .

Table II.I.4 The comparison of the structures of the different compound.

Complexes Ni(Me ₆ tren)X-Y	Axial ligand X	Counter anion Y	Crystal system	C ₃ symmetry	Measure temperature (K)
*	Cl	ClO ₄	trigonal	✓	100
2-3	Cl	PF ₆	trigonal	✓	100
2-6	Br	PF ₆	trigonal	✓	100
2-1(c)	Cl	Cl	cubic	✓	200
*	Br	Br	cubic	✓	100
2-5	Br	ClO ₄	cubic	✓	100
2-7	I	I	cubic	✓	100
2-1(a/b)	Cl	Cl	orthorhombic	×	40 / 100
2-1(d)	Cl	Cl	orthorhombic	×	100
2-4	Cl	CF ₃ SO ₃	orthorhombic	×	100
2-2	Cl	BPh ₄	monoclinic	×	100

The complexes with "*" are the results from reference [12].¹²

2.3.2 Magnetism

Measurements of dc magnetic susceptibilities (χT) have been conducted on complexes **2-1** to **2-7** in the temperature range of 300 - 2 K and the magnetic field of 1 T. The magnetization vs. the applied magnetic field have been measured in the field 0 – 6 T and under several temperature conditions: 2, 4, 6 and 8 K. The data were corrected for the diamagnetic contribution of the sample holder and eicosane.

2.3.2.1 Magnetic properties of Complex 2-1

In order to investigate the effect of the phase transition and the capture of water molecules in **2-1** by magnetic study and be able to compare the results, we carried out the following experiments:

- 1- Microcrystalline powder of the hydrated form of **2-1(d)** was prepared as explained in the experimental section. It was introduced in the SQUID magnetometer at low temperature and the $M = f(\mu_0 H)$ data measured at different temperatures. Then the sample was heated up to 300 K in order to record the $\chi T = f(T)$ curve.

2- At $T = 300$ K, the sample was kept in the SQUID (under reduced pressure) and the magnetization measured for 15 hours. This allows the dehydration of the sample as we have already checked in a separate experiment and leads to compound **2-1(c)** that is cubic and where the complex has a local trigonal symmetry. The evolution of the magnetization value with time (Figure II.5) shows that the magnetization increases with time.

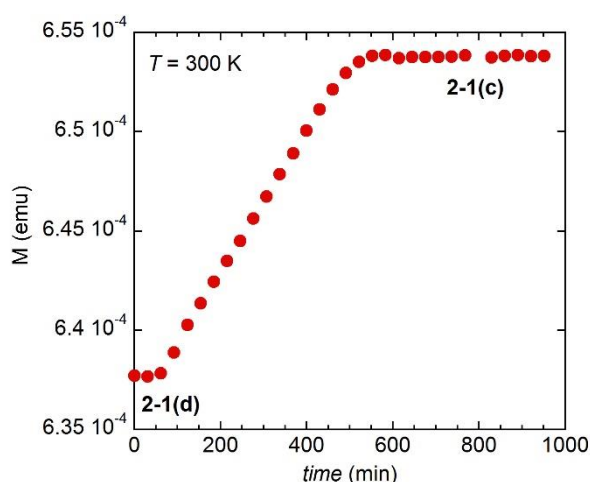


Figure II.5 Magnetization versus time at $T = 300$ K showing the evolution from the hydrated **2-1(d)** compound to the non-hydrated **2-1(c)** compound.

3- The dehydrated sample was then cooled down from 300 to 2 K in order to measure the dependence of its χT with temperature, and at then the $M = f(\mu_0 H)$ curves were recorded at different temperatures. Cooling induces a phase transition for cubic to orthorhombic (compounds **2-1(a/b)**) where the structure of the complex is not trigonal.

Therefore, the magnetization data at low temperature of compound **2-1(c)** cannot be measured because of the phase transition. In addition, the χT data of **2-1(c)** and **2-1(a/b)** cannot be fitted because the presence of the phase transition. Only the magnetization data of **2-1(a/b)** can be analyzed. While for the compound **2-1(d)** that contains the two water molecules, χT and magnetization were measured and analyzed.

The temperature dependence of χT for the whole cycle is shown in Figure II.6.

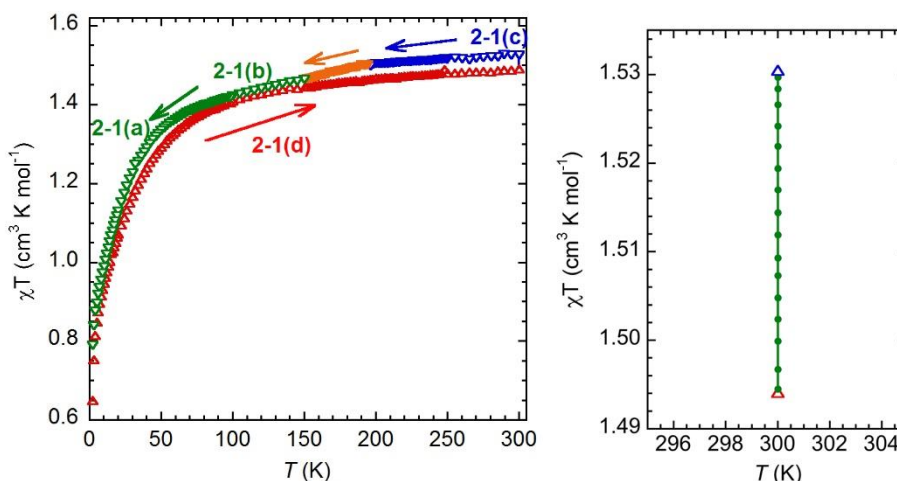


Figure II.6 Left: Temperature dependence of the χT product for the whole cycle; Right: the collected χT values of the hydrated sample **2-1(d)** at $T = 300$ K.

The hydrated sample (**2-1(d)**) (Figure II.6-left, red curve) shows a steady thermal variation of χT expected for a mononuclear Ni(II) complex with no accident. At 300 K (Figure II.6-right), χT increases from about 1.49 cm³ mol⁻¹ K and reaches saturation after 550 minutes at a value close to 1.53 cm³ mol⁻¹ K corresponding to the dehydrated compound (**2-1(c)**). When cooling down the dehydrated sample (Figure II.6-left, blue curve) from 300 K, a sudden decrease of χT is observed around $T = 190$ K, then the curve keeps the same expected behavior. The break in the χT curve corresponds to the phase transition observed by X-ray crystallography from compound **2-1(c)** to **2-1(b)**. It is worth noting that the χT values are impacted by the structural change even at 300 K, which is due to a change of the value of the g factor. It is not possible to fit the χT data for the non-hydrated sample because the break in the curve. The data for the hydrated compound (**2-1(d)**) were fitted using the following spin Hamiltonian:

$$\hat{H} = g\mu_B\hat{S} \cdot \vec{H} + D \left[\hat{S}_z^2 - \frac{S_T(S_T + 1)}{3} \right] + E(\hat{S}_x^2 - \hat{S}_y^2)$$

where \hat{S} , \hat{S}_x , \hat{S}_y , \hat{S}_z , are spin operators, \vec{H} is the applied dc magnetic field vector, g the Landé factor, μ_B the Bohr Magneton, D and E the axial and rhombic ZFS parameters, respectively. The simultaneous fitting of the $\chi T = f(T)$ and the $M = f(\mu_0 H)$ data at $T = 2, 4$ and 6 K gives the following values: $g = 2.38$, $D = -50.0$ cm⁻¹, $E = 0.91$ cm⁻¹ and TIP = 2.6x10⁻⁴

$4 \text{ cm}^3 \text{ mol}^{-1}$ (Figure II.7 and Figure II.8). For the dehydrated samples (**2-1(a/b/c)**), only the magnetization data at low temperatures were fitted, which correspond to compound **2-1(a/b)**. The best fit leads to the following values $g = 2.38$, $D = -34.8 \text{ cm}^{-1}$, $E = 0 \text{ cm}^{-1}$ and $TIP = 2.6 \times 10^{-4} \text{ cm}^3 \text{ mol}^{-1}$ (Figure II.9). It is worth noting that even if the fit leads to a rhombic parameter $E = 0$, this parameter cannot be strictly zero because of the distortion in the equatorial plane of the Ni(II) complex that deviates the symmetry from a strict trigonal one and induces rhombicity. However, this value must be very weak.

The important difference between the hydrated and the dehydrated samples two polymorphs is the value of the axial parameter that is larger (in absolute value) for the former than for the latter. The analysis of the ZFS parameters of these two compounds is performed in the theoretical section.

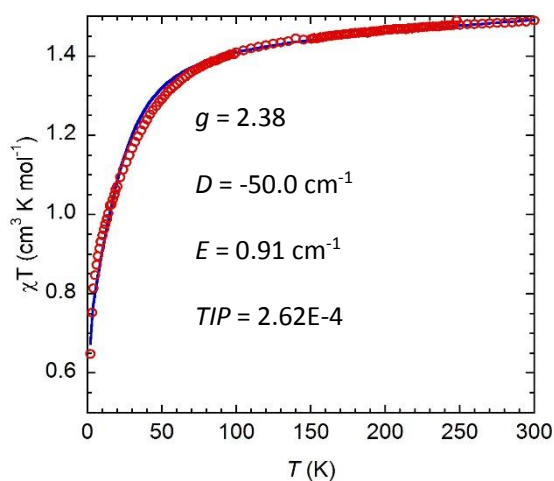


Figure II.7 Temperature dependence of the χT product for **2-1(d)**.

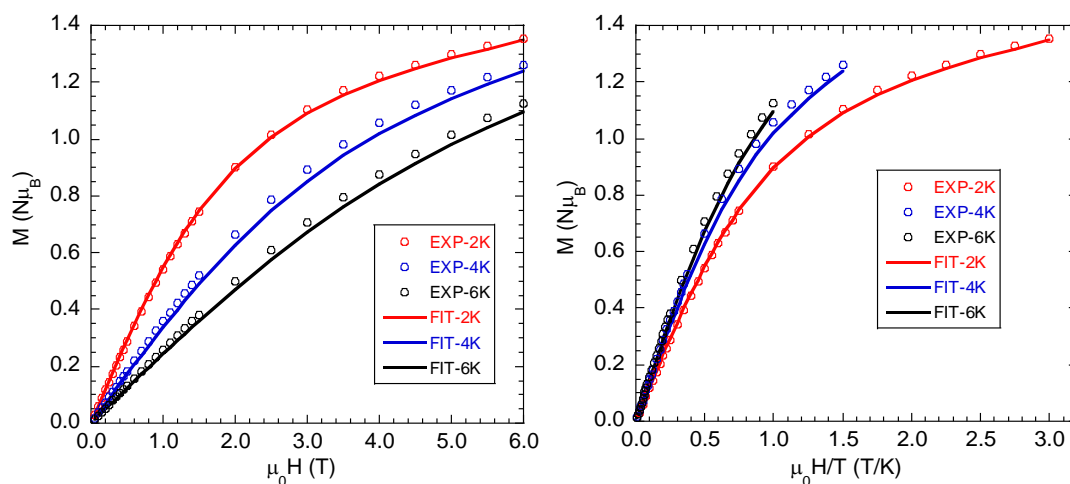


Figure II.8 Magnetization vs. $\mu_0 H$ (left) and vs. $\mu_0 H/T$ (right) at variable temperatures for **2-1(d)**.

The magnetization value at saturation for an $S = 1$ system is: $M_{sat} = g \cdot S$ ($2.38 \mu_B$ (Bohr Magneton)) for **2-1(a)** and $2.38 \mu_B$ for **2-1(d)**. The observed magnetization values at 6 T for the two compounds at $T = 2$ K are much smaller than this value and the $M = f(\mu_0 H/T)$ curves are not superimposed. All these characteristics are qualitative indications of the presence of large ZFS for the two complexes.

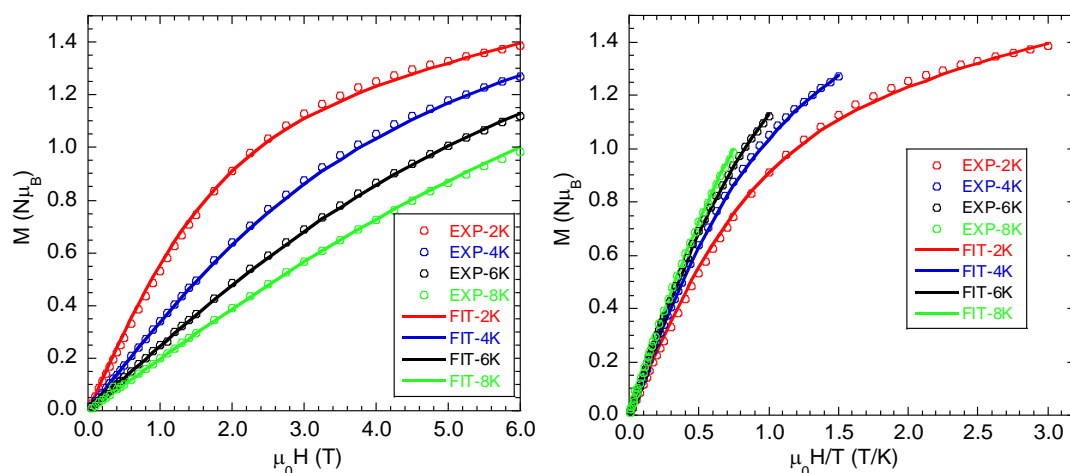


Figure II.9 Magnetization vs. $\mu_0 H$ (left) and vs. $\mu_0 H/T$ (right) at variable temperatures for **2-1(a)**.

2.3.2.2 Magnetic properties of Complexes 2-2, 2-3, 2-4

The thermal variation of the χT products for complexes **2-2**, **2-3** and **2-4** are plotted separately in Figure II.10, Figure II.12 and Figure II.14. The magnetization vs. the applied dc magnetic field for complex **2-2**, **2-3** and **2-4**, collected at different temperatures, are

plotted in the form of $M = f(\mu_0 H)$ and $M = f(\mu_0 H/T)$ in Figure II.11, Figure II.13 and Figure II.15, respectively. The figures show that these three complexes have similar magnetic behaviors.

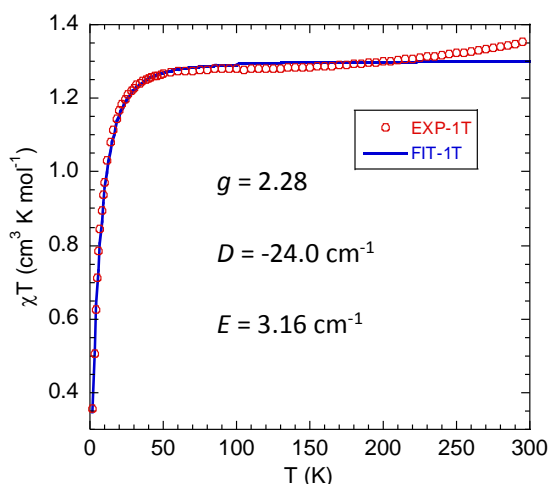


Figure II.10 Temperature dependence of the χT product for **2-2**.

For **2-2**, the χT vs. T product shows that the χT values is constant from room temperature to 40 K. The observed value is around $1.29 \text{ cm}^3 \text{ mol}^{-1} \text{ K}$, which is close to the expected result for a spin-only Ni(II) mononuclear complex ($1.21 \text{ cm}^3 \text{ mol}^{-1} \text{ K}$ when $g = 2.20$). When the temperature decreases, the χT collapses to $0.35 \text{ cm}^3 \text{ mol}^{-1} \text{ K}$, illustrating the existence of ZFS. Through fitting the magnetic data, g -value was found equal to 2.28.

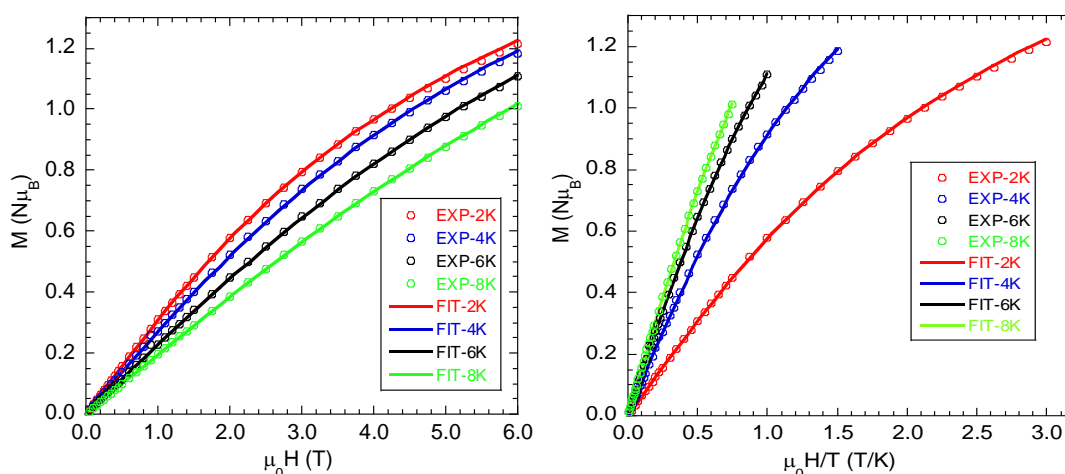


Figure II.11 Magnetization vs. $\mu_0 H$ (left) and vs. $\mu_0 H/T$ (right) at variable temperatures for **2-2**.

The magnetization vs. the applied dc magnetic field for complex **2-2** is displayed in Figure II.11. The observed magnetization at $T = 2$ K and $\mu_0 H = 6$ T is $1.21 \mu_B$, well below the saturated one ($2.28 \mu_B$) and weaker than the values found for the the $[\text{Ni}(\text{Me}_6\text{tren})\text{Cl}]\text{Cl}$ compounds. The fit of the data leads to ZFS parameters: $D = -24.0 \text{ cm}^{-1}$, $E = 3.16 \text{ cm}^{-1}$.

The χT vs. T product for complex **2-3** is presented in Figure II.12. The χT value at room temperature is $1.43 \text{ cm}^3 \text{ mol}^{-1} \text{ K}$, but it starts to decrease at 100 K when conducting the measurement from 300 K - 2 K. The value at room temperature is higher than the expected one, ascribed to the orbital contribution. The magnetization vs. the applied dc magnetic field is plotted in Figure II.13. The largest magnetization observed at $T = 2$ K and $\mu_0 H = 6$ T ($1.36 \mu_B$) is lower than the saturated one. By fitting the magnetic data, we can obtain the results as follows: $g = 2.40$; $D = -40.7 \text{ cm}^{-1}$; $E = 0.70 \text{ cm}^{-1}$. It's necessary to mention that the χT vs. T product and the plot of M vs. $\mu_0 H$ cannot be well fitted simultaneously because of its symmetric molecular structure.

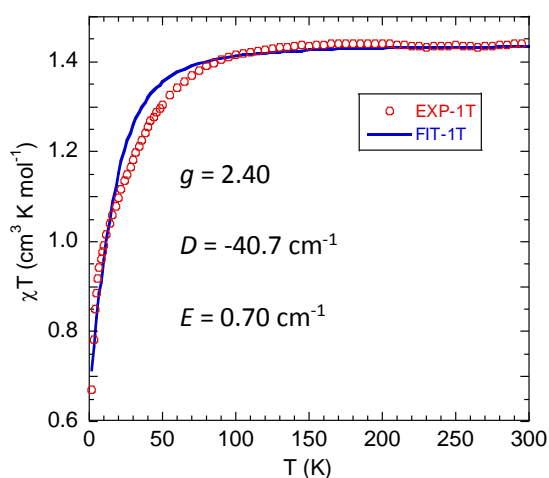


Figure II.12 Temperature dependence of the χT product for **2-3**.

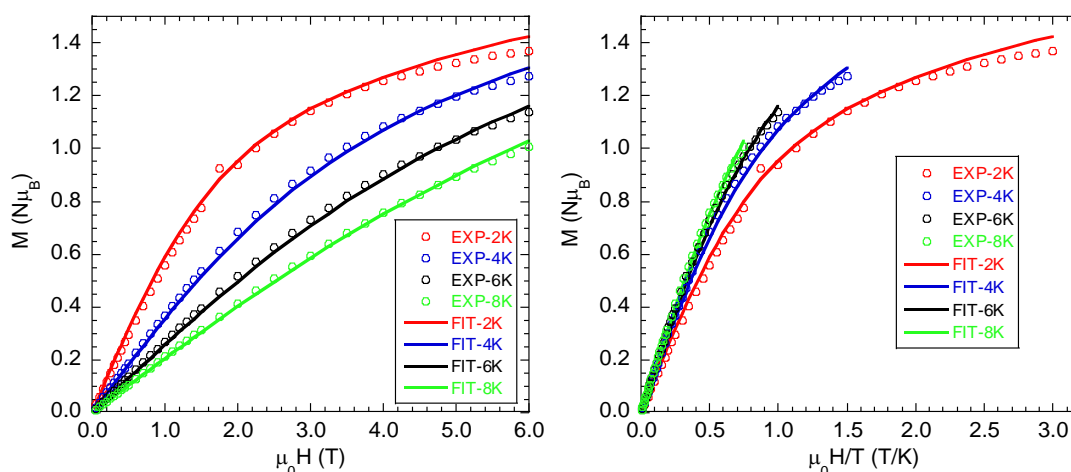


Figure II.13 Magnetization vs. μ_0H (left) and vs. μ_0H/T (right) at variable temperatures for **2-3**.

The χT vs. T product for complex **2-4** is presented in Figure II.14. At room temperature, the χT value is $1.49 \text{ cm}^3 \text{ mol}^{-1} \text{ K}$, higher than the expected $1.21 \text{ cm}^3 \text{ mol}^{-1} \text{ K}$ ($g = 2.20$). The χT value decreases at 110 K as the temperature goes down. The magnetization vs. the applied dc magnetic field is displayed in Figure II.15. The largest magnetization is measured as $1.43 \mu_B$ at 2 K and 6 T, lower than the saturated one. Fitting the magnetic data leads to: $g = 2.45$; $D = -36.5 \text{ cm}^{-1}$; $E = 1.07 \text{ cm}^{-1}$.

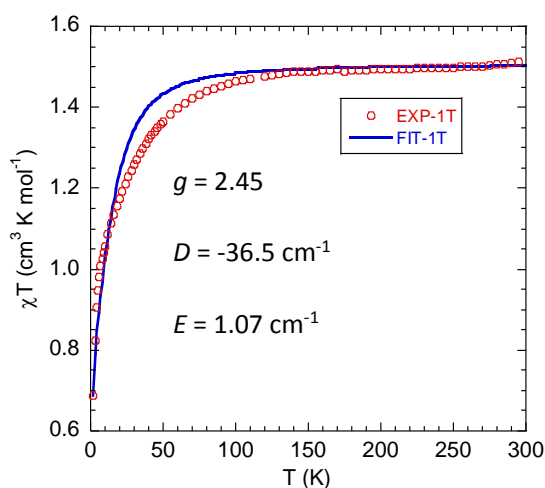


Figure II.14 Temperature dependence of the χT product for **2-4**.

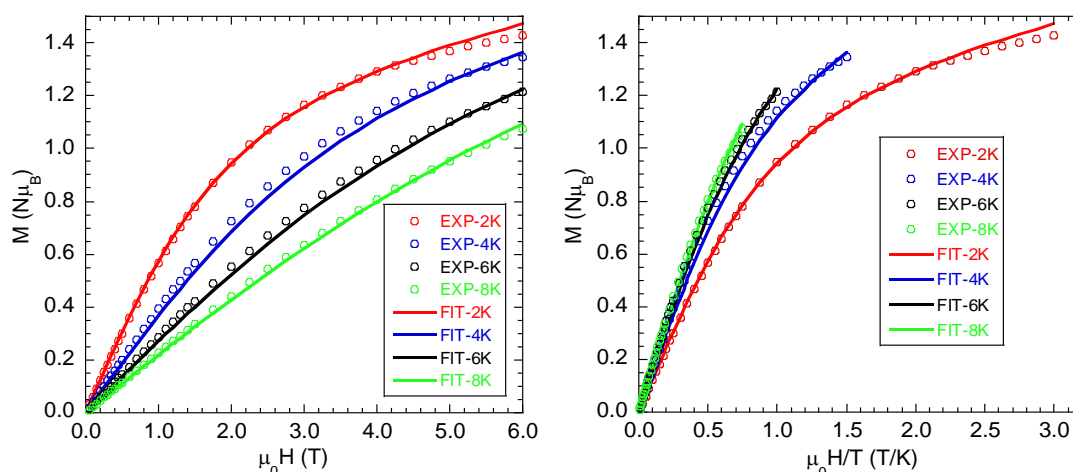


Figure II.15 Magnetization vs. μ_0H (left) and vs. μ_0H/T (right) at variable temperatures for **2-4**.

The fit of the magnetic data of these three compounds that possess the same axial ligand (Cl) but differ by their counter anions needs to be commented. Compound **2-2** ($Y = \text{BPh}_4$) has the most distorted geometry with the larger deviation of around 20° for the NNiN angle in equatorial plane from the average value (around 119°) that is expected to introduce a large deviation from strict axuality and thus decrease the absolute value of D and induce a relatively large E value. The fit of the data is excellent, and the values obtained from the fit are reliable and their magnitude are in agree with the structural analysis.

The situation for compound **2-3** is different. The coordination sphere of Ni is strictly trigonal and is this case a very large (in absolute value) D is expected, while the fit of the data leads to a value of -40.7 cm^{-1} larger than that of compound **2-2** but still too weak. Examining the fit of the χT data (Figure II.12), one notices that the agreement with the experimental data is poor. The experimental data decreases more quickly below 100 K than the fit data, which is the signature of a larger ZFS. However, it is not possible to obtain a different set of parameters with larger D when fitting the χT and magnetization data in the same time with a better agreement for the χT curve. The reason is probably due to the high symmetry of the complex and thus to the presence of a quasi first order spin orbit coupling leading to splitting of the states that do not follow the Hamiltonian we are using. This was the case of the trigonal $[\text{Ni}(\text{Me}_6\text{tren})\text{Cl}]\text{ClO}_4$ that had the same behavior.¹²

For compound **2-4** (Y = CF₃SO₃), the distortion in the equatorial plane is weaker than for **2-2**; two NiN_{eq} bond lengths are equal and the largest deviation of the NNiN angles from the average one is only 6°. The axial ZFS parameter is thus expected to be larger than for **2-2** but weaker than for the more symmetric complex **2-3**. This tendency is respected but the value found from the fit is probably underestimated as for **2-3** because the fit of the χT data is poor.

In summary, the magnitude of the axial ZFS parameters (in absolute values) is the one expected; the complex that has the largest distortion leads to the weaker D value (in absolute). But, only the fit of the data of the more distorted complex (**2-2**, Y = BPh₄) leads to reasonable ZFS parameters because in this case the distortion is large enough and the Hamiltonian used to fit the data is suitable.

2.3.2.3 Magnetic properties of Complexes 2-5 and 2-6.

Complexes **2-5** (X = Br, Y = ClO₄) and **2-6** (X = Br, Y = PF₆) have the strict trigonal symmetry. The data have the general same behavior as for the other complexes, we will thus not comment in detail the experimental values that can be found in the Figures below. Usually, in order to get an accurate value for the g factor that is then used to fit the ZFS parameters, we perform the measurement at high temperature using a pellet. But because the presence of perchlorate, compound **2-5** was not pressed and the data were recorded by blocking the crystals with eicosane. So, only the magnetization data are fitted (Figure II.16). The fit leads to the following values: $g = 2.53$; $D = -69.7 \text{ cm}^{-1}$ and E was set to be zero.

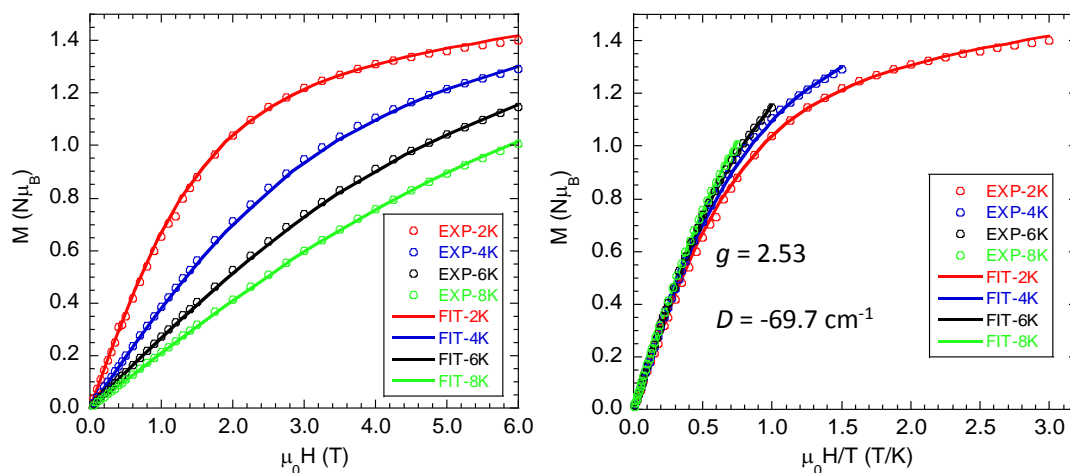


Figure II.16 Magnetization vs. μ_0H (left) and vs. μ_0H/T (right) at variable temperatures for **2-5**.

For complex **2-6**, despite the poor quality of the χT curve at high temperature, we performed a fit for $\chi T = f(T)$ and the magnetization data (Figure II.17 and Figure II.18) that led to $g = 2.48$, $D = -85.9 \text{ cm}^{-1}$ and $E = 0.92 \text{ cm}^{-1}$.

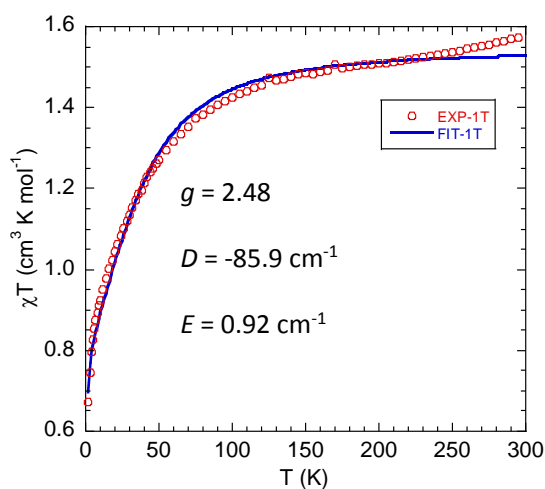


Figure II.17 Temperature dependence of the χT product for **2-6**.

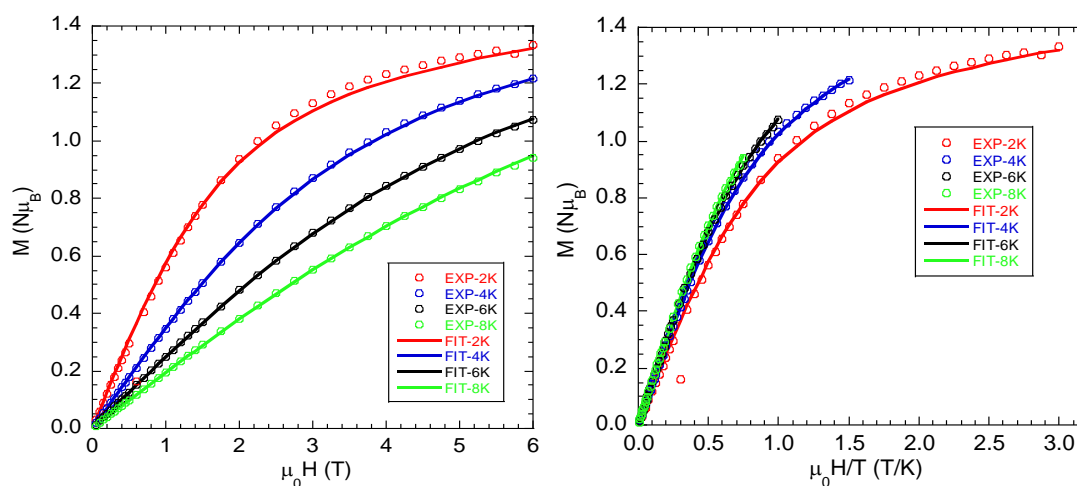


Figure II.18 Magnetization vs. μ_0H (left) and vs. μ_0H/T (right) at variable temperatures for **2-6**.

It is not straightforward to comment the ZFS parameters obtained from the fit. They are probably lower than the real values for the same reasons as for **2-3**. It is, however, worth noting that the D is larger (in absolute value) when $X = \text{Cl}$ than when Br is the axial ligand. This tendency was already observed for similar complexes but with Co(II) and associated to the weaker π -donating effect of Br^- than Cl^- that influences the energy of the d orbitals and subsequently the axial ZFS parameters. A detailed analysis requires full *ab initio* calculations on these compounds that is underway.

2.3.2.4 Magnetic properties of Complex 2-7

For complex **2-7**, the temperature dependence of the χT product is presented in Figure II.19. The χT product gives a constant value of $1.47 \text{ cm}^3 \text{ mol}^{-1} \text{ K}$ at room temperature that is almost constant down to 150 K and corresponds to a g value of 2.43. Below 150 K, χT decreases and reaches a value of $0.7 \text{ cm}^3 \text{ mol}^{-1} \text{ K}$ at $T = 2 \text{ K}$. Around $T = 15 \text{ K}$, there is a very weak bump in the χT curve. This bump was observed in almost all the other compounds apart from **2-2** where the distortion is large, and a good fit of the data could be obtained with a relatively weak D value. The magnetization vs. the applied dc magnetic field, collected at different temperatures, are plotted in the form of $M = f(\mu_0H)$ and $M = f(\mu_0H/T)$ in Figure II.20 and Figure II.21. The magnetization reaches its maximum ($1.32 \mu_B$) at $T = 2 \text{ K}$ and $\mu_0H = 5 \text{ T}$, lower than saturated magnetization.

When fitting the magnetic data, we found that the χT product and magnetization cannot be well fitted simultaneously with the same parameters. The best fitting results for magnetic data are displayed in the left of Figure II.19 and Figure II.20, which gives the parameters: $g = 2.44$; $D = -63.7 \text{ cm}^{-1}$; $E = 0.59 \text{ cm}^{-1}$. In this case, the fitting for magnetization is good but not for χT . The hump at 15 K in χT requires a D value around -80 cm^{-1} and a larger E parameter (larger than 1 cm^{-1}), but in this case the fit of the magnetization data is not as good as with previous values. It's as if the curve of χT was shifted by a constant. Thus, we tried to introduce a paramagnetic $S = 1$ and $g = 2$ impurity, which is considered as another type of Ni with small or no axial magnetic anisotropy. When the impurity is 23.8%, a perfect χT fitting is obtained (right, Figure II.19), but the fitting of the magnetization data (Figure II.21) is not as good as the one without impurity. Here, the fit parameters are: $g = 2.56$; $D = -88.1 \text{ cm}^{-1}$; $E = 1.78 \text{ cm}^{-1}$. In this situation, the rate of impurity has a key impact. The χT fit gets better when increasing the ratio of the impurity (the maximum is 23.8%). Taking an impurity with a $g > 2$ decreases the amount of the impurity.

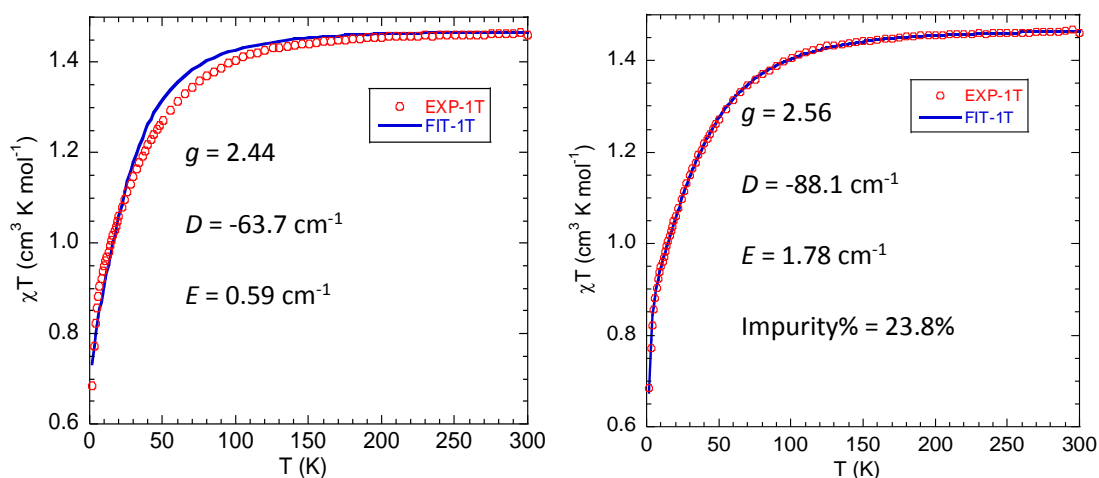


Figure II.19 Temperature dependence of the χT products and their fitting without impurity (left) and with impurity (right) for **2-7**.

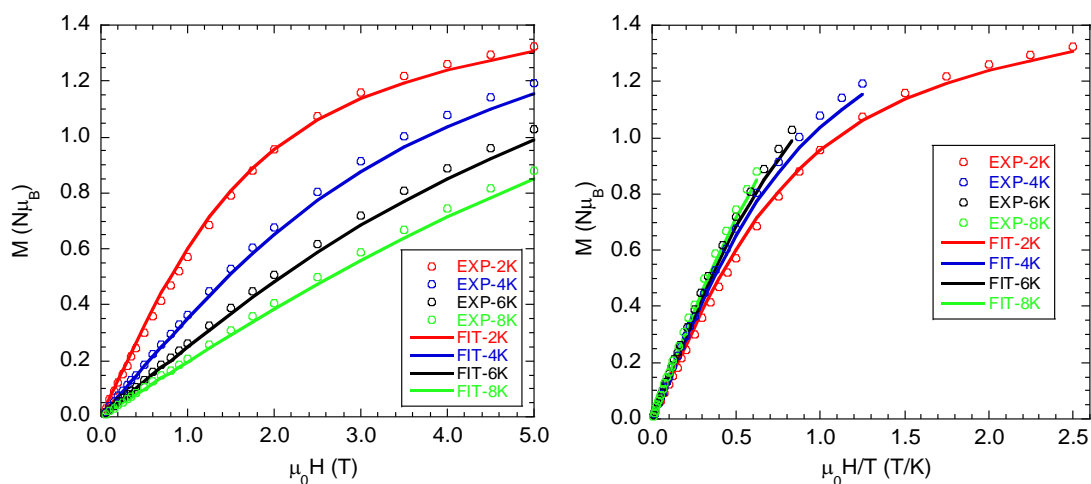


Figure II.20 Magnetization vs. μ_0H (left) and vs. μ_0H/T (right) at variable temperatures (without impurity) for **2-7**.

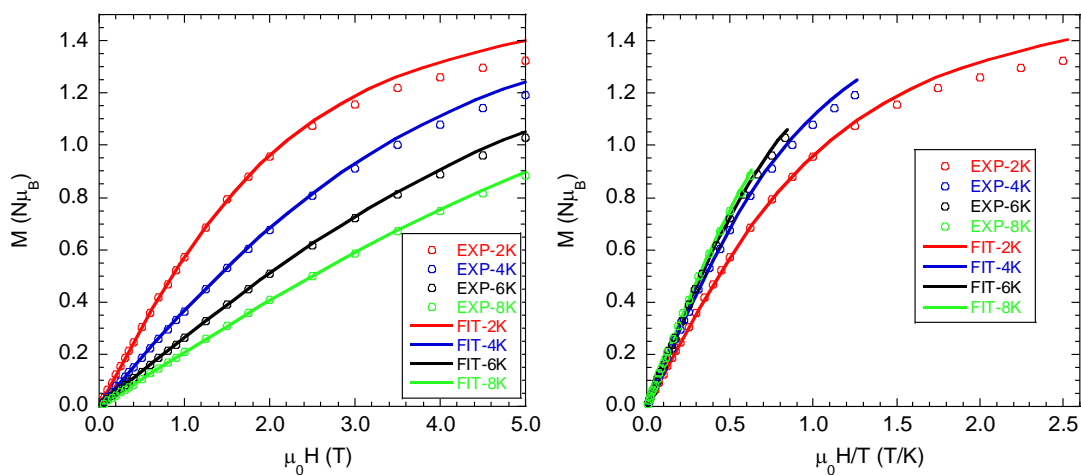


Figure II.21 Magnetization vs. μ_0H (left) and vs. μ_0H/T (right) at variable temperatures (with impurity) for **2-7**.

In summary for this compound, D (in absolute value) is large and has a value close to the compounds that the crystallographic data show to be trigonal. It is much larger than the distorted complexes.

All the fitting results together with local symmetry of the complexes are summarized in Table II.I.5.

Table II.I.5 ZFS parameters and g -value obtained from fitting for complexes **2-1** to **2-7**

complex	2-1(a)	2-1(d)	2-2	2-3	2-4	2-5	2-6	2-7 (without impurity)	2-7 (impurity 23.8%)
g	2.38	2.38	2.28	2.40	2.45	2.53	2.48	2.44	2.56
D (cm ⁻¹)	-34.8	-50.0	-24.0	-40.7	-36.5	-69.7	-85.9	-63.7	-88.1
E (cm ⁻¹)	0	0.91	3.16	0.70	1.07	0	0.92	0.59	1.78
C_3	✗	✗	✗	✓	✗	✓	✓	✓	✓

The parameters extracted from the fit of the magnetic data show that the complexes that possess a local C_3 symmetry axis have large D in absolute value, while the distorted ones have weaker D . Compound **2-3** is an exception, it has a D value of -40.7 cm⁻¹ despite its trigonal symmetry. However, the fit is not of good quality particularly for the χT product. Figure II.10 shows the presence of a bump around 15 K as for the complexes that possess a large D (in absolute value). Therefore, $|D|$ must be larger.

In order to analyze further the data, we carried out *ab initio* calculations using the ORCA package²⁴ on compounds **2-1(d)** and **2-1(b)** that have a distorted local structure; they correspond to the hydrated and non-hydrated forms of **2-1** ($X = Y = \text{Cl}$).

2.4 Theoretical Calculations

Before presenting the results of the calculations, we present briefly in a qualitative manner the electronic configuration of Ni(II) complexes in a trigonal symmetry and the corresponding ZFS and its impact on magnetic anisotropy. Then, we show the effect of distortion on the magnitude of ZFS.

As briefly mentioned in the introduction, in the framework of the mono-electronic approximation the lift of the degeneracy of the d orbitals of a Ni(II) complex placed in trigonal symmetry C_{3v} leads to three levels of symmetry e , e and a_1 as depicted in Figure II.22.

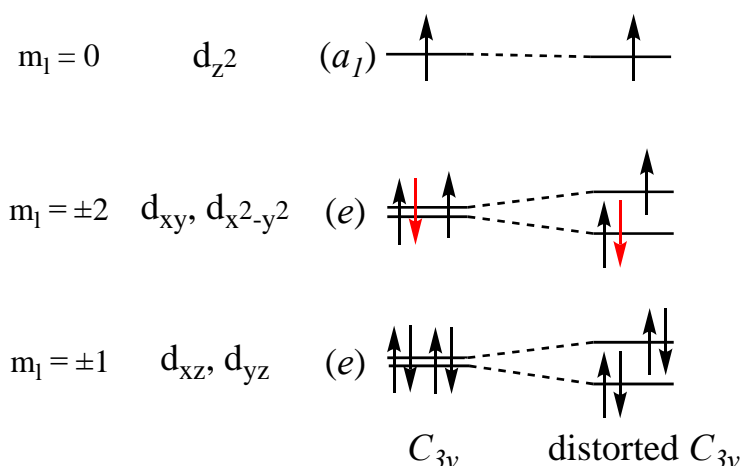


Figure II.22 Lift of the degeneracy of the d orbitals in a strict C_{3v} and a distorted C_{3v} symmetry.

In the case of a strict C_{3v} symmetry, the ground electronic state (3E) is degenerate, the angular orbital momentum is different from zero and the spin orbit coupling is of first order. The electron (red in Figure II.22) circulates freely between the xy , x^2-y^2 orbitals that have same m_l values creating a large orbital momentum perpendicular to the xy plane that blocks the spin angular momentum along the z direction. In other terms the spin sub-levels are splitted with the $m_s = \pm 1$ lying lower than the $m_s = 0$ with an energy difference corresponding to the spin-orbit coupling parameter ζ . However, because of the Jahn-Teller effect, the complexes will have a small distortion that leads to a lift of the degeneracy of the e orbitals as depicted in Figure II.22. The electronic ground state (before considering the spin orbit coupling) is not degenerate anymore; its angular momentum is, therefore, equal to zero so that the spin sub-levels remain degenerate and no ZFS occurs. The ZFS appears when considering the interaction between the ground state and the excited ones that may be coupled by the spin-orbit operator. The lowest excited state is obtained by the promotion of an electron (red) from xy (x^2-y^2) to the x^2-y^2 (xy) orbitals. Because these two orbitals possess the same m_l values, the coupling between the ground and the lowest excited states occurs via the $I_z S_z$ component of the spin orbit operator that couples states with the same m_l and the same m_s values. One can show that the coupling between the $m_s = \pm 1$ sublevels of the ground and the excited states is larger than between the $m_s = 0$ ones leading to a larger stabilization of the ground $m_s = \pm 1$ sub-levels and thus bringing a negative contribution to the overall axial ZFS parameter value. This effect is similar to the

first order spin orbit coupling because the electron “circulates” between two orbitals of the same m_l values, but it has a weaker effect in the distorted case because the two orbitals have different energies while they are degenerate for the strict C_{3v} symmetry. The effect of the second lowest electronic excited state must be considered. It may bring a negative contribution to D as the first excited state making D more negative or it may have an opposite effect rendering D less negative and thus reducing the overall anisotropy. The second lowest excited state is obtained from an excitation involving the xz (yz) and the xy (x^2-y^2). In this case, there is change in the m_l value (from ± 1 to ± 2 , see Figure II.22) so that the l_{+s} + l_{-s} part of the spin orbit operator must be considered. Therefore, the m_s sub-levels belonging to the ground and the second lowest excited states that have *different* values couple together. The result is a larger stabilization of the $m_s = 0$ sublevel of the ground state bringing a positive contribution to D (Figure II.23); which is an opposite effect to the lowest excited states reducing the negative overall D value. However, because the second excited state is higher in energy than the lowest one, its (positive) contribution to D is weaker than that of the lowest excited state (that is negative) so that D remains negative. The overall D value is thus expected to be negative in these complexes despite the distortion. The other excited states also contribute and only *ab initio* calculations may allow a detailed analysis of their effect.

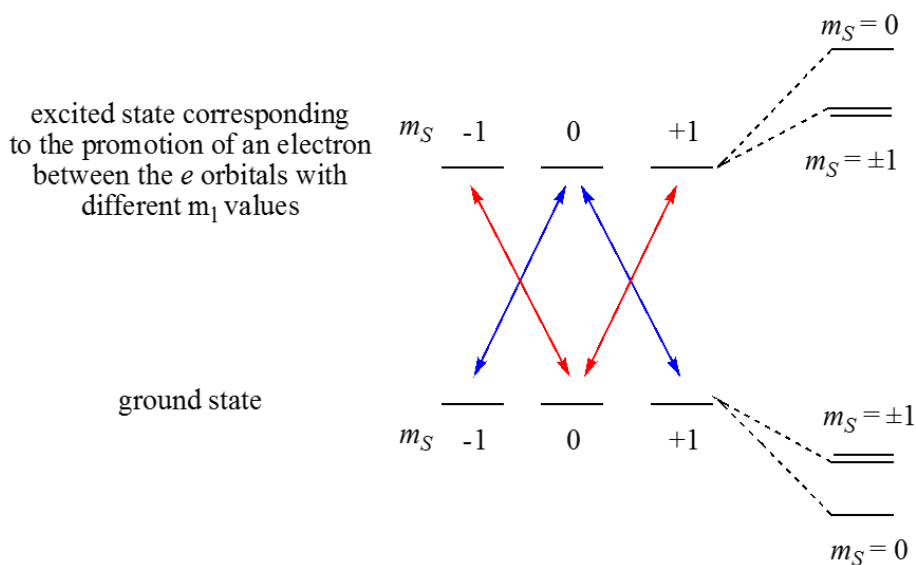


Figure II.23 Scheme showing the larger stabilization of the $m_s = \pm 0$ sublevels of the ground state.

In order to analyze in detail these effects, we carried out *ab initio* calculations using the ORCA package for compounds **2-1(b)** and **2-1(d)** (hydrated) using the structures at $T = 100$ K. The full calculation considering dynamical correlation effects leads to the ZFS shown in Table II.6. The calculations give large axial ZFS parameters that are relatively close, probably, reflecting the close degree of distortion within the two compounds. In order to analyze the effects of the electronic states, their energy and their relative contributions are given in Table II.7.

Table II.6 Calculated ZFS parameters for compounds **2-1(b)** and **2-1(d)**.

	D (cm ⁻¹)	E (cm ⁻¹)
2-1(b)	-87.5	0.4
2-1(d)	-68.1	1.36

Table II.7 Energy levels before SOC and their contribution to D and E .

E (cm ⁻¹) 2-1(b)	Contribution to D	Contribution to E	E (cm ⁻¹) 2-1(d)	Contribution to D	Contribution to E
0.0000	0.0000 (3)	0.0000	0.0000 (3)	0.0000	0.0000
1691.1 (3)	-148.04 (3)	0.11100	2048.1 (3)	-124.11	0.1010
5069.3 (3)	22.290 (3)	-18.242	5410.0 (3)	21.145	-10.142
5906.5 (3)	15.906 (3)	15.119	6182.6 (3)	15.770	8.3940
7628.2 (3)	3.5950 (3)	2.5140	8209.5 (3)	3.0220	-0.551
8831.7 (3)	2.9750 (3)	-2.5470	9440.9 (3)	2.6120	-0.094
10344	0.669	0.56100	10903	0.64100	-0.035
15589	-0.167	0.14600	15477	-0.1080	-0.0060
17546	-0.0040	0.00300	17559	-0.0040	0.0010
19054 (1)	19.113 (1)	-0.00500	19396 (1)	18.712	-0.0080
21624 (1)	-6.5340 (1)	5.5910	21964 (1)	-6.3740	3.5370
22442 (1)	-5.9370 (1)	-5.1920	22713 (1)	-5.8570	-3.4720
23540	0.0860	0.078000	23907	0.09200	0.0680
24688	0.12400	-0.10400	25087	0.12400	-0.0650
26635	-0.0090	0.0040000	27193	-0.0080	-0.0010
27343	0.22100	-0.23400	27612	0.043000	-0.0690
28388	-0.0050	0.0060000	28649	-0.0310	0.0310
29051	-0.0530	0.054000	29381	-0.10700	0.065
31381	-0.2000	-0.22000	31960	-0.13800	-0.018
32027	-0.00400	-0.00200	32604	0.027000	0.010
32257	-0.0570	0.064000	32777	0.27600	-0.039

32513	1.1830	-0.015000	33102	0.78400	0.054
33071	-1.7130	1.1820	33607	-1.6440	-0.195
33208	-1.4800	-0.97700	33852	-1.3460	0.202
66493	-0.00100	0.0010000	66903	-0.00100	0.000

Orbital	E (cm ⁻¹) 2-1(b)	E (cm ⁻¹) 2-1(d)
d _{yz}	0	0
d _{xz}	333.1	153.2
d _{xy}	1992.9	459.7
d _{x²-y²}	2031.6	3169.5
d _{z²}	9402.2	9871.6

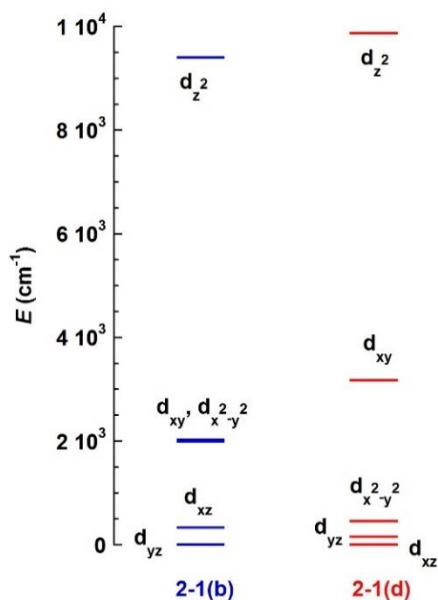


Figure II.24 Energy of the d orbitals

The energy of the d orbitals obtained from calculation are given in Figure II.24. For **2-1(b)**, the energy of the d orbitals is similar to what one expects from a trigonal symmetry with weak distortion i.e. the xz and yz orbitals are close in energy (difference of 300 cm⁻¹), the xy and x²-y² orbitals are almost degenerate and the z² orbital is at higher energy than the other four. While for **2-1(d)**, the first three orbitals are relatively close, the xy is higher (by about 3200 cm⁻¹) and the z² is much higher. From this scheme, one observes that the xy and the x²-y² orbitals are much closer for **2-1(b)** than for **2-1(d)**. The excitation among these two orbitals that have the same *m_l* values brings a negative *D* that is larger (in absolute value) when the orbitals are closer. The examination of Table II.7 shows that the first excited state is closer to the ground state for **2-1(b)** than for **2-1(d)** and the contribution to *D* is larger in the former than in the latter. The overall *D* values keep the same relative magnitude as the contributions of the first excited states because these states have the largest contributions to *D* (in absolute values). However, the overall *D* value, even though is still negative, is weaker (in absolute value) than the contribution of the lowest excited

state (-87.5 in comparison to -148 cm⁻¹ for **2-1(b)**). The rationalization of the E value is much more difficult because as one observes (Table II.7), it comes from different contributions that can be large and of opposite signs.

Figure II.25 shows the composition of the wave functions of the ground and the first two excited states. One observes that the ground state is mixture of two Slater determinant with one electron on the xy and the x^2-y^2 orbitals. This is also the case of the wavefunctions forming the first excited state that lies at 1691 cm⁻¹ (Table II.6) above the ground state. The transition from the ground to the excited state involves only the the xy and the x^2-y^2 orbitals bringing, therefore, a large negative contribution to D (-148 cm⁻¹, Table II.7). One can also observe that the excitation from the ground to the second lowest excited state occur only between orbitals having different m_l values, therefore, bringing a positive contribution to D (+22.3 cm⁻¹, see Table II.7). Table II.7 shows that almost all the excited states contribute in an opposite way to the first excited state reducing the overall negative D value.

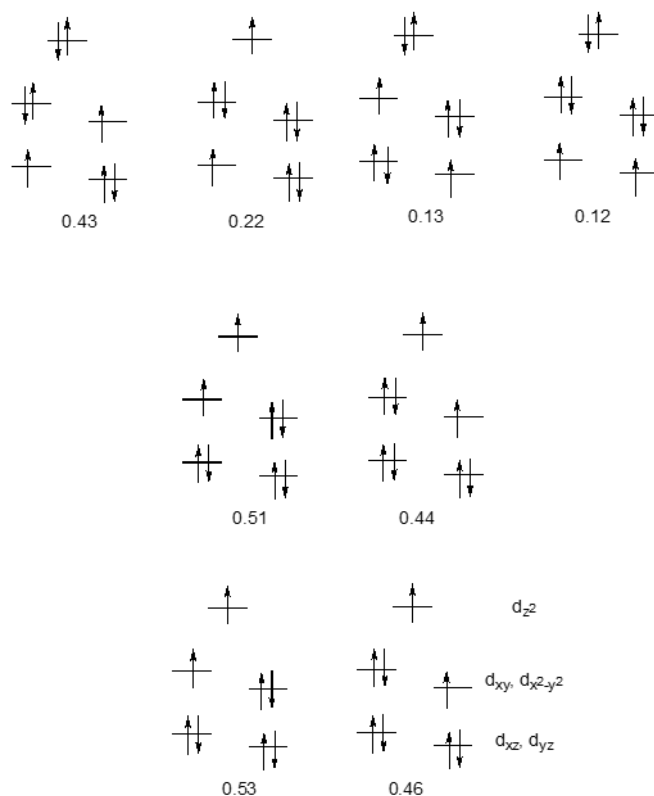


Figure II.25 Composition of the wavefunctions corresponding to the ground and the first two excited states; the numbers corresponds to the weight of each Slater determinant and only those larger than 10% are depicted.

The comparison of the calculated ZFS parameters to those obtained from fitting the magnetic data is not good at all. Only the sign and the magnitude were reproduced, but the relative values do not correspond to experience. There are several reasons. The most important one is the difficulty to fit the magnetic data when the axial ZFS parameter is very large because the excited states are much higher in energy than the temperature at which the experiment is carried out. In order to obtain accurate ZFS parameters, it is necessary to perform High Field-High Frequency Electron Paramagnetic Resonance Spectroscopy (HF-HFEPR) that will allow in the present case to determine the rhombic term. The axial term is still too large to be determined by HF-HFEPR, one must use neutron scattering and/or terahertz spectroscopy. These studies are underway.

2.5 Conclusions

We presented the syntheses, the structural studies and the magnetic properties of seven trigonal bipyramidal mononuclear Ni(II) complexes, that have the same core structure: Ni(Me₆tren)X-Y. Complexes **2-1** to **2-4** have a Cl as axial ligand and different counter anions (Cl⁻, BPh₄⁻, PF₆⁻, CF₃SO₃⁻), complexes **2-5** and **2-6** have Br as an axial ligand and ClO₄⁻ and PF₆⁻ as counterions, and I⁻ acting as both axial ligand and counter anion for complex **2-7**.

For **2-1**, the complex has two different states: dehydrated one and hydrated. The dehydrated one undergoes a phase transition around 200 K that can be observed from X-ray single crystal diffraction and from magnetic studies. The water molecules in the hydrated complex stabilize the molecular structure in orthorhombic crystal system. The difference in the coordination sphere of Ni(II) is mainly within the equatorial plane and lead to ZFS parameters that are not very different. Theoretical calculations confirm the negative value of *D* for the two compounds.

For complex **2-2** to **2-4**, the size of the counter anions and the packing in the crystal determine their significant molecular structure difference. The low symmetry of the anion leads to a low local symmetry for complex **2-4**. Complexes **2-5** and **2-6** both have a Br axial

ligand and possess strict C_{3v} symmetry. The magnetic studies show axial ZFS parameter is larger than the distorted ones as expected.

Complex **2-7** has I⁻ as axial ligand and counter anion. The crystal has a cubic symmetry and the complex is strictly trigonal. The fit of the magnetic data was not possible. It was necessary to introduce $S = 1$ impurity to have a good fit. The complex will be prepared and studied in order to solve this problem.

We have prepared and performed the preliminary studies of a series of mononuclear Ni(II) complexes that possess relatively large negative D values and a relatively weak E values leading to a very interesting situation where the two low-lying levels $m_S = \pm 1$ (separated by $2E$) are well separated from the $m_S = 0$ sub-level (D) by more than few tens of cm^{-1} . Therefore, at low temperature the complexes can be considered as two-level systems and can play the role of quantum bits with relatively large relaxation time (T_2). In order to determine the relaxation time of the different complexes, we will perform pulsed EPR experiments on single crystals. If the relaxation time is large enough (more than 0.1 ms), the next step consists in preparing binuclear complexes with weak exchange coupling that can be used as quantum gates.

We have in this thesis already explored the possibility of preparing trinuclear complexes based on Ni(II) and Co(II) with weak exchange coupling as a first step to construct quantum gates. This is the subject of the next chapter.

2.6 References

- 1 Lis, T. Preparation, structure, and magnetic properties of a dodecanuclear mixed - valence manganese carboxylate. *Acta Crystallographica Section B* **36**, 2042-2046 (1980).
- 2 Sessoli, R., Gatteschi, D., Caneschi, A. & Novak, M. Magnetic bistability in a metal-ion cluster. *Nature* **365**, 141 (1993).
- 3 Caneschi, A. *et al.* Alternating current susceptibility, high field magnetization, and millimeter band EPR evidence for a ground $S = 10$ state in $[\text{Mn}_{12}\text{O}_{12}(\text{CH}_3\text{COO})_{16}]$

- (H₂O) 4]. 2CH₃COOH. 4H₂O. *Journal of the American Chemical Society* **113**, 5873-5874 (1991).
- 4 Hill, S. *et al.* high-sensitivity electron paramagnetic resonance of Mn 12-acetate. *Physical review letters* **80**, 2453 (1998).
- 5 Ruamps, R. *et al.* Ising-type magnetic anisotropy and single molecule magnet behaviour in mononuclear trigonal bipyramidal Co (II) complexes. *Chemical Science* **5**, 3418-3424 (2014).
- 6 Gomez-Coca, S., Cremades, E., Aliaga-Alcalde, N. & Ruiz, E. Mononuclear single-molecule magnets: tailoring the magnetic anisotropy of first-row transition-metal complexes. *J Am Chem Soc* **135**, 7010-7018, doi:10.1021/ja4015138 (2013).
- 7 Boča, R., Miklovič, J. & Titiš, J. n. Simple mononuclear cobalt (II) complex: A single-molecule magnet showing two slow relaxation processes. *Inorganic chemistry* **53**, 2367-2369 (2014).
- 8 Zadrozny, J. M. & Long, J. R. Slow magnetic relaxation at zero field in the tetrahedral complex [Co(SPh)₄]₂. *J Am Chem Soc* **133**, 20732-20734, doi:10.1021/ja2100142 (2011).
- 9 Zadrozny, J. M., Telser, J. & Long, J. R. Slow magnetic relaxation in the tetrahedral cobalt(II) complexes [Co(EPh)₄]₂⁻ (EO, S, Se). *Polyhedron* **64**, 209-217, doi:10.1016/j.poly.2013.04.008 (2013).
- 10 Tu, D., Shao, D., Yan, H. & Lu, C. A carborane-incorporated mononuclear Co (II) complex showing zero-field slow magnetic relaxation. *Chemical communications* **52**, 14326-14329 (2016).
- 11 Rogez, G. *et al.* Very Large Ising - Type Magnetic Anisotropy in a Mononuclear Nill Complex. *Angewandte Chemie International Edition* **44**, 1876-1879 (2005).
- 12 Ruamps, R. *et al.* Giant Ising-type magnetic anisotropy in trigonal bipyramidal Ni(II) complexes: experiment and theory. *J Am Chem Soc* **135**, 3017-3026, doi:10.1021/ja308146e (2013).
- 13 Marriott, K. E. R. *et al.* Pushing the limits of magnetic anisotropy in trigonal bipyramidal Ni(ii). *Chemical Science* **6**, 6823-6828, doi:10.1039/C5SC02854J (2015).
- 14 Craig, G. A. *et al.* Probing the origin of the giant magnetic anisotropy in trigonal bipyramidal Ni(ii) under high pressure. *Chem Sci* **9**, 1551-1559, doi:10.1039/c7sc04460g (2018).
- 15 Rogez, G. *et al.* Very large Ising-type magnetic anisotropy in a mononuclear Ni(II) complex. *Angewandte Chemie* **44**, 1876-1879, doi:10.1002/anie.200462294 (2005).

- 16 Shao, F. *et al.* Tuning the Ising-type anisotropy in trigonal bipyramidal Co(II) complexes. *Chemical communications* **51**, 16475-16478, doi:10.1039/c5cc07741a (2015).
- 17 Shao, F. *et al.* Structural Dependence of the Ising-type Magnetic Anisotropy and of the Relaxation Time in Mononuclear Trigonal Bipyramidal Co(II) Single Molecule Magnets. *Inorg Chem* **56**, 1104-1111, doi:10.1021/acs.inorgchem.6b01966 (2017).
- 18 Britovsek, G. J., England, J. & White, A. J. Non-heme iron (II) complexes containing tripodal tetradentate nitrogen ligands and their application in alkane oxidation catalysis. *Inorganic chemistry* **44**, 8125-8134 (2005).
- 19 Sheldrick, G. M. SHELXL-97. *Program for crystal-structure refinement* (1997).
- 20 Sheldrick, G. M. A short history of SHELX. *Acta Crystallographica Section A: Foundations of Crystallography* **64**, 112-122 (2008).
- 21 Farrugia, L. J. WinGX program features. *J. Appl. Crystallogr* **32**, 837-838 (1999).
- 22 Chilton, N. F., Anderson, R. P., Turner, L. D., Soncini, A. & Murray, K. S. PHI: A powerful new program for the analysis of anisotropic monomeric and exchange - coupled polynuclear d - and f - block complexes. *Journal of computational chemistry* **34**, 1164-1175 (2013).
- 23 Borrás - Almenar, J., Clemente - Juan, J. M., Coronado, E. & Tsukerblat, B. MAGPACK 1 A package to calculate the energy levels, bulk magnetic properties, and inelastic neutron scattering spectra of high nuclearity spin clusters. *Journal of Computational Chemistry* **22**, 985-991 (2001).
- 24 Neese, F. The ORCA program system. *Wiley Interdisciplinary Reviews: Computational Molecular Science* **2**, 73-78 (2012).

Chapter III

Ni(II) and Co(II) molecular magnets based on Trithiocyanurate (TTC)

3.1 Introduction

Multinuclear complexes based on transition metals with well-defined polyhedral geometries have emerged rapidly as an area of coordination chemistry, which allow the possibilities in many fields, like catalysis,¹ optoelectronics² and magnetic materials.³ In this chapter, we focus on the design of trinuclear complexes containing Co(II) and Ni(II) complexes. The synthesis approach consists in assembling three mononuclear complexes around a central tris-bidentate organic ligand. The mononuclear precursors have two types of ligands: (i) chelating ligand(s) that impose high thermodynamic stability so that they cannot be substituted by the central one and (ii) terminal ligands that can be substituted by the atoms of the central ligands. This imposes a larger thermodynamic stability of the central ligand than with those present on the mononuclear precursor. The mononuclear complex must be designed in a way to keep a large ZFS when linked to central assembling. Furthermore, the central ligand must be large enough in order to minimize the exchange coupling between the metal ions. In summary we aim at designing trinuclear complexes with large local ZFS and weak *antiferromagnetic* exchange coupling interaction to be candidates for quantum logic gates. This work is exploratory and not easy to achieve knowing the different specifications.

We choose trithiocyanurate ion (TTC^{3-} , see Figure III.1) as the central assembling tris-bidentate. TTC^{3-} has a symmetric structure with three N and three S atoms in a planar ring. The N and S atoms provide coordination sites for central atoms. They are able to produce multinuclear complexes with diverse coordination modes. TTC^{3-} has the ability to act as a

bidentate ligand by chelating N, S atoms to form mononuclear,⁴ binuclear,⁵ trinuclear^{6,7} or multinuclear⁸ complexes. Also, polynuclear complexes can be generated through coordinating with either N or S atom, as for $[\text{Au}_3(\text{PPh}_3)_3(\text{TTC})]\cdot\text{Et}_2\text{O}$ where only the S atoms act as coordination sites.⁹ The first study of coordination polymer with TTC was carried out by Beezer,¹⁰ who found that it is possible to assign the molar ratio between metal ions and ligands by tuning their stoichiometry and the pH of the solution.

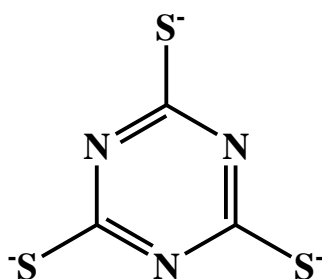


Figure III.1 Schematic view of trithiocyanurate ion (TTC^{3-}).

Because its chelating power, TTC^{3-} plays a significant role in industry, especially in wastewater treatments. The univalent and divalent heavy metals can be removed from the waste water.^{11,12} Besides, its applications in biology cannot be ignored.¹³ Until now, several coordination complexes containing the TTC^{3-} ligand are reported, most of which are trinuclear complexes mostly based on Cu, Mn, Zn, Ni and Co.^{6-8,14-17}

A trinuclear Ni(II) complex $[\text{Ni}_3(\text{TTC})(\text{pmdien})_3](\text{ClO}_4)_3$ was obtained by Kopel and his team in 2009 (pmdien = pentamethyldiethylenetriamine). The Ni(II) ion in this molecule is penta-coordinated with three N atoms of one pmdien molecule and one N atom and one S atom of TTC^{3-} bridge, forming a distorted trigonal bipyramidal geometry coordination. The paper reports a ferromagnetic exchange interaction among the Ni(II) bridged through the TTC^{3-} ligand and a single molecule magnet behavior. The Ni(II) ions in this trinuclear complex have a pentacoordinate geometry as required for large negative ZFS. And the coupling is expected to be weak because the large distance between the metal ions. The paper reports a ferromagnetic exchange coupling that seemed to us larger than one would expect and more importantly, a bump in the $\chi T = f(T)$ curve is present that should not be there. We,

thus, decided to investigate the magnetic behavior of this complex and then to extend to other Ni(II) and Co(II) ones with different peripheral ligands.

In this thesis, we describe the syntheses and characterization of the two trinuclear Co(II) complexes: $[\text{Co}_3(\text{TTC})(\text{pmdien})_3](\text{ClO}_4)_3$ (**3-1**) and $[\text{Co}_3(\text{TTC})(\text{TPA})_3](\text{ClO}_4)_3(\text{H}_2\text{O})_2$ (**3-2**) (TPA = Tris(2-pyridylmethyl)amine), three Ni(II) complexes: $[\text{Ni}_3(\text{TTC})(\text{APMPDA})_4(\text{ClO}_4)](\text{ClO}_4)_2(\text{H}_2\text{O})_8(\text{CH}_3\text{OH})$ (**3-3**), $[\text{Ni}_6(\text{TTC})_3(\text{TMEDA})_6(\text{ClO}_4)(\text{CO}_3)](\text{H}_2\text{O})_3(\text{CH}_3\text{OH})_{2.5}$ (**3-4**) and $[\text{Ni}_3(\text{TTC})(\text{pmdien})_3](\text{ClO}_4)_3(\text{H}_2\text{O})$ (**3-5**) (APMPDA = N1-(3-Aminopropyl)-N1-methylpropane-1,3-diamine; TMEDA = tetramethylethylenediamine). The prepared complexes were characterized by infrared spectroscopy, element analysis, X-ray single crystal diffraction and magnetic measurements.

3.2 Experimental section

3.2.1 Syntheses

All the reagents used for these syntheses were purchased commercially and were used directly without further purification unless exceptionally stated.

Caution: The Perchlorate salts may have unpredictable behavior and may explode. They must be handled with care under a protected hood and must never be heated. We always take care to use very small amount.

$[\text{Co}_3(\text{TTC})(\text{pmdien})_3](\text{ClO}_4)_3$ (Complex 3-1)

10 mL pmdien (105 μL , 0.5 mmol) methanolic solution was added to a 20 mL methanol solution of $\text{Co}(\text{ClO}_4)_2 \cdot 6\text{H}_2\text{O}$ (182.9 mg, 0.5 mmol) dropwise; the solution turned to dark red immediately. It was stirred for 30 min, then 2 mL methanol solution of $\text{Na}_3(\text{TTC})$ (70 mg, 0.167 mmol) was added to the solution slowly, violet precipitate was obtained. The reaction was left overnight. The solid was filtered and washed with methanol for three times. It was dried under the vacuum and yield 79.02%, 154 mg. The powder was redissolved in acetonitrile/acetone (v/v 1:1), and diethyl ether diffused into the solution

to obtain red brown crystals suitable for X-ray single crystal diffraction. Elem. Anal. for $[\text{Co}_3(\text{TTC})(\text{pmdien})_3](\text{ClO}_4)_3$ Calc: C, 30.82; H, 5.95; N, 14.37. Found: C, 30.36; H, 5.98; N, 13.92. $M_w = 1169.30$ g/mol. Single-crystal unit cell: Hexagonal, space group $P-62c$, $a = 13.3628(8)$ Å, $b = 13.3628(8)$ Å, $c = 49.734(3)$ Å, $\alpha = 90^\circ$, $\beta = 90^\circ$, $\gamma = 120^\circ$, $V = 7690.9(10)$ Å³. IR (KBr) ν/cm^{-1} : 3426 (s), 2975 (m), 2902 (m), 2873 (m), 2814 (w), 2383 (w), 2092 (w), 2018 (w), 1835 (w), 1741 (w), 1710 (w), 1633 (w), 1473 (s), 1449 (s), 1433 (s), 1300 (w), 1285 (w), 1224 (s), 1178 (w), 1142 (s), 1090 (s), 1044 (m), 1019 (m), 1004 (w), 984 (m), 930 (m), 908 (w), 869 (m), 800 (s), 777 (m), 771 (m), 749 (w), 636 (m), 624 (s), 579 (w), 493 (w), 459 (w), 440 (w), 383 (w), 301 (w).

$[\text{Co}_3(\text{TTC})(\text{TPA})_3](\text{ClO}_4)_3(\text{H}_2\text{O})_2$ (Complex 3-2)

1 mL methanol solution of $\text{Na}_3(\text{TTC})$ (70 mg, 0.167 mmol) was added to a 20 mL methanol solution of $\text{Co}(\text{ClO}_4)_2 \cdot 6\text{H}_2\text{O}$ (183 mg, 0.5 mmol) dropwise, generating some green-grey solid. It was stirred for 30 min, then 10 mL TPA methanolic solution (145.2 mg, 0.5 mmol) was added to the suspension slowly, and the red-brown powder was obtained. The reaction was left overnight. The solid was filtered and washed with methanol for three times, dried under vacuum. A yield of 77.5% (201 mg) was obtained. The powder was redissolved in acetonitrile, and the red-brown crystals suitable for X-ray single crystal diffraction were obtained by diffusing diethyl ether into the solution. Elem. Anal. for $[\text{Co}_3(\text{TTC})(\text{TPA})_3](\text{ClO}_4)_3(\text{H}_2\text{O})_2$ Calc: C, 43.98; H, 3.76; N, 13.50. Found: C, 44.01; H, 3.73; N, 13.71. $M_w = 1556.52$ g/mol. Single-crystal unit cell: Triclinic, space group $P-1$, $a = 12.5812(4)$ Å, $b = 13.7959(4)$ Å, $c = 21.1712(6)$ Å, $\alpha = 73.5590(10)^\circ$, $\beta = 84.140(2)^\circ$, $\gamma = 75.5840(10)^\circ$, $V = 3411.46(18)$ Å³. IR (KBr) ν/cm^{-1} : 3421 (s), 3066 (w), 3026 (w), 2918 (w), 2856 (w), 2103 (w), 2019 (w), 1873 (w), 1635 (m), 1606 (s), 1572 (w), 1483 (m), 1437 (s), 1309 (w), 1289 (w), 1265 (w), 1235 (s), 1143 (s), 1090 (s), 1053 (s), 1020 (m), 1098 (w), 1008 (w), 907 (w), 868 (m), 840 (w), 770 (s), 733 (w), 636 (m), 625 (s), 502 (w), 475 (w), 420 (m), 331 (w).

[Ni₃(TTC)(APMPDA)₄(ClO₄)](ClO₄)₂(H₂O)₈(CH₃OH) (Complex 3-3)

1 mL methanol solution of Na₃(TTC) (70 mg, 0.167 mmol) was added to a 20 mL methanol solution of Ni(ClO₄)₂·6H₂O (182.9 mg, 0.5 mmol) dropwise, generating a yellow-green solid. It was stirred for 30 min, then 10 mL APMPDA (80.6 μL, 0.5 mmol) methanolic solution was added to the suspension slowly with stirring. The precipitate disappeared, and the solution turned to blue. The reaction was left overnight. It was then filtered, and the solution left to evaporate slowly to obtain blue crystals suitable for X-ray single crystal diffraction. Elem. Anal. for [Ni₃(ttc)(APMPDA)₄(ClO₄)](ClO₄)₂(H₂O)₈(CH₃OH) Calc: C, 27.34; H, 6.88; N, 14.94. Found: C, 27.10; H, 5.99; N, 14.95. M_w = 1405.83 g/mol. Single-crystal unit cell: Monoclinic, space group *P2*₁, *a* = 15.1573(6) Å, *b* = 23.8748(9) Å, *c* = 15.1614(5) Å, *α* = 90°, *β* = 98.363(2)°, *γ* = 90°, *V* = 5428.2(3) Å³. IR (KBr) v/cm⁻¹: 3437 (s), 3334 (s), 3286 (s), 2932 (m), 2880 (m), 2406 (w), 2024 (w), 1600 (m), 1448 (s), 1438 (s), 1332 (w), 1305 (w), 1280 (w), 1268 (w), 1242 (s), 1214 (w), 1141 (s), 1121 (s), 1092 (s), 1015 (m), 990 (m), 932 (m), 917 (w), 875 (s), 813 (w), 772 (m), 752 (w), 636 (m), 626 (s), 506 (w), 480 (w), 409 (w), 338 (w).

[Ni₆(TTC)₃(TMEDA)₆(ClO₄)(CO₃)(H₂O)₃](CH₃OH)_{2.5} (Complex 3-4)

1 mL methanol solution of Na₃(TTC) (70 mg, 0.167 mmol) was added to a 20 mL methanol solution of Ni(ClO₄)₂·6H₂O (182.9 mg, 0.5 mmol) dropwise, generating some yellow-green solid. It was stirred for 30 min, then 10 mL TMEDA (150 μL, 1 mmol) solution was added to the suspension slowly while stirring. The solid disappeared and the solution turned to green. The reaction was left overnight. It was then filtered, and the filtrate was left to evaporate slowly to obtain green crystals suitable for X-ray single crystal diffraction. Elem. Anal. for [Ni₆(TTC)₃(TMEDA)₆(ClO₄)(CO₃)(H₂O)₃](CH₃OH)_{2.5} Calc: C, 31.22; H, 6.05; N, 15.76. Found: C, 31.17; H, 5.99; N, 15.63. M_w = 1865.75 g/mol. Single-crystal unit cell: Trigonal, space group *P3*₁*c*, *a* = 13.6676(7) Å, *b* = 13.6676(7) Å, *c* = 24.7022(14) Å, *α* = 90°, *β* = 90°, *γ* = 120°, *V* = 3996.2(5) Å³. IR (KBr) v/cm⁻¹: 3389 (s), 2973 (w), 2888 (m), 2840 (m), 2796 (w), 2393 (w), 2095 (w), 1629 (w), 1567 (w), 1453 (s), 1433 (s), 1284 (w), 1267 (w), 1228 (s), 1194 (w), 1168 (w), 1121 (m), 1108 (m), 1097 (s), 1063 (w), 1047 (w), 1024 (m), 1010 (w),

954 (m), 878 (s), 803 (s), 765 (m), 738 (w), 636 (w), 624 (m), 566 (w), 492 (w), 447 (w), 391 (w).

[Ni₃(TTC)(pmdien)₃](ClO₄)₃(H₂O) (Complex 3-5)

The synthesis of Complex **3-5** was carried out according to a previous report in the literature.¹⁸ But, we never succeeded to obtain single crystals of this compound. Only microcrystalline powder was obtained. Therefore, all the following measurement were made the microcrystalline powder after checking that its powder diffraction diagram fits the calculated one base on the published structure (reference CCDC **676655**).

A solution of pmdien (0.2 mL, 1 mmol) was added to a 50 mL EtOH solution of Ni(ClO₄)₂·6H₂O (366 mg, 1 mmol) dropwise, and then an aqueous solution of Na₃(TTC) (140 mg, 0.33 mmol) (2 mL) was slowly added with stirring. A green solid was obtained directly during the addition. The reaction was left for stirring for 1 h. The solid was filtered and washed with EtOH for three times and dried under vacuum and yield 77%, 305 mg. Elem. Anal. for [Ni₃(ttc)(pmdien)₃](ClO₄)₃(H₂O) Calc: C, 30.36; H, 6.03; N, 14.16. Found: C, 30.17; H, 5.87; N, 14.09. M_w = 1186.59 g/mol. IR (KBr) v/cm⁻¹: 3425 (s), 2992 (w), 2961 (w), 2902 (w), 2852 (w), 2804 (w), 2397 (w), 2106 (w), 1867 (w), 1635 (m), 1474 (s), 1426 (s), 1404 (s), 1306 (w), 1291 (w), 1226 (s), 1187 (w), 1179 (w), 1143 (s), 1127 (s), 1083 (s), 1040 (m), 1028 (m), 1015 (w), 974 (m), 936 (m), 918 (w), 880 (s), 803 (s), 775 (m), 764 (m), 636 (m), 624 (s), 584 (w), 494 (w), 459 (w), 445 (w), 392 (w).

3.2.2 Physical Measurements

The physical measurements refer to the section 2.2.2. The powder X-ray diffraction measurement was carried out on a Panalytical X-Pert Pro MPD with Cu Kα1 as ray source.

For the X-ray Crystallography measurement, the data for complex **3-1** was collected by using a VENTURE PHOTON100 CMOS Bruker diffractometer with Micro-focus IuS source Mo Kα radiation. X-ray diffraction data for complexes **3-2**, **3-3**, **3-4** and **3-5** were collected by using a X8 APEXII CCD Bruker diffractometer with graphite-monochromated MoKα

radiation. All crystals were mounted on a CryoLoop (Hampton Research) with Paratone-N (Hampton Research) as cryoprotectant and then flash frozen in a nitrogen-gas stream at 100 K.

3.3 Results and discussion

3.3.1 Molecular Structures Description

3.3.1.1 Molecular structure of Complexes 3-1 and 3-2

Complex **3-1** crystallizes in the space group $P-62c$ (Table A 4). A perspective view of the cation structure for complex **3-1** is shown in Figure III.2. Two crystallographically independent molecules can be observed in the unit cell (see Figure III.2a), reference isomers **3-1(i)** and **3-1(ii)** below. They both are composed of one TTC ligand, three Co(II) ions and three pmdien capping ligands. All the Co ions are penta-coordinated with one pmdien tridentate ligand and N and S from TTC in their coordination sphere. Their charge balance are provided by three perchlorate anions for one trinuclear complex.

For isomer **3-1(i)**, the plane of TTC is slightly bent (Figure III.2a, left), the plane of three Co ions lies 0.2303 Å away from the plane of three S atoms and 0.3362 Å from the plane of N atoms. For isomer **3-1(ii)**, the Co(II) ions lie in the same plane of the TTC ligand (Figure III.2a, right), while the carbon atoms of pmdien ligands are disordered. We analyzed with SHAPE^{19,20} and found that the coordination sphere of Co1 and Co2 are both trigonal bipyramids (all analysis results are presented in Table III.1). The smaller the value is, the closer the coordination geometry to the ideal model is. Comparing to Co1, the coordination geometry of Co2 is slightly more distorted. The distance between Co ion and TTC ligand varies from isomer **3-1(i)** to **3-1(ii)**. The Co-N bond length of **3-1(i)** (2.1398 Å) is longer than **3-1(ii)** (2.1203 Å), while the Co-S is shorter (2.3607 Å and 2.3788 Å for **3-1(i)** and **3-1(ii)**, respectively). The $\widehat{N1Co1S1}$ (69.926°) is larger than $\widehat{N5Co2S2}$ (69.317°). More information is listed in Table III.2, Table III.3 and Table A 4.

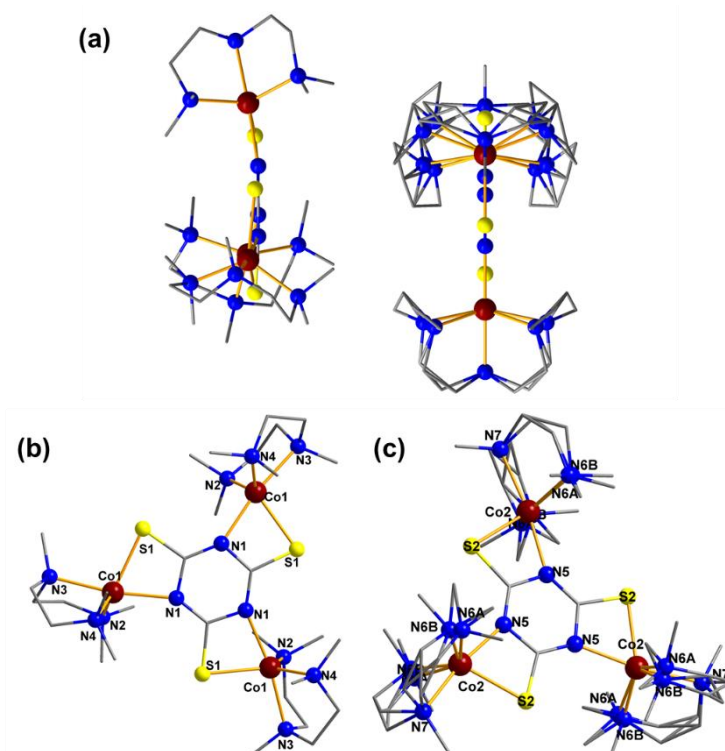


Figure III.2 (a): Crystal structure of complex **3-1**. (b) and (c): Molecular structure of complex **3-1(i)** and **3-1(ii)**, respectively. Perchlorate anions, H atoms are omitted for clarity.

Table III.1 Shape analysis of five-coordinate geometry in complex **3-1**. For **3-1(ii)**, the Co2(AA): the coordination atoms involved are N6A, N6A; Co2(AB): N6A, N6B, and Co2(BB): N6B, N6B.

Label	JTBPY	SPY	TBPY	vOC	PP
Symmetry	D_{3h}	C_{4v}	D_{3h}	C_{4v}	D_{5h}
Co1	4.585	6.402	1.599	8.610	30.716
Co2(AA)	5.522	5.050	2.061	5.813	28.738
Co2(AB)	4.923	6.083	1.825	8.142	29.240
Co2(BB)	4.765	6.496	2.135	8.123	32.242

Abbreviation: JTBPY Johnson trigonal pyramid J2, SPY – Spherical square pyramid, TBPY – Trigonal bipyramid, vOC – Vacant octahedron, PP – Pentagon.

Table III.2 Some relevant Co-ligand bond lengths (Å) for Complexes **3-1** and **3-2**.

Complex 3-1		Complex 3-2			
$d_{\text{Co1-N1}}$	2.1398(57)	$d_{\text{Co1-N1}}$	2.3807(19)	$d_{\text{Co2-N2}}$	2.2063(13)
$d_{\text{Co1-S1}}$	2.3607(19)	$d_{\text{Co1-S1}}$	2.3936(5)	$d_{\text{Co2-S2}}$	2.4709(6)
$d_{\text{Co1-N2}}$	2.0796(55)	$d_{\text{Co1-N4}}$	2.2066(16)	$d_{\text{Co2-N8}}$	2.2183(17)
$d_{\text{Co1-N3}}$	2.1899(53)	$d_{\text{Co1-N5}}$	2.0933(19)	$d_{\text{Co2-N9}}$	2.1288(19)

d _{Co1-N4}	2.0821(47)	d _{Co1-N6}	2.1135(20)	d _{Co2-N10}	2.1387(16)
d _{Co2-N5}	2.1203(59)	d _{Co1-N7}	2.1062(16)	d _{Co2-N11}	2.0968(17)
d _{Co2-S2}	2.3788(30)	d _{Co3-N3}	2.1791(19)	d _{Co3-N13}	2.1228(18)
d _{Co2-N6A}	2.1769(28)	d _{Co3-S3}	2.4746(8)	d _{Co3-N14}	2.0930(21)
d _{Co2-N6B}	1.9807(27)	d _{Co3-N12}	2.1977(19)	d _{Co3-N15}	2.1113(18)
d _{Co2-N7}	2.1749(79)				

Table III.3 Some relevant Co-ligand angle (°) for Complex **3-1** and **3-2**.

Complex 3-1		Complex 3-2			
S1Co1N1	69.926(16)	S1Co1N1	66.138(43)	N9Co2N10	134.045(67)
S1Co1N2	117.342(20)	S1Co1N4	170.545(49)	N9Co2N11	103.268(68)
S1Co1N3	101.349(16)	S1Co1N5	108.953(52)	N10Co2N11	105.239(69)
S1Co1N4	119.629(17)	S1Co1N6	94.489(52)	S2Co2N2	66.324(46)
N1Co1N2	97.937(19)	S1Co1N7	104.367(54)	S2Co2N8	171.566(47)
N1Co1N3	170.947(18)	N1Co1N4	122.618(60)	S2Co2N9	110.032(49)
N1Co1N4	103.543(19)	N1Co1N5	82.331(62)	S2Co2N10	105.599(48)
N2Co1N3	83.791(18)	N1Co1N6	160.615(63)	S2Co2N11	96.663(52)
N2Co1N4	122.947(21)	N1Co1N7	77.019(64)	S3Co3N3	67.394(46)
N3Co1N4	82.687(18)	N4Co1N5	77.150(67)	S3Co3N12	176.396(49)
S2Co2N5	69.317(24)	N4Co1N6	76.758(65)	S3Co3N13	99.175(54)
S2Co2N6A	110.415(11)	N4Co1N7	75.873(67)	S3Co3N14	100.942(56)
S2Co2N6B	122.126(84)	N5Co1N6	104.602(68)	S3Co3N15	104.284(58)
S2Co2N7	101.944(24)	N5Co1N7	128.893(70)	N3Co3N12	110.260(64);
N5Co2N6A	98.726(94)	N6Co1N7	110.244(69)	N3Co3N13	85.615(68);
N5Co2N6B	102.712(70)	N2Co2N8	119.913(63)	N3Co3N14	167.065(71);
N5Co2N7	171.261(27)	N2Co2N9	82.919(64)	N3Co3N15	92.717(71);
N6ACo2N7	84.146(92)	N2Co2N10	80.212(65)	N12Co3N13	77.753(70)
N6BCo2N7	81.735(68)	N2Co2N11	162.966(68)	N12Co3N14	81.098(71)
N6ACo2N6A	139.008(93)	N8Co2N9	77.218(64)	N12Co3N15	78.36(7)
N6ACo2N6B	127.306(98)	N8Co2N10	74.992(62)	N13Co3N14	91.017(76)
N6BCo2N6B	115.597(10)	N8Co2N11	77.095(67)	N13Co3N15	153.813(76)
				N14Co3N15	95.755(76)

For complex **3-2** (Figure III.3), the Co(II) sites are all hexa-coordinated because the TPA ligand is tetradentate, its coordination sphere is composed of one S atom and five N atoms

from the TTC bridge ligand and the TPA ligand. Three types of Co(II) ions are observed in this molecular structure. The Co-N distances (the N atoms in TTC ligand) range from 2.3807 Å to 2.1791 Å and the Co-S distances from 2.3936 Å to 2.4746 Å (see Table III.2), with a decrease in Co-N bond length and an increase in Co-S bond length from Co1 to Co3. The SHAPE analysis results indicate a difference in the coordination geometry of the Co ions: the coordination sphere for Co1 and Co2 is between octahedral and trigonal prism, while that of Co3 is closer to an octahedron (details in Table III.4). The angle of $\widehat{N1Co1S1}$ is equal to 66.138° , and $\widehat{N2Co2S2}$ is 66.324° , and $\widehat{N3Co3S3}$ is 67.394° , displaying a rise in the angle of \widehat{NCoS} . More information about the molecular structure can be found in Table III.2, Table III.3 and Table A 4.

Comparing with **3-1**, the distance of Co-TTC in **3-2** is longer in average, and the angle is smaller, which probably has an impact on their magnetic properties.

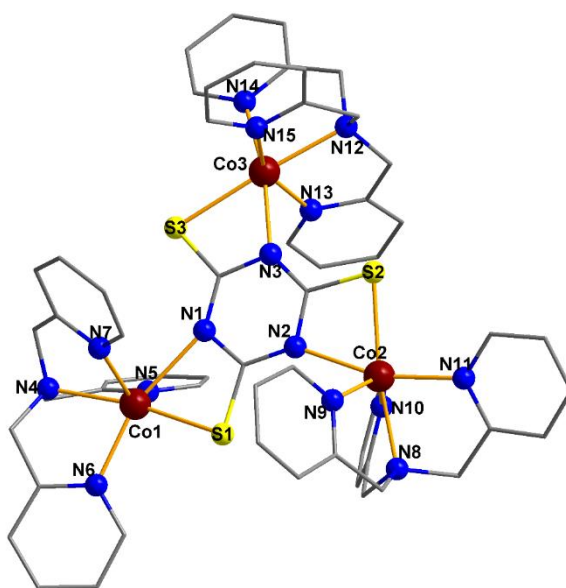


Figure III.3 Molecular structure of complex **3-2**. Three perchlorate anions, H atoms and water molecules are omitted for clarity.

Table III.4 Shape analysis of six-coordinate geometry in complex **3-2**.

Label	JPPY	TPR	OC	PPY	HP
Symmetry	C _{5v}	D _{3h}	O _h	C _{5v}	D _{6h}
Co1	14.907	7.356	8.811	11.728	31.007

Co2	17.194	7.721	7.480	13.939	30.990
Co3	24.692	11.938	3.553	21.026	29.146

Abbreviation: JPPY – Johnson pentagonal pyramid J2, TPR – Trigonal prism, OC – Octahedron, PPY – Pentagonal pyramid, HP – Hexagon.

3.3.1.2 Molecular structure of Complexes 3-3 and 3-4

Complex **3-3** crystallized in the space group $P2_1$ (see Table A 5). A perspective view of the cation structure for **3-3** is shown in Figure III.4. Two independent molecules exist in the unit cell (Figure III.4a): isomer **3-3(i)** and **3-3(ii)**. In both two molecules, three Ni(II) ions share four APMPDA capping ligands: each Ni(II) ion has one individual APMPDA ligand, and two of them share one additional capping ligand, and the remaining Ni ion is coordinated to a perchlorate ion. Therefore, the Ni(II) ions are all hexa-coordinated. The SHAPE analysis results reflect the octahedral coordination geometry of these Ni(II) ions (details in Table III.5). Two perchlorate ions provide the charge balance.

For isomer **3-3(i)**, the Ni1 and Ni2 share the fourth capping ligand, and Ni3 is the one which connected with one perchlorate ion. The carbon atoms in the fourth capping ligand are disordered (Figure III.4b). For isomer **3-3(ii)**, Ni4 is coordinated with one capping ligand and one disordered perchlorate ion, while the remaining three capping ligands are equally distributed by Ni5 and Ni6 (Figure III.4c).

The differences in the distance between Ni ions and TTC ligands are displayed in Table III.6. The Ni-N bond lengths decrease from 2.1385 Å to 2.1025 Å in isomer **3-3(i)**. The Ni-S bond lengths in isomer **3-3(i)** have the same tendency with Ni-N bond lengths, from 2.5520 Å to 2.4758 Å. For isomer **3-3(ii)**, the bond lengths of the Ni ion coordinated to perchlorate is shorter (the bond length of Ni4-N4 equals to 2.0731 Å and Ni4-S4 is 2.4709 Å) than the those of the other two Ni ions. The Ni-N bond lengths increase to 2.1237 Å (Ni5-N5) and to 2.1429 Å (Ni6-N6). The Ni-S bond length decreases from 2.5534 Å (Ni5-S5) to 2.5337 Å (Ni6-S6). In average, the Ni ions coordinated to perchlorate ions have shorter Ni-N and Ni-S bonds. Correspondingly, the \widehat{NNiS} angles are relatively larger. For isomer **3-3(i)**, the $\widehat{N1N1S1}$ and $\widehat{N2N2S2}$ angle are equal to 66.385° and 66.735°, while the $\widehat{N3N3S3}$ one is

equal to 68.015° . The same trend can be observed in isomer **3-3(ii)**: the $\widehat{N4N14S4}$ angle (68.407°) is larger than the other ones (66.560° for $\widehat{N5N15S5}$ and 66.009° for $\widehat{N6N16S6}$). More detailed information about the angles can be found in Table III.7.

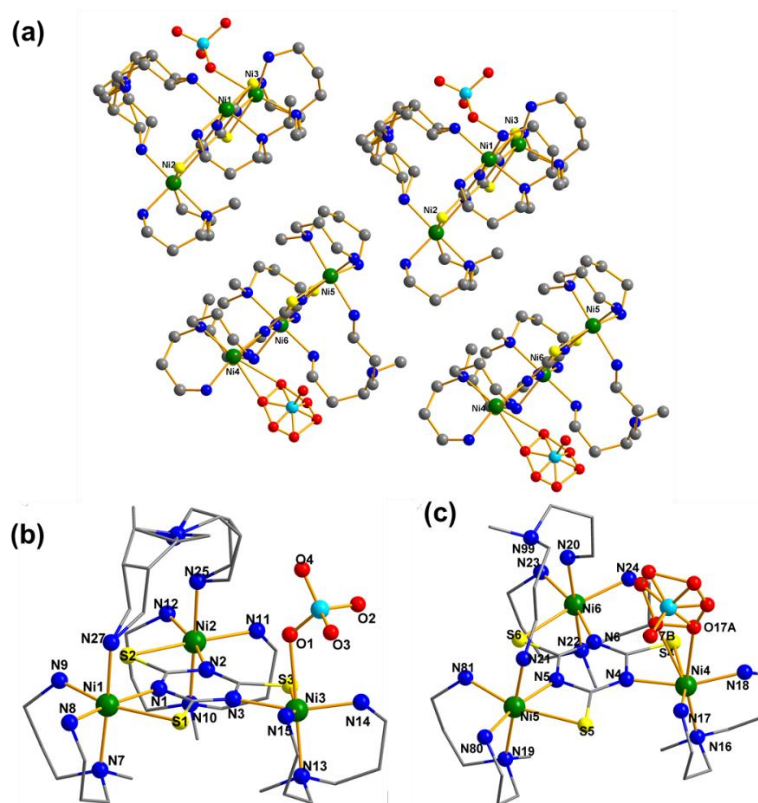


Figure III.4 (a): Crystal structure of complex **3-3**. (b) and (c): Molecular structure of complex **3-3(i)** and **3-3(ii)**, respectively. Perchlorate anions, H atoms are omitted for clarity.

Table III.5 Shape analysis of six-coordinate geometry in complex **3-3**. For Ni4, the Ni4A: the coordination atom involved is O17A; Ni4B: O17B.

Label	JPPY	TPR	OC	PPY	HP
Symmetry	C_{5V}	D_{3h}	O_h	C_{5V}	D_{6h}
Ni1	29.408	13.842	1.711	25.853	30.212
Ni2	29.356	15.001	1.442	25.905	29.259
Ni3	27.324	13.663	1.721	24.138	29.613
Ni4A	26.896	11.803	2.866	22.667	31.524
Ni4B	28.253	13.741	2.168	24.934	28.045
Ni5	29.057	14.086	1.670	25.409	30.467
Ni6	28.841	13.385	1.714	25.449	30.553

Abbreviation: JPPY - Johnson pentagonal pyramid J2, TPR – Trigonal prism, OC – Octahedron, PPY – Pentagonal pyramid, HP – Hexagon.

Table III.6 Some relevant Ni-ligand bond lengths (Å) for Complex **3-3** and **3-4**.

Complex 3-3						Complex 3-4	
d _{Ni1-N1}	2.1385(64)	d _{Ni3-N3}	2.1025(67)	d _{Ni5-N5}	2.1237(60)	d _{Ni1-N1}	2.0600(22)
d _{Ni1-S1}	2.5520(24)	d _{Ni3-S3}	2.4758(22)	d _{Ni5-S5}	2.5534(28)	d _{Ni1-S1}	2.5008(84)
d _{Ni1-N7}	2.2035(67)	d _{Ni3-N13}	2.1204(73)	d _{Ni5-N19}	2.1827(92)	d _{Ni1-N4}	2.1365(25)
d _{Ni1-N8}	2.0861(78)	d _{Ni3-N14}	2.0522(77)	d _{Ni5-N21}	2.1700(74)	d _{Ni1-N5}	2.1560(20)
d _{Ni1-N9}	2.0753(64)	d _{Ni3-N15}	2.0602(76)	d _{Ni5-N80}	2.0953(76)	d _{Ni1-O1}	2.1848(18)
d _{Ni1-N27}	2.1757(93)	d _{Ni3-O1}	2.4824(73)	d _{Ni5-N81}	2.0918(65)	d _{Ni1-O2}	2.1636(19)
d _{Ni2-N2}	2.1154(61)	d _{Ni4-N4}	2.0731(72)	d _{Ni6-N6}	2.1429(67)	d _{Ni2-N2}	2.0871(27)
d _{Ni2-S2}	2.5276(21)	d _{Ni4-S4}	2.4709(23)	d _{Ni6-S6}	2.5337(21)	d _{Ni2-S2}	2.4714(80)
d _{Ni2-N10}	2.2125(68)	d _{Ni4-N16}	2.0822(67)	d _{Ni6-N20}	2.1515(67)	d _{Ni2-N3}	2.1506(24)
d _{Ni2-N11}	2.0892(71)	d _{Ni4-N17}	2.0577(78)	d _{Ni6-N22}	2.1985(73)	d _{Ni2-S3}	2.4518(66)
d _{Ni2-N12}	2.0805(62)	d _{Ni4-N18}	2.0546(89)	d _{Ni6-N23}	2.0849(67)	d _{Ni2-N6}	2.1263(24)
d _{Ni2-N25}	2.1796(74)	d _{Ni4-O17A}	2.5361(14)	d _{Ni6-N24}	2.0843(61)	d _{Ni2-N7}	2.1641(21)
		d _{Ni4-O17B}	2.6419(21)				

Table III.7 Some relevant Ni-ligand angles (°) for Complex **3-3**.

3-3(i)				3-3(ii)			
S1Ni1N1	66.385(180)	N1Ni1N7	95.249(241)	S4Ni4N4	68.407(193)	N4Ni4N16	100.535(257)
S1Ni1N7	92.576(181)	N1Ni1N8	165.329(267)	S4Ni4N16	97.532(181)	N4Ni4N17	96.567(293)
S1Ni1N8	99.254(235)	N1Ni1N9	96.672(244)	S4Ni4N17	160.131(222)	N4Ni4N18	160.138(322)
S1Ni1N9	162.389(192)	N1Ni1N27	89.456(299)	S4Ni4N18	95.216(252)	N4Ni4017	97.042(376)
							67.202(498)
S1Ni1N27	88.406(253)	N7Ni1N8	88.141(284)	S4Ni4017	91.162(288)	N16Ni4N17	98.013(284)
					79.153(483)		
N7Ni1N9	93.822(284)	S2Ni2N2	66.735(170)	N16Ni4N18	92.482(335)	S5Ni5N5	66.560(203)
					162.255(356)		
N7Ni1N27	175.194(305)	S2Ni2N10	92.373(166)	N16Ni4017	167.701(483)	S5Ni5N19	93.974(229)
N8Ni1N9	87.058(336)	S2Ni2N11	164.866(188)	N17Ni4N18	96.394(307)	S5Ni5N21	84.384(211)
					77.442(357)		
N8Ni1N27	97.339(281)	S2Ni2N12	99.105(175)	N17Ni4017	83.049(536)	S5Ni5N80	99.938(226)
N9Ni1N27	86.587(306)	S2Ni2N25	86.059(205)	N18Ni4017	71.258(401)	S5Ni5N81	162.046(191)
					99.592(549)		
N2Ni2N10	93.255(246)	N10Ni2N12	88.576(249)	N5Ni5N19	96.190(308)	N19Ni5N80	87.048(314)
N2Ni2N11	99.176(241)	N10Ni2N25	178.322(264)	N5Ni5N21	87.457(314)	N19Ni5N81	93.463(281)

N2N̄1N̄2N̄12	165.771(247)	N11N̄1N̄2N̄12	94.766(257)	N5N̄5N̄5N̄80	166.249(266)	N21N̄1N̄5N̄80	88.631(318)
N2N̄1N̄2N̄25	85.580(269)	N11N̄1N̄2N̄25	87.383(282)	N5N̄5N̄5N̄81	96.395(273)	N21N̄1N̄5N̄81	89.447(279)
N10N̄1N̄2N̄11	94.00(26)	N12N̄1N̄2N̄25	92.258(271)	N19N̄1N̄5N̄21	175.047(311)	N80N̄1N̄5N̄81	96.744(277)
S3N̄3N̄3N̄3	68.015(183)	N3N̄3N̄3N̄13	100.746(268)	S6N̄6N̄6N̄6	66.009(169)	N6N̄6N̄6N̄20	89.261(247)
S3N̄3N̄3N̄13	97.647(210)	N3N̄3N̄3N̄14	158.902(277)	S6N̄6N̄6N̄20	87.310(171)	N6N̄6N̄6N̄22	94.389(268)
S3N̄3N̄3N̄14	94.594(215)	N3N̄3N̄3N̄15	96.458(271)	S6N̄6N̄6N̄22	94.219(204)	N6N̄6N̄6N̄23	163.756(247)
S3N̄3N̄3N̄15	160.761(216)	N3N̄3N̄3O1	79.919(246)	S6N̄6N̄6N̄23	97.935(175)	N6N̄6N̄6N̄24	97.922(239)
S3N̄3O1	86.628(181)	N13N̄3N̄3N̄14	93.123(290)	S6N̄6N̄6N̄24	162.482(179)	N20N̄6N̄6N̄22	176.350(266)
N13N̄3N̄3N̄15	96.385(291)	N14N̄3O1	87.468(271)	N20N̄6N̄6N̄23	87.439(250)	N22N̄6N̄6N̄24	93.953(270)
N13N̄3O1	175.618(270)	N15N̄3O1	79.233(270)	N20N̄6N̄6N̄24	87.474(251)	N23N̄6N̄6N̄24	97.666(250)
N14N̄3N̄3N̄15	97.719(296)			N22N̄6N̄6N̄23	89.067(271)		

Different from the other complexes, complex **3-4** that was prepared using the bidentate tetramethyl ethylene diamine ligand is hexanuclear. It crystallizes in the space group $P31c$ (see Table A 5). A cage-like molecular structure was obtained (Figure III.5), containing three TTC bridging ligands, six Ni(II) ions and six TMEDA capping ligands, and one carbonate ion. Six Ni-TMEDA species are connected by three TTC bridge ligands and one carbonate ion. The complex has a three-fold symmetry axis perpendicular the carbonate leading to two types of Ni(II) in the molecular structure: Ni1 and Ni2. Ni1 ions are hexa-coordinated with two N atoms from TEMDA capping ligand, one S atom and one N atom from TTC, one O atom from carbonate ion and one O from water molecule. For Ni2 ions, they are also hexa-coordinated, however, their coordination atoms are two S atoms and two N atoms from two TTC ligands and one capping ligand. The SHAPE analysis results confirm their octahedral coordination geometry (details in Table III.8), and the one of Ni2 is slightly more distorted.

The information about the bond lengths involved Ni-TTC bridge ligands are listed in the Table III.6. We can find that the Ni1-S1 is the longest (2.5008 Å) among all the Ni-S bonds (2.4714 Å for bond Ni2-S2 and 2.4518 Å for bond Ni2-S3), and the Ni1-N1 (TTC) bond is the shortest (2.0600 Å) among all the Ni-N bonds (2.0871 Å for Ni2-N2 and 2.1506 Å for Ni2-N3). For the angles (see Table III.9), $S1N̄1N̄1$ (67.489°), is smaller than the ones with Ni2 (68.299° for $S2N̄1N̄2$ and 68.430° for $S3N̄1N̄3$).

In the molecular structure of complex **3-4**, some unknown solvent molecules were detected in the structure, but too disordered to model. Therefore, the solvent contributions to the scattering have been removed by the SQUEEZE procedure²¹ in PLATON.²² SQUEEZE calculated a void volume of approximately 402 Å³, occupied by 201 electrons per unit cell, which points to the presence of solvent molecule per formula unit.

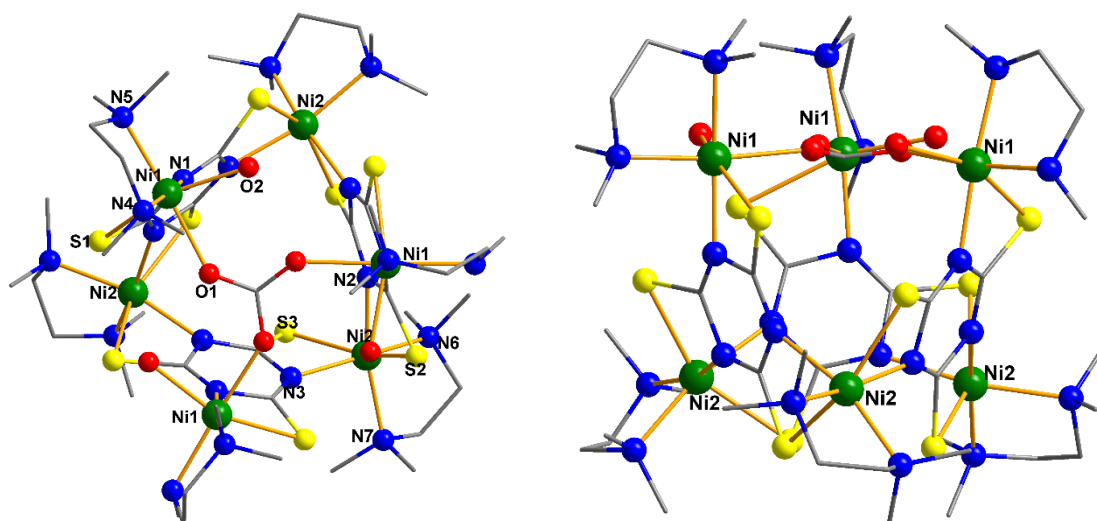


Figure III.5 View of the structure of complex **3-4** (left) perpendicular and (right) along the pseudo three fold axis of the molecule. Perchlorate anion, methanol molecules and H atoms are omitted for clarity.

Table III.8 Shape analysis of six-coordinate geometry in complex **3-4**.

Label	JPPY	TPR	OC	PPY	HP
Symmetry	C_{5v}	D_{3h}	O_h	C_{5v}	D_{6h}
Ni1	25.793	11.918	2.376	22.092	29.693
Ni2	26.654	9.862	3.641	22.601	31.057

Abbreviation: JPPY - Johnson pentagonal pyramid J2, TPR – Trigonal prism, OC – Octahedron, PPY – Pentagonal pyramid, HP – Hexagon.

Table III.9 Some relevant Ni-ligand angles (°) for Complex **3-4**.

Complex 3-4					
$S1\widehat{Ni}1N1$	67.489(657)	$N1\widehat{Ni}1N4$	174.242(922)	$N4\widehat{Ni}1O1$	88.329(797)
$S1\widehat{Ni}1N4$	106.909(729)	$N1\widehat{Ni}1N5$	94.095(897)	$N4\widehat{Ni}1O2$	90.977(906)
$S1\widehat{Ni}1N5$	97.711(735)	$N1\widehat{Ni}1O1$	92.227(759)	$N5\widehat{Ni}1O1$	173.498(845)
$S1\widehat{Ni}1O1$	83.319(595)	$N1\widehat{Ni}1O2$	94.773(800)	$N5\widehat{Ni}1O2$	99.664(902)
$S1\widehat{Ni}1O2$	155.993(507)	$N4\widehat{Ni}1N5$	85.229(932)	$O1\widehat{Ni}1O2$	81.296(774)

$S2\overline{Ni2N2}$	68.299(677)	$N2\overline{Ni2S3}$	92.016(737)	$S3\overline{Ni2N6}$	98.385(684)
$S2\overline{Ni2S3}$	151.086(255)	$N2\overline{Ni2N3}$	92.484(918)	$S3\overline{Ni2N7}$	102.747(640)
$S2\overline{Ni2N3}$	90.679(596)	$N2\overline{Ni2N6}$	94.955(877)	$N3\overline{Ni2N6}$	165.109(895)
$S2\overline{Ni2N6}$	104.054(643)	$N2\overline{Ni2N7}$	165.232(854)	$N3\overline{Ni2N7}$	92.635(852)
$S2\overline{Ni2N7}$	97.796(672)	$S3\overline{Ni2N3}$	68.430(66)	$N6\overline{Ni2N7}$	83.357(853)

3.3.1.3 Molecular structure of Complex 3-5

Below is the symmetrical molecular structure of complex **3-5** reported in the literature¹⁸ (Figure III.6, left). All the Ni(II) ions are penta-coordinated with TTC bridge ligand and one pmdien capping ligand. The coordination geometry can be described as deformed trigonal bipyramid. Since the failure in crystallization, powder X-ray diffraction was carried out on the powder product we obtained. The comparison of pattern of **3-5** powder and calculated pattern from literature (**CCDC 676655**) confirms that they are the same compound (Figure III.6, right). Detailed information can be found in the literature.¹⁸

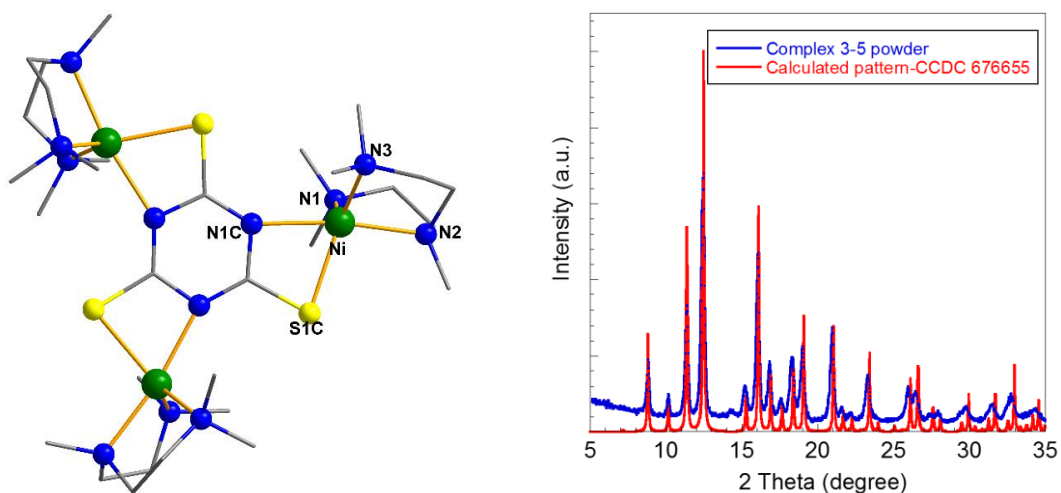


Figure III.6 Left: Crystal structure of complex **3-5** in literature.¹⁸ Perchlorate anion and H atoms are omitted for clarity. Right: PXRD pattern of complex **3-5** powder.

3.3.2 Magnetism

Measurements of dc magnetic susceptibilities (χT) have been conducted on complexes **3-1** to **3-5** in the temperature range of 300 - 2 K and in the magnetic field of 1 T. The magnetization vs. the applied magnetic field have been measured in the field 0 – 6 T and

under several temperature conditions. The data were corrected for the diamagnetic contribution of the sample holder and eicosane.

3.3.2.1 Magnetic properties of Complex 3-1 and 3-2

The thermal variation of the molar magnetic susceptibility (χT) for complexes **3-1** and **3-2** are plotted in Figure III.7. The shape of the curves show that χT has the similar behavior for these two complexes.

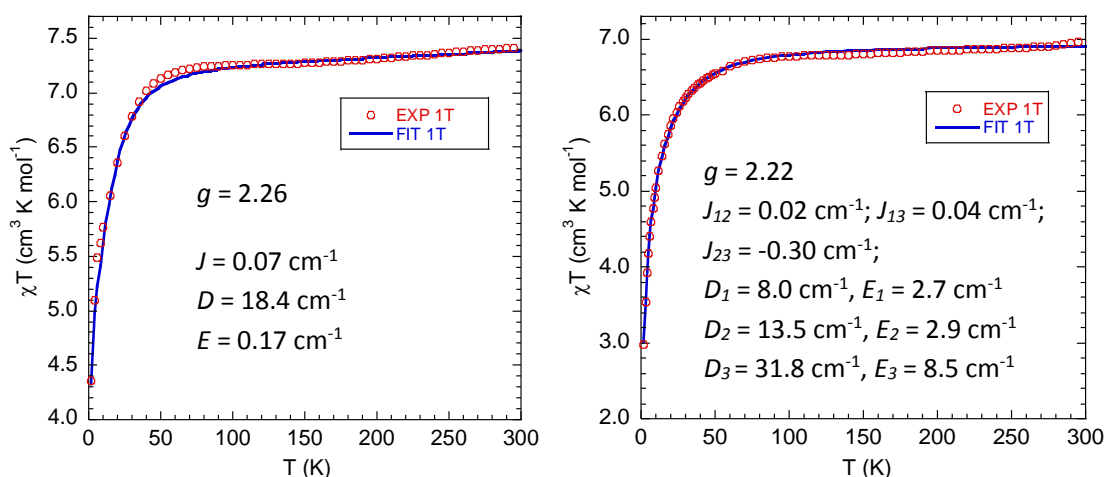
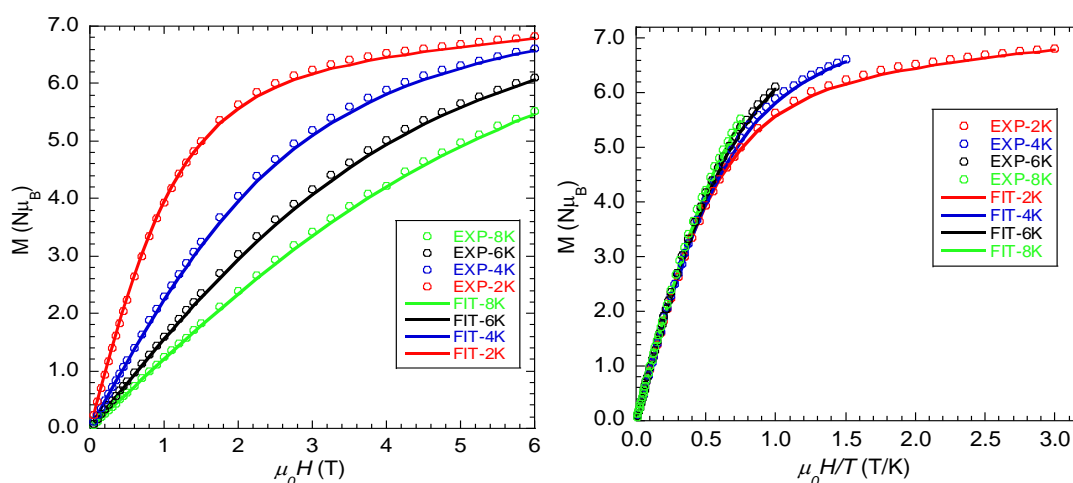
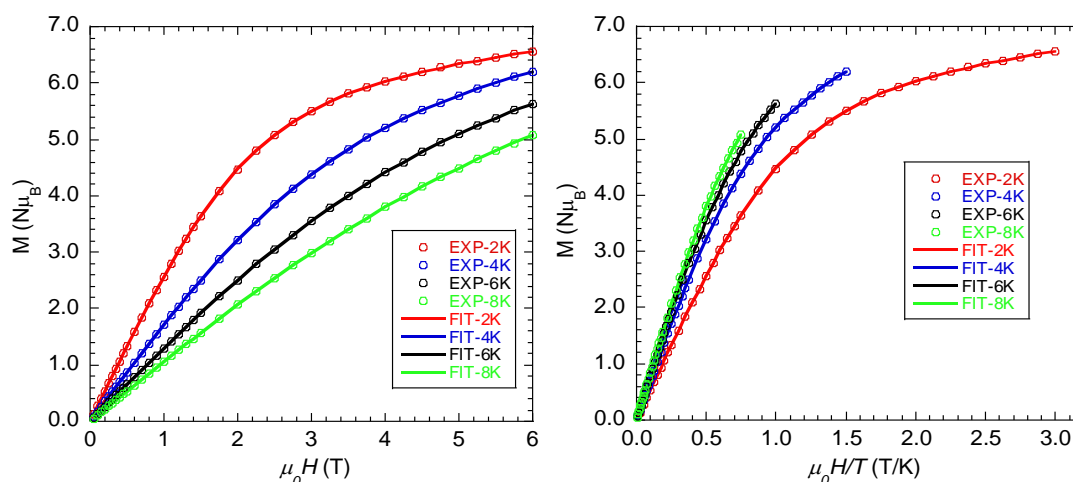


Figure III.7 Temperature dependence of the χT product for complexes **3-1** (left) and **3-2** (right)

The χT product is constant from ca. 70 K to room temperature for both complexes. χT is equal to 7.3 and 6.6 cm³ mol⁻¹ K at room temperature for complex **3-1** and **3-2** respectively. The computed g -values considering a $S = 3/2$ spin moment are equal to 2.26 and 2.22 for **3-1** and **3-2** respectively. Upon cooling, the χT values decrease and reach, at $T = 2$ K, 4.36 and 2.97 cm³ mol⁻¹ K for **3-1** and **3-2** respectively, which is the result of the presence of ZFS and probably some antiferromagnetic exchange coupling through the TTC bridge.

Figure III.8 Magnetization vs. μ_0H (left) and vs. μ_0H/T (right) at variable temperatures for **3-1**.Figure III.9 Magnetization vs. μ_0H (left) and vs. μ_0H/T (right) at variable temperatures for **3-2**.

The magnetization vs. the applied magnetic field at variable temperatures for complexes **3-1** and **3-2** are plotted in the form of $M = f(\mu_0H)$ and $M = f(\mu_0H/T)$ in Figure III.8 and Figure III.9. Similar behaviors are displayed for these two complexes.

For complex **3-1**, the magnetization reaches the maximum (around $6.82 \mu_B$) at $T = 2$ K and $\mu_0H = 6$ T. The saturated magnetization for three $S = 3/2$ possessing $g = 2.26$ and no ZFS or antiferromagnetic coupling is equal $10.17 \mu_B$ ($M_{sat} = g * S$ in the unit of Bohr Magneton). The behavior is also observed for complex **3-2**.

To quantify the magnitude of the ZFS parameters for the two complexes, we fitted the magnetic data with the spin Hamiltonian $\hat{H} = \sum_i g_i \mu_B \hat{S}_i \cdot \vec{H} + \sum_i D_i \left[\hat{S}_{iz}^2 - \frac{S_T(S_T+1)}{3} \right] + \sum_i E (\hat{S}_{ix}^2 - \hat{S}_{iy}^2) + (-2J_{ij} \cdot \sum_{i,j} \hat{S}_i \cdot \hat{S}_j)$ for $S = 3/2$ where \hat{S}_i , \hat{S}_{ix} , \hat{S}_{iy} , \hat{S}_{iz} are the local spin operators, \vec{H} is the applied dc magnetic field vector, g the Landé factor, μ_B the Bohr Magneton, J_{ij} the exchange coupling parameter, D_i and E_i the local axial and rhombic ZFS parameters, respectively. When the metal ions are not related by a symmetry axis, one must thus fit using local ZFS and three different exchange coupling parameters. In order to simplify the procedure and because the coordination spheres of the metal ions are not very different, we first try to fit with one local axial ZFS parameter D ($= D_1 = D_2 = D_3$), the same for the E parameter. We also, first, assume, one exchange parameter. If, it is not possible to reach a good fit with these approximations, we introduce different D values and exchange coupling parameters by examining the structure, in order to minimize their number. But when the metal ions are related by a symmetry axis as for complex **3-1**, only one D , E and J parameters are present. For **3-1**, there are two different trinuclear complexes, so ideally there should be a set of parameters for each, but the coordination sphere of the metal ions is very close, we thus performed the fit for one set of D , E and J parameters for compound **3-1**. The best fit of the data leads to D and E values equal to 18.4 and 0.17 cm^{-1} respectively and $J = 0.07 \text{ cm}^{-1}$, referring to a very weak ferromagnetic coupling between the Co(II) ions. The very weak value of the exchange coupling parameter is expected, and it is found to be ferromagnetic. However, the coupling may well be antiferromagnetic with slightly different ZFS parameters. We did not explore the different possibilities, but we will further comment this value together with the ZFS values in the theoretical section.

For complex **3-2**, the three Co(II) ions have different coordination spheres and the best fit leads to three different ZFS and three different exchange coupling parameters. The ZFS parameters are equal to 8.0 cm^{-1} , 13.5 cm^{-1} and 31.8 cm^{-1} for D values corresponding to Co1, Co2 and Co3, and the corresponding E values are 2.65 cm^{-1} , 2.95 cm^{-1} and 8.50 cm^{-1} , respectively. The magnetic coupling between Co1 and Co2 is 0.02 cm^{-1} (J_{12}), 0.04 cm^{-1} for Co1 and Co3 (J_{13}), and -0.30 cm^{-1} for the interaction between Co2 and Co3 (J_{23}).

3.3.2.2 Magnetic properties of Complex 3-3 and 3-4

The temperature dependence of the molar magnetic susceptibility (χT) for complex **3-3** and **3-4** are plotted in Figure III.10. The curves show a similar behavior of χT for the two complexes.

For complex **3-3**, the χT product is constant between 115 K to room temperature, with a value equal to $3.75 \text{ cm}^3 \text{ mol}^{-1} \text{ K}$ at room temperature corresponding to three $S = 1$ species with $g = 2.34$. Upon cooling, χT decreases and reaches a value of $0.57 \text{ cm}^3 \text{ mol}^{-1} \text{ K}$ at $T = 2$ K. For **3-4**, χT is equal to $6.93 \text{ cm}^3 \text{ mol}^{-1} \text{ K}$ at room temperature corresponding to six $S = 1$ species with $g = 2.20$. Upon cooling, χT decreases slightly more rapidly than the previous trinuclear complex.

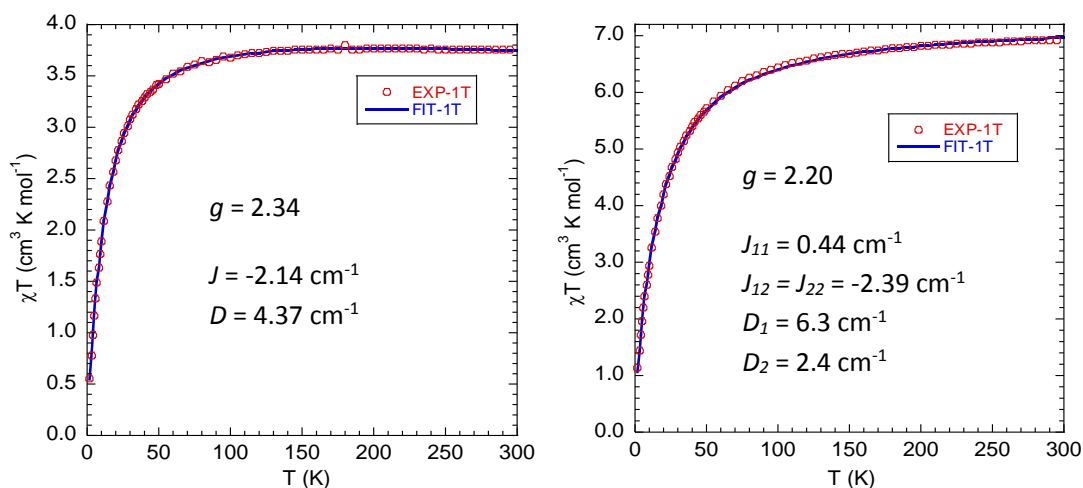
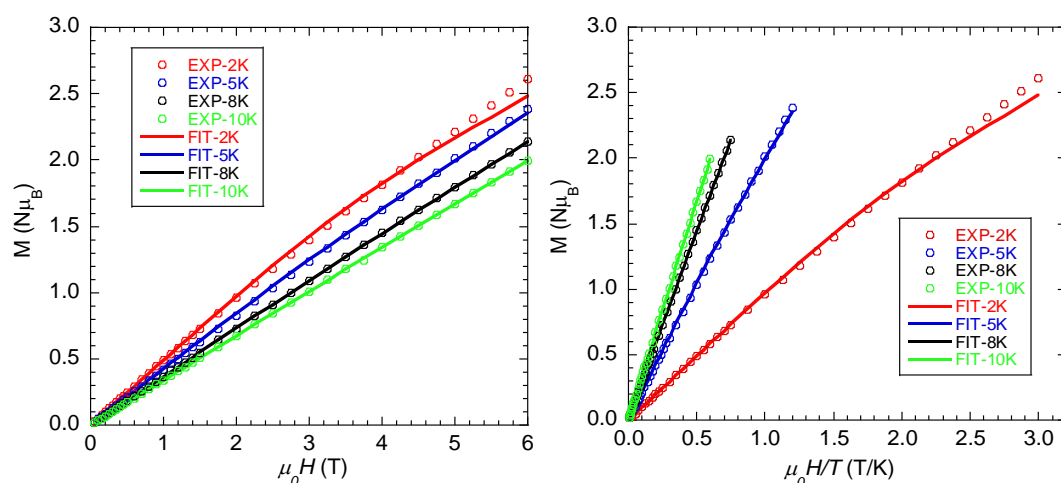
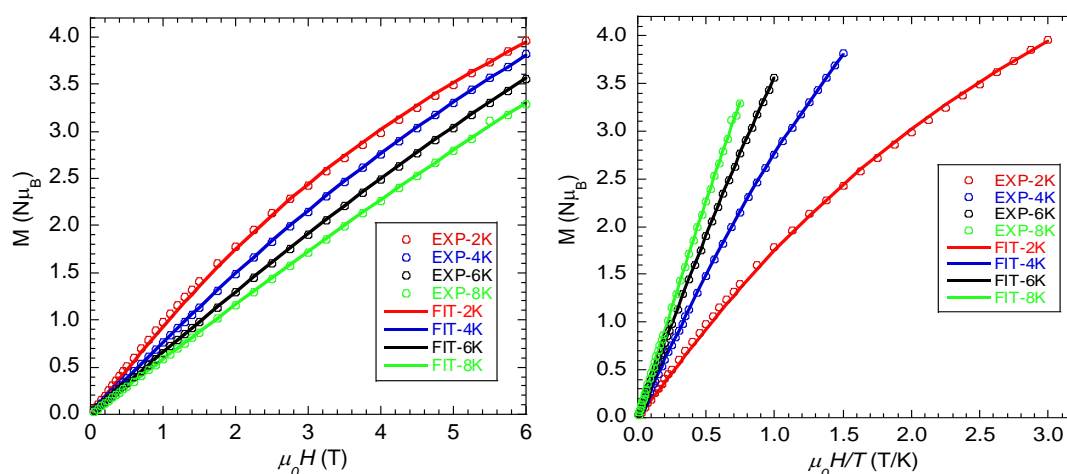


Figure III.10 Temperature dependence of the χT product for complexes **3-3** (left) and **3-4** (right).

The magnetization vs. the applied magnetic field at different temperatures for complexes **3-3** and **3-4** are plotted in the form of $M = f(\mu_0 H)$ and $M = f(\mu_0 H/T)$ in Figure III.11 and Figure III.12. Similar behavior is displayed for these two complexes. The magnetization values at saturation are lower than those expected for the three and six $S = 1$ species in the absence of ZFS.

Figure III.11 Magnetization vs. μ_0H (left) and vs. μ_0H/T (right) at variable temperatures for **3-3**.Figure III.12 Magnetization vs. μ_0H (left) and vs. μ_0H/T (right) at variable temperatures for **3-4**.

Despite the different geometries of the three Ni(II) ions in **3-3**, the data could be fitted with one D and one J parameters: $D = 3.37 \text{ cm}^{-1}$ and $J = -2.14 \text{ cm}^{-1}$ illustrating a relatively weak antiferromagnetic coupling between the Ni(II) ions, but much larger than for the Co-containing complexes. For **3-4**, because of the three-fold symmetry of the complex, two ZFS (D_1 and D_2) and three exchange coupling parameters (J_{11} , J_{12} and J_{22}) are needed. J_{11} , and J_{22} correspond to the exchange coupling parameters among the three Ni1 through the carbonate bridge and the three Ni2 through the TTC bridge, while J_{12} expresses the coupling between Ni1 and Ni2 through the TTC bridge (see coupling scheme in Figure III.13).

In order to minimize the number of parameters to be fitted, we assumed $J_{22} = J_{12}$. The best fit leads to $D_1 = 6.3 \text{ cm}^{-1}$ and $D_2 = 2.4 \text{ cm}^{-1}$; and $J_{11} = 0.44 \text{ cm}^{-1}$ and $J_{12} = J_{22} = -2.39 \text{ cm}^{-1}$. It is worth noting that the exchange coupling parameters between the Ni ions bridged by the TTC ligands are very close for the two complexes. The ZFS parameters are relatively weak as expected from the octahedral geometry of the metal ions. Their nature (negative and positive sign) can only be understood by analyzing the results of theoretical calculations.

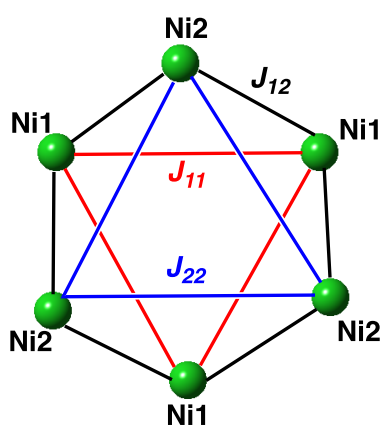


Figure III.13 Scheme of exchange coupling interactions of **3-4**.

3.3.2.3 Magnetic properties of Complex 3-5.

As stated above, this complex was our first target and we discovered that it was already reported. But the reported magnetic data did not correspond to what one may expect from the crystal structure. We, thus, decided to investigate its behavior for two reasons: (i) it has the structure that we think is the best suited to have a large negative D value for the Ni(II) ions and the coupling is expected to be very weak and (ii) understand the published magnetic data. But, as mentioned above, we did not succeed to grow a single crystal suitable for structural studies. Instead, we obtained another complex (already reported) made from 7 Ni(II) ions. We, thus, performed the study on a powder whose PXRD pattern correspond to the trinuclear complex (Figure III.6).

The dc magnetic susceptibility measurement was carried out from 2 K to 300 K at $B = 1 \text{ T}$. The temperature dependence of the molar magnetic susceptibility (χT) is plotted in Figure III.14, left. it corresponds to the expected curve for a trinuclear Ni(II) complex. The data from the literature (Figure III.14, right) have the same behavior at high temperature when

one observes that χT slightly decreases upon cooling. But, around 20 K χT increases and then decreases (the authors used the reduced $\chi T/C_0$, where $C_0 = N_A \mu_0 \mu_B^2 / k_B$).

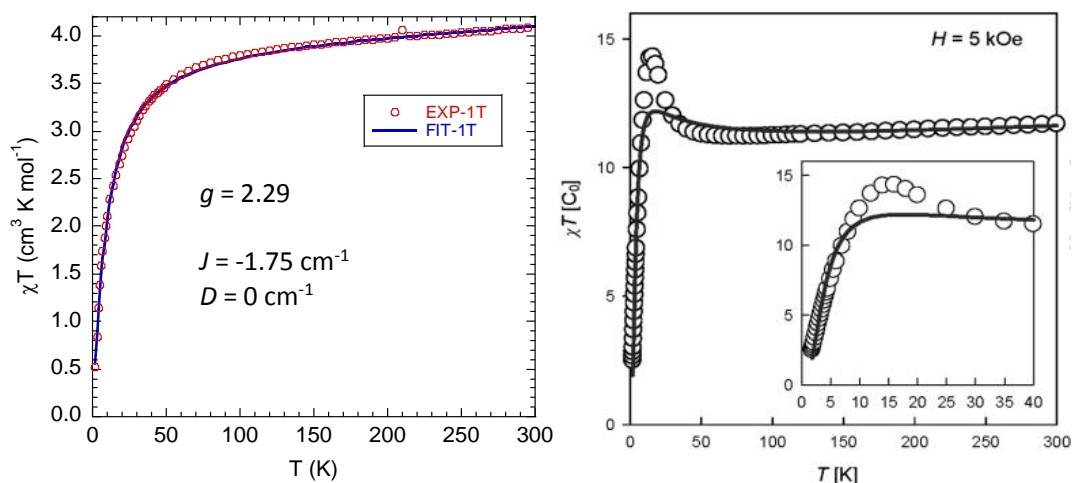


Figure III.14 Left: temperature dependence of the χT product for complexes **3-5**; Right: Product function in literature. Reproduced with permission from reference [18].¹⁸

The magnetization vs. the applied magnetic field at $T = 2$ K for complex **3-5** are plotted in the form of $M = f(\mu_0 H)$ in Figure III.15: left is our result and the right from literature. The two magnetization curves are similar and have an inflexion point. The main difference comes from the behavior at weak fields. The data from the literature were fitted considering a ferromagnetic coupling among the Ni(II) ions and antisymmetric exchange with the following values $g = 2.40$; $J = +3.31 \text{ cm}^{-1}$; $D = 17.1 \text{ cm}^{-1}$ for the anisotropy model; and $g_x = 1.265$; $g_z = 2.009$; $J = +1.67 \text{ cm}^{-1}$; $d_z = 4.95 \text{ cm}^{-1}$ for the antisymmetric exchange model (d_z is the single antisymmetric exchange parameter). But, the bump in the χT curve could not be reproduced.

It is possible to fit our data with $J = -1.75 \text{ cm}^{-1}$ and $D = 0$. The J value reproduces the inflexion point of the magnetization curve but not the value of the magnetization at higher fields. An inflexion point in the magnetization curve is expected because a $S = 0$ ground state is expected from the antiferromagnetic coupling among the three Ni(II) ions. When the coupling is weak, the first excited state $S = 1$ is close in energy and can be populated upon increasing the magnetic field. If the ZFS parameter is introduced, it is not possible to reproduce the magnetic data, which is strange because the geometry of the Ni(II) ions is

trigonal bipyramidal as for the complexes reported in the previous chapter where the ZFS parameter is negative and very large.

In summary, we do not succeed to fit the magnetic data may be because the powder has an impurity that cannot be detected by XRPD because it is amorphous, as it is unexpected to not be able to reproduce the data for such simple trinuclear complex that possess a three-fold symmetry axis and thus one D and J values.

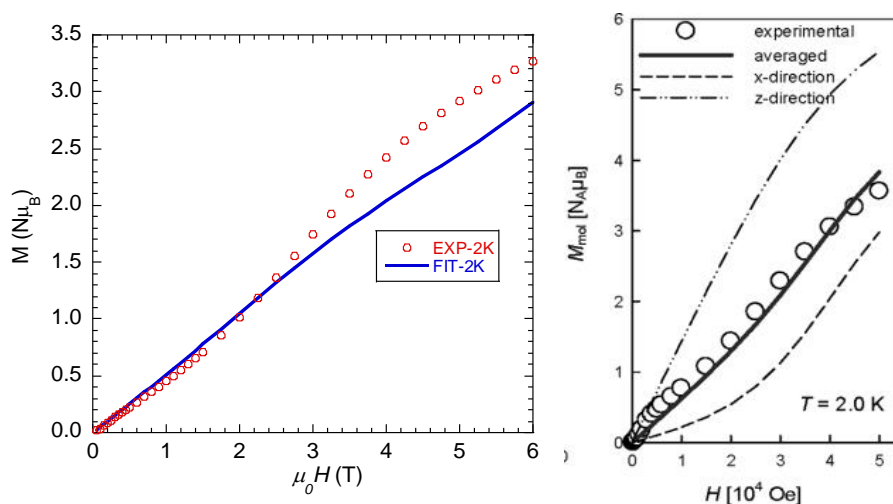


Figure III.15 Field dependent magnetization at variable temperatures for complexes **3-5** (left), and in literature (right). Reproduced with permission from reference [18].¹⁸

3.4 Theoretical Calculations

3.4.1 Theoretical studies for Complexes **3-1** and **3-2**

In order to analyze the origin of the ZFS within the trinuclear complexes, its magnitude and its sign, we carried out theoretical wave function-based calculations at the CASSCF and then when necessary at the NEVPT2 levels using the ORCA package. The calculations of the ZFS are made on the mononuclear species only and not on the whole complex because the size of the molecules is too large. When the mononuclear moieties are related by symmetry as in the case of complex **3-1**, it is sufficient to perform the calculation on one species. When no symmetry is present, the calculations are performed on the three different moieties as for **3-2**. We also calculated when possible the exchange coupling

parameters at different levels, using Density Functional Theory and also WF based theory when possible.

The results of the calculations made on the Co(II) moiety of complex **3-1** at the NEVPT2 level give the following ZFS values: $D = 25.9 \text{ cm}^{-1}$ and $E = 3.1 \text{ cm}^{-1}$. The agreement with the D value extracted from the fit of the magnetic data ($D = 18.4 \text{ cm}^{-1}$) is fair but the E value is larger (0.17 cm^{-1}). One possible reason is the presence of an exchange coupling that is not taken into account in the calculations. In order to analyze the sign and the magnitude of the ZFS parameters, we will consider the different electronic states and their contribution to ZFS and then, we will analyze the wavefunction of each state to understand the origin of its contribution. Figure III.16 and Table III.10 give the energy of the first five quartet states before spin-orbit coupling that contribute to the overall ZFS D value and the composition of the wavefunctions after considering SOC for each electronic state. Among the five quartet states, three have a large contribution (Q_1 , Q_3 and Q_4). Q_1 have a negative contribution of -5 cm^{-1} , while Q_3 and Q_4 have larger (in absolute values) positive contributions of 14.7 and 10.5 cm^{-1} .

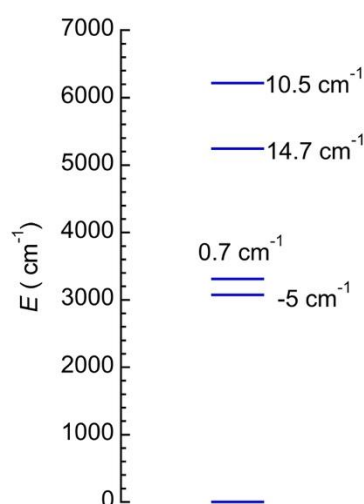


Figure III.16 Energy of the electronic states before SOC for the Co(II) moiety of complex **3-1** and contribution of each state to the overall D value after considering SOC.

Table III.10 Energy of the electronic states before SOC for the Co(II) moiety of complex **3-1**, contribution of each state to the overall D value after considering SOC and composition of the wavefunction of each state.

States	E (cm ⁻¹)	Contribution to D (cm ⁻¹)	Wavefunction composition
Q ₀	0	0	74% dz ² dx ² -y ² dxy / 11% dz ² dxzdyz / 11% dz ² dxydxz
Q ₁	3074	-5	64% dz ² dxydyz / 30% dz ² dx ² -y ² dxz
Q ₂	3312	0.69	
Q ₃	5244	14.7	50% dz ² dx ² -y ² dyz / 23% dxydx ² -y ² dxz / 20% dz ² dxydxz
Q ₄	6215	10.5	54% dz ² dx ² -y ² dxz / 24% dxydx ² -y ² dyz / 20% dz ² dxydyz
Q ₅	14829	0.12	

The ligand field orbitals are depicted in Figure III.17. They correspond to what is expected for a trigonal geometry that is slightly distorted leading to a slight energy difference within the xz, yz and the xy, x²-y² orbitals of 849 and 1060 cm⁻¹ respectively.

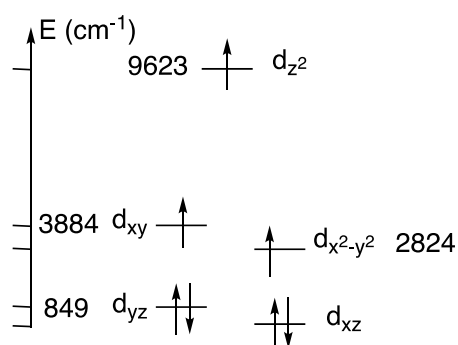


Figure III.17 Lift of the degeneracy of the d orbitals of the Co(II) moiety in complex **3-1**.

In order to rationalize the sign of D for each electronic state, we can analyze the composition of their wavefunctions made from linear combination of the different Slater determinants based of the ligand orbitals (Table III.10) and expressed in Figure III.18.

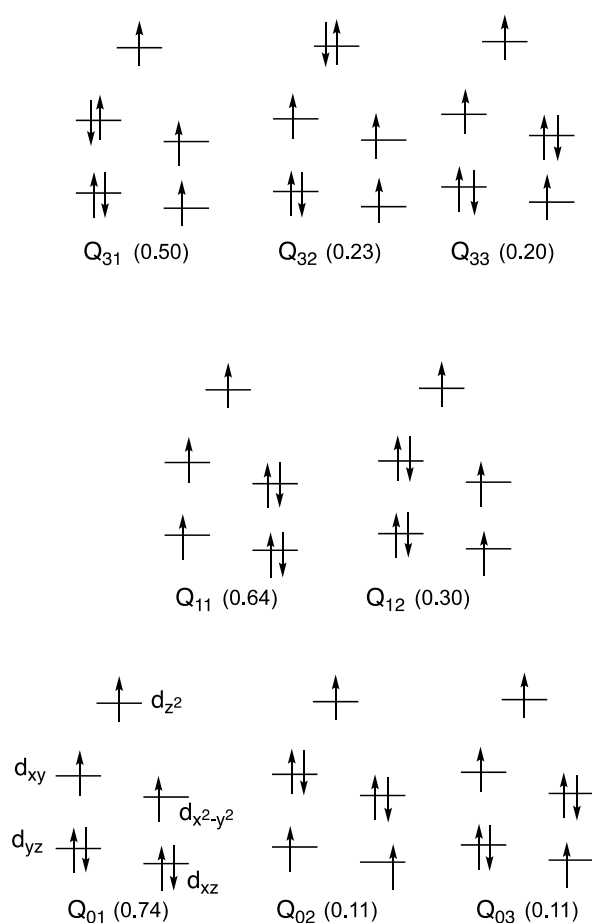


Figure III.18 Composition of the wavefunctions of the quintet electronic states Q_0 , Q_1 and Q_3 . The composition of the Q_4 state is not drawn because it is similar to that of Q_3 and have thus a similar contribution.

The coupling between Q_0 and Q_1 through the SOC operator correspond to excitations between the Slater determinants of Q_0 and Q_1 . One observes that the excitation from Q_{01} and Q_{02} to Q_{11} and Q_{12} involve orbitals with different m_l values (from (xz, yz) to (xy, x^2-y^2)), which as explained in the previous chapter give positive contributions to D . The excitation between Q_{03} and Q_{11} and Q_{12} involve orbitals possessing the same m_l values leading to a negative contribution to D . These qualitative arguments do not allow to rationalize the sign of D of Q_1 but demonstrate that D cannot be large, because it is the result of positive and negative contributions. The full calculations show that it is negative but weak (-5 cm^{-1}). When considering the excitations between Q_0 and Q_3 , one observes that apart from one (Q_{03} to Q_{31}), they all involve orbitals with different m_l values thus contributing positively to D . The effect of Q_4 is similar to Q_3 . Therefore, the overall D value is due to the opposite

contribution of the excited states and in this case the positive contributions are the dominant one. It is worth noting that for the strictly C_{3v} symmetrical complexes $[\text{Co}(\text{Me}_6\text{tren})\text{X}]^{2+}$ ($\text{X} = \text{Cl}, \text{Br}, \text{NCS}, \text{N}_3$), the negative contribution of the first excited state is the dominant one and the overall D value was always found to be negative.^{23,24} The main difference with the symmetrical case is the composition of the first excited state Q_1 wavefunction that has Slater determinants equivalent to Q_{03} that brings negative contributions to D and that are absent in the Q_1 of the present complex. Therefore, in order to have an overall negative D value in trigonal bipyramid complexes, the first excited state must have a large negative contribution and this contribution is largest when the symmetry is as close as possible to C_{3v} . Keeping a symmetry close to C_{3v} is difficult to achieve in the present case because the bite angle of the TTC^{3-} ligand is too weak (70°) (Figure III.19, the pseudo three-fold axis is along the N1Co1N3 direction) instead of 98° and 103° for N1Co1N2 and N1Co1N4 that brings the sulfur atom out the equatorial plane of the pseudo trigonal bipyramid geometry and thus reduces the symmetry of the complex.

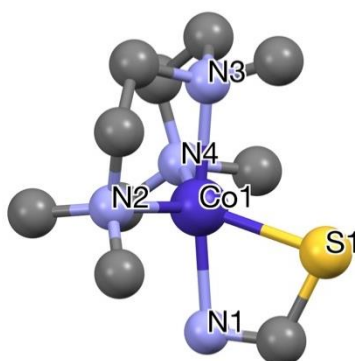


Figure III.19 Scheme of the geometry around the Co moiety showing the weak N1Co1S1 bite angle of the TTC^{3-} bridge of complex **3-1**; the pseudo three-fold axis is along the N1Co1N3 direction.

The calculations give directly the orientation of the \mathbf{D} tensor relatively to the molecular frame as depicted in Figure III.20. The z axis (blue) is oriented very close to the pseudo three-fold axis of the Co moiety and because the three-fold axis of the molecules, the axes of three tensors lie in the same plane as the TTC^{3-} ligand.

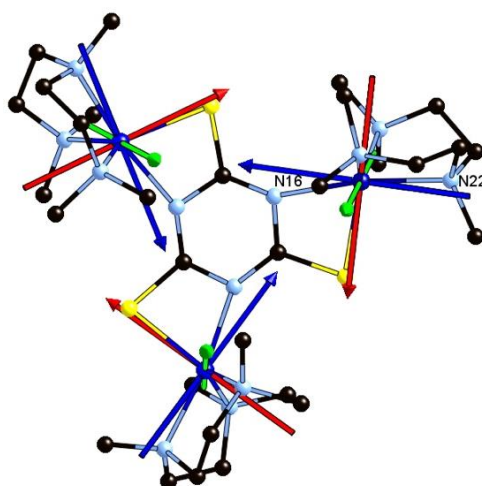


Figure III.20 Orientation of **D** tensor axes; x (red), y (green) and z (blue), the N22CoN16 direction correspond to the pseudo three-fold axis of the Co moiety.

The exchange coupling parameter was calculated considering a dinuclear Co(II) species using broken symmetry DFT and WF-based methods. Depending on the type of calculations ferro- or antiferromagnetic exchange coupling interaction are found but always with values lower than 0.05 cm^{-1} . It is, therefore, not possible to conclude on the nature of the exchange interaction apart that it is very weak.

The calculations for complex **3-2** where the Co(II) ions are in octahedral give following values for the three Co ions: Co1 ($D_1 = 6.9 \text{ cm}^{-1}$, $E_1 = 0.9 \text{ cm}^{-1}$, $E/D = 0.13$), Co2 ($D_2 = 11.6 \text{ cm}^{-1}$, $E_2 = 1.6 \text{ cm}^{-1}$, $E/D = 0.22$), Co3 ($D_3 = 35.1 \text{ cm}^{-1}$, $E_3 = 7.3 \text{ cm}^{-1}$, $E/D = 0.21$). Despite the octahedral geometry, the ZFS is relatively axis since E/D is smaller than 0.33. The calculated values are in good agreement with those extracted from fitting the magnetic data : Co1 ($D_1 = 8.0 \text{ cm}^{-1}$, $E_1 = 2.7 \text{ cm}^{-1}$), Co2 ($D_2 = 13.5 \text{ cm}^{-1}$, $E_2 = 2.9 \text{ cm}^{-1}$), Co3 ($D_3 = 31.8 \text{ cm}^{-1}$, $E_3 = 8.5 \text{ cm}^{-1}$, $E/D = 0.21$). The examination of the energy of the states before spin orbit coupling and their contribution to ZFS (after considering the spin orbit effect) (Table III.11) show that the first two excited states contribute positively to D while the third (fourth for Co3) contribute negatively. The negative contributions are not very different (see Table III.11). The origin of the difference between the ZFS values of Co1 and Co2 on one hand and Co3 on the other hand is the larger positive contribution to D of the first two excited states for the latter than for the formers. This larger positive contribution of the two first excited

states of Co3 is due to the smaller energy separation with the ground state (1682 and 2019 cm^{-1}), while for Co1 and Co2 this separation is 4150 and 5472 cm^{-1} and 3384 and 4535 cm^{-1} respectively. The more the excited states are close to the ground state the larger their contribution to D are, which is the case here.

Table III.11 Energy (cm^{-1}) of the first 5 quintet states for the three Co(II) ions before spin orbit coupling, contribution of each state to the axial ZFS parameter D and values of the ZFS parameters D and E .

Species	State	Energy	Contribution to D (cm^{-1})	D (cm^{-1})	E (cm^{-1})
Co1	Q0	0.0	0	6.9	0.9
	Q1	4149.9	11.2		
	Q2	5472	7.0		
	Q3	8398.1	-13.9		
	Q4	10262.4	2.7		
	Q5	12112.7	0.2		
Co2	Q0	0.0	0.0	11.6	1.6
	Q1	3384.5	13.2		
	Q2	4535.7	7.4		
	Q3	8920.4	-12.1		
	Q4	10324.2	2.2		
	Q5	12040.9	0.7		
Co3	Q0	0,0	0	35.1	7.3
	Q1	1682.1	19.2		
	Q2	2018.9	17.1		
	Q3	10212.4	1.6		
	Q4	10228.1	-9.3		
	Q5	11771.2	2.1		

We will not analyze the composition of the wavefunctions as for **3.1**, the interpretation being the same. Here the axes of the \mathbf{D} tensors (Figure III.21) are not oriented along the Co-ligand directions apart for Co3 where the y direction of the tensor is close to the pyridine-Co-pyridine direction as depicted in Figure III.22.

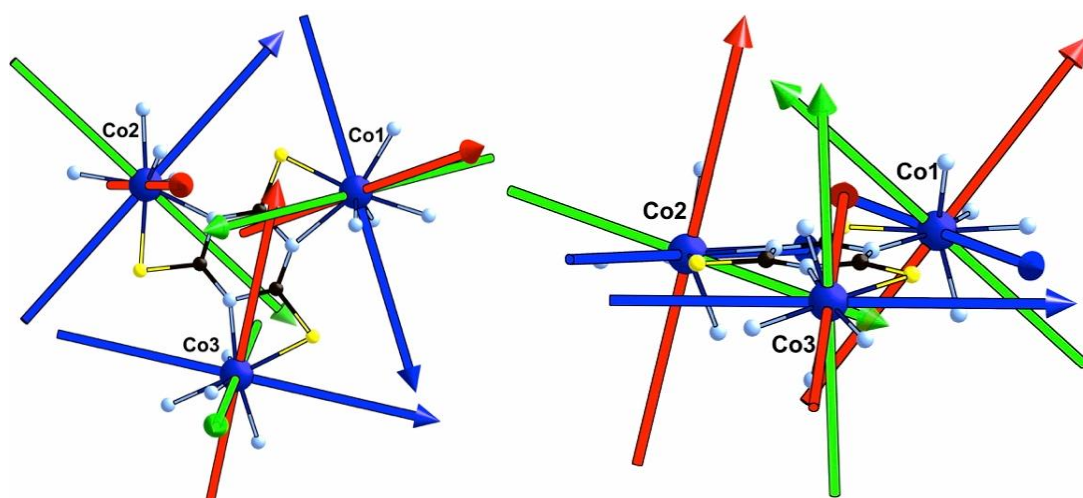


Figure III.21 Relative orientation of the **D** tensor axes for the three metal ions; (left) the bridging ligand lies in the plane of the page and (right) the bridging ligand is perpendicular to the page plane, x (red), y (green) and z (blue).

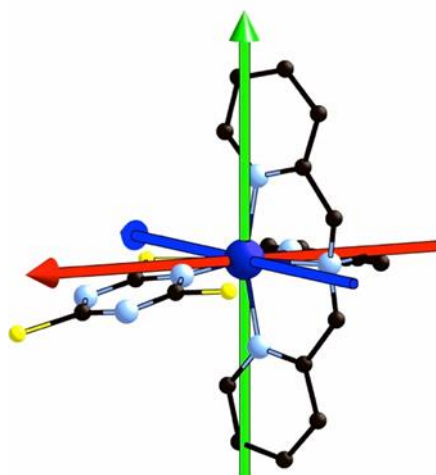


Figure III.22 Orientation of the **D** tensor axis for Co3; x (red), y (green), z (blue).

It is worth noting that the principle axes (blue) of the of three Co(II) ions lie almost in the plane of the bridging ligand (Figure III.21). This was also the case for the previous complex. Further analysis is necessary in order to check whether this observation is a coincidence or whether the bridging ligand imposes by its electronic properties such orientation.

3.4.2 Theoretical studies for Complex 3-3

The same calculations were carried on the trinuclear Ni complexes **3-3** and **3-5** but not on the hexanuclear one **3-4**. For **3-3**, the compound has two different trinuclear independent

molecules with different environments for each Ni mononuclear species, which makes 6 different mononuclear species to consider for calculations. But, the environment of the three Ni species in the two independent trinuclear molecules are close, we will, therefore, give the results for one trinuclear species, the one where the organic ligands are not disordered and are labeled Ni4, Ni5 and Ni6. The D values for Ni4, Ni5 and Ni6 are $D_4 = 9.3 \text{ cm}^{-1}$, $D_5 = -2.4 \text{ cm}^{-1}$ and $D_6 = 1.8 \text{ cm}^{-1}$ respectively. Table III.12 gives the energy of the electronic states and their contribution to D .

Table III.12 Energy (cm^{-1}) of the triplet (T_i) and singlet (S_i) states that have the largest contributions to D for the three Ni(II) species before spin orbit coupling, contribution of each state to the axial ZFS parameter D and values of the ZFS parameters D and E .

Species	State	Energy	Contribution to D (cm^{-1})	D (cm^{-1})	E (cm^{-1})
Ni4	T0	0	0	9.3	1.4
	T1	8853.8	23.6		
	T2	9518.4	21.1		
	T3	12745.8	-32.1		
	S2	24079.2	-7.6		
	S3	24581	-7.1		
	S4	27747.6	12.3		
Ni5	T0	0	0	-2.4	0.5
	T1	10987.3	-27.6		
	T2	11324.2	6.6		
	T3	12038.5	17.9		
	S2	26366.4	13.5		
	S3	26744.1	-6.3		
	S4	27367.6	-6.8		
Ni6	T0	0	0	1.8	0.5
	T1	11144.7	19.0		
	T2	11275.6	18.0		
	T3	12118.4	-34.7		
	S2	26525.6	-7.0		
	S3	26707.3	-6.7		
	S4	27452.2	13.4		

It is worth noting that the overall D values for the three species comes from the contributions of almost all the triplet states and also from part of the singlet states that contribute in a non-negligible manner. It is, therefore, not easy to relate the overall D values for each species to some local structural parameters as in the case of high symmetrical coordination spheres. The magnetic data were fitted with one D value that

was found equal 4.4 cm^{-1} , which is a fair average of the values obtained from calculations. We also calculated the exchange coupling parameters J_{45} , J_{46} and J_{56} by broken symmetry DFT and found -0.9 , -1.4 and -1.8 cm^{-1} respectively. These values are in fair agreement with the value obtained from fitting the magnetic data (-2.1 cm^{-1}) and confirm that the coupling is antiferromagnetic. The exchange coupling parameter for the Ni complex is much larger than for the Co(II) containing complexes (-2.1 in comparison to $\pm 0.1 \text{ cm}^{-1}$), this may be due to the presence of additional ferromagnetic pathways for the Co(II) complexes absent in the Ni(II) ones, due to the larger number of electrons. Actually, for a Ni(II) dimer there are 4 exchange pathways, while 9 are present for Co(II) dimers. The additional pathways are usually ferromagnetic because they involve orbitals of different symmetries and they may counterbalance the dominant antiferromagnetic pathway.

3.4.3 Theoretical studies for Complex 3-5

Complex **3-5** has its three Ni species related by a three-fold symmetry axis, they, therefore, have the same coordination sphere. The calculations were thus made on one Ni species and gave the following ZFS parameters: $D = -125.1 \text{ cm}^{-1}$ and $E = 1.9 \text{ cm}^{-1}$ ($E/D = 0.02$). The origin of the very large negative D value is the quasi trigonal symmetry of the Ni species as depicted in Figure III.23.

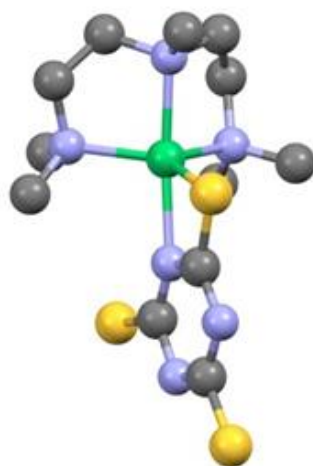


Figure III.23 View of the Ni(pmdien)TTC mononuclear coordination sphere belonging to the trinuclear complex **3-5**.

As for the other complexes, the energy of the electronic excited states and their contribution to the overall D value are given in Table III.13. The first excited triplet state T1 has the largest contribution to D that is negative as found for the $[\text{Ni}(\text{Me}_6\text{tren})\text{X}]^{2+}$ complexes.²⁵ All the other states contribute positively (apart from S2) reducing the overall D value. Because of the relatively high symmetry, the d orbitals are relatively pure in the magnetic axes frame (frame of the \mathbf{D} tensor), their relative energy are given in Table III.14. One observes that they are grouped in three sets: two, two and one with a small energy separation within the first and the second sets as expected from a trigonal bipyramid distortion in the equatorial plane.

Table III.13 Energy (cm^{-1}) of the triplet (T_i) and singlet (S_i) states that have the largest contributions to D for the Ni(II) ion before spin orbit coupling, contribution of each state to the axial ZFS parameter D , composition of the states wavefunctions and values of the ZFS parameters D and E .

Species	State	Energy	Contribution to D (cm^{-1})	Composition of the wave functions	D (cm^{-1})	E (cm^{-1})
Ni	T0	0	0	92% $ dz_2dxy $ / 8% $ dz_2dx_2-y_2 $	-125.1	1.9
	T1	2012.4	-186.9	92% $ dz_2dx_2-y_2 $ / 8% $ dz_2dxy $		
	T2	8510.8	19.8	39% $ dz_2dxz $ / 28% $ dyzdx_2 $ / 13% $ dyzdz_2 $		
	T3	9149.5	16.7	40% $ dyzdz_2 $ / 26% $ dxzdx_2 $ / 14% $ dz_2dxz $		
	T4	13026.2	4.2			
	T5	13195.7	3.3			
	S2	17397.4	21.0	80% $ dz_2dx_2-y_2 $ / 8% $ dxydz_2 $ / 5% dxy without an electron		
	S3	22898.9	-6.3			

Table III.14 Energy (cm^{-1}) of the d orbitals

Orbitals	Energy
dxz	0
dyz	608.2
dx^2-y^2	2689.6
dxy	4428.8
dz^2	10183.6

The origin of the large negative D contribution can be easily understood when examining the composition of the wave functions of T0 and T1, where one observes that the coupling between the two states is due to an excitation among the dx^2-y^2 and the dxy orbitals that have the same m_l values (Figure III.24). The coupling between T0 on one hand and T2 and T3 on the other hand involves excitation between orbitals with m_l differing by ± 1 , thus contributing positively to D .

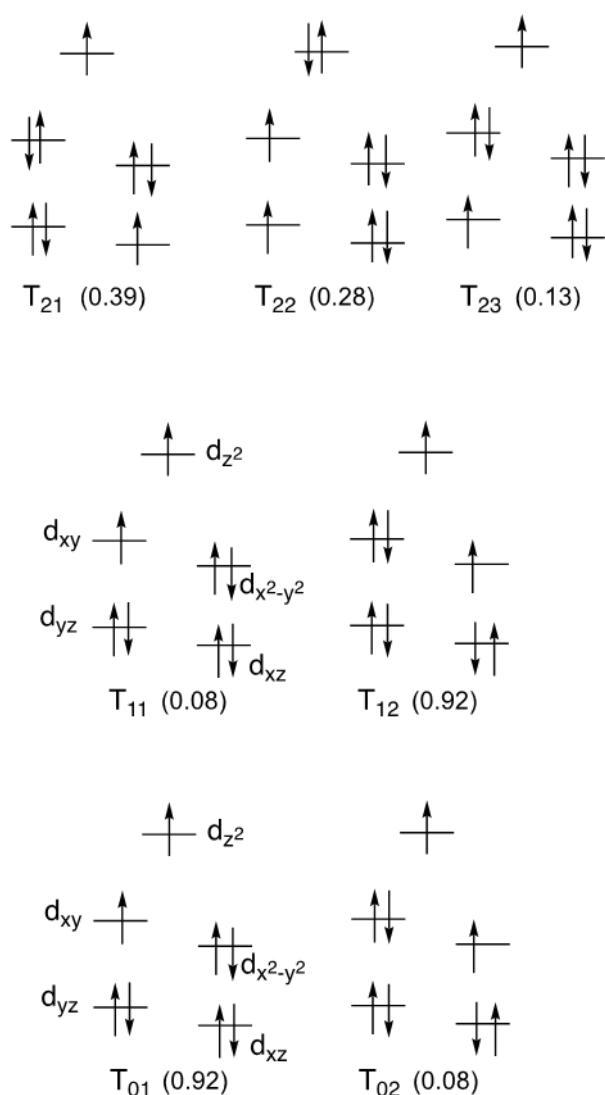


Figure III.24 Composition of the wave functions for T0, T1 and T2.

The calculations for complex **3-5** correspond to what is expected from its geometry and is similar to the M_6 tren based complexes of Chapter 2. However, the experimental magnetic data were fitted without including ZFS parameters which is surprising. We tried to simulate the magnetic data by using the ZFS calculated parameters and different exchange coupling parameters values in the range found for the other TTC^{3-} bridged complexes. The curves obtained are very different from the experimental ones and only when D is very weak the agreement starts to be fair. We do not have an explanation, yet, for these observations. One possibility is that the compound we prepared and measured is not the right one, but

XRPD pattern fits the calculated one based on the single crystal structure and the elemental analysis correspond to the expected data.

3.5 Conclusions

In summary, we prepared five polynuclear complexes with the TTC^{3-} bridging ligand and studied their molecular structures and magnetic properties. Complex **3-1** and **3-2** are both trinuclear molecules based on Co(II), with pmdien and TPA as blocking ligands, respectively. The analysis of the theoretical calculations allows rationalizing the ZFS parameters for **3-1**. For **3-2**, the analysis is much difficult because the very low symmetry of the octahedral coordination sphere of the Co(II) ions, but the ZFS values extracted from fitting the magnetic data are in fair agreement with calculations.

For Ni(II), when using the tridentate blocking ligand APMPDA in the objective of obtaining pentacoordinate geometry close to a trigonal bipyramid, the structure shows that the Ni coordination sphere was octahedral. The sixth site was occupied by an additional APMPDA ligand that bridges two Ni(II) of the trinuclear complex and the third Ni species had a coordinated perchlorate. The octahedral coordination geometry was preferred, probably, because this geometry is more stable and also because the tridentate ligand is not bulky enough to prevent the approach of the sixth ligand in the coordination sphere of Ni(II). The magnetic data could be fitted with the same ZFS parameter for the three different Ni(II) and corresponds to the average value of those obtained from theoretical calculations. The good fit of the magnetic data with one ZFS parameter was possible, probably, because the geometry of the three Ni(II) species is not so different.

When using the bidentate ligand TMEDA that blocks only two coordination sites, a hexanuclear complex obtained. The coordination sphere of three of the Ni(II) metal ions has the blocking ligand and two TTC^{3-} bridges, and the other three Ni(II) has one blocking ligand, one TTC^{3-} , one solvent molecule and one oxygen atom from a bridging carbonate. Again here, it was not possible to have a pentacoordinate geometry around Ni(II).

In order to impose a pentacoordinate trigonal bipyramidal geometry, we used the tridentate pmdien ligand that has methyl group on the amine groups as bulky species to prevent the formation of an octahedral geometry and obtain a complex similar to the Co containing one **3-1**. Such complex was reported in the literature as stated above. The theoretical calculations give the large axial D parameter we expected, but unfortunately the magnetic data do not correspond to those expected. Further work must be done of this compound to understand the origin of its magnetic behavior. Finally, the exchange coupling interaction was found to weak, larger than the for the Co(II) complexes, and antiferromagnetic as expected.

3.6 References

- 1 Seo, J. S. *et al.* A homochiral metal–organic porous material for enantioselective separation and catalysis. *Nature* **404**, 982 (2000).
- 2 Wang, Q. H., Kalantar-Zadeh, K., Kis, A., Coleman, J. N. & Strano, M. S. Electronics and optoelectronics of two-dimensional transition metal dichalcogenides. *Nature nanotechnology* **7**, 699 (2012).
- 3 Bar, A. K., Pichon, C. & Sutter, J.-P. Magnetic anisotropy in two-to eight-coordinated transition–metal complexes: Recent developments in molecular magnetism. *Coordination Chemistry Reviews* **308**, 346-380 (2016).
- 4 Kopel, P. *et al.* Coordination compounds of nickel with trithiocyanuric acid. Part IV. Structure of $[\text{Ni}(\text{pmdien})(\text{ttcH})]$ (pmdien= N, N, N', N', N' - pentamethyldiethylenetriamine, ttcH= trithiocyanuric acid). *Transition Metal Chemistry* **26**, 282-286 (2001).
- 5 Trávníček, Z., Marek, J. & Čermáková, Š. μ -Trithiocyanurato- κ 4N1,S2:N3,S4-bis[(N,N,N',N',N' -pentamethyldiethylenetriamine-3N,N',N')zinc(II)] perchlorate monohydrate. *Acta Crystallographica Section E Structure Reports Online* **63**, m795-m797, doi:10.1107/s1600536807007349 (2007).
- 6 Marek, J., Trávníček, Z. & Čermáková, Š. (μ 3-Trithiocyanurato- κ 6N1,S2:N3,S4:N5,S6)tris[(N,N,N',N',N' -pentamethyldiethylenetriamine- κ 3N,N',N')zinc(II)] tris(perchlorate). *Acta Crystallographica Section E Structure Reports Online* **63**, m1411-m1413, doi:10.1107/s1600536807016595 (2007).
- 7 Trávníček, Z., Marek, J. & Čermáková, Š. (μ 3-Trithiocyanurato- κ 6N1,S2:N3,S4:N5,S6)tris[(N,N,N',N',N' -pentamethyldiethylenetriamine-

- κ^3N,N',N'' copper(II)] tris(perchlorate). *Acta Crystallographica Section E Structure Reports Online* **63**, m1742-m1743.
- 8 Bieńko, A. *et al.* Synthesis, crystal structure and magnetic properties of trithiocyanurate or thiodiacetate polynuclear Ni(II) and Co(II) complexes. *Inorganica Chimica Acta* **416**, 147-156, doi:10.1016/j.ica.2014.03.009 (2014).
- 9 Hunks, W. J., Jennings, M. C. & Puddephatt, R. J. Gold Complexes of Trithiocyanuric Acid: A Two-Dimensional Polymer Assembled through Gold (I) $\odot \odot \odot$ Gold (I) Interactions. *Inorganic chemistry* **38**, 5930-5931 (1999).
- 10 Beezer, A. & Chudy, J. Elucidation of coordination polymer stoichiometry via thermometric titrimetry: metal complexes of trithiocyanuric acid. *Thermochimica Acta* **6**, 231-237 (1973).
- 11 Henke, K. R., Robertson, D., Krepps, M. K. & Atwood, D. A. Chemistry and stability of precipitates from aqueous solutions of 2, 4, 6-trimercaptotriazine, trisodium salt, nonahydrate (TMT-55) and mercury (II) chloride. *Water Research* **34**, 3005-3013 (2000).
- 12 Matlock, M. M., Henke, K. R., Atwood, D. A. & Robertson, D. Aqueous leaching properties and environmental implications of cadmium, lead and zinc trimercaptotriazine (TMT) compounds. *Water research* **35**, 3649-3655 (2001).
- 13 Kopel, P. *et al.* Biological Activity and Molecular Structures of Bis(benzimidazole) and Trithiocyanurate Complexes. *Molecules* **20**, 10360-10376, doi:10.3390/molecules200610360 (2015).
- 14 Chan, C.-K., Cheung, K.-K. & Che, C.-M. Structure and spectroscopic properties of a luminescent inorganic cyclophane from self-assembly of copper (I) and two ligand components. *Chemical communications*, 227-228 (1996).
- 15 Čermáková, Š., Herchel, R., Trávníček, Z. & Šebela, M. Syntheses and magnetic properties of trinuclear trithiocyanurato-bridged manganese(II) complexes involving bidentate aromatic N-donor heterocycles. *Inorganic Chemistry Communications* **13**, 778-781, doi:10.1016/j.inoche.2010.03.045 (2010).
- 16 Kopel, P. *et al.* Synthesis and properties of a trinuclear copper (II) complex with trithiocyanurate bridge. *Polish Journal of Chemistry* **81**, 327 (2007).
- 17 Prushan, M. J. *et al.* Synthesis, characterization and reactivity of a trinuclear copper(II) thiocyanurate complex: A spin-frustrated molecular propeller. *Inorganic Chemistry Communications* **10**, 631-635, doi:10.1016/j.inoche.2007.02.015 (2007).
- 18 Kopel, P. *et al.* Ferromagnetic Properties of a Trinuclear Nickel(II) Complex with a Trithiocyanurate Bridge. *European Journal of Inorganic Chemistry* **2009**, 5475-5482, doi:10.1002/ejic.200900617 (2009).

- 19 Alvarez, S. *et al.* Shape maps and polyhedral interconversion paths in transition metal chemistry. *Coordination Chemistry Reviews* **249**, 1693-1708 (2005).
- 20 Casanova, D., Llunell, M., Alemany, P. & Alvarez, S. The rich stereochemistry of eight - vertex polyhedra: a continuous shape measures study. *Chemistry–A European Journal* **11**, 1479-1494 (2005).
- 21 Spek, A. L. PLATON SQUEEZE: a tool for the calculation of the disordered solvent contribution to the calculated structure factors. *Acta Crystallographica Section C: Structural Chemistry* **71**, 9-18 (2015).
- 22 Spek, A. L. Structure validation in chemical crystallography. *Acta Crystallographica Section D: Biological Crystallography* **65**, 148-155 (2009).
- 23 Ruamps, R. *et al.* Ising-type magnetic anisotropy and single molecule magnet behaviour in mononuclear trigonal bipyramidal Co (II) complexes. *Chemical Science* **5**, 3418-3424 (2014).
- 24 Cahier, B., Maurice, R., Bolvin, H., Mallah, T. & Guihéry, N. Tools for predicting the nature and magnitude of magnetic anisotropy in transition metal complexes: Application to Co (II) complexes. *Magnetochemistry* **2**, 31 (2016).
- 25 Ruamps, R. *et al.* Giant Ising-type magnetic anisotropy in trigonal bipyramidal Ni(II) complexes: experiment and theory. *J Am Chem Soc* **135**, 3017-3026, doi:10.1021/ja308146e (2013).

Chapter IV

Ni(II) and Co(II) molecular magnets based on Hexahydroxytriphenylene (HHTP)

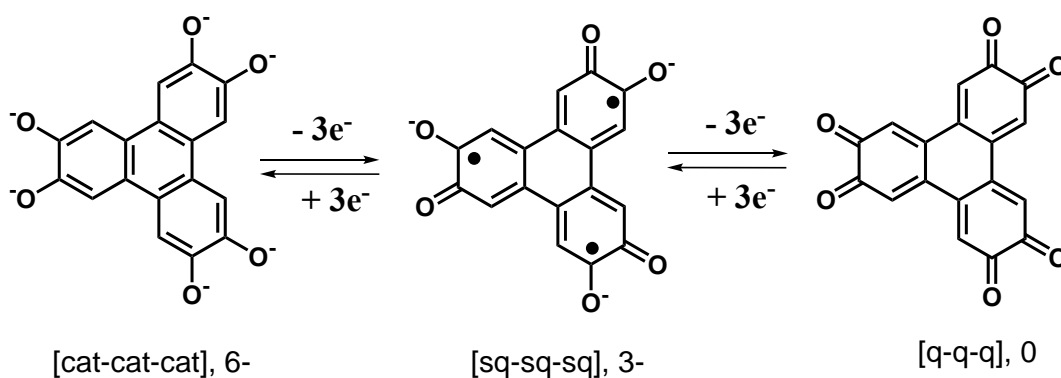
4.1 Introduction

As mentioned in Chapter I, the polynuclear molecular complexes with large ZFS and weak antiferromagnetic exchange coupling interactions have the potential to be good candidates for quantum gates thanks to the coupling between two or three individual qubits. Another way to build quantum gates is to use a central spin to couple peripheral ones that may allow the manipulation of the different states providing that the Lande factors g of the central and the peripheral species are different. The detail of the mechanism is complicated and is out of the scope of this thesis that focuses on designing the complexes, while, of course, having in mind the motivation.

One possible approach is to use non-innocent ligands to control the coupling between the mononuclear species in a polynuclear complex by oxidation and/or reduction. Such system would be viable on a substrate where electron injection can be carried out. Therefore, the objective is to design trinuclear complexes using a non-innocent bridging ligand that can be oxidized and/or reduced.

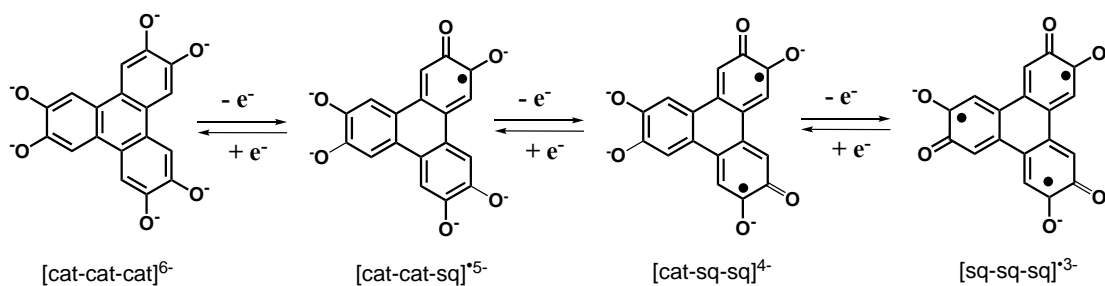
Triphenylene derivatives, good π -donating molecules,¹⁻³ are representative non-innocent ligands that can undergo reversible interconversions among three oxidation states: catecholate (cat, 2-), semiquinonate (sq, 1-) and quinone (q, 0). The different states can be characterized by their absorption spectra where usually a band is present in the near-IR region corresponding to ligand-to-ligand charge transfer. During the redox reaction a π -radical can be generated and magnetically couple with the metal ions.⁴⁻⁷

2,3,6,7,10,11-hexahydroxytriphenylene (HHTP) is a good candidate to prepare trinuclear complexes when deprotonated (Scheme IV.1). Generally, HHTP^{n-} is used as a connector in constructing porous Metal Organic Frameworks (MOFs).⁸⁻¹⁰ The fully deprotonated species HHTP^{6-} , a typical redox-active linker, has the potential to act as a non-innocent bridging ligand, as shown in Scheme 4.1, where only three states are presented.



Scheme IV.1 The three main species of deprotonated HHTP.

The ligand can also be in intermediate states between those depicted in scheme IV.1. The most pertinent ones that allow the coordination of metal ions are depicted in Scheme IV.2. Among them, two are radicals and have single electrons. The more oxidized species containing the quinone groups are not expected to form trinuclear complexes because of the reduced electron density on the quinone parts. It is worth noting that the electrons are expected to be delocalized onto the whole molecule. The $[\text{sq-sq-sq}]^{3-}$ can have three single electrons only if the symmetry of the molecule is strictly trigonal, which is usually not the case, particularly, in the solid state. In such a case, only one single electron remains unpaired. For the same reasons, the $[\text{cat-sq-sq}]^{4-}$ intermediate is expected to be diamagnetic.



Scheme IV.2 The four species of deprotonated HHTP that can coordinate to metal ions

Two Co based systems: $\text{Co}_3(\text{HHTP})(\text{H}_2\text{O})_{12}$ (a trinuclear complex) and $\text{Co}_3(\text{HHTP})_2(\text{H}_2\text{O})_6$ (a bidimensional network) were reported by Yaghi *et al.* The valence of the HHTP linker in the first complex was found to be 6- because the complex is neutral; the ligand is thus in the completely reduced [cat-cat-cat]⁶⁻ state. While for the second, electroneutrality leads to an average charge of 3- for HHTP corresponding to the [sq-sq-sq]³⁻ state.¹¹ Apart from the coordination networks, HHTP is also popular for building porous Covalent Organic Frameworks (COFs).¹²⁻¹⁶ However, rare single molecules with HHTP have been reported, which is probably due to the difficulty of obtaining single crystals. So far, only one trinuclear complex formed by HHTP and a first-row transition metal ion can be found in literature: $\text{Co}_3(\text{HHTP})(\text{TPA})_3(\text{BF}_4)_4$. In this complex, the metal ions are in the oxidation degree III and the HHTP bridge in the oxidation state [cat-cat-sq]⁵⁻. Its magnetic study shows that χT at room temperature is equal to $0.44 \text{ cm}^3 \text{ K mol}^{-1}$, corresponding to the spin-only value for an $S = 1/2$ system. It demonstrates that the generated radical is the only magnetic center.¹⁷ We can also find some examples based on other metal ions, like ruthenium^{18,19} and titanium,²⁰ but due to their different features, we will not discuss more about them here. When non-innocent ligands are introduced to react with redox-active metal ions (like Co, Fe, Mn...),²¹⁻²³ the transfer of electron from the metal to the ligand and vice versa is possible to take place, which gives rise to valence tautomerism.

In this dissertation, three polynuclear complexes were successfully obtained: the hexanuclear $[(\text{Ni}_2\text{O})_3(\text{HHTP})_2(\text{TMEDA})_6](\text{H}_2\text{O})_9$ (**4-1**), and the two trinuclear $\text{Ni}_3(\text{HHTP})[\text{BH}(\text{TP}^{\text{Ph,Ph}})_3]_3(\text{C}_3\text{H}_6\text{O})_{0.5}$ (**4-2**) and $\text{Co}_3(\text{HHTP})[\text{BH}(\text{TP}^{\text{Ph,Ph}})_3]_3$ (**4-3**). The prepared complexes were characterized by infrared spectroscopy, element analysis, X-ray single crystal diffraction, magnetic measurements, UV-Vis spectroscopy and electrochemical studies.

4.2 Experimental section

4.2.1 Syntheses

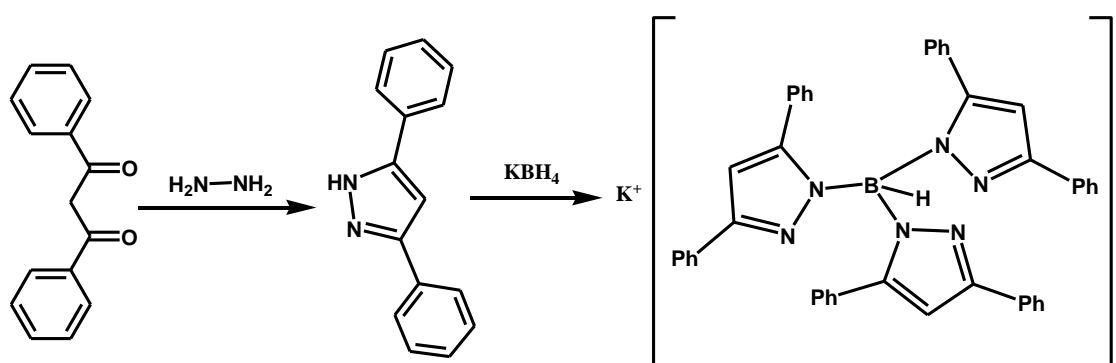
All the reagents used for these syntheses were purchased commercially and were used directly without further purification unless exceptionally stated.

Potassium Tris(3,5-diphenyl-1H-pyrazol-1-yl)(hydrido)borate $\text{KBH}(\text{TP}^{\text{Ph,Ph}})_3$

The ligand $\text{KBH}(\text{TP}^{\text{Ph,Ph}})_3$ was synthesized through two steps according to a previous report,²⁴ (see Scheme IV.3).

Dibenzoylmethane (10 mmol, 2.24 g) and hydrazine monohydrate (64%) (10 mmol, 0.5 g) were mixed in a mortar and ground, then 2 drops of concentrated sulfuric acid were added into the mixture. The mixture was ground for 10 min and left still for 1 hour. The solid obtained was washed with 10% of Na_2CO_3 solution and then water was added; the suspension was kept stirring at 80 °C for 30 min. A yellow solid formed after cooling. The solid was mixed with 200 mL of hot heptane (reflux). After cooling and separation by filtration, the solid was left to dry in vacuum, a beautiful white solid $\text{TP}^{\text{Ph,Ph}}$ was obtained. Yield: 1.64 g, 75%. Chemical formula: $\text{C}_{15}\text{H}_{12}\text{N}_2$, $M_{\text{W}} = 220.27$ g/mol.

7 g of $\text{TP}^{\text{Ph,Ph}}$ and 0.57 g of KBH_4 were mixed and ground in a mortar, then the mixture was transferred to a round flask equipped with a bubbler to observe the release of hydrogen. The flask was heated to 150 °C slowly to maintain a reasonable gas release with stirring. The temperature was gradually increased to 250 °C and the heating kept for 3 hours. The end of the H_2 release was observed after 1 hour. The generated solid was washed with 80 mL of hot toluene and then filtered. The solid was dissolved in acetone and filtered on celite. Acetone was removed under vacuum. The residue was washed with heptane (5 mL) and then dried under vacuum. A white solid was obtained with a yield of 65%: 4.9 g. Chemical formula: $\text{KC}_{45}\text{H}_{34}\text{BN}_6$. $M_{\text{W}} = 708.39$ g/mol.

Scheme IV.3 Synthesis of Ligand $\text{KBH}(\text{TP}^{\text{Ph,Ph}})_3$

$[(\text{Ni}_2\text{O})_3(\text{HHTP})_2(\text{TMEDA})_6](\text{H}_2\text{O})_9$ (Complex 4-1)

A 10 mL methanolic solution of TMEDA (tetramethy ethylenediamine) (1 mmol, 150 μL) was added dropwise into the methanolic solution of $\text{Ni}(\text{BF}_4)_2 \cdot 6\text{H}_2\text{O}$ (0.5 mmol, 170.2 mg). HHTP (0.167 mmol, 54 mg) was dissolved in 30 mL of methanol with 140 μL (triethyl)amine (TEA). The two solutions were mixed slowly, and a blackish blue solid was generated immediately, the mixture was kept stirring overnight. The solid was filtered and washed with methanol, and then dried in air. Yield, 31%, 130 mg. Crystals suitable for X-ray analysis are obtained by vapor diffusion of diethyl ether into a DMF solution of the precipitate. Elem Anal. for $[(\text{Ni}_2\text{O})_3(\text{HHTP})_2(\text{TMEDA})_6](\text{H}_2\text{O})_9$ Calc: C, 45.46%; H, 6.99%; N, 8.84%; Found: C, 45.41%; H, 6.74%; N, 8.81%. $M_w = 1902.04$ g/mol. Single-crystal unit cell: Trigonal, space group, $R32$. $a = 18.443(2)$ \AA , $b = 18.443(2)$ \AA , $c = 22.759(3)$ \AA , $\alpha = 90^\circ$, $\beta = 90^\circ$, $\gamma = 120^\circ$, $V = 6704.2(17)$ \AA^3 . IR (KBr) v/cm^{-1} : 3386 (m), 2892 (w), 2843 (w), 1645 (m), 1546 (s), 1514 (s), 1454 (s), 1431 (s), 1407 (s), 1365 (s), 1326 (s), 1296 (s), 1250 (s), 1215 (s), 1124 (w), 1084 (w), 1046 (w), 1024 (w), 955 (m), 933 (w), 865 (m), 804 (s), 771 (w), 688 (w), 628 (m), 552 (m), 499 (w), 447 (w), 391 (m), 381 (m), 290 (w).

$\text{Ni}_3(\text{HHTP})[\text{BH}(\text{TP}^{\text{Ph,Ph}})_3]_3(\text{C}_3\text{H}_6\text{O})_{0.5}$ (Complex 4-2)

$\text{KBH}(\text{TP}^{\text{Ph,Ph}})_3$ (1.89 g, 2.7 mmol) was dissolved in 60 mL CHCl_3 , and the colorless solution was added into a methanolic solution of $\text{NiCl}_2 \cdot 6\text{H}_2\text{O}$ (0.71 g, 3 mmol) with stirring. A pink precipitate was generated immediately. Two hours later, the solid was filtered and washed

with small amount of CHCl_3 , then dried in vacuum. The pink solid obtained corresponds to $\text{Ni}[\text{BH}(\text{TP}^{\text{Ph,Ph}})_3]\text{Cl}$.

HHTP (32.5 mg, 0.01 mmol) was dissolved in a methanolic solution (15 mL) containing 0.6 mL of tetrabutylammonium hydroxide (TBAOH). The obtained dark violet solution was added to a 15 mL CH_2Cl_2 solution of $\text{Ni}[\text{BH}(\text{TP}^{\text{Ph,Ph}})_3]\text{Cl}$ (229 mg, 0.3 mmol) with stirring. A darkish blue suspension was produced. The reaction was left overnight, and then filtered. A black precipitate was obtained, it was thoroughly washed with methanol. Yield 62%, 156 mg. The solid was redissolved in CHCl_3 , and the final solution was obtained after chromatography (SiO_2). The solvent was completely removed using a rotatory evaporator. The solid obtained was dissolved in acetone and crystals suitable for X-ray analysis were obtained by slowly evaporating acetone. Elem Anal. for $\text{Ni}_3(\text{HHTP})[\text{BH}(\text{TP}^{\text{Ph,Ph}})_3]_3(\text{C}_3\text{H}_6\text{O})_{0.5}$ Calcd: C, 73.19%; H, 4.53%; N, 9.94%; Found: C, 73.14%; H, 4.35%; N, 10.04%. $M_w = 2535.19$ g/mol. Single-crystal unit cell: Triclinic, space group, $P-1$. $a = 14.2552(18)$ Å, $b = 17.287(2)$ Å, $c = 32.407(4)$ Å, $\alpha = 94.408(4)^\circ$, $\beta = 101.051(4)^\circ$, $\gamma = 101.473(4)^\circ$, $V = 7626.4(17)$ Å³. IR (KBr) ν/cm^{-1} : 3456 (w), 3062 (w), 2617 (w), 1603 (w), 1545 (s), 1502 (s), 1479 (s), 1462 (s), 1364 (m), 1329 (m), 1282 (w), 1232 (w), 1170 (m), 1118 (w), 1064 (m), 1013 (m), 972 (w), 915 (w), 844 (w), 827 (w), 803 (s), 759 (s), 696 (s), 669 (m), 619 (w), 571 (m), 543 (m), 403 (w), 353 (w).

$\text{Co}_3(\text{HHTP}) [\text{BH}(\text{TP}^{\text{Ph,Ph}})_3]_3$ (Complex 4-3)

$\text{KBH}(\text{TP}^{\text{Ph,Ph}})_3$ (1.89 g, 2.7 mmol) was dissolved in 60 mL CHCl_3 , and the colorless solution was added into a methanolic solution of $\text{CoCl}_2 \cdot 6\text{H}_2\text{O}$ (0.71 g, 3 mmol) with stirring, generating a blue precipitate immediately. After two hours, the solid was filtered and washed with small amount of CHCl_3 , then dried in vacuum. The blue solid obtained corresponds to $[\text{CoBH}(\text{TP}^{\text{Ph,Ph}})_3]\text{Cl}$.

HHTP (32.5 mg, 0.01 mmol) was dissolved in a 15 mL methanolic solution containing 0.6 mL of tetrabutylammonium hydroxide (TBAOH). The dark violet solution was added into a 15 mL CH_2Cl_2 solution of $\text{Co}[\text{BH}(\text{TP}^{\text{Ph,Ph}})_3]\text{Cl}$ (228 mg, 0.3 mmol) with stirring, producing a darkish blue suspension. The reaction was left overnight. A black precipitate was obtained

by filtering and the solid was washed with methanol for three times. Yield 28%, 70 mg. The residue was redissolved in CHCl_3 , and the final solution was obtained after chromatography (SiO_2). The solvent was removed by vacuum. The solid was dissolved in acetone and crystals suitable for X-ray analysis were obtained by evaporating acetone slowly. Elem Anal. for $\text{Co}_3(\text{HHTP})[\text{BH}(\text{TP}^{\text{Ph,Ph}})_3]_3$ Calcd: C, 73.30%; H, 4.46%; N, 10.06%; Found: C, 73.14%; H, 4.33%; N, 10.03%. $M_w = 2506.87$ g/mol. Single-crystal unit cell: Triclinic, space group, $P-1$. $a = 16.821(3)$ Å, $b = 17.771(3)$ Å, $c = 26.730(4)$ Å, $\alpha = 97.162(5)^\circ$, $\beta = 90.043(5)^\circ$, $\gamma = 105.344(4)^\circ$, $V = 7641(2)$ Å³. IR (KBr) ν/cm^{-1} : 3430 (w), 3058 (w), 2614 (w), 1949 (w), 1545 (s), 1501 (s), 1478 (s), 1463 (s), 1431 (s), 1415 (s), 1360 (m), 1326 (m), 1274 (m), 1228 (w), 1168 (m), 1119 (w), 1063 (m), 1010 (m), 970 (w), 914 (w), 865 (w), 821 (w), 803 (w), 759 (s), 695 (s), 673 (m), 618 (w), 569 (m), 536 (m), 425 (w), 400 (w), 356 (w), 252 (w).

4.2.2 Physical Measurements

The physical measurements refer to section 2.2.2. For the X-ray Crystallography measurement, the data for complex **4-1** was collected by using a X8 APEXII CCD Bruker diffractometer with graphite-monochromated $\text{MoK}\alpha$ radiation. The X-ray diffraction data for complexes **4-2** and **4-3** were collected by using a VENTURE PHOTON100 CMOS Bruker diffractometer with Micro-focus IuS source $\text{Mo K}\alpha$ radiation. All crystals were mounted on a CryoLoop (Hampton Research) with Paratone-N (Hampton Research) as cryoprotectant and then flash frozen in a nitrogen-gas stream at 100 K. The electronic spectra were collected by the Cary 5000 spectrophotometer, ranged from 175 nm to 3000 nm. The data of electrochemical measurements were collected by AUTOLAB PGSTAT320.

4.3 Results and discussion

4.3.1 Molecular Structures Description

4.3.1.1 Molecular structure of Complex 4-1

The compound crystallizes in the trigonal space group $R\bar{3}2$ (Table A 6). The molecular structure of complex 4-1 is a hexanuclear complex formed by two identical layers of three Ni-TMEDA species bridged by HHTP; the complex has a three-fold symmetry axis. The two layers of $\text{Ni}_3(\text{HHTP})(\text{TMEDA})_3$ are linked via their Ni(II) ions by three O atoms (Figure IV.1 and Figure IV.2-left). Two oxygen atoms coming from the two HHTP ligands (O2 and O1) and one (O3) is an oxo that was generated during the synthesis (Figure IV.1). The Ni(II) ions in the molecule are all hexa-coordinated, and the SHAPE analysis^{25,26} indicates that the geometry of Ni(II) ion is octahedron (Table IV.3). However, the geometry is close to an elongated octahedron along the O1Ni2 direction where the bond distances are larger than the four others. The shortest distances involving a bridging oxygen atom are with O3 (Ni-O3 = 1.996 Å), while the Ni-O1 bond lengths are longer and are different (Ni-O1 = 2.261 and 2.066 Å). The NiO3Ni angle is close to 90°, while the NiO1Ni ones are much smaller (close to 81°) (see Table IV.1 for selected bond distances and angles). The top view of the structure reveals that the two layers are non-overlapping, being displaced from each other by an angle close to 30° (Figure IV.2-left). The side view shows that the HHTP planes are bent (right, Figure IV.2). The distance between the two triangular planes defined by the central benzene rings is equal to 3.194 Å, which is in the range of π - π stacking. However, because the two triangular planes are bent on the edges (Figure IV.2-left), the shortest C-C distance between them is equal to 2.78 Å (dotted line in Figure IV.2-right), which corresponds to large interaction between the two HHTP ligands through the carbon atoms of the C-O groups.

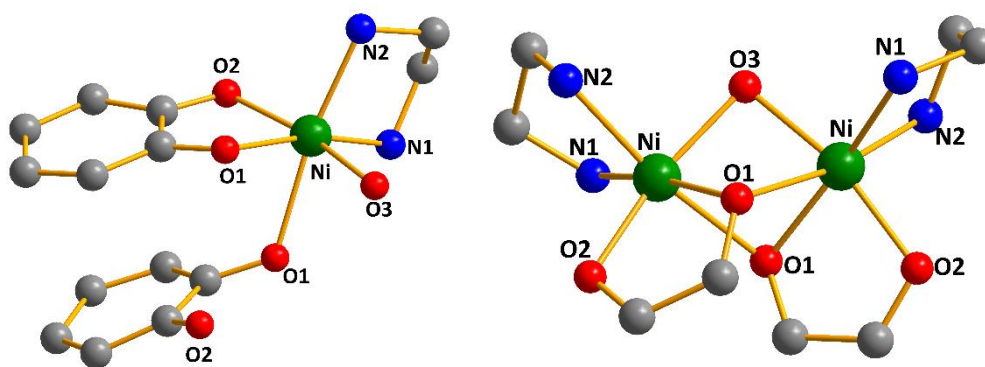


Figure IV.1 View of the coordination sphere around the Ni atom.

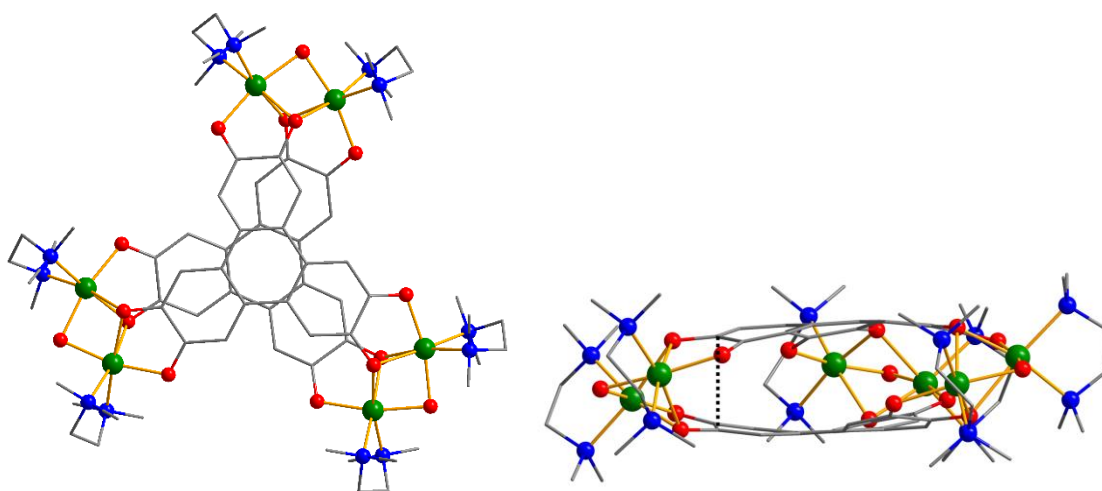


Figure IV.2 The top view (left) and the side view (right) of complex **4-1**.

According to the molecular structure and elemental analysis results, the chemical formula of **4-1** can be proposed as $[(\text{Ni}_2\text{O})_3(\text{HHTP})_2(\text{TMEDA})_6](\text{H}_2\text{O})_9$. Assuming that the oxygen atom O3 bridging the Ni(II) belonging to the two layers are O^{2-} , the charge of HHTP is computed to be equal to 3^- , which corresponds to the $[\text{sq-sq-sq}]^{\bullet 3-}$ state. Because of the three-fold symmetry axis, one may assume that each HHTP has three single electrons localized on the three sq parts and the short C-C bonds between the two layers leads to antiferromagnetic coupling between them as depicted in Figure IV.3-right. The C-C distance being much longer than an ordinary C-C single bond (around 1.5 \AA),²⁷ therefore, it is a weak interaction between the two electrons, rather than a real C-C bond.

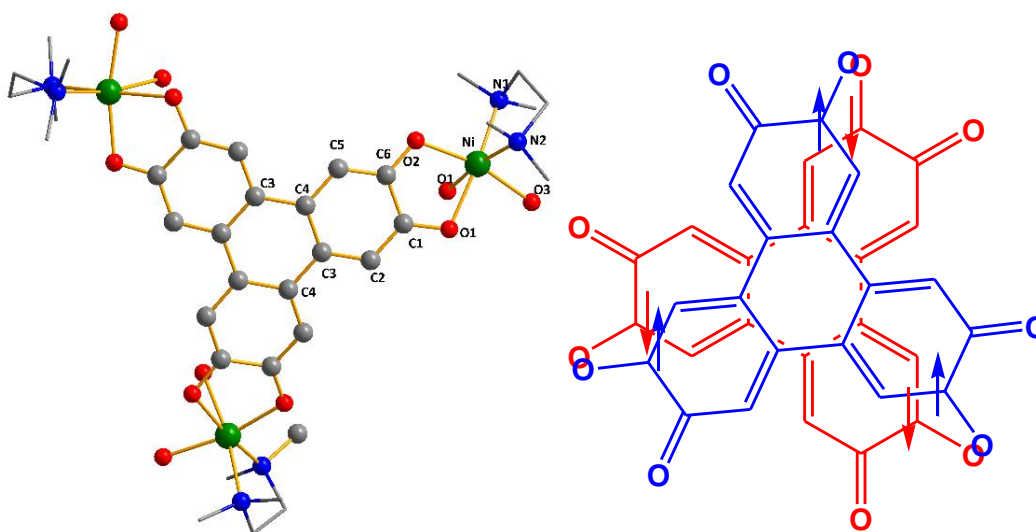


Figure IV.3 Left: The structure of one single layer within complex **4-1**; Right: the scheme of the interaction between two electrons within the two layers.

The single layer structure within complex **4-1** is displayed in Figure IV.3-left. Generally, C-C bond lengths vary from 1.39 Å (bond in a benzene ring) to 1.6 Å (single bond).²⁷ Within HHTP, the C1-C6 bond (1.4663 Å) and the C3-C4 bond (1.4436 Å and 1.4506 Å) are longer than the other bonds (from 1.39 Å to 1.40 Å), and are in the range between of C-C benzene ring bond and single bond. An ordinary C-O single bond is around 1.4 Å and a C-O double bond is normally 1.2 Å.²⁷ For the C-O bonds within the complex, the C1-O1 bond is equal to 1.3124 Å, and C6-O2 1.2866 Å, which is intermediate between single and double C-O bond and consistent with the bond lengths found in semi-quinone. The Ni-O1 and Ni-O2 are equal to 2.0658 Å and 1.9988 Å, respectively. The distance between the Ni(II) ions and the connecting O3 atom is 1.9964 Å, and O3 atom lies 0.079 Å below the plane of O1, O2 and Ni. The angle of $\widehat{O1NiO2}$ is 82.550°, and $\widehat{O1NiO3}$ and $\widehat{O1'NiO3}$ are equal to 83.975° and 79.088°. More details about some selected bond lengths and angles can be found Table IV.1.

Table IV.1 Some selected bonds distances and angles of complex **4-1**.

Bond length (Å)				Angles (°)	
d_{Ni-N1}	2.0865(38)	d_{C1-C2}	1.3894(46)	$\widehat{O1NiO2}$	82.550(11)
d_{Ni-N2}	2.1329(33)	d_{C2-C3}	1.3990(36)	$\widehat{O1NiO1'}$	75.860(91)
d_{Ni-O1}	2.0658(29)	d_{C4-C5}	1.3943(47)	$\widehat{O1NiO3}$	83.975(70)
d_{Ni-O2}	1.9988(26)	d_{C5-C6}	1.4013(37)	$\widehat{O2NiO3}$	166.336(78)

$d_{\text{Ni-O1}'}$	2.2606(25)	$d_{\text{C1-C6}}$	1.4663(59)	$\widehat{\text{O1}'\text{NiO3}}$	79.088(64)
$d_{\text{C1-O1}}$	1.3124(34)	$d_{\text{Ni-O3}}$	1.9964(10)	$\widehat{\text{NiO3Ni}'}$	90.089(23)
$d_{\text{C6-O2}}$	1.2866(43)	$d_{\text{C3-C4}}$	1.4436(56)	$\widehat{\text{N1NiN2}}$	85.944(12)
			1.4506(46)		

O1' and Ni' represent the O1 and Ni in the other layer.

4.3.1.2 Molecular structure of Complex 4-2

Our first objective was to prepare trinuclear complexes using the HHTP ligand, but we were not successful when using “simple” tetra- or tridentate ligands as blocking ligands for Ni(II). Actually, we think that we obtained such complexes in solution but never had single crystals. When we used the bidentate TMEDA as the blocking ligand, the reaction was carried out using 2 molar equivalents of TMEDA for one Ni. However, we always obtained the hexanuclear complex **4-1** even when an excess or less of the TMEDA was used, the only complex obtained was **4-1**. This means that this complex is thermodynamically very stable and the driving force may well be the dimerization of the trinuclear species due to the presence of the radicals. In order to prevent such dimerization, we used a very bulky ligand to block the coordination sphere of Ni(II). This is how complexes **4-2** and **4-3** were obtained. And we were lucky to obtain single crystals suitable for structural determination.

The compound **4-2** crystallizes in the triclinic space group *P*-1 (Table A 6). Complex **4-2** is constructed by one HHTP bridging ligand, three Ni ions and three blocking ligand $[\text{BH}(\text{TP}^{\text{Ph,Ph}})_3]^-$ (left, Figure IV.4). The capping ligand is bulky preventing the Ni(II) ions from coordinating with other atoms from solvent and form dimerization as for **4-1**. Therefore, the Ni(II) ions are all penta-coordinated with two O atoms from HHTP, three N atoms from ligand $[\text{BH}(\text{TP}^{\text{Ph,Ph}})_3]^-$. The three Ni(II) ions are non-identical, as well as their coordination geometries. The results of SHAPE analysis show that the geometry of Ni1 is trigonal bipyramid and for Ni2 and Ni3 are both vacant octahedrons (close to a square pyramid; details are displayed in Table IV.3).

The framework of complex **4-2** is shown in Figure IV.4-right. The Ni-O distances vary from 1.9568 Å (Ni1-O2) to 2.0388 Å (Ni1-O1). The longest and shortest Ni-O bond lengths are

those bonds containing Ni1, and the minimum difference of Ni-O bond lengths occurs in the ones with Ni2. Correspondingly, the angle of $\widehat{O1Ni1O2}$ is the largest (81.953°), and $\widehat{O3Ni2O4}$ has the smallest angle: 81.841° . For the Ni-N bond distances, Ni1-N2 is the shortest (1.9878 \AA) and Ni1-N3 is the longest (2.0681 \AA).

The chemical formula is posed by molecular structure and elemental analysis: $Ni^{2+}_3(HHTP)^{3-}[BH(TP^{Ph,Ph})_3]_3(C_3H_6O)_{0.5}$. The valence of HHTP ligand in **4-2** is 3-, corresponding to its semiquinonate state [sq-sq-sq]. From measuring the C-O bond distances, we can find that bond length C9-O3, C15-O5 and C10-O4, C16-O6 are either 1.29 \AA and 1.27 \AA , however, the longest and shortest bond lengths appear in the bond C4-O2 (1.3010 \AA , close to a C-O single bond) and C3-O1 (1.2464 \AA , close to a double C-O bond), indication the trisemiquinonate form.²⁸ According to the previous reports and because of the absence of a three-fold symmetry axis,^{11,19} we assume that two of these three electrons pair together leading to one single electron on HHTP.

The C-C bond of the OCCO group is larger for the oxygen atoms linked to Ni1 than for the others. In summary, it appears that not only the coordination sphere of Ni1 is different but also the Ni1-O bond and also the C-C bond of the OCCO group. The OCCO group linked to Ni1 has a larger sq character than the two others suggesting that the single electron is localized near Ni1, while the other two electrons have paired and would be more delocalized on the whole bridging HHTP. Selected bond lengths and angles are listed in Table IV.2.

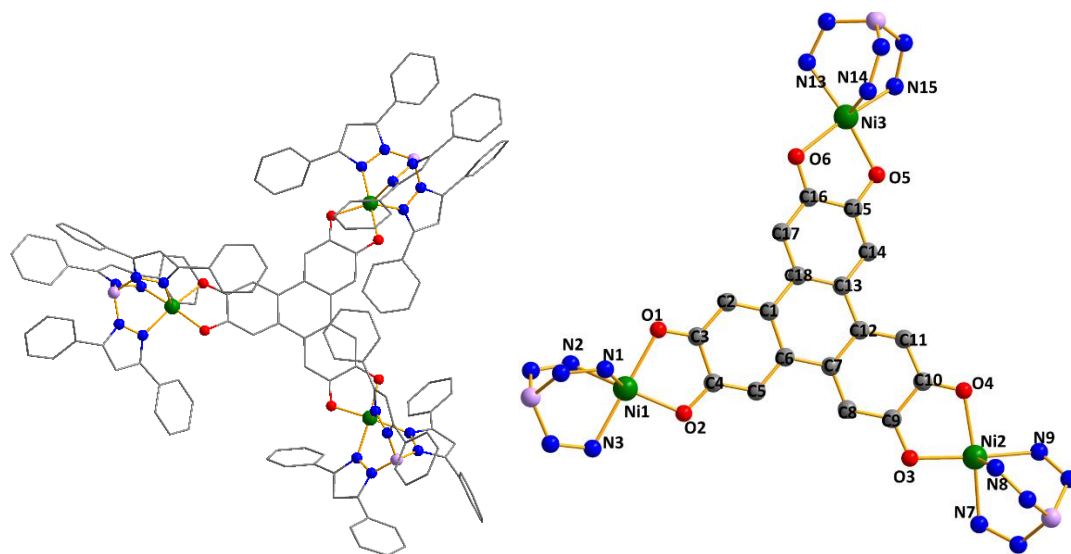


Figure IV.4 Molecular structure (left) and a simple frame (right) of complex **4-2**. H atoms, solvent and the carbon atoms in capping ligand are removed for clarify.

Table IV.2 Some selected bonds distances and angles of complex **4-2** and **4-3**.

Complex 4-2				Complex 4-3			
d_{Ni1-N1}	2.0083(59)	$d_{Ni3-N13}$	2.0385(57)	d_{Co1-N1}	2.0458(24)	$d_{Co3-N13}$	2.0407(24)
d_{Ni1-N2}	1.9878(40)	$d_{Ni3-N14}$	2.0190(50)	d_{Co1-N2}	2.1418(23)	$d_{Co3-N14}$	2.1128(21)
d_{Ni1-N3}	2.0681(60)	$d_{Ni3-N15}$	2.0284(56)	d_{Co1-N3}	2.0421(21)	$d_{Co3-N15}$	2.0543(24)
d_{Ni1-O1}	2.0388(43)	d_{Ni3-O5}	1.9713(47)	d_{Co1-O1}	1.9603(19)	d_{Co3-O5}	2.1099(17)
d_{Ni1-O2}	1.9568(47)	d_{Ni3-O6}	2.0223(49)	d_{Co1-O2}	2.1123(19)	d_{Co3-O6}	1.9603(20)
d_{Ni2-N7}	2.0566(79)	d_{C3-O1}	1.2463(72)	d_{Co2-N7}	2.1523(24)	d_{C3-O1}	1.3158(34)
d_{Ni2-N8}	2.0313(68)	d_{C4-O2}	1.3010(90)	d_{Co2-N8}	2.0403(24)	d_{C4-O2}	1.2579(34)
d_{Ni2-N9}	2.0402(63)	d_{C9-O3}	1.2928(12)	d_{Co2-N9}	2.0307(21)	d_{C9-O3}	1.2766(27)
d_{Ni2-O3}	1.9845(59)	d_{C10-O4}	1.2704(81)	d_{Co2-O3}	2.0768(19)	d_{C10-O4}	1.2918(32)
d_{Ni2-O4}	2.0208(58)	d_{C15-O5}	1.2905(91)	d_{Co2-O4}	1.9599(16)	d_{C15-O5}	1.2559(34)
$\widehat{O1Ni1O2}$	81.953(18)	d_{C16-O6}	1.2784(87)	$\widehat{O1Co1O2}$	80.793(73)	d_{C16-O6}	1.3044(28)
$\widehat{O3Ni2O4}$	81.841(23)	$\widehat{O5Ni3O6}$	81.919(82)	$\widehat{O3Co2O4}$	80.786(72)	$\widehat{O5Co3O6}$	80.752(72)

4.3.1.3 Molecular structure of Complex 4-3

The compound **4-3** crystallizes in the triclinic space group $P-1$ (Table A 6). Complex **4-3** possess a similar structure as **4-2**, constructed by one HHTP bridging ligand and three $Co[BH(TP^{Ph,Ph})_3]^+$ species (the molecular structure and its framework are displayed in Figure IV.5). The Co ions in this structure are all penta-coordinated with two O atoms from HHTP, three N atoms from ligand $[BH(TP^{Ph,Ph})_3]^+$. The SHAPE analysis results present the trigonal

bipyramid geometry for the three Co ions (details are displayed in Table IV.3), and the one for Co2 is slightly more distorted.

The pseudo trigonal geometry of the three Co ions allows to define an equatorial plane made of two N atoms from the blocking ligand and one O atom from HHTP and two apical positions containing one N atom from the blocking ligand and one O atom from HHTP. The apical Co-N bond lengths for Co1 and Co2 are around 2.15 Å larger than the corresponding one for Co3 and larger than the Co-O apical bond length. There are two different Co-O_{HHTP} bond lengths around 1.96 Å and 2.10 Å. The C-O bond lengths of each OCCO groups are different (1.26 and 1.30 Å) and the C-C bonds are in the range 1.45-1.48 Å. In summary, at the difference of the Ni-containing complex **4-2** where the structural surroundings of one Ni(II) was different, here the difference in the structural features around the Co atoms is less marked and the structural parameters of the Co coordination sphere are compatible with Co(II) metal ions than with Co(III). Another difference with the Ni complex is the large distortion of the HHTP ligand that is more planar for Ni₃ than for Co₃ (Figure IV.6). Selected bond lengths and angles are listed in Table IV.2.

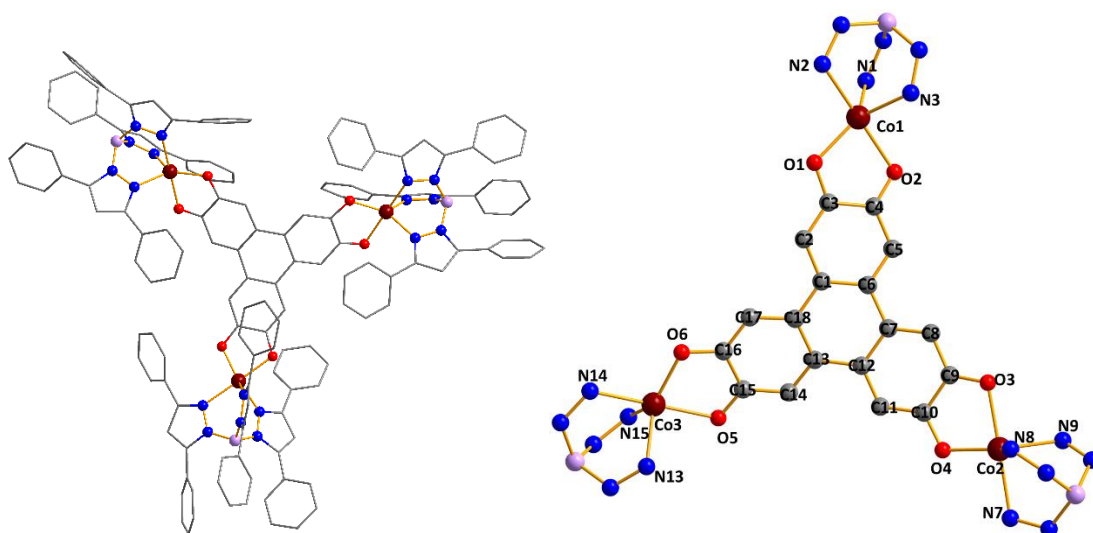


Figure IV.5 Molecular structure (left) and a simple frame of complex **4-3**. H atoms and the carbon atoms in capping ligand are removed for clarify.

Table IV.3 SHAPE analysis of coordination geometry in complex **4-1**, **4-2** and **4-3**.

4-1	Label	JPPY	TPR	OC	PPY	HP
------------	--------------	-------------	------------	-----------	------------	-----------

	Symmetry	C_{5v}	D_{3h}	O_h	C_{5v}	D_{6h}
	Ni	27.012	11.801	1.347	24.287	28.888
	Label	JTBPY	SPY	TBPY	vOC	PP
	Symmetry	D_{3h}	C_{4v}	D_{3h}	C_{4v}	D_{5h}
4-2	Ni1	4.097	3.575	2.132	4.061	29.034
	Ni2	7.787	1.086	5.657	0.667	30.199
	Ni3	7.785	0.881	5.819	0.872	29.496
4-3	Co1	3.715	3.061	1.960	3.979	29.428
	Co2	3.795	3.510	2.054	4.171	29.017
	Co3	3.670	3.974	1.783	5.083	29.130

Abbreviation: JPPY – Johnson pentagonal pyramid J2, TPR – Trigonal prism, OC – Octahedron, PPY – Pentagonal pyramid, HP – Hexagon; JTBPY Johnson trigonal pyramid J2, SPY – Spherical square pyramid, TBPY – Trigonal bipyramid, vOC – Vacant octahedron, PP – Pentagon.

The chemical formula proposed by molecular structure and elemental analysis is $\text{Co}^{2+}_3(\text{HHTP})^3\text{[BH(TP}^{\text{Ph,Ph}})_3\text{]}_3$. Similar to **4-2**, HHTP is in the oxidation state of tri-semi-quinonate [sq-sq-sq] and the 3- negative charge. Two of the electrons couple but it is not possible from analyzing the bonds lengths to suggest whether the single electron lies near one Co(II) ion or delocalized along the aromatic ring.

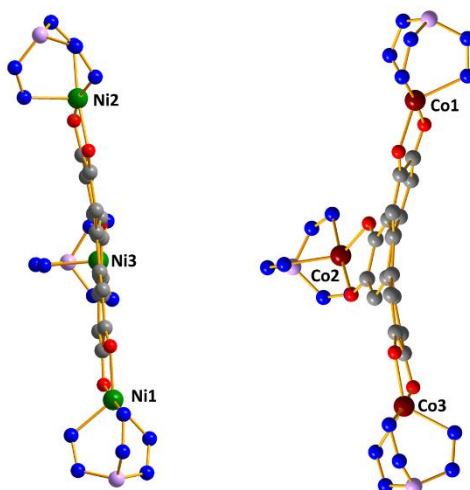


Figure IV.6 The comparison of the molecular structures of complex **4-2** (left) and **4-3** (right).

4.3.2 Magnetism

Measurements of dc magnetic susceptibilities (χT) have been conducted on complexes **4-1** to **4-3** in the magnetic field of 1 T and the temperature range of 300 - 2 K. The magnetization vs. the applied magnetic field have been measured in the field 0 – 6 T and under several temperature conditions: 2 K, 4 K, 6 K and 8 K. All the magnetic properties measurements were conducted with pellet samples, eliminating the diamagnetic contribution of eicosane.

4.3.2.1 Magnetic properties of Complex 4-1

The temperature dependence of the χT product for **4-1** is plotted in Figure IV.7. The χT value is at around $7.67 \text{ cm}^3 \text{ mol}^{-1} \text{ K}$ at room temperature, close to the value of six spin only Ni(II) ions ($7.67 \text{ cm}^3 \text{ mol}^{-1} \text{ K}$ when $g = 2.20$), which confirms the absence of radicals on the HHTP. When cooling down, the χT value remain almost constant down to 35 K and then decreases sharply to reach a value of $2.3 \text{ cm}^3 \text{ mol}^{-1} \text{ K}$ at 2 K. This behavior is consistent with very weak antiferromagnetic coupling between the Ni(II) ions or no coupling but only zero-field splitting. It is surprising that only a very weak coupling is present despite the oxo bridging the Ni(II) ions of the two different layers. The magnetization vs. the applied dc magnetic field for complex **4-1**, collected at different temperatures, are plotted in the form of $M = f(\mu_0 H)$ and $M = f(\mu_0 H/T)$ in Figure IV.8. The largest value can be observed as $10.40 \mu_B$ at $T = 2 \text{ K}$ and $\mu_0 H = 6 \text{ T}$, smaller than the saturated magnetization ($13.20 \mu_B$ for $g = 2.20$). The magnetization data reveal the existence of ZFS from the non-superimposition of the $M = \mu_0 H/T$ curves (Figure IV.8-right).

The simultaneous fitting of the $\chi T = f(T)$ and the $M = f(\mu_0 H)$ data gives the following values: $g = 2.27$, $D = 6.31 \text{ cm}^{-1}$, $J_{NiONi} = -0.52 \text{ cm}^{-1}$. The analysis of the magnetic data indicates a very weak antiferromagnetic coupling between the two Ni(II) ions connected by one O atom within the (TMEDA-Ni)₂O species. However, no detectable coupling can be observed between HHTP³⁻ bridge. The Ni coordination spheres are elongated octahedra with the bridging oxo ion lying in the xy plane (the z axis is defined along the elongation axis). The

two x^2-y^2 orbitals are, thus, orthogonal because the NiONi angle is close to 90° . The exchange coupling through the oxo ligand should thus be ferromagnetic. The exchange coupling through the O1, an oxygen atom belonging to HHTP involves a z^2 orbital of one Ni and a x^2-y^2 orbital of the other Ni. This coupling is expected to be antiferromagnetic because the NiONi angle is around 81° leading to a non-zero overlap integral. However, the magnitude of the contribution is expected not to be large because the single electron in the z^2 orbital is weakly delocalized on the bridging O (O1) because the rather large Ni-O1 bond length (2.261 Å). There are two such antiferromagnetic contributions. The two (weak) antiferromagnetic contributions, probably, compensate the ferromagnetic one leading overall to the weak antiferromagnetic exchange observed.

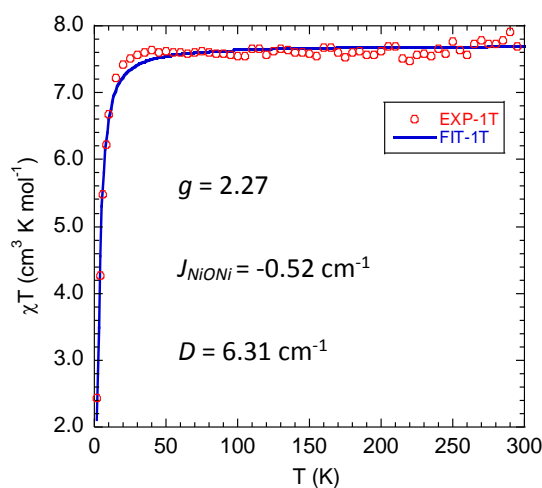
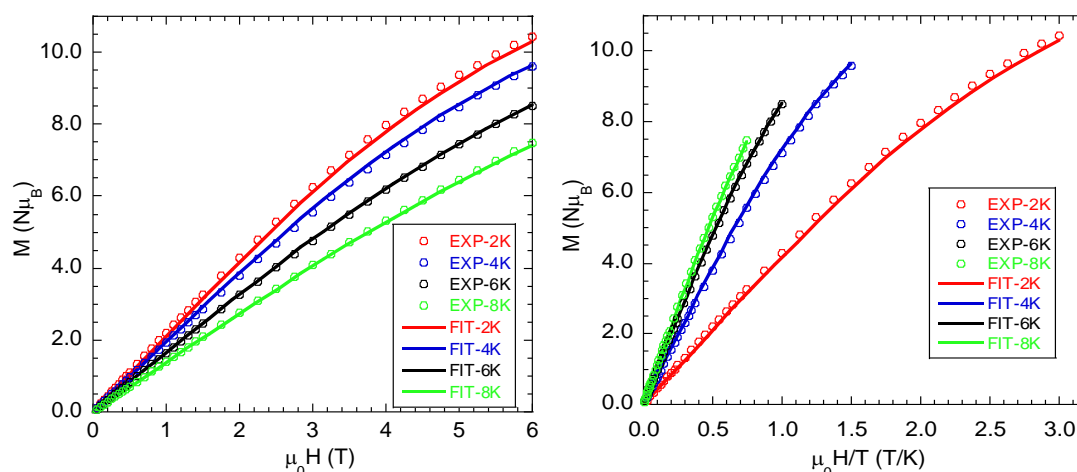
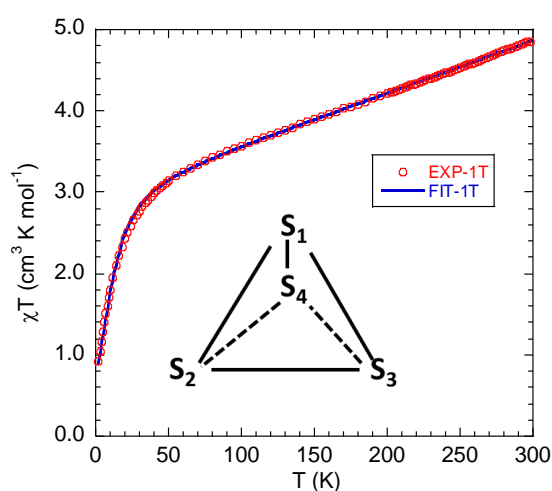


Figure IV.7 Temperature dependence of the χT product for **4-1**.

Figure IV.8 Magnetization vs. μ_0H (left) and vs. μ_0H/T (right) at variable temperatures for **4-1**.

4.3.2.2 Magnetic properties of Complex 4-2

The temperature dependence of the χT product for **4-2** is plotted in Figure IV.9. No plateau is observed. The value of χT is large ($4.86 \text{ cm}^3 \text{ mol}^{-1} \text{ K}$) at 300 K, higher than the spin-only value for three high-spin Ni^{2+} centers and one $S = 1/2$ ($4 \text{ cm}^3 \text{ mol}^{-1} \text{ K}$ with $g_{\text{Ni}} = 2.20$ and $g_{\text{rad}} = 2$). χT decreases continuously upon cooling from room temperature to 50 K, then more abruptly and reaches a value of $0.8 \text{ cm}^3 \text{ mol}^{-1} \text{ K}$ at 2 K (Figure IV.9). The magnetization vs. the applied dc magnetic field for complex **4-2**, collected at different temperatures, are plotted in the form of $M = f(\mu_0H)$ and $M = f(\mu_0H/T)$ in Figure IV.10.

Figure IV.9 Temperature dependence of the χT product for **4-2**. The insert is the simulation spin mode. $S_1 = S_2 = S_3 = 1$; $S_4 = 1/2$. S_1 represents Ni1, S_2 -Ni2, S_3 -Ni3, and S_4 is the radical.

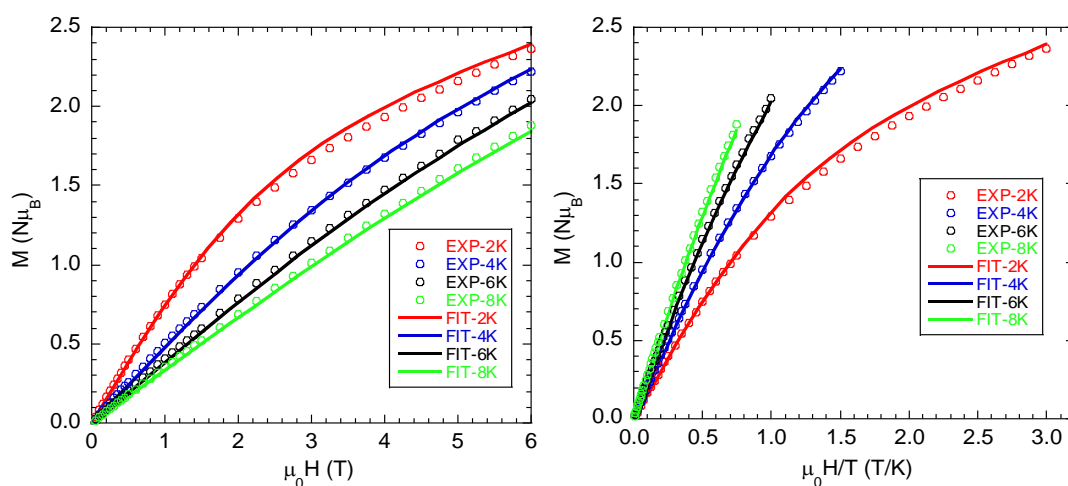


Figure IV.10 Magnetization vs. $\mu_0 H$ (left) and vs. $\mu_0 H/T$ (right) at variable temperatures for **4-2**.

Based on its molecular structure and on the assumption that the radical is located close to the trigonal bipyramid Ni, four magnetic centers can be considered: S_1 to S_3 corresponding to Ni1 to Ni3 respectively and S_4 to the organic radical that is assumed closer to Ni1. The magnetic data were, thus, fitted, assuming the model depicted in the insert of Figure IV.9, where the direct coupling between the Ni(II) ions was neglected, corresponding to the following Hamiltonian : $\mathbf{H} = -2J(S_1 \cdot S_4 + S_2 \cdot S_4 + S_3 \cdot S_4)$. Fitting simultaneously the magnetization and the susceptibility data leads to different sets of parameters that are different but relatively close (Table IV.4). The main difference concerns the ZFS parameters E and D for Ni2 and Ni3. The ZFS parameters are in agreement with the expected ones for Ni(II) ions in the corresponding geometry: Ni2 and Ni3 have a geometry close to square pyramidal and a positive large D value is expected.²⁹ For Ni1, we found that the D value has almost no effect on the fit, this is because the radical was assumed close to this Ni that has a trigonal bipyramid geometry (preliminary theoretical calculations confirm this assignment) and undergoes an large exchange coupling. Finally, the exchange coupling parameter between the radical and Ni1 was found to be large (-400 cm^{-1}) as expected from a radical localized on the semi-quinone part of the ligand. For the same reason the coupling between the radical and Ni2 and Ni3 is weak (-1.18 cm^{-1}). The g value for Ni1 is larger than those of Ni2 and Ni3 as expected from their geometries.

The fitting results for χT and magnetization displayed in Figure IV.9 and Figure IV.10 correspond to the **Set-3** that leads to the best fitting for the χT product but slightly less perfect for the magnetization. Slight changes in the parameters can cause small changes to the fitting curves: a better fitting for magnetization will result in a slightly less good result for χT and it's impossible to have one set of parameters that leads to perfect fittings for both χT product and magnetization, Set-3 being the best compromise.

Table IV.4 Different results obtained by fitting.

	Set-1	Set-2	Set-3	Set-4
g_1	2.38	2.38	2.38	2.38
g_2	2.17	2.17	2.17	2.17
g_3	2.17	2.17	2.17	2.17
g_4	2	2	2	2
D_1 (cm ⁻¹)		Any value from -60 to 40		
D_2 (cm ⁻¹)	27.6	28.7	33.3	30.6
D_3 (cm ⁻¹)	27.6	28.7	33.3	30.6
E_1 (cm ⁻¹)	0	0	0	0
E_2 (cm ⁻¹)	0.7	0.7	10.0	0
E_3 (cm ⁻¹)	0.7	0.7	10.0	0
J_{14} (cm ⁻¹)	-400	-400	-400	-400
J_{24} (cm ⁻¹)	0	-0.55	-1.18	-1.16
J_{34} (cm ⁻¹)	0	-0.55	-1.18	-1.16

4.3.2.3 Magnetic properties of Complex 4-3

The χT versus T plot for complex **4-3** is presented in the left of Figure IV.11. χT is equal to 7.67 cm³ mol⁻¹ K at room temperature. When cooling down from 300 K to 2 K, χT decreases slowly from 300 to 100 K and then suddenly and reaches a value of 3.4 cm³ mol⁻¹ K at $T = 2$ K. The magnetization curves have the usual shape. The value at $T = 2$ K and $H = 6$ T is 4.6 μ_B . This value is much weaker than the one corresponding to three $S = 3/2$ and a $S = 1/2$ species (10 μ_B assuming an average g value equal to 2). This may be due to a large ZFS that reduces the magnetization value.

We tried to simultaneously fit the χT and the magnetization curves with no success. It turned out impossible to have even a reasonable fit. We, therefore, tried to fit first the susceptibility data with the same spin Hamiltonian and the same model as for complex **4-2**. The simulation gives the following values: $g_1 = g_2 = g_3 = 2.49$, $g_4 = 2$; $D_1 = D_3 = -31.7 \text{ cm}^{-1}$, $D_2 = -29.6 \text{ cm}^{-1}$; $J_{24} = -210.8 \text{ cm}^{-1}$. The exchange parameter value is reasonable if one assumes that the single electron of the radical is close to one of the Co(II) ions. But, the sign of the ZFS parameter does not correspond to the expected one for a distorted trigonal bipyramid, where a positive D value is expected.²⁹

With these values, it is not possible to reproduce the magnetization data as shown in (Figure IV.11-right).

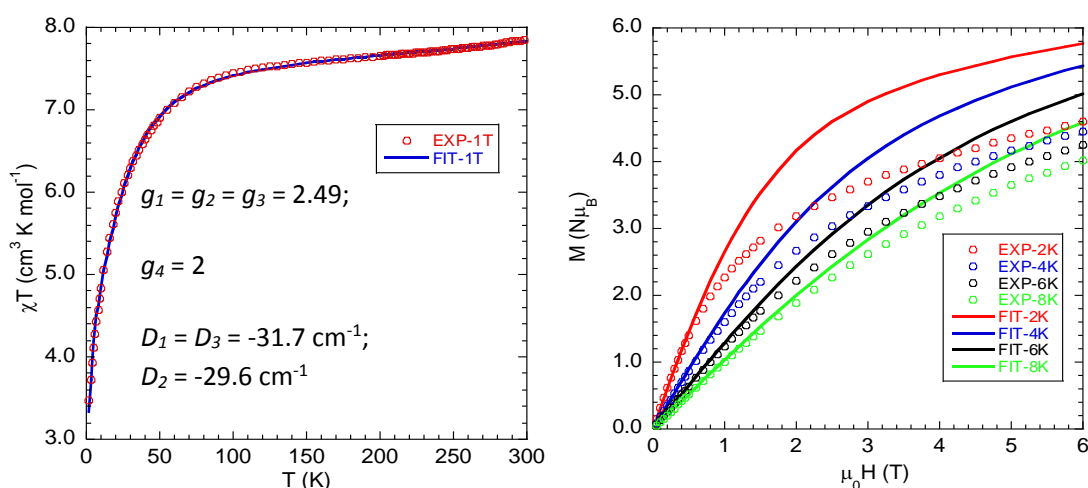


Figure IV.11 Temperature dependence of the χT product (left) and magnetization vs. $\mu_0 H$ (right) at variable temperatures for **4-3**.

By analyzing the magnetization data, one observes that the value of $4.6 \mu_B$ at $T = 2 \text{ K}$ and $H = 6 \text{ T}$ may correspond to two Co(II) ions. One possible assumption is that one Co(II) was oxidized to Co(III) and the radical reduced. This situation is well-known in Co(II)-semiquinone complexes.²⁸ It is, however, puzzling that the oxidation/reduction process occurred at low temperature. It is important to note that the measurements of χT and M were carried out successively without removing the sample from the SQUID magnetometer.

The situation is summarized in Figure IV.12, where S_1 , S_2 and S_3 represent the high-spin Co(II) ions ($S = 3/2$), S_4 the radical ($S = 1/2$), and S_2' the low-spin Co(III) ion ($S = 0$).

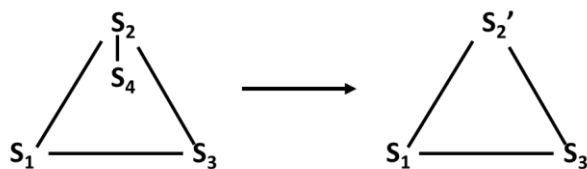


Figure IV.12. Coupling spin models before and after the oxidation/reduction process for **4-3**.

The magnetization data were, thus fitted considering two Co(II) ions. A very good fit (Figure IV.13) was obtained with $g = 2.49$, $D = -10.2 \text{ cm}^{-1}$ and $J = 0$. No magnetic coupling was detected between the two Co(II) centers. More measurement should be carried out in order to understand the behavior of this complex.

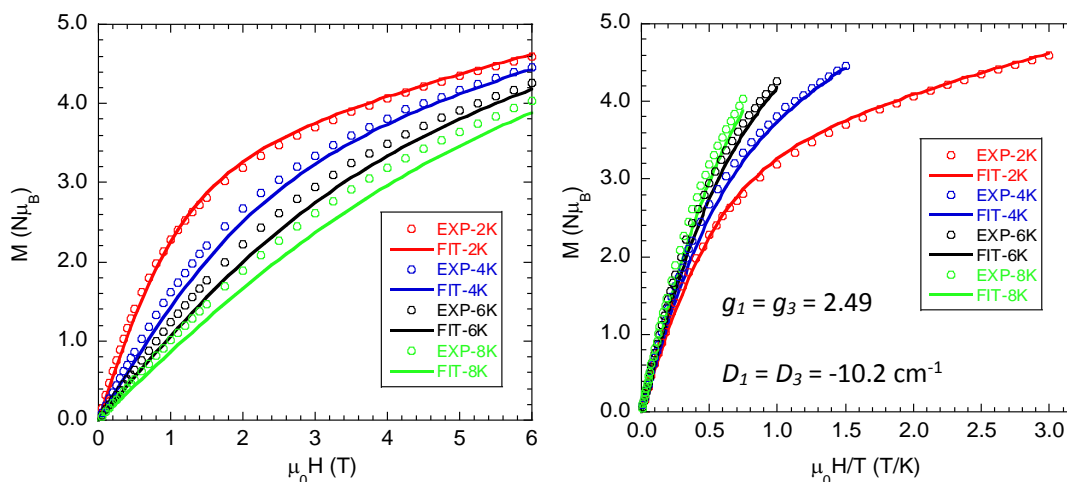


Figure IV.13 Magnetization vs. μ_0H (left) and vs. μ_0H/T (right) at variable temperatures for **4-3**.

4.3.3 Electronic Spectra and Electrochemical properties

All the electrochemical measurements were carried out in an electrochemical cell at room temperature, under the atmosphere of Ar. Glassy carbon was used as working electrode, with platinum wire and saturated calomel electrode (SCE) acting as counter electrode and reference electrode, respectively. The step scan was set as 0.1 V/s. The solution of complexes introduced in the cell is 1 mmol/L, 5 mL.

4.3.3.1 Electronic spectrum and electrochemistry of Complex 4-1

The electronic spectrum of complex **4-1** in DMF is displayed in Figure IV.14. The absorption in the near infrared region (1052 nm, $\epsilon = 30000 \text{ cm}^{-1}\text{mol}^{-1}\text{L}$) can be ascribed to the $\pi\text{-}\pi^*$ ligand centered transition because it occurs at the lowest energy. The other two bands at higher energy may be assigned to metal-to-ligand charge transfer or also to other transitions centered on the ligand. Theoretical calculations are needed to assign the different bands.

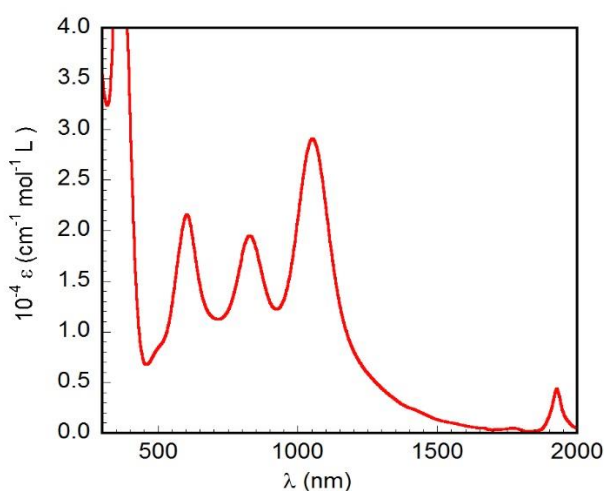


Figure IV.14 Room temperature electronic spectrum of complex **4-1** in DMF.

The electrochemical study was conducted on a 0.1 mol/L DMF solution of Bu_4NPF_6 , containing **4-1** with a concentration of 1 mmol/L. The cyclic voltammogram (CV) is displayed in Figure IV.15. The scan starts at -0.12 V where the current is equal to zero and goes towards negative potential values (-2.0 V) to perform reduction, and then back to -0.12 V. Three reversible redox waves are observed at potential values of -0.64 V, -1.02 V and -1.35 V vs. SCE. They correspond to the successive injection of three electrons into the organic part of the complex. A fourth reduction process is observed around -1.7 V but it seems not to be reversible. The process at -1.35 V seems also not to be completely reversible. When the potential is scanned in the oxidation part above -0.12 V, a completely irreversible wave due to the $[\text{sq-sq-sq}]/[\text{sq-sq-q}]$ process is observed (not shown). The

origin of the irreversibility is the formation of the quinone that is a very poor ligand to Ni(II), probably leading to the de-coordination of the metal ion.

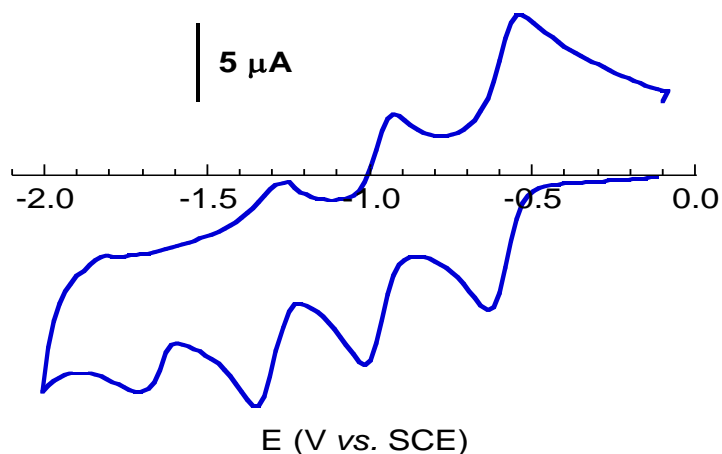


Figure IV.15 Room temperature CV of **4-1** with Bu_4NPF_6 as supporting electrolyte in DMF.

4.3.3.2 Electronic spectrum and electrochemistry of Complex **4-2**

The Figure IV.16 exhibits the absorption spectrum of complex **4-2** in CH_2Cl_2 . The near-IR band (1155 nm, $\epsilon = 10000 \text{ cm}^{-1}\text{mol}^{-1}\text{L}$) that can be assigned to the transition centered on the HHTP^{3-} ligand is at lower energy (8660 instead of 9500 cm^{-1}) than that of complex **4-1**, which is consistent of a larger delocalization of the electron in **4-2**.

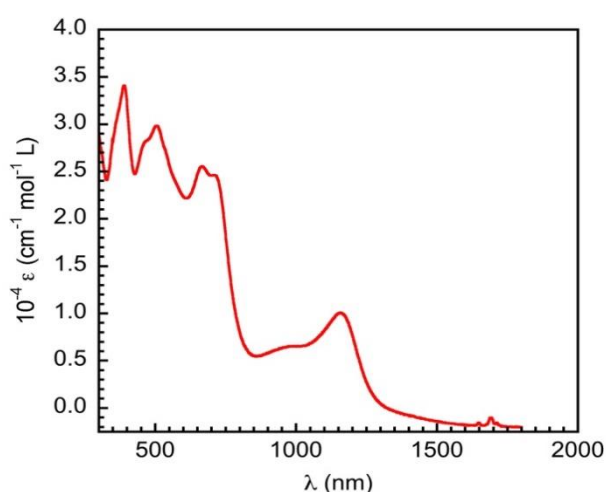


Figure IV.16 Room temperature electronic spectrum of CH_2Cl_2 solution of complex **4-2**.

The electrochemical study was carried out in the same condition as for **4-1** (Figure IV.17). The open circuit potential is at 0.15 V. Upon reduction, three waves are observed: the first at -0.28 V, corresponding to the reduction of the bridging ligand from HHTP³⁻ to HHTP⁴⁻ i.e. from [sq-sq-sq] to [cat-sq-sq], then, at -0.78 V corresponding to the reduction from [cat-sq-sq] state (HHTP⁴⁻) to [cat-cat-sq] state (HHTP⁵⁻) and finally at -1.17 V, suggesting the generation of HHTP⁶⁻, the [cat-cat-cat] state. As the scanning goes back to the positive direction, correspondingly, three oxidation waves are observed. The stepwise reversible redox waves imply the one electron redox process on the bridging ligand. The first reduction potential for the trinuclear complex is at less negative value than for the hexanuclear one (-0.28 instead of -0.64 V). In addition, the difference between the redox couples is larger in the trinuclear than in the hexanuclear complex, which is consistent with a larger electronic interaction in the former than in the latter. This is reasonable because the two additional electrons in the hexanuclear complex feel less electron-electron repulsion than for the trinuclear one because their larger delocalization on two HHTP ligands; while for the trinuclear one, the two electrons are on one HHTP ligand. In summary, in the pristine complexes the overall electron delocalization on the HHTP³⁻ (**4-2**) is larger than that on the [HHTP-HHTP]⁶⁻ dimerized species (**4-1**), so the injection of one electron on **4-2** occurs at less negative potential. However, the injection of the second (and third) electron is relatively easier on the hexanuclear complex because of the reduced electron-electron repulsion due to its delocalization on two HHTP species.

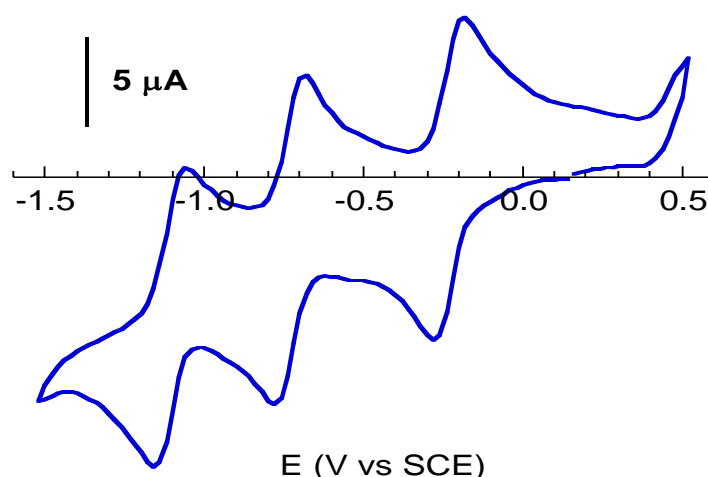


Figure IV.17 Room temperature CV of **4-2** with Bu_4NPF_6 as supporting electrolyte in CH_2Cl_2 .

The spectro-electrochemical studies on this complex at different values of the potential are depicted in Figure IV.18. The reduction from 0 to -0.5 V leads to the appearance of an absorption band close to 1360 nm (7350 cm^{-1}) that can be assigned to a transition within the reduced [cat-sq-sq] species. The energy of this band is lower than that corresponding to the [sq-sq-sq] (1150 nm , 8660 cm^{-1}) species suggesting that the electron delocalization is larger in reduced form. Reducing further (-0.7 V) leads to a decrease of the intensity of the 1360 nm band and to the appearance of a new band around 940 nm (at higher energy; 10640 cm^{-1}). This is consistent with reduced delocalization in the [cat-cat-sq] species. Further reduction leads to other changes in the absorption spectra but their interpretation is underway. It is tempting to assign the lower degree of delocalization in the [sq-sq-sq] and the [cat-cat-sq] species that have single electrons to the fact that the single electron is close to one of the three metal ions. While, the diamagnetic [cat-sq-sq] species has a higher degree of delocalization because the three paired electrons are in molecular orbitals delocalized on the organic ligand. Further studies are necessary to elucidate the electronic properties of the different species.

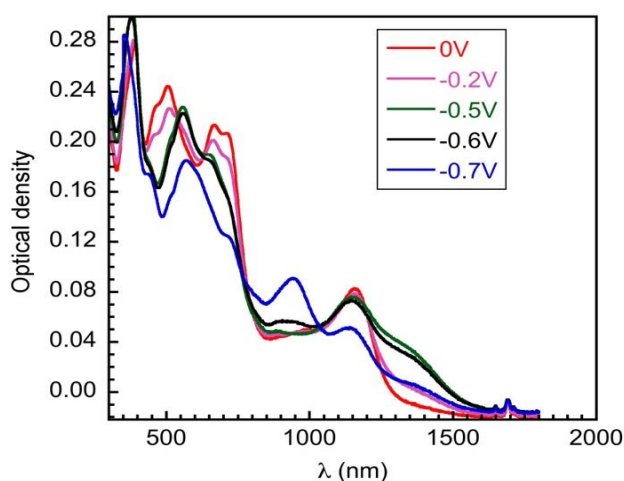


Figure IV.18 Electronic absorption spectra of **4-2** at different reducing potential values.

4.3.3.3 Electronic spectrum and electrochemistry of Complex **4-3**

The electronic spectrum, displayed in Figure IV.19, is almost identical to that of the Ni-containing compound. The near-IR band, at 1126 nm (8880 cm^{-1}), is slightly shifted towards higher energy in comparison to the Ni complex **4-2** (8660 cm^{-1}), showing that the organic ligand has almost the same electronic configuration in the two complexes.

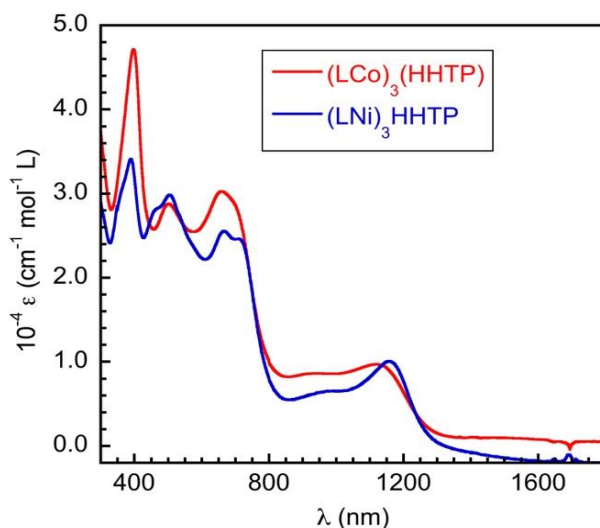


Figure IV.19 Room temperature electronic spectrum of CH_2Cl_2 solution of complex **4-3**.

The electrochemical study of **4-3** was carried out in CH_2Cl_2 solution in the same condition as for the Ni based complex. A similar CV is obtained (Figure IV.20) with the three reversible

redox waves (-0.22, -0.66 and -1.04V) being at slightly less negative potential than for **4-2** (-0.28, -0.78 and -1.17 V).

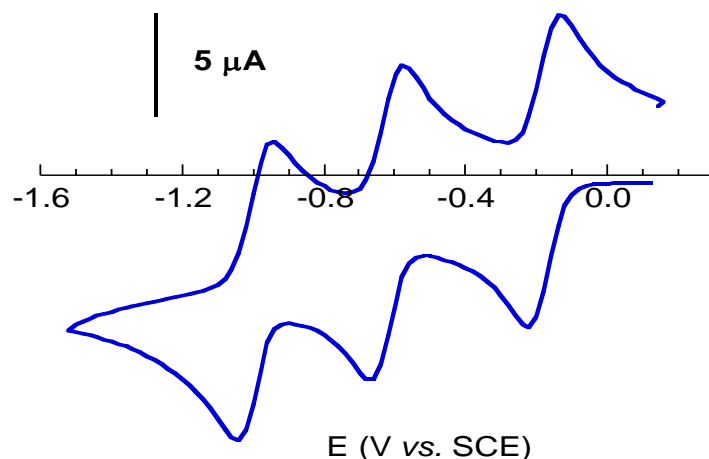
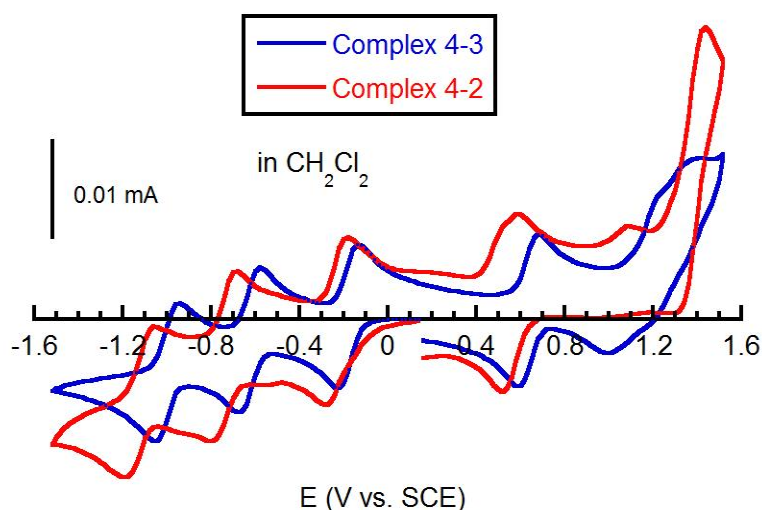


Figure IV.20 Room temperature CV of **4-3** with Bu_4NPF_6 as supporting electrolyte in CH_2Cl_2 .

The CVs of the two compounds are shown in Figure IV.21. The first redox couple corresponding to the reduction of HHTP from [sq-sq-sq] to [cat-sq-sq] is shifted by only 0.06 V towards negative values for the Ni-containing complex in comparison the Co one. But, the two following reduction processes are further shifted (0.12 V). This is consistent with a slightly larger electron-electron repulsion for the Ni complex than for the Co one, upon injecting electrons. The spectro-electrochemical studies would allow to have more insight in the difference between the two complexes, but they have not been conducted yet on the Co complex. On the oxidation side, one quasi reversible wave is observed around +0.6 and +0.7 V for the Ni and the Co containing complexes respectively. For Co, the oxidation wave is reversible, while for Ni two waves are observed for oxidation and only one for reduction. At higher potential, no reversible waves could be observed. The one electron oxidation of the ligand leads to the [sq-sq-q] species. The quinone part is a poor ligand and de-coordination of one NiL species is expected. The de-coordination may be avoided if the quinone is not localized on one end of the HHTP ligand, or when the solvent is not a coordinating one as is the case of CH_2Cl_2 . These studies are preliminary and must be completed with CVs at different speeds and with spectro-electrochemical studies.

Figure IV.21 Comparison of the cyclo-voltammograms of **4-2** and **4-3**.

4.4 Theoretical Calculations

Preliminary theoretical calculations were carried out on the Ni trinuclear complex **4-2**. They present two important features. The first is that the three electrons on the ligand couple together and lead to a doublet ($S = 1/2$) ground state with the excited doublet and quartet ($S = 3/2$) at 2600 and 4600 cm^{-1} respectively, which correspond to an antiferromagnetic exchange coupling parameter J around -3060 cm^{-1} ($H = -J\mathbf{S}_1 \cdot \mathbf{S}_2$ with $S_1 = S_2 = 1/2$) between two of the three electrons and an exchange coupling parameter J' of about -440 cm^{-1} between the remaining electron and the two others ($H = -J'(\mathbf{S}_3 \cdot \mathbf{S}_2 + \mathbf{S}_3 \cdot \mathbf{S}_1)$ with $S_3 = 1/2$). This scheme is consistent with our assumption that the three electrons on the HHTP^{3-} can be described as a pair and a single electron. The second feature is that the remaining single electron is localized near the Ni(II) (Figure IV.22) that has the trigonal bipyramid geometry (Ni1) and undergoes an antiferromagnetic exchange coupling with this Ni that was calculated to be around -200 cm^{-1} , which is half of the value found from fitting the magnetic data.

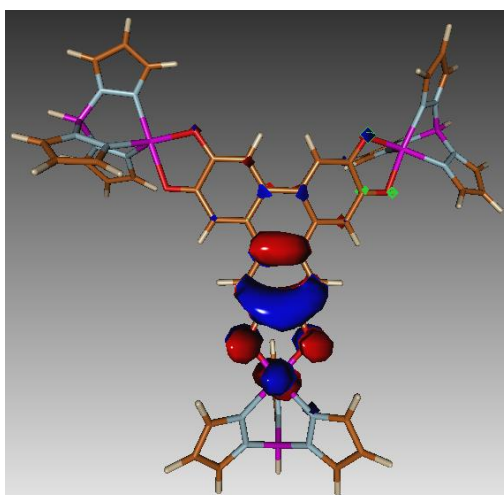


Figure IV.22 View of the molecular orbital that describes the single electron on HHTP³⁻.

The overall electronic picture that was suggested from the structural features of the complex and from the magnetic data are perfectly consistent with the results of the theoretical calculations. Complementary theoretical studies on the pristine complex are underway in order to assign the absorption spectrum and also on the reduced species that may allow to rationalize the spectro-electrochemical results.

4.5 Conclusions

To summarize, we presented the syntheses, molecular structures, magnetic studies, electronic spectra and electrochemical properties of three polynuclear complexes, where the metal ions are bridged by the non-innocent ligand HHTP. For the three complexes, the charge of HHTP was found to be 3-, corresponding to the [sq-sq-sq] state. The synthesis was made starting from the deprotonated tris-catecholate ligand that evolved in solution during the reaction to give the three oxidized species [sq-sq-sq]. We did not investigate the oxidation process during the reaction and this should be done in the future.

These three complexes must be further investigated and more importantly the different species obtained from the three reduction steps must be chemically isolated and studied.

We have carried out preliminary EPR studies of the pristine (LNi₃)HHTP species and those obtained by the three successive reduction processes. The EPR spectra follow the trend

expected, but they were not fully analyzed yet. The trinuclear Co complex was not studied by EPR, such study will help to understand its magnetic behavior in the solid state. However, the analysis of the EPR spectra is expected to be difficult because, unlike Ni(II), resonances centered on Co(II) can be observed by X-band EPR. The presence of valence tautomerism would be detected in the EPR spectra.

4.6 References

- 1 Bechgaard, K. & Parker, V. D. Mono-, di-, and trications of hexamethoxytriphenylene. Novel anodic trimerization. *Journal of the American Chemical Society* **94**, 4749-4750 (1972).
- 2 Breslow, R., Jaun, B., Kluttz, R. Q. & Xia, C.-z. Ground state Pi-electron triplet molecules of potential use in the synthesis of organic ferromagnets. *Tetrahedron* **38**, 863-867 (1982).
- 3 Chiang, L., Johnston, D., Stokes, J. & Bloch, A. Synthesis and study of multiple cationic salts of hexamethoxytriphenylene (HMTP). *Synthetic Metals* **19**, 697-702 (1987).
- 4 Caneschi, A., Dei, A., Lee, H., Shultz, D. A. & Sorace, L. Ferromagnetically coupled bis (semiquinone) ligand enforces high-spin ground states in bis-metal complexes. *Inorganic chemistry* **40**, 408-411 (2001).
- 5 Caneschi, A. *et al.* High-spin metal complexes containing a ferromagnetically coupled tris (semiquinone) ligand. *Inorganic chemistry* **41**, 1086-1092 (2002).
- 6 Dutta, S. K., Beckmann, U., Bill, E., Weyhermüller, T. & Wieghardt, K. 1, 2-Bis (pyridine-2-carboxamido) benzenate (2-), (bpb) 2-: A Noninnocent Ligand. Syntheses, Structures, and Mechanisms of Formation of [(n-Bu) 4N][FeIV2 (μ-N)(bpb) 2 (X) 2](X= CN-, N3-) and the Electronic Structures of [MIII (bpb) 1(CN) 2](M= Co, Fe). *Inorganic chemistry* **39**, 3355-3364 (2000).
- 7 Hoshino, N. & Akutagawa, T. A Trinuclear Iron(III) Complex of a Triple Noninnocent Ligand for Spin-Structured Molecular Conductors. *Chemistry* **24**, 19323-19331, doi:10.1002/chem.201804280 (2018).
- 8 Campbell, M. G., Liu, S. F., Swager, T. M. & Dinca, M. Chemiresistive Sensor Arrays from Conductive 2D Metal-Organic Frameworks. *J Am Chem Soc* **137**, 13780-13783, doi:10.1021/jacs.5b09600 (2015).
- 9 Li, W.-H. *et al.* Conductive Metal-Organic Framework Nanowire Array Electrodes for High-Performance Solid-State Supercapacitors. *Advanced Functional Materials* **27**, 1702067, doi:10.1002/adfm.201702067 (2017).

- 10 Smith, M. K., Jensen, K. E., Pivak, P. A. & Mirica, K. A. Direct Self-Assembly of Conductive Nanorods of Metal–Organic Frameworks into Chemiresistive Devices on Shrinkable Polymer Films. *Chemistry of Materials* **28**, 5264-5268, doi:10.1021/acs.chemmater.6b02528 (2016).
- 11 Hmadeh, M. *et al.* New porous crystals of extended metal-catecholates. *Chemistry of Materials* **24**, 3511-3513 (2012).
- 12 Spitler, E. L. *et al.* A 2D covalent organic framework with 4.7-nm pores and insight into its interlayer stacking. *J Am Chem Soc* **133**, 19416-19421, doi:10.1021/ja206242v (2011).
- 13 Calik, M. *et al.* Extraction of photogenerated electrons and holes from a covalent organic framework integrated heterojunction. *J Am Chem Soc* **136**, 17802-17807, doi:10.1021/ja509551m (2014).
- 14 Calik, M. *et al.* From Highly Crystalline to Outer Surface-Functionalized Covalent Organic Frameworks--A Modulation Approach. *J Am Chem Soc* **138**, 1234-1239, doi:10.1021/jacs.5b10708 (2016).
- 15 Medina, D. D. *et al.* Room temperature synthesis of covalent-organic framework films through vapor-assisted conversion. *J Am Chem Soc* **137**, 1016-1019, doi:10.1021/ja510895m (2015).
- 16 Zeng, Y. *et al.* Covalent organic frameworks formed with two types of covalent bonds based on orthogonal reactions. *J Am Chem Soc* **137**, 1020-1023, doi:10.1021/ja510926w (2015).
- 17 Suenaga, Y. *et al.* Crystal Structure and Characterization of Trinuclear Cobalt(III) Complex with 2,3,6,7,10,11-Hexahydroxytriphenylene. *Chemistry Letters* **43**, 562-564, doi:10.1246/cl.131090 (2014).
- 18 Barthram, A. M., Cleary, R. L., Kowallick, R. & Ward, M. D. A new redox-tunable near-IR dye based on a trinuclear ruthenium (II) complex of hexahydroxytriphenylene. *Chemical communications*, 2695-2696 (1998).
- 19 Grange, C. S., Meijer, A. J. & Ward, M. D. Trinuclear ruthenium dioxolene complexes based on the bridging ligand hexahydroxytriphenylene: electrochemistry, spectroscopy, and near-infrared electrochromic behaviour associated with a reversible seven-membered redox chain. *Dalton transactions* **39**, 200-211 (2010).
- 20 Muranaka, A. *et al.* Solid-phase synthesis of phthalocyanine and tetraazaporphyrin triangular prisms. *Tetrahedron Letters* **49**, 5084-5086, doi:10.1016/j.tetlet.2008.06.025 (2008).

- 21 Gaudette, A. I. *et al.* Electron Hopping through Double-Exchange Coupling in a Mixed-Valence Diiminobenzoquinone-Bridged Fe₂ Complex. *J Am Chem Soc* **137**, 12617-12626, doi:10.1021/jacs.5b07251 (2015).
- 22 Evangelio, E. *et al.* Coexistence of Two Thermally Induced Intramolecular Electron Transfer Processes in a Series of Metal Complexes [M (Cat - N - BQ)(Cat - N - SQ)]/[M (Cat - N - BQ) ₂](M= Co, Fe, and Ni) bearing Non - Innocent Catechol - Based Ligands: A Combined Experimental and Theoretical Study. *Chemistry – A European Journal* **16**, 6666-6677 (2010).
- 23 Glaser, T. *et al.* Trinuclear nickel complexes with triplesalen ligands: simultaneous occurrence of mixed valence and valence tautomerism in the oxidized species. *Inorganic chemistry* **44**, 5467-5482 (2005).
- 24 Wang, Z.-X. & Qin, H.-L. Solventless syntheses of pyrazole derivatives Electronic supplementary information (ESI) available: analytical and spectroscopic data. . *Green Chemistry* **6**, 90, doi:10.1039/b312833d (2004).
- 25 Casanova, D., Lluell, M., Alemany, P. & Alvarez, S. The rich stereochemistry of eight - vertex polyhedra: a continuous shape measures study. *Chemistry – A European Journal* **11**, 1479-1494 (2005).
- 26 Alvarez, S. *et al.* Shape maps and polyhedral interconversion paths in transition metal chemistry. *Coordination Chemistry Reviews* **249**, 1693-1708 (2005).
- 27 Gordy, W. Dependence of Bond Order and of Bond Energy Upon Bond Length. *The Journal of Chemical Physics* **15**, 305-310, doi:10.1063/1.1746501 (1947).
- 28 Beni, A., Dei, A., Laschi, S., Rizzitano, M. & Sorace, L. Tuning the charge distribution and photoswitchable properties of cobalt-dioxolene complexes by using molecular techniques. *Chemistry* **14**, 1804-1813, doi:10.1002/chem.200701163 (2008).
- 29 Cahier, B. *et al.* Magnetic Anisotropy in Pentacoordinate Ni(II) and Co(II) Complexes: Unraveling Electronic and Geometrical Contributions. *Chemistry–A European Journal* **23**, 3648-3657 (2017).

Chapter V

Conclusion and future work

5.1 Conclusion

In this dissertation, two main parts are presented.

The first part focuses on the study of the magnetic anisotropic of mononuclear complexes based on Ni(II) of general formula $[\text{Ni}(\text{Me}_6\text{tren})\text{X}]\text{Y}$ ($\text{X} = \text{Cl}, \text{Br}, \text{I}; \text{Y} = \text{Cl}^-, \text{BPh}_4^-, \text{PF}_6^-, \text{CF}_3\text{SO}_3^-, \text{ClO}_4^-$ and I^-) possessing a trigonal bipyramidal geometry. Depending on the nature of the counter anion, complexes with strict C_{3v} symmetry or distorted were obtained. The magnetic data were fitted with different axial ZFS parameters with the larger values (negative) corresponding to the high symmetry complexes. However, the spin Hamiltonian approximation does not hold when the axial ZFS parameter is very large corresponding to first order or quasi first order spin orbit coupling. Theoretical calculations were carried out on two compounds ($\text{X} = \text{Y} = \text{Cl}$) that have different distortions and magneto-structural correlations were made. Calculations on the other distorted complexes ($\text{X} = \text{Cl}, \text{Y} = \text{CF}_3\text{SO}_3$ and $\text{X} = \text{Cl}, \text{Y} = \text{BPh}_4$) are underway, which will allow to carry out a more complete magneto-structural correlation. The rhombic parameters E are difficult to extract from the magnetic data because their interdependence with the axial ones; High Field-High Frequency EPR studies are necessary and are underway to experimentally determine these parameters and try to elaborate correlation with their structure.

The second part of the dissertation concerns the elaboration of polynuclear Ni(II) and Co(II) complexes with, on one hand, innocent ligands and, on the other hand, non-innocent ones.

For the innocent ligand, we used a tris-bidentate molecule in order to prepare polynuclear complexes with controlled local ZFS and weak exchange coupling. This is relevant for

complexes that may play the role entangled (by exchange coupling) quantum bits. The exchange coupling was found to be very weak as expected but it was not straightforward to determine whether it was ferro- or antiferromagnetic, even though the magnetic data are consistent with an antiferromagnetic coupling. EPR studies are necessary to determine the nature of the ground state for these complexes. Theoretical calculations were carried out on the mononuclear species of the trinuclear complexes and magneto-structural correlations were done to relate the structure to the axial ZFS parameters to the structure. When the geometry is not very distorted as for the pentacoordinate Co(II) species, correlation is possible. However, for the highly distorted octahedral geometry, it is difficult to draw simple conclusions.

For the non-innocent ligand, we used a tris-catecholate one that can undergo three oxidation processes to lead to the tris semi-quinonate species that was found to coordinate to the metal ions. We obtained, by serendipity, a hexanuclear $\text{Ni}_6(\text{HHTP})_2$ complex made of two trinuclear species forming two parallel layers. The magnetic data are consistent with very weakly antiferromagnetically coupled Ni(II) metal ions. It was possible to isolate the targeted trinuclear $(\text{LCo})_3\text{HHTP}$ and $(\text{LNi})_3\text{HHTP}$ complexes using a bulky and chelating L ligand that prevents the formation of the hexanuclear complex. The HHTP ligand was found to be in the tris semi-quinonate state bearing, therefore, a single electron. Preliminary electrochemical studies on the hexanuclear and the trinuclear complexes showed four and three reversible reduction processes respectively. The stepwise reversible wave peaks observed in the electrochemical studies disclosed that they are ligand-centered, which is testified by their electronic spectra. For the trinuclear complexes, it is possible to reduce the ligand from the tris semi-quinonate species to the tris catecholate one. Preliminary spectro-electrochemical studies were carried out on the $(\text{LNi})_3\text{HHTP}$ complex, but further studies are necessary. We also performed in situ EPR study on the reduced species that confirmed the presence of a single electron on the HHTP ligand, probably, interacting with the Ni(II) ions as assumed from the magnetic data. The EPR signal vanishes upon the first reduction step and another signal appears after the second process as expected, but it has a different shape. The electrochemical behavior of

the $(\text{LCo})_3\text{HHTP}$ complex is similar to the Ni(II) one. But, the magnetic data suggest that an oxydo-reduction process occurred during the magnetic study. This behavior must be elucidated.

5.2 Future work

The future work based on this study can be carried out in the following ways:

1. Conducting the theoretical calculations for the mononuclear complexes and making a further comparison among the complexes to draw a more complete magneto-structural correlation.
2. Carrying out the EPR measurements on these complexes to obtain the experimental g and E values, providing more information for the fitting of magnetic measurements and theoretical calculations. It is also necessary to use other techniques in order to determine experimentally the accurate values of the axial parameters D that are too large for EPR. Neutron Inelastic Scattering (NIS) studies are programmed in July and terahertz spectroscopy will be done at National Magnetic Laboratory (USA, Florida) during the summer.
3. For the complexes containing the non-innocent bridge, further electrochemical and spectroelectrochemical measurements should be carried out coupled to theoretical calculations to get insight into the nature of the ligand orbitals involved in the electrochemical processes.
4. Doing more measurements to understand the oxidation behavior from the high-spin Co(II) ion to low-spin Co(III) ion within complex $\text{Co}_3(\text{HHTP})[\text{BH}(\text{TP}^{\text{Ph,Ph}})_3]_3$ and to determine the temperature of the phase transition if any.
5. Isolating the reduced intermediate species to be able to perform their magnetic study. The preliminary in situ electrochemical-EPR studies are encouraging.

6. Assembling the complexes as single monolayers on diamagnetic and ferromagnetic substrates to investigate their magnetic and electronic behavior when interacting with metallic (charge transfer) and ferromagnetic (induced magnetism) substrates.

Appendix I The Crystallographic data

1.1 The complexes based on ligand Me₆tren

Table A 1 The crystallographic data structure refinement for complex 2-1

Complexes	2-1 (a)	2-1 (b)	2-1 (c)	2-1 (d)
Formula		NiC ₁₂ H ₃₀ Cl ₂ N ₄		NiC ₁₂ H ₃₀ Cl ₂ N ₄ , 2(H ₂ O)
<i>M_r</i>		360.01		396.04
Crystal size, mm ³	0.13 x 0.08 x 0.60		0.13 x 0.12 x 0.80	0.17 x 0.12 x 0.04
Crystal system	orthorhombic		cubic	orthorhombic
Space group	<i>P2₁2₁2₁</i>		<i>P2₁3</i>	<i>Pbca</i>
a, Å	11.374(4)	11.478(6)	11.8520(5)	9.1699(4)
b, Å	11.919(5)	11.966(7)	11.8520(5)	15.6319(5)
c, Å	12.038(4)	12.096(8)	11.8520(5)	26.5895(10)
α, °	90	90	90	90
β, °	90	90	90	90
γ, °	90	90	90	90
Cell volume, Å ³	1632.0(10)	1661.5(16)	1664.8(2)	3811.4(3)
Z ; Z'	4 ; 1		4 ; 1/3	8 ; 1
T, K	40(2)	100(1)	200(1)	100(1)
Radiation type; wavelength Å	Mo Kα ; 0.71073			
F ₀₀₀		768		1696
μ, mm ⁻¹	1.502	1.483	1.473	1.307

Appendix I The Crystallographic data

θ range, °	2.405 - 30.983	2.394 - 30.629	2.430 - 40.283	2.606 - 30.609
Reflection collected	38824	35367	79496	138587
Reflections unique	4989	5058	3510	5860
R_{int}	0.0613	0.0619	0.0506	0.0491
GOF	1.062	1.057	1.132	1.035
Flack parameter	0.025(7)	0.027(6)	0.001(3)	/
Refl. obs. ($I > 2\sigma(I)$)	4385	4496	2711	4174
Parameters		178		196
wR_2 (all data)	0.1459	0.1013	0.0853	0.1225
R value ($I > 2\sigma(I)$)	0.0566	0.0447	0.0325	0.0475
Largest diff. peak and hole ($e^- \cdot \text{\AA}^{-3}$)	2.280; -1.210	1.407; -0.731	1.380; -0.723	3.687; -0.647

Table A 2 The crystallographic data structure refinement for complexes **2-2**, **2-3**, **2-4**.

Complexes	2-2	2-3	2-4
Formula	NiC ₁₂ H ₃₀ ClN ₄ BC ₂₄ H ₂₀	NiC ₁₂ H ₃₀ ClN ₄ PF ₆	NiC ₁₂ H ₃₀ N ₄ ClCF ₃ SO ₃
M_r	643.77	469.51	473.61
Crystal size, mm ³	0.28 x 0.21 x 0.17	0.15 x 0.11 x 0.03	0.23 x 0.23 x 0.14
Crystal system	monoclinic	trigonal	orthorhombic
Space group	$P2_1/n$	$R\bar{3}-2$	$Pnma$
a, Å	12.5673(3)	10.2529(5)	16.1142(4)
b, Å	12.3077(3)	10.2529(5)	10.3982(3)
c, Å	21.6480(6)	16.0206(9)	12.2412(3)
α , °	90	90	90
β , °	97.7550(10)	90	90
γ , °	90	120	90
Cell volume, Å ³	3317.77(15)	1458.49(16)	2051.12(9)
Z ; Z'	4 ; 1	3 ; 1/6	4 ; 1/2
T, K	100(1)	100(1)	100(1)

Appendix I The Crystallographic data

Radiation type; wavelength Å	MoK α ; 0.71073	MoK α ; 0.71073	MoK α ; 0.71073
F ₀₀₀	1376	732	992
μ , mm ⁻¹	0.697	1.276	1.224
θ range, °	1.908 - 35.916	2.623 - 32.566	2.089 - 37.646
Reflection collected	117 566	13 273	57 176
Reflections unique	15 606	1 356	5 651
R _{int}	0.0304	0.0499	0.0231
GOF	1.030	1.087	1.097
Flack parameter	/	0.059(8)	/
Refl. obs. ($I > 2\sigma(I)$)	13 647	1 305	5 193
Parameters	394	69	190
wR ₂ (all data)	0.0713	0.0861	0.0633
R value ($I > 2\sigma(I)$)	0.0255	0.0335	0.0239
Largest diff. peak and hole (e ⁻ ·Å ⁻³)	0.542 ; -0.321	0.490 ; -0.616	0.806 ; -0.631

Table A 3 The crystallographic data structure refinement for complexes **2-5**, **2-6**, **2-7**

Complexes	2-5	2-6	2-7
Formula	NiC ₁₂ H ₃₀ BrN ₄ ClO ₄	NiC ₁₂ H ₃₀ BrN ₄ PF ₆	NiC ₁₂ H ₃₀ IN ₄ I
<i>M_r</i>	468.47	513.96	542.91
Crystal size, mm ³	0.14 x 0.13 x 0.06	0.13 x 0.09 x 0.03	0.24 x 0.20 x 0.13
Crystal system	cubic	trigonal	cubic
Space group	<i>P2</i> ₁ <i>3</i>	<i>R3-2</i>	<i>P2</i> ₁ <i>3</i>
<i>a</i> , Å	12.4541(7)	10.3670(8)	12.3830(3)
<i>b</i> , Å	12.4541(7)	10.3670(8)	12.3830(3)
<i>c</i> , Å	12.4541(7)	15.9714(13)	12.3830(3)
α , °	90	90	90
β , °	90	90	90
γ , °	90	120	90

Cell volume, Å ³	1931.7(3)	1486.6(3)	1898.79(14)
Z ; Z'	4 ; 1/3	3 ; 1/6	4 ; 1/3
T, K	100(1)	100(1)	100(1)
Radiation type ; wavelength Å	MoKα ; 0.71073	MoKα ; 0.71073	MoKα ; 0.71073
F ₀₀₀	968	786	1056
μ, mm ⁻¹	3.233	3.133	4.269
θ range, °	2.313 - 32.522	2.602 - 33.709	2.326 - 30.781
Reflection collected	73 560	25 974	28 240
Reflections unique	2 355	1 516	1 827
R _{int}	0.0671	0.0596	0.0245
GOF	1.091	1.097	1.027
Flack parameter	0.033(4)	0.054(5)	0.000(8)
Refl. obs. (<i>I</i> > 2σ(<i>I</i>))	2 185	1 424	1 797
Parameters	72	69	1318
wR ₂ (all data)	0.0865	0.0490	0.0394
R value (<i>I</i> > 2σ(<i>I</i>))	0.0316	0.0205	0.0142
Largest diff. peak and hole (e ⁻ ·Å ⁻³)	1.078 ; -0.472	0.557 ; -0.446	0.522 ; -0.966

1.2 The complexes based on ligand TTC

Table A 4 The crystallographic data structure refinement for complexes **3-1** and **3-2**.

Compounds	3-1	3-2
Formula	Co ₃ C ₃₀ H ₆₉ N ₁₂ S ₃ , 3(ClO ₄)	Co ₃ C ₅₇ H ₅₄ N ₁₅ S ₃ , 3(ClO ₄), 2(C ₂ H ₃ N)
<i>M_r</i>	1169.29	1602.58
Crystal size, mm ³	0.12 x 0.11 x 0.03	0.29 x 0.16 x 0.07
Crystal system	hexagonal	triclinic
Space group	<i>P</i> -62 <i>c</i>	<i>P</i> -1

Appendix I The Crystallographic data

a, Å	13.3628(8)	12.5812(4)
b, Å	13.3628(8)	13.7959(4)
c, Å	49.734(3)	21.1712(6)
α , °	90	73.5590(10)
β , °	90	84.140(2)
γ , °	120	75.5840(10)
Cell volume, Å ³	7690.9(10)	3411.46(18)
Z ; Z'	6 ; 2	2 ; 1
T, K	100(1)	100(1)
Radiation type ; wavelength Å	MoK α ; 0.71073	MoK α ; 0.71073
F ₀₀₀	3654	1642
μ , mm ⁻¹	1.291	0.942
θ range, °	2.146 - 30.543	1.921 - 32.651
Reflection collected	198724	99306
Reflections unique	7951	23611
R _{int}	0.0727	0.0483
GOF	1.242	1.038
Flack parameter	0.046(3)	/
Refl. obs. ($I > 2\sigma(I)$)	7 551	17 393
Parameters	346	940
wR ₂ (all data)	0.1509	0.1115
R value ($I > 2\sigma(I)$)	0.0580	0.0438
Largest diff. peak and hole (e ⁻ .Å ⁻³)	1.109 ; -0.811	1.033 ; -0.795

Table A 5 The crystallographic data structure refinement for complexes **3-3**, **3-4**.

Compounds	3-3	3-4
Formula	C ₃₁ H ₇₆ ClN ₁₅ Ni ₃ O ₄ S ₃ , 2(ClO ₄), 1.5(CH ₄ O)	C ₄₆ H ₉₆ N ₂₁ Ni ₆ O ₆ S ₉ , ClO ₄ , [+ solvent]
<i>M_r</i>	1277.78	1779.60

Appendix I The Crystallographic data

Crystal size, mm ³	0.28 x 0.10 x 0.03	0.14 x 0.09 x 0.02
Crystal system	monoclinic	trigonal
Space group	<i>P</i> 2 ₁	<i>P</i> 31 <i>c</i>
a, Å	15.1573(6)	13.6676(7)
b, Å	23.8748(9)	13.6676(7)
c, Å	15.1614(5)	24.7022(14)
α, °	90	90
β, °	98.363(2)	90
γ, °	90	120
Cell volume, Å ³	5 428.2(3)	3996.2(5)
Z ; Z'	2 ; 1	2 ; 1/3
T, K	100(1)	100(1)
Radiation type ; wavelength Å	MoKα ; 0.71073	MoKα ; 0.71073
F ₀₀₀	2692	1872
μ, mm ⁻¹	1.363	1.714
θ range, °	1.358 - 30.565	1.908 - 30.548
Reflection collected	157 352	57 241
Reflections unique	32 855	8 073
R _{int}	0.0627	0.0798
GOF	1.031	1.278
Flack parameter	0.023(4)	0.296(9)
Refl. obs. (<i>I</i> >2σ(<i>I</i>))	26 459	7 269
Parameters	1281	190
wR ₂ (all data)	0.1756	0.4970
R value (<i>I</i> >2σ(<i>I</i>))	0.0651	0.1781
Largest diff. peak and hole (e ⁻ ·Å ⁻³)	1.748; -1.543	-3.244; 3.528

1.3 The complexes based on ligand HHTP

Table A 6 The crystallographic data structure refinement for complexes 4-1, 4-2, 4-3.

Compounds	4-1	4-2	4-3
Formula	C ₇₂ H ₁₀₈ N ₁₂ Ni ₆ O ₁₅	C ₁₅₃ H ₁₁₁ B ₃ N ₁₈ Ni ₃ O ₆ 7(C ₃ H ₆ O)	C ₁₅₃ H ₁₁₁ B ₃ CO ₃ N ₁₈ O ₆ 8(C ₃ H ₆ O)
<i>M_r</i>	1733.86	2912.70	2971.50
Crystal size, mm ³	0.32 x 0.29 x 0.24	0.10 x 0.09 x 0.03	0.08 x 0.07 x 0.03
Crystal system	trigonal	triclinic	triclinic
Space group	<i>R</i> 3 2	<i>P</i> -1	<i>P</i> -1
<i>a</i> , Å	18.443(2)	14.2552(18)	16.821(3)
<i>b</i> , Å	18.443(2)	17.287(2)	17.771(3)
<i>c</i> , Å	22.759(3)	32.407(4)	26.730(4)
α , °	90	94.408(4)	97.162(5)
β , °	90	101.051(4)	90.043(5)
γ , °	120	101.473(4)	105.344(4)
Cell volume, Å ³	6704.2(17)	7626.4(17)	7641(2)
<i>Z</i> ; <i>Z'</i>	3 ; 1/6	2 ; 1	2 ; 1
<i>T</i> , K	100(1)	100(1)	100(1)
Radiation type ; wavelength Å	MoK α ; 0.71073	MoK α ; 0.71073	MoK α ; 0.71073
<i>F</i> ₀₀₀	3300	3046	3120
μ , mm ⁻¹	1.260	0.399	0.391
θ range, °	1.558 - 32.697	2.156 - 30.951	2.171 - 30.676
Reflection collected	50978	217860	523133
Reflections unique	5491	47603	47141
<i>R</i> _{int}	0.0335	0.3232	0.3751
GOF	1.100	1.015	0.917
Refl. obs. (<i>I</i> > 2 σ (<i>I</i>))	5109	16901	17910

Appendix I The Crystallographic data

Parameters	214	1 856	1 961
wR ₂ (all data)	0.1197	0.3390	0.1400
R value ($I > 2\sigma(I)$)	0.0417	0.1390	0.0769
Largest diff. peak and hole (e ⁻ ·Å ⁻³)	1.032 ; -1.551	1.483 ; -1.003	1.220 ; -1.064

Résumé

L'objectif consistant à élaborer des «aimants par conception» peut être atteint en adaptant les structures moléculaires des complexes de coordination. Les molécules conçues devraient présenter les caractéristiques requises pour des applications spécifiques, résultant virtuellement de leur riche diversité structurale. Des complexes mononucléaires à base de Ni avec une grande anisotropie magnétique, des molécules polynucléaires à base de Ni et de Co pontés par un ligand innocent et un ligand non innocent sont conçus dans cette thèse. Les synthèses, les études magnétiques et les propriétés électrochimiques des complexes contenant un ligand pont non innocent sont examinées, couplées aux calculs théoriques sur certains de ces complexes.

Les complexes mononucléaires Ni(II) à géométrie bipyramide trigonale ont été préparés en ajustant les ligands axiaux et les contre-anions. Dans cette partie, nous avons introduit le ligand Me₆tren pour préparer les complexes (Me₆tren = Tris(2-(diméthylamino)éthyle)amine). L'effet de la nature des ligands axiaux et le changement structurel induit par les contre-anions sur l'anisotropie magnétique ont été étudiés expérimentalement et analysés à l'aide de calculs théoriques. Les résultats ont révélé que la taille des contre-anions et la nature du tassement dans les cristaux affectaient la symétrie locale des structures moléculaires. Dans le complexe [Ni(Me₆tren)Cl]Cl·2H₂O, les molécules d'eau ont réduit sa symétrie locale, en comparaison avec le complexe déshydraté [Ni (Me₆tren)Cl]Cl à 100 K. Les études magnétiques et théoriques ont révélé que le Ni(II) les complexes présentant une symétrie plus élevée de la structure moléculaire possèdent un paramètre ZFS axial plus grand, D (en absolu), et un paramètre transverse E plus faible. Pour les complexes avec d'autres ligands axiaux, les complexes avec Cl possèdent une anisotropie magnétique plus grande.

De grandes molécules organiques ont été utilisées pour concevoir des complexes polynucléaires à grande anisotropie magnétique et à couplage d'échange faible. Plusieurs complexes polynucléaires à base de Ni et de Co avec TTC³⁻ agissant en tant que ligand

pontant innocent et HHTP en tant que ligand non innocent typique ont été préparés et cristallisés avec diverses structures moléculaires (TTC = Trithiocyanurate; HHTP = Hexahydroxytriphénylène).

Pour les complexes pontés par un ligand innocent (TTC³⁻), les couplages d'échange se sont avérés très faibles, comme prévu. Les calculs théoriques ont été effectués, mais il est difficile de tirer des conclusions simples sur la corrélation entre les structures moléculaires et les paramètres ZFS axiaux.

Pour les complexes contenant le ligand non innocent (HHTP), un complexe hexanucléaire Ni(II) de structure bicouche et deux complexes trinuécléaires à base de Ni et de Co ont été synthétisés et la charge du pont HHTP dans ces complexes a été trouvée être 3-, à l'état d'oxydation de la tri-semiquinone. Dans le complexe hexanucléaire Ni, la structure moléculaire montrait que les interactions faibles entre les deux couches rendaient le complexe thermodynamiquement stable et les données magnétiques révélaient un très faible couplage d'échange antiferromagnétique au sein de l'espèce dimère et qu'il n'existait pas d'électrons non-appariés dans le complexe. Dans le complexe trinuécléaire Ni(II), des radicaux ont été produits et délocalisés dans le cycle aromatique, ce qui a pour résultat qu'un plus grand caractère de semiquinone apparaît près d'un ion Ni(II). La combinaison de spectroscopie spectro-électrochimique et paramagnétique d'électrons couplée à des études électrochimiques a permis d'étudier la délocalisation des électrons sur les radicaux organiques générés et le couplage d'échange entre les ions métalliques. Les pics d'onde réversibles par étapes observés dans les études électrochimiques ont révélé que les processus de réduction étaient centrés sur le ligand, ce qui a été attesté par ses spectres électroniques. Le complexe trinuécléaire à base de Co présentait une structure moléculaire et un comportement électrochimique similaires à ceux du complexe trinuécléaire Ni. Cependant, les propriétés magnétiques suggéraient probablement qu'un processus d'oxydo-réduction avait lieu à basse température pendant la mesure. Davantage de mesures devraient être effectuées pour fournir des preuves de ce tautomérisme de valence, le cas échéant.

Titre : Synthèses, structures cristallines et caractérisations d'aimants moléculaires mono- et polynucléaires à base de Ni et de Co

Mots clés : Chimie de coordination, Aimants moléculaires, Anisotropie magnétique, Complexes mononucléaires et polynucléaires

Résumé : L'objectif consistant à élaborer des «aimants par conception» peut être atteint en adaptant les structures moléculaires des complexes de coordination. Les molécules conçues devraient présenter les caractéristiques requises pour des applications spécifiques, qui résultent de leur riche diversité structurale. Des complexes mononucléaires à base de Ni avec une grande anisotropie magnétique et des molécules polynucléaires à base de Ni et de Co sont préparés et étudiés dans cette thèse. Les synthèses, les études magnétiques et les propriétés électrochimiques des complexes contenant un ligand pontant non innocent sont étudiées.

Les complexes mononucléaires Ni(II) à géométrie bipyramide trigonale sont préparés avec des ligands axiaux et les contre-anions différents. L'effet de la nature des ligands axiaux et du changement structural induit par les contre-anions sur l'anisotropie magnétique est étudié expérimentalement et analysé

à l'aide de calculs théoriques.

Des molécules organiques sont utilisées pour concevoir des complexes trinucéaires à grande anisotropie magnétique et à couplage d'échange faible. Plusieurs complexes polynucléaires à base de Ni et de Co où le TTC^{3-} agit comme un ligand pontant innocent et le HHTP^{3-} comme un ligand non innocent typique sont cristallisés avec diverses structures (TTC = Trithiocyanurate; HHTP = Hexahydroxytriphenylène). Pour les complexes contenant le ligand non innocent (HHTP), les anions radicalaires sont produits par électrochimie. La combinaison de la spectro-électrochimie et de la spectroscopie à résonance paramagnétique électronique couplée à des études d'électrochimie permet d'étudier la délocalisation des électrons sur les radicaux organiques générés et le couplage d'échange entre les ions métalliques.

Title : Syntheses, crystal structures and characterizations of mono- and polynuclear Ni- and Co-based molecular magnets

Keywords : Coordination chemistry, Molecular magnets, Magnetic anisotropy, Mononuclear and polynuclear complexes

Abstract : The objective of elaborating “magnets by design” can be achieved by tailoring the molecular structures of coordination complexes. The designed molecules are expected to exhibit the characteristics required for specific applications, virtually resulting from their rich structural diversity. Mononuclear Ni-based complexes with large magnetic anisotropy and polynuclear Ni- and Co-based molecules are designed in this dissertation. The syntheses, magnetic studies, and electrochemical properties of the complexes containing non-innocent bridge ligand are investigated.

The Ni(II) mononuclear complexes with trigonal bipyramid geometry are prepared by tuning the axial ligands and the counter anions. The effect of the nature of the axial ligands and the structural change induces by the counter anions on magnetic

anisotropy is studied experimentally and analyzed with the help of theoretical calculations.

Large organic molecules are used to design trinuclear complexes with large magnetic anisotropy and weak exchange coupling. Several polynuclear Ni- and Co-based complexes with TTC^{3-} acting as an innocent bridging ligand and HHTP as a typical non-innocent ligand, are crystalized with various structures (TTC = Trithiocyanurate; HHTP = Hexahydroxytriphenylene). For the complexes containing the non-innocent ligand (HHTP), radical anions are produced by electrochemistry. The combination of spectroelectrochemical and Electron Paramagnetic Spectroscopy coupled to electrochemistry studies allow investigating the delocalization of the electrons on the generated organic radicals and the exchange coupling among the metal ions.

